PRACTICAL ENGINEERING METHODS FOR PRE[

HOT GAS REINGESTION CHARACTERISTIC[

V/STOL AIRCRAFT JET-LIFT ENGINE[

**dynasciences** CORPORATION

# PRACTICAL ENGINEERING METHODS FOR PREDICTING

# HOT GAS REINGESTION CHARACTERISTICS OF

# V/STOL AIRCRAFT JET-LIFT ENGINES

By

L. Gray
E. Kisielowski

February 1971

## ABSTRACT

Engineering methods are presented for predicting the temperatures and velocities in the vicinity of vertical lift engines of jet V/STOL aircraft operating near the ground. The methods are based on existing theoretical analyses, available test data, and empirical and semiempirical approaches. Parametric variations in engine nozzle diameter, pressure, temperature, height, and ambient crosswind velocity are considered for single-, two-, and four-nozzle (rectangular) arrangements. Additional test data will be required to adequately verify some of the prediction methods.

## SUMMARY

This report presents practical engineering methods for
predicting the velocity and temperature distributions of the flow
field in the vicinity of vertical jet lift engines of V/STOL
aircraft operating in ground proximity. These methods are based
on the existing theoretical analyses, available test data and
empirical and semi-empirical approaches some of which will be
required to be verified by future test results. Parametric vari-
ations in engine nozzle diameter, pressure, temperature, height,
and ambient crosswind velocity are considered for single-, two-,
and four-nozzle (rectangular) configurations. For these nozzle
configurations design procedures are also presented for estimating
the inlet air temperature rise characteristics for top-mounted and
forward-facing inlets.

# FOREWORD

This work was performed by the Scientific Systems Division (SSD) of Dynasciences Corporation, Blue Bell, Pennsylvania for the National Aeronautics and Space Administration (NASA), Langley Research Center, Hampton, Virginia, under contract number NAS 1-9564 during the period from September 1969 through October 1970.

# CONTENTS

# LIST OF SYMBOLS

$A_i$     area of engine intake, $ft^2$

$A_j$     area of single engine exhaust nozzle, $ft^2$

$A_w$     wing area, $ft^2$

$C_D$     jet nozzle mass flow discharge coefficient, defined as actual/ideal ratio

$C_H$     jet nozzle differential total temperature discharge co-efficient, defined as actual/ideal ratio

$D$     diameter, ft

$G$     gas constant for air, (1716 ft. lb./slug $^{o}R$)

$g$     gravitational acceleration, 32.2 ft./sec.$^2$

$H$     height coordinate above ground plane, ft.

$h$     wall jet height coordinate above ground plane, ft.

$h_p$     wall-jet pressure boundary height, defined by $(\Delta P_t) = 0.25 \ (\Delta P_{t\omega})$, ft.

$h_t$     wall-jet temperature boundary height, defined by $(\Delta T_t) = 0.5 \ (\Delta T_{t\omega})$, ft.

ITR     inlet temperature rise, $^{o}F$.

$K,k$     constants, as defined in text.

$K_n$     constant to account for effect of engine exhaust nozzle geometry

ln     logarithm to base e

$M$     Mach number

$M_{( \ )}$     momentum, lbs. force/sec.

$m_{( \ )}$     mass flow, slugs/sec.

$P$     absolute static pressure, $lbs/ft^2$

$\Delta P$     differential static pressure, measured above ambient static, $lbs/ft^2$

$P_t$      absolute total pressure, lbs/ft$^2$.

$\Delta P_t$      differential total pressure, measured above ambient static, lbs/ft$^2$

q      dynamic pressure, $(1/2 \rho \, u^2)$, lbs/ft$^2$.

R      ground radial coordinate measured from ground impingement stagnation point.

$R_w$      Reynolds number for wall jet flow, $(0.83 \, h_p \, u_w / \nu)$

r      radial coordinate for free-jet measured in plane perpendicular to the local jet center-line, ft.

$r_C$      local radius of the potential core in the free jet, ft.

$r_p$      free-jet pressure boundary radius, defined by $\Delta Pt = 0.25$ $(\Delta P_{tc})$, ft.

$r_t$      free-jet temperature boundary radius, defined by $\Delta Tt = 0.5 \, (\Delta T_{tc})$, ft.

$\bar{r}$      normalized free-jet radial coordinate, $(r/r_j)$.

S      jet centerline coordinate measured along the jet path downstream from the nozzle exit plane, ft.

T      absolute static temperature, $^\circ$R.

$\Delta T$      differential temperature, measured above ambient static, $^\circ$F.

Tt      absolute total temperature, $^\circ$R.

$\Delta T_t$      differential total temperature, measured above ambient static, $^\circ$F.

u      gas velocity, ft/sec.

Xj      longitudinal separation between jet axes of multi-nozzle configurations.

Yj      lateral separation between jet axes of multi-nozzle configurations.

x      horizontal co-ordinate through center of nozzle exit, measured positive rearward relative to aircraft axes, ft.

$x_w$      horizontal coordinate through center of nozzle exit, measured positive along crosswind vector

| | |
|---|---|
| y | horizontal co-ordinate normal to x, ft. |
| z | vertical co-ordinate, measured positive down from jet nozzle exit plane, ft. |
| $\beta$ | angle between local wall jet flow and interaction plane |
| $\gamma$ | ratio of specific heats for ambient air, (1.4) |
| $\mu$ | crosswind ratio, $\sqrt{(\Delta P_{t\infty}/\Delta P_{tj})}$ |
| $\nu$ | dynamic viscosity, $ft^2/sec$ |
| $\phi$ | azimuthal co-ordinate of ground radius vector, measured from upstream wind vector, degrees |
| $\rho$ | density, $slugs/ft^3$ |
| $\psi$ | angle between ambient wind vector and -x axis, degrees |
| $\theta$ | angle between tangent to local free-jet centerline and downwind |
| $\theta_t$ | angle between tangent vector to the free jet axis at impingement and the local wall jet vector |
| $S_1$ to $S_4$ | axial correlation parameters for free-jet region, defined by equations 3,4,13 and 14. |

## SUFFIXES

| | |
|---|---|
| a | ambient static conditions |
| B | denotes boundary of jet flow, as defined in text |
| b | conditions denoting limit of hot gas penetration |
| C | conditions at edge of potential core of free-jet |
| c | conditions on centerline of free jet |
| e | dimension based on equivalent single nozzle diameter for multi-nozzle configurations |
| f | conditions on axis of hot gas fountain |
| g | reference conditions in free jet used for defining ground impingement parameters |
| h | conditions on axis of convective flow in the recirculation region |

i      conditions in engine intake plane

j      conditions in plane of nozzle exit

s      conditions at point of separation by ground flow

w      conditions for peak total/static pressure and total temperature close to the groundplane

$\infty$      freestream conditions (non-zero)

NOTE: Unless otherwise defined, a bar subscript denotes ratio to jet nozzle parameters $\Delta Ptj$, $\Delta Ttj$, or $Dj$ as appropriate

# PRACTICAL ENGINEERING METHODS FOR PREDICTING HOT GAS REINGESTION CHARACTERISTICS OF V/STOL AIRCRAFT JET-LIFT ENGINES

By L. Gray, E. Kisielowski
DYNASCIENCES CORPORATION

## SECTION I

## INTRODUCTION

One of the most serious operational problems associated with V/STOL jet-lift aircraft operating in ground proximity is the down-wash impingement of hot gas efflux from the lift engines and accompanying hot gas recirculation and ingestion into the engines.

The ingestion of hot exhaust gases causes elevated engine inlet air temperatures and consequently can result in a significant degradation of engine thrust performance and in possible over-temperature operation of the engine. A thrust loss of about 1% for each 3°F increase in mean inlet air temperature is typical for current jet-lift engine designs. Furthermore, the rapid temperature fluctuation and severe spatial temperature distortion that may occur in an engine inlet are known to cause compressor blade stall. Such compressor blade stall is usually followed by a large and abrupt thrust loss which constitutes a serious safety hazard for both aircraft and crew.

It is, therefore, essential to provide the airframe and engine designers with reliable engineering methods for predicting the inlet temperature rise (ITR) characteristics of a given aircraft configuration in order that engine thrust performance and susceptibility to engine stall may be estimated and avoided through early design modifications. In addition, quantitative information pertaining to velocity and temperature distributions in the vicinity of V/STOL jet-lift aircraft is required for airframe design purposes.

During the past decade and particularly in recent years, the flow field characteristics associated with hot gas ingestion have been the subject of extensive theoretical and experimental studies involving both small and large scale model testing. As a result of these studies, there now exists a qualitative understanding of the mechanism of hot gas recirculation. In essence, the hot gas jet impinging on the ground spreads radially along the ground until the horizontal flow no longer has the energy to overcome the shear forces along the ground. At this point, the hot gas flow rolls up into a torus shaped cloud pattern around the jet-lift engine. The roll up is

hastened by hot gas buoyancy effects which increase the vertical velocity component of the initial radial flow. During the entire process, extensive turbulent mixing with the surrounding atmosphere takes place. The engine air intake acts as a sink at the center of the torus of hot gas and in consequence some of the hot gas is ingested into the engine air inlet. Ambient wind velocities as low as a few knots can distort the hot gas flow pattern to such extent that, depending on aircraft configuration, the hot gas ingestion may be significantly increased or decreased.

Although there is a qualitative understanding of the hot gas recirculation and ingestion mechanism, no systematic and comprehensive theoretical treatments or practical (semi-empirical) approaches have been developed and verified by adequate full- and large-scale experimental data for the purpose of providing fundamental guidelines to the design of jet-lift V/STOL aircraft. The results of a substantial number of relevant theoretical and experimental studies are, however, available for isolated portions of the flow field. Several investigators have condensed generalized analytical methods for major regions of the exhaust flow by a selection of appropriate part-solutions (mostly theoretical) from reviews of the literature. However, these methods lack sufficient detail and are not entirely suited to practical engineering methods.

The present investigation, therefore, re-evaluates the available existing technical literature, both theoretical and experimental, in order to develop a unified engineering approach for predicting velocity and temperature distributions of the flow in the vicinity of the jet-lift engines of V/STOL aircraft operating in ground proximity. The following analysis is restricted to hovering flight with consideration given to the effects of ambient crosswinds.

2

SECTION 2

THEORETICAL ANALYSIS

Presented in this section is a brief review of available theoretical approaches for predicting hot gas reingestion characteristics of typical direct-lift turbojet-powered V/STOL aircraft operating in ground proximity. An evaluation of existing theoretical treatments and available test data formed the basis for the development of practical engineering methods for predicting the velocity and temperature distributions as presented in Section 3. The basis for selection and the adequacy of the analytical methods used in formulating the engineering flow model are discussed below.

2.1 GENERAL CONSIDERATIONS

A cursory examination of the flow conditions of jet lift engines operating in ground proximity shows that the physical characteristics of the jet efflux correspond to those of a convergent nozzle operating at stagnation pressure ratios up to approximately 2 and at temperatures typically in the range 1000 to 2000°F. Since this range of operating condition includes high subsonic and even underexpanded sonic flow at the nozzle exit, the resulting flow field in the vicinity of jet-lift engines will be largely dependent on jet density changes, buoyancy effects, and turbulent mixing of hot gases with cooler surrounding air.

A complete analytical treatment of the hot gas characteristics including the effects of turbulent mixing, compresibility and buoyancy effects is indeed a very formidable task and no reliable solutions to the problem are presently available. However, several investigations have attempted analyses which are applicable to limited portions (regions) of the flow field.

2.2 DEFINITION OF FLOW REGIONS

While a unified theoretical treatment of the hot gas flow field does not exist, a composite analytical model can be constructed by subdividing the entire flow field into a number of convenient regions as shown in Figure 1. Each individual region is chosen on the basis that the enclosed flow field approximately corresponds to a simplified type of flow behavior for which theoretical treatments are available. Thus the entire hot gas recirculation phenomenon can, in principle, be represented by a linked chain of isolated analyses, each applicable to a specific region. The various regions, as shown in Figure 1(a), are defined as follows:

3

Flow Regions

| | |
|---|---|
| A | Free Jet |
| B | Ground Impingement |
| C | Radial Wall Jet |
| D | Far-Field Recirculation |
| E | Intake Near Field |
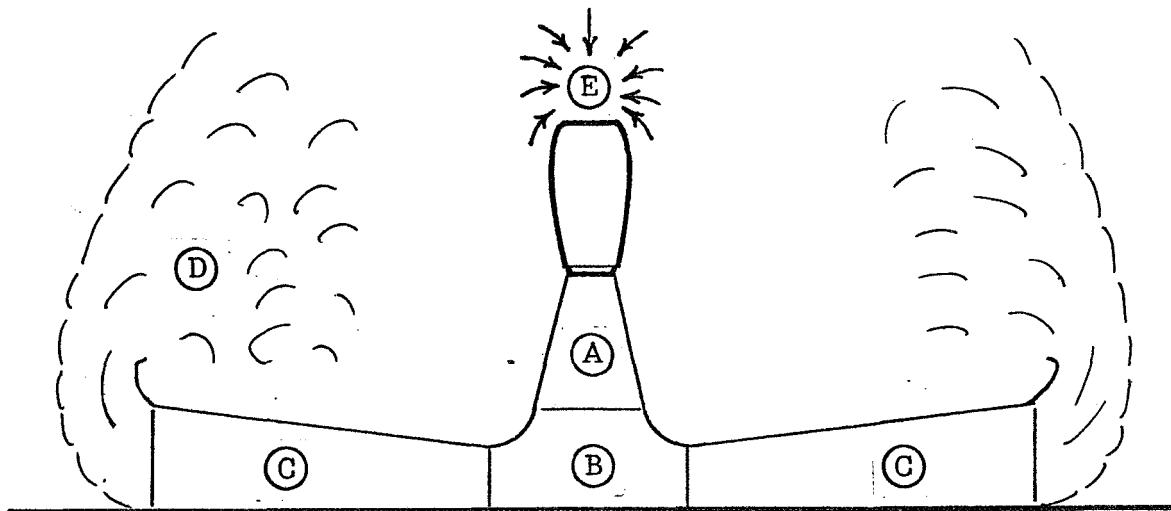
(a) Flow Field Under Static Ambient Conditions
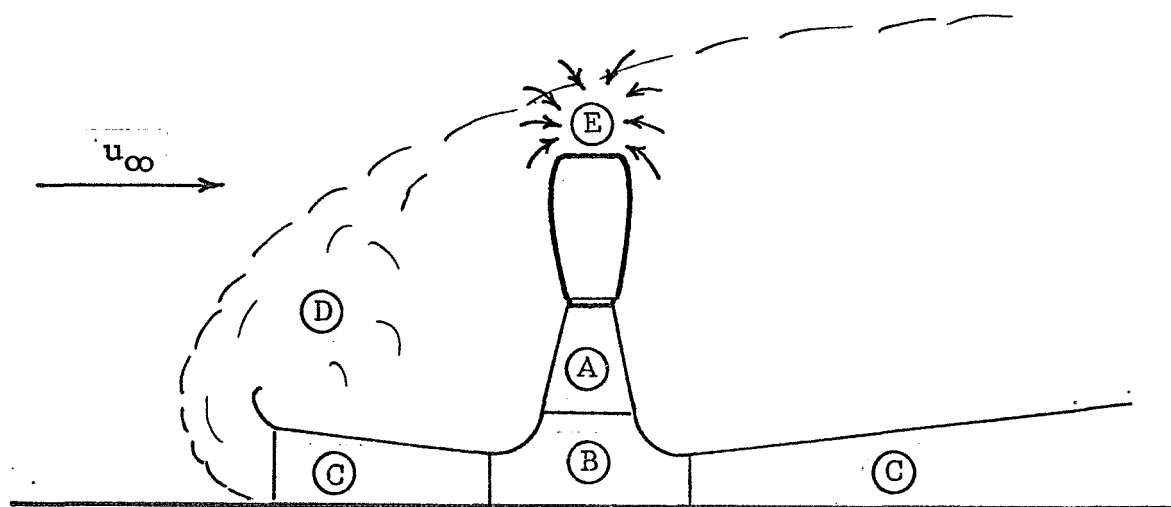
(b) Flow Field Under Steady Crosswind Conditions

Figure 1.- Analytical Representation of the Hot Gas Flow
Field in the Vicinity of a Single Engine.

4

## REGION A. Free Jet Flow

This region extends downwards from the engine exhaust nozzle
and is characterized by free turbulent mixing with the sur-
rounding air. This results in a progressive growth and ex-
pansion of the vertical jet flow for which the effects of
ground proximity can be neglected. In the presence of a
crosswind (See Figure 1(b)) jet flow is distorted and curves
toward the direction of the crosswind.

To facilitate formulation of the mathematical model, this
flow region is divided into four distinct axial flow sub-
regions as shown in Figure 2. These sub-regions are defined
as follows:

### 1. Potential Core Region

This is approximately a conical flow region whose base is
contained by the jet exit and whose apex lies several diameters
downstream on the jet axis. This is the only region of the
flow field which is essentially isolated from the turbulent mix-
ing process with the ambient air and is characterized by a uniform
velocity approaching the value at the jet exit.

### 2. Annular Mixing Zone

The potential core region defined above is bounded by an
annular mixing zone where turbulent mixing between the jet and
ambient air takes place. The external boundary of this region
spreads outward as the flow moves downstream, and the mixing
process eventually permeates the whole jet at the apex of the
potential core.

### 3. Transition Region

This region pertains to flow between the end of the potential
core and the start of the characteristic decay region described
below. Its length is about the same as that of the potential
core. It is completely permeated by the turbulent mixing process
but the decay of axial velocity along the jet axis has not yet
reached the inverse function relationship, whereby the axial
velocity is inversely proportional to axial distance.

### 4. Characteristic Decay Region

This region is completely permeated by the turbulent mixing
process. It extends downstream from a point beyond the limit of
the potential core where the entire flow reaches and maintains a
profile similarity and where the velocity along the jet axis de-
cays approximately in inverse proportion to the downstream
distance.

5
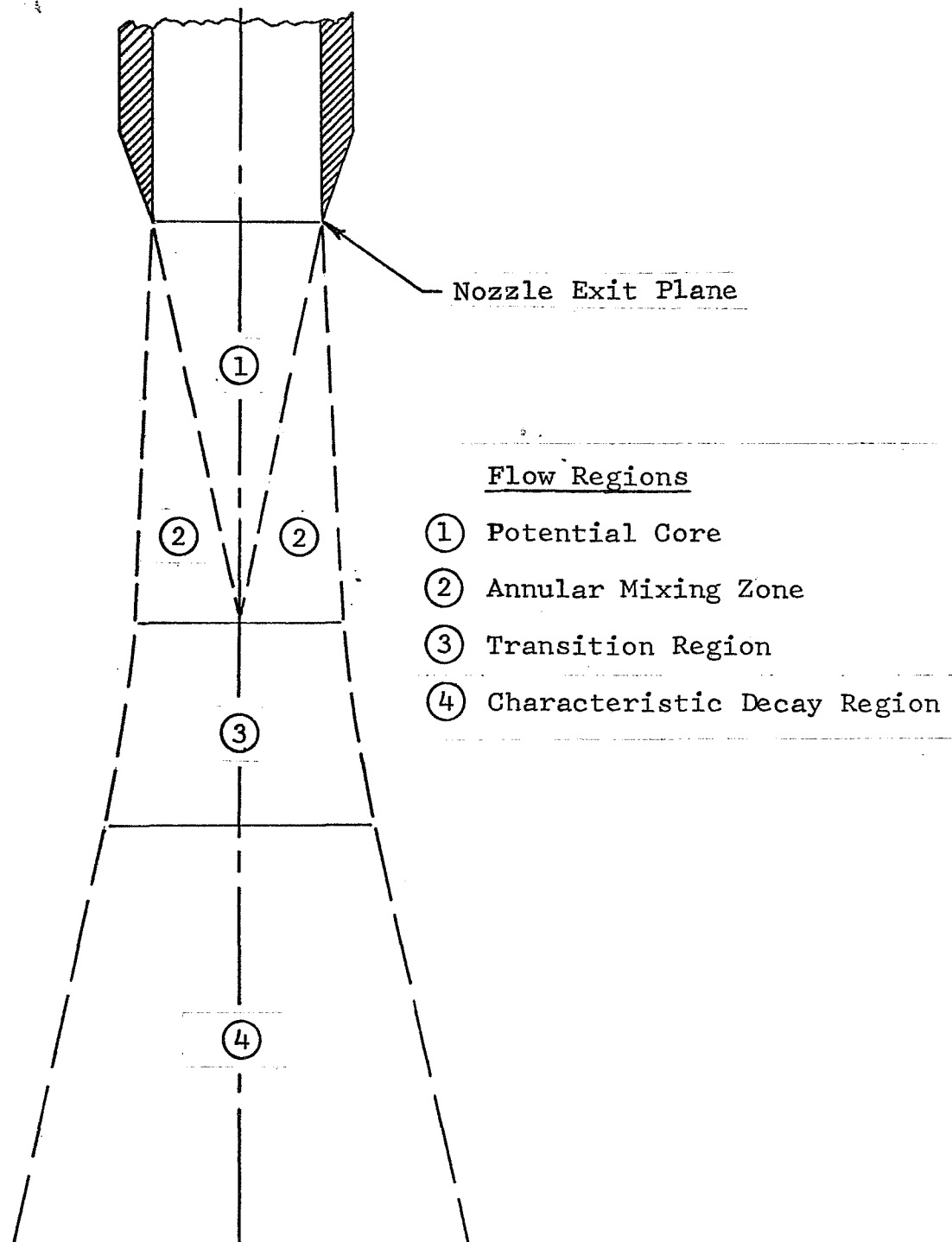
Figure 2.- Characteristic Flow Regions Downstream of a
Uniform Axisymmetric Free Jet Exhausting
Under Static Conditions.

6

REGION B. Ground Impingement Flow

As the flow in the free jet approaches the ground, the jet core undergoes a rapid deceleration and interchange of kinetic and pressure energy as it turns radially outward along the ground. This region as shown in Figure 1 represents continuation of the flow between the free jet, the ground plane, and the wall jet region (described below).

REGION C. Radial Wall Jet Flow

After the flow turning process associated with ground impingement is completed, the ground flow soon achieves a condition of stable radial expansion and decay. Here, the flow field is characterized by free turbulent mixing with surrounding air and a boundary layer along the ground plane. In the case of a hot jet this flow eventually becomes unstable and separates from the ground due to buoyancy forces overcoming the radial shear and momentum forces. The process of ground separation can be hastened under the influence of adverse crosswinds, (See Figure 1(b)).

REGION D. The Far-Field Recirculation Flow

The separated wall jet flow is influenced by the effects of hot gas buoyancy, crosswinds, and also the combined "sink" effect of the intake flow and turbulent mixing process in Regions A, B, and C. The recirculating flow is contained within an envelope which represents the outer boundary of the turbulent mixing process with the ambient air.

REGION E. The Intake Near-Field Flow

Air is drawn into the engine inlets by the "sink" effect of the intakes. The magnitude and spatial distribution of the temperatures at the inlet plane are therefore sensitive to the temperature properties of the recirculating flow surrounding the inlets.

REGION F. The Interaction Plane Flow

The interaction flow is produced by mutual impingement of jet flows from two or more engines. Although it is possible for multi-jet exhausts to coalesce prior to ground impingement, this interaction flow is more generally caused by the impingement of opposing wall jets. Such a flow is characterized by an interchange of kinetic and pressure forces and by a change in the flow vector from the horizontal to vertical direction. This flow region (shown in Figure 3) is also referred to as the hot gas fountain, whose strength and direction depend on

7

Flow Regions

A  Free Jet
B  Ground Impingement
C  Radial Wall Jet
D  Far-field Recirculation
   & Entrainment
E  Intake Near-field
F  Groundflow Interaction
   & Hot Gas Fountain
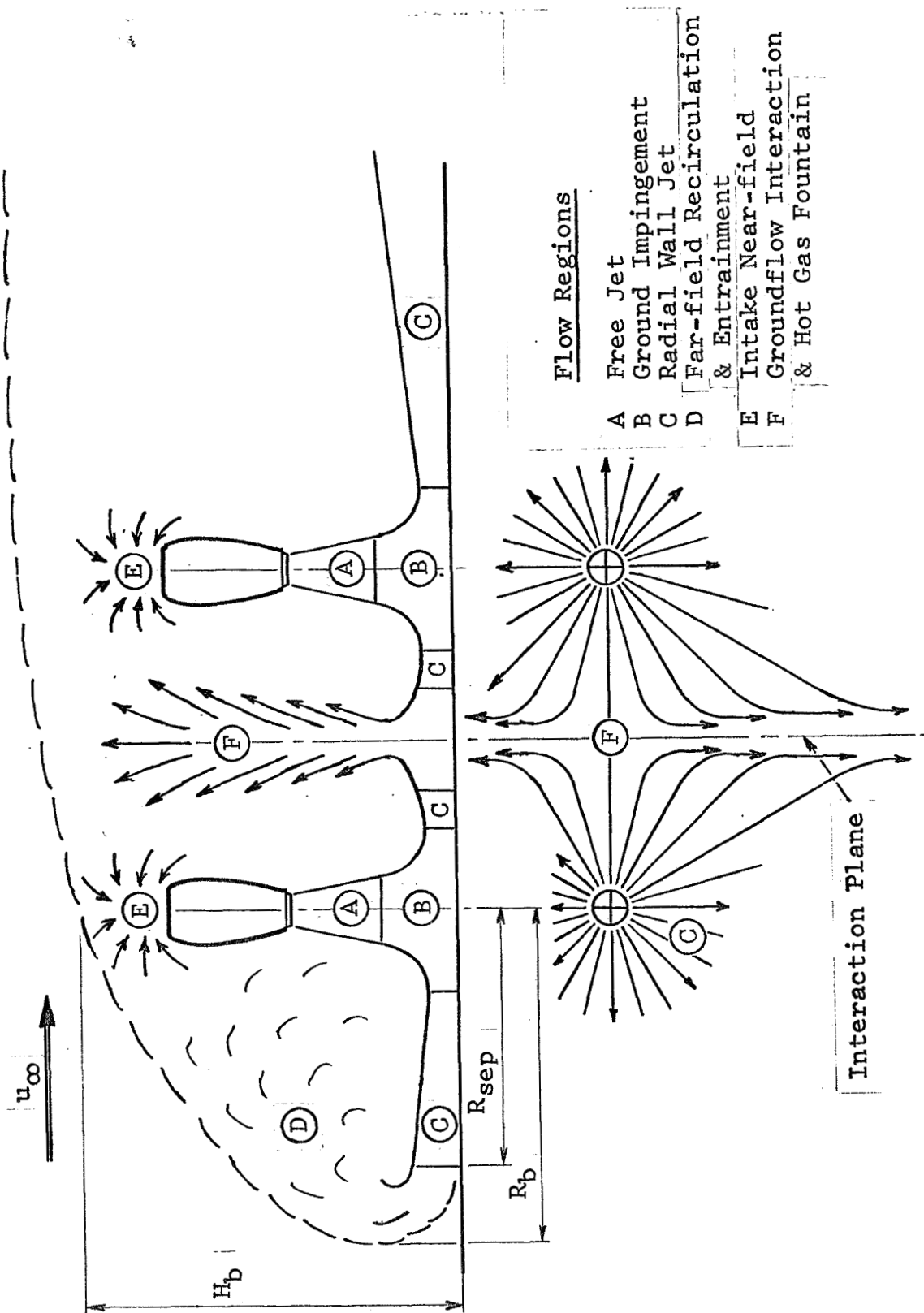
Figure 3.— General Representation of the Hot Gas Flow Field
in the Vicinity of Multi-Nozzle Configurations.

aircraft/engine geometry and flow conditions of the particular nozzle configuration.

In formulating the mathematical model for predicting flow characteristics in each of the above defined flow regions, it is convenient to initiate the analysis for a single engine jet flow in ground proximity. The effect of steady ambient crosswinds and treatments for multi-nozzle configurations are included by utilizing empirical methods as discussed later in the text.

## 2.3  REVIEW OF THE EXISTING ANALYTICAL APPROACHES

In reviewing the available technical literature it is noted that most theoretical treatments of the three-dimensional flow from a jet nozzle rely upon assumptions that the velocity in the plane of the nozzle exit is both uniform and axial (i.e. no swirl). These assumptions result in a substantial simplification of the mathematical considerations.

Available analyses, which are normally limited to circular nozzles with no crosswind effects, consider the time-variant and/or time-average flow behavior of which only the latter type is of direct interest here. However, most of these analyses are generally considered inadequate for providing practical engineering solutions and therefore utilization of test data is generally recommended wherever possible. Major difficulties lie in the fact that the application of the existing theories strongly depends on the empirical evaluation of time-average the turbulent mixing phenomena. This naturally leads to time-average flow solutions which generally are in a fair to good agreement with the available test data, although usually only for limited ranges of flow conditions.

The sub-sections below present a more detailed discussion of the available theoretical approaches pertaining to each specific flow region described previously. This discussion considers flow conditions with and without crosswinds.

## 2.3.1  Region A- Free Jet Flow

A number of theoretical and experimental studies for axially symmetric free jets have been performed by various investigators. The most pertinent information on turbulent mixing of free jets was published by Forstall and Shapiro (Reference 1), Halleen (Reference 2), and Kryzwoblocki (Reference 3). Although these analyses are limited to incompressible isothermal flow conditions they are important in establishing the basic flow field behavior within each sub-region of the free jet as shown in Figure 2.

9

An early analytical solution for the potential core and the annular mixing region of free jets was obtained by Kuethe (Reference 4) by using Prandtl's mixing length concept. This solution although limited to incompressible isothermal flow conditions, indicates that the length of the potential core is about five nozzle diameters and that the velocity profile in the annular mixing region is approximately affine and can be represented by an exponential form. Agreement with experimental data obtained for incompressible conditions is shown to be generally good.

Such a representation is, however, inadequate for the present investigation since it is necessary to calculate temperature distributions and to account for flow compressibility and temperature differential effects. Although these effects are shown by experimental data to be appreciable, there are no known analyses which yield satisfactory results.

Numerous theoretical studies of the flow in the characteristic decay region have been reported. Most are based on rational assumptions of a uniform static pressure and a flow profile similarity at all downstream distances. The analytical results thus obtained are generally in a good agreement with the data of many experimental tests.

While many theories (for e.g., References 5 and 6) do not account for the presence of jet compressibility effects and temperature differential, these considerations have recently received substantial attention in both theoretical and experimental investigations. Warren, (Reference 7), obtained experimental results for high subsonic and fully-expanded supersonic heated jets exhausting into a static enviornment. The application of a momentum integral analysis to the test data indicates that the local downstream flow characteristics are primarily governed by the nozzle exit Mach number $(Mj)$ and stagnation temperature ratio $(Ttj/Ta)$. Experimental comparison was made with the analytical predictions based on the assumption of a constant mixing rate parameter. This yields poorer correlation for high-subsonic jet velocities and indicates that the mixing rate parameter should in fact vary with the initial jet Mach number.

Later, an extension of Warren's analysis to allow for the mixing of dissimilar gases was developed by Donaldson (Reference 8). The experimental measurements show that the mixing rate parameter could be more adequately expressed, to first order, solely in terms of a suitably chosen local flow Mach number. Although good predictions are obtained over a wide range of conditions, this method requires a step-by-step numerical solution.

Many other theories (References 9 to 14) attempt to account for different combinations of jet compressibility, temperature, and density effects by employing various assumptions in solving the basic equations of motion. However, practical solutions to the more generalized theories (for example, References 7, 8, 10, and 14) are usually tedious and require numerical integration techniques. Alternatively, other analyses which offer relatively simple closed-form solutions through additional approximations normally lead to results that do not satisfactorily account for the full range of jet conditions considered here. At this point special mention should be made of the work of Kleinstein (Reference 12), whose analysis offers an approximate solution that includes the transition region. More recently, Cook and Singer (Reference 14) have extended Kleinstein's analysis to include the variation of mixing rate parameter determined by Donaldson (Reference 8) but their method also requires a step-by-step numerical solution.

None of these theories are suitable for predicting the flow characteristics of under-expanded sonic jets, which are also of interest in the present investigation. This is due to the occurrence of rapid changes in the jet flow structure as the stagnation pressure ratio ($P_{tj}/P_a$) is increased. Experimental observations (References 15, 16 and 17) show that moderately under-expanded sonic jets ($P_{tj}/P_a \geqslant 2.0$) exhibit a system of interacting shock patterns which dominate the potential core and may extend for many nozzle diameters downstream. Donaldson (Reference 8) suggested that the flow may be treated in terms of an effective jet Mach number and jet diameter appropriate to isentropic shock-free expansion of the jet flow to the ambient pressure value. However, no validation of this method is given.

In view of the above discussion, it seems clear that a mathematical model of the free-jet region should be largely empirical. Although much of the available data pertains to incompressible isothermal flow ($M_j < 0.4$, $T_{tj} = T_a$), References 7, 9, 13, 17, 18, 19, and 20 are considered to be important sources of experimental data where temperature differential and compressibility effects are isolated. This data is used as the basis for developing an empirical flow model, as detailed later in section 3.

When a vertical axisymmetric jet is subjected to a cross-wind the resulting path curvature (Reference 21) implies that the jet-to-free-stream mixing process is asymmetric about the local jet axis. This makes analytical treatment particularly complex.

It is apparent from the results of many investigations (References 22 through 33) that theoretical analyses detailing the physical flow field behavior for a free jet with crosswind effects are generally unsuitable for application as simple prediction tools. In this respect the work of Braun and McAllister (Reference 34) is considered noteworthy although their analysis does not specifically account for either compressibility or temperature effects.

In many of the published analytical studies (for example, References 22 through 27) empirical, or semi-empirical, distributed sink and vorticity representations of the jet were utilised to calculate the aerodynamic interference velocities and loadings on a wing or flat surface representative of certain V/STOL configurations in transition flight. However, these jet models offer no useful mathematical description of the flow field other than an expression for the jet centerline path. Other analytical predictions for the jet path have also been developed and are reported in References 28 through 32.

Early analyses (References 11, 32) explained the jet path curvature by a free-stream drag force acting along the jet. However, this requires the use of unrealistic drag coefficients to approximate the jet path. Recently, the use of mass-entrainment and momentum-conservation techniques have proven more successful, as exemplified by Wooler (Reference 25) and Braun and McAllister (Reference 34). These solutions, however, do not account for flow compressibility and jet temperature differential effects. Furthermore, these solutions do not offer a significant advantage over empirical formulations within limited ranges of crosswind-to-jet velocity ratio ($u_\infty/u_j$).

The analysis of hot gas ingestion characteristics on typical V/STOL aircraft configurations indicates that values of $(u_\infty/u_j) < 0.1$ and exhaust nozzle heights less than 10 nozzle diameters are of primary interest. While many empirical equations for the jet path have been developed, that due to Ivanov, as presented by Abramowich in Reference 11, is considered to be most representative for the above range of crosswind-to-jet velocity ratios.

Ivanov's expression was based on experimental measurements for an isothermal jet. However, Abramowich (Reference 11) reports that the dynamic pressure ratio $(q_\infty/q_j)$ used in place of $(u_\infty/u_j)$, enables variations in the jet path due to a jet nozzle temperature ratio in the range $1 \leqq (T_{tj}/T_a) \leqq 3$.

In conclusion, it should be mentioned that several analyses (notably that in Reference 34) have shown that crosswinds

12

promote an increase in the jet mass entrainment rate in addition to a cross-sectional deformation. This results in more rapid jet centerline decay and boundary growth functions compared to the behavior under static conditions. The increase in mass entrainment is indicated to be less than about 50% for $(u_\infty/v_j) < 0.07$.

## 2.3.2 Region B- Ground Impingement Flow

Most of the analyses for the ground impingement region are based on the assumption that the jet is initially axisymmetric, uniform, parallel, inviscid and incompressible at some specified finite height above the ground plane. Theoretical approaches have been attempted by means of potential flow and vortex representation methods.

A semi-empirical approach satisfying the conditions of a potential flow solution was employed by Leclerc (Reference 35), who found the free boundary shape by electrolytic analog techniques and then numerically computed the internal jet flow field using relaxation methods. This technique has the disadvantage of being too tedious.

The major theoretical treatments which are based on a potential flow approach are those due to Schach, Shen, and Strand (References 36, 37, and 38 respectively). The principal disadvantage of these methods is the associated complexity in obtaining practical solutions. These analyses dependent on satisfying the shape of the boundary streamline of the flow field, represented as a series of discrete point singularities. This results in a complex trial and error solution. An iterative method was suggested by Shen but not attempted. Strand, however, obtained a much simpler simultaneous solution of linear equations by satisfying only the end conditions on the boundary streamline. With the assumption of a uniform jet exit velocity profile, a satisfactory agreement between theory and experiment was demonstrated for nozzle heights of between 1 and 4 nozzle diameters.

A second approach to an inviscid treatment of the normally impinging jet is based on replacing the jet boundary by a vortex sheet. An early study made by Sowyrda, as reported by Vidal (Reference 39), is considered inadequate because the physical flare of the jet, as it nears the ground, is not properly represented. This problem was overcome by Brady and

Ludwig (References 40, 41) who utilized the jet flare boundary
due to Schach (Reference 36) and obtained reasonable agreement
with experimental data. An improved solution was developed in
subsequent studies (Reference 42) by using an iterative scheme
to calculate the jet boundary. However, this method involved a
very slow convergence, since it required some seventy iterations
to obtain a solution for one given jet height/diameter ratio.

A major deficiency in the aforementioned analyses is that
they depend on a uniform velocity profile in the vertical jet
prior to impingement. This assumption suggests that such methods
are valid only for a narrow range of nozzle height-to-diameter
ratios.

Few investigations (References 43 through 46) have
attempted analyses for a non-uniform jet profile, but have re-
tained the basic assumptions of an inviscid flow in order to
make the analysis tractable. In Reference 43, Tani and Komatsu
present a polynomial series solution to the radial variation of
velocity along the ground. However, this solution is restricted
by its dependence upon an empirical evaluation of a similar
polynomial expression for the velocity on the vertical jet
axis.

By assuming a Gaussian normal curve variation for the initial
jet velocity distribution, Barnes and Sullivan (Reference 44)
obtained a linear series solution to the flow. A good agreement
with experimental data on both the free jet profile and radial
ground plane static pressure distribution is reported. In
addition, the static pressure distribution can be closely approx-
imated by the simple Gaussian normal curve. This is similar
to the results presented by Schlichting (Reference 45).

An examination of existing analyses shows that the static
pressure distribution along the ground is well represented by
inviscid jet analyses with both uniform and fully-developed
profiles. However, in practice, the flow is subject to viscous
shear phenomena and inviscid theory cannot be expected to give
an adequate prediction of the total pressure distribution towards
the outer boundary of the flow field. Available experimental
data indicates that a practical estimate of the impinging be-
havior should be limited to variations along the vertical jet
axis and adjacent to the ground plane. Therefore empirical
methods are developed, where necessary, to predict these pressure
and temperature variations.

14

One aspect of the flow near the ground is the presence of
a boundary layer which originates near the ground stagnation
point. This has been analysed by Brady and Ludwig (Reference 40)
on the assumption that the surface flow variation obtained from
their inviscid analysis is equivalent to the behavior at the
outer edge of the boundary layer. Good estimates of the lam-
inar portion of the boundary layer were obtained by using the
method due to Smith (Reference 47). However, it was found that
two-dimensional stability criteria (Reference 39) failed to
predict the transition point to a turbulent boundary layer
flow. This was attributed to the turbulent mixing process in
the main jet flow.

The effect of crosswinds on flow characteristics within
the ground impingement region have been represented by a number
of analytical approaches such as perturbation and superposition
methods. However, the method utilizing a concept of an equiv-
alent oblique jet appears to be most representative of the
actual flow conditions. Known theoretical investigations of
an obliquely impinging jet are presented in References 48
through 50, all of which consider the uniform inviscid jet.

In Reference 48 a simplified momentum balance approach for
a static inclined jet (no crosswinds) yielded a solution for the
radial mass flow distribution. However, no experimental
verification was obtained.

Strand (Reference 49) has demonstrated a successful
extension of his previous potential flow analysis for a vertical
jet (Reference 38) to small inclinations ($\leq 10^{\circ}$) by using
perturbation theory. The solution, however, depends upon a
systematic iterative approach. More recently, Unitt (Reference
50) re-interpreted Strand's solution as representing the case
of a light crosswind on a normally impinging jet, but no
experimental verification  is available.

It should be noted that the above analyses do not strictly
represent true physical conditons for the case of wind-induced
oblique impingement. The effects of jet-free-stream mixing
are expected to result in a non-uniform jet velocity component
due to the crosswind.

## 2.3.3  Region C-  Radial Wall Jet Flow

As noted earlier in section 2.1, the wall jet is characterised by two interdependent flow strata; a boundary layer flow adjacent to the ground where viscous shearing stresses predominate, and an outer layer where free turbulent mixing with the ambient fluid occurs.  While the outer layer tends to spread and decay in a manner similar to that of the free jet, there is a growth of the boundary layer due to both entrainment of the outer layer flow and a momentum loss associated with the viscous shearing forces at the surface.

The classic analytical treatment of the incompressible turbulent radial wall jet is presented by Glauert in Reference 51.  Glauert shows that there are appreciable variations in the wall jet velocity profile, boundary growth rate and peak decay characteristics which are dependent on the local Reynolds number (Rw).  These characteristics are summarised in Figure 4. In practice, however, local wall jet Reynolds numbers associated with the full-scale hot gas flow are large ( of the order of $10^6$) and therefore it is reasonable to assume affine profiles and unique growth and decay rates within the limits of experimental error.

Based on a comparison between Glauert's profiles, the Gaussian normal distribution curve and the available test data it appears that latter representation is more accurate, especially in the outer regions of the wall jet flow.  Therefore, the Gaussian representations have been employed in the current analysis.

Several other theoretical treatments of radial wall jet flows are available, as noted in the extensive bibliography due to Rajaratnam and Subramanya (Reference 52).  Two of these, published in References 53 and 54, are of special interest to the present analysis because they consider the wall jet flow field due to a vertical jet impinging normally to the ground. Both theories employ simplified mathematical models of the flow field and obtain results which show that the wall jet behavior is functionally dependent on both the radial coordinate (R) and nozzle height (Hj).  Using appropriate empirical constants, the theoretical results are in a good agreement with available experimental data presented in References 18, 20, 41, and 54 through 57.
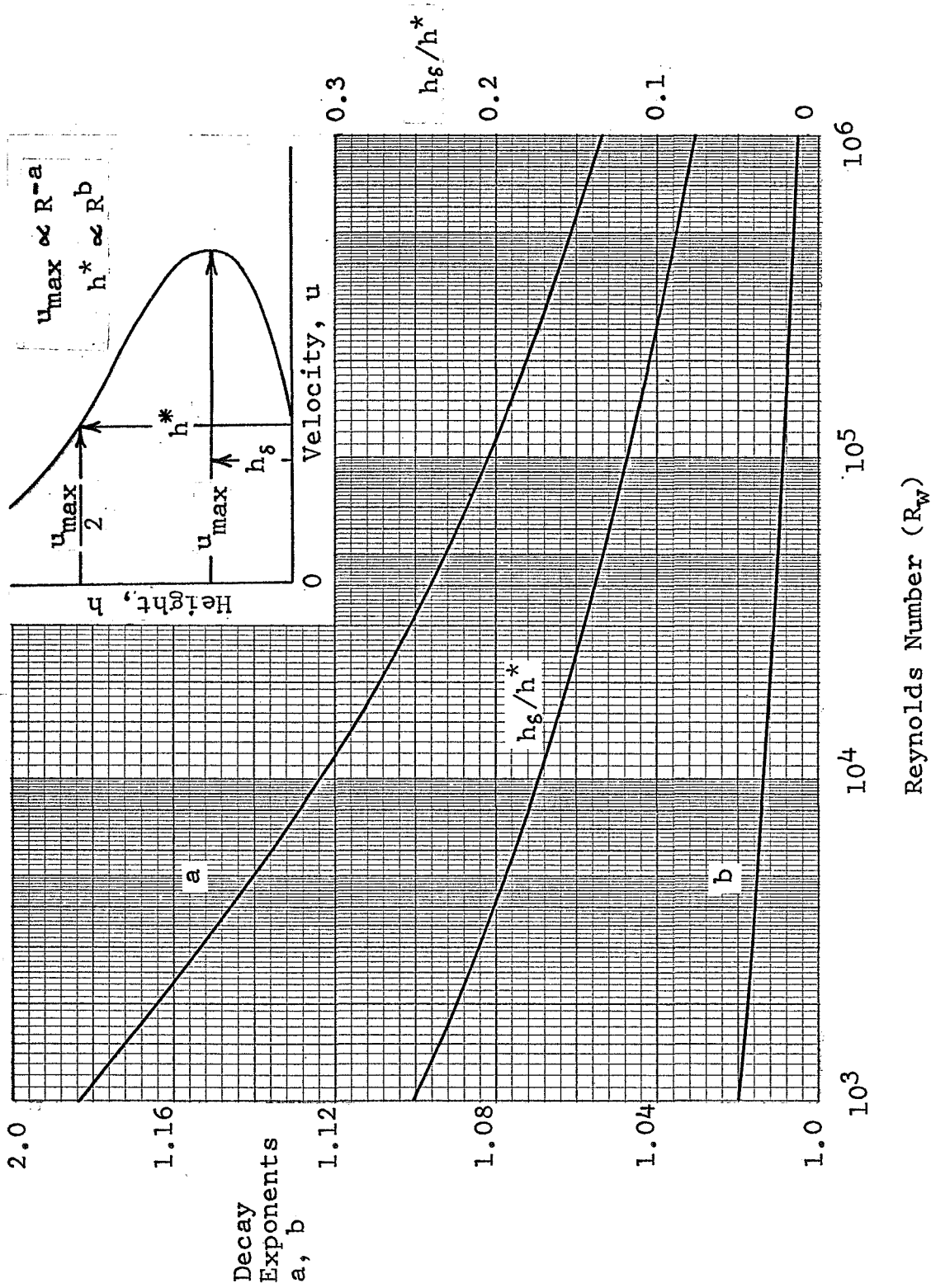
16

Figure 4.— Summary of Wall Jet Parameters Due to Glauert, From Reference 51.

17

Although the theories discussed above do not account for the effects of a temperature differential in the wall jet, empirical methods can be obtained on the basis of test data from References 18 and 56.

In the case of a hot wall jet flow, natural buoyancy forces counteract the radial momentum and shear flow at the ground. Near the origin of the wall jet buoyancy forces are normally secondary to momentum forces. However, since the local jet momentum decays at about twice the rate of the differential temperature, the strengths of these two forces will eventually reach similar magnitudes. At this point flow separation occurs.

One of the foremost analyses of the wall jet separation phenomenon is reported by Abbott in Reference 56. Using a simplified representation of the radial wall jet flow due to a single vertical nozzle, Abbott developed an approximate relationship between the jet momentum and buoyancy forces. This leads to the formulation of a functional expression for the radius at which flow separation should occur. Experimental measurements for low nozzle stagnation pressure ratios less than 1.2 were shown to yield a reasonable verification of this functional dependence, which is used in the present analysis.

An analysis of crosswind effects on the decay of radial wall jets has received little theoretical and experimental attention. This type of flow is more complex than that of a two-dimensional wall jet where the primary flow is along one axis only. While the latter type of flow is reasonably well represented by theoretical methods as given in References 11, 58, and 59, it is not certain whether such methods can be extended to the case of radial flow since experimental data is not available for verification.

Therefore, the radial wall jet in the presence of crosswinds is treated in this analysis by making an analogy to the wall jet flow which results from the oblique impingement of an inclined jet exhausting under static conditions. Although this representation has not been successfully analysed on a theoretical basis, there is, however, sufficient experimental data presented in References 55 and 60 which can be used to formulate a limited empirical model. This is detailed later in section 3.

The effect of adverse crosswinds on the separation of the

18

radial wall jet may be treated in a manner analogous to that of the hot gas buoyancy effect by relating the magnitude of the locally opposing momentum forces between the jet and a cross-wind. It is shown by Abbott (Reference 55) that the ratio of the free-stream to wall-jet differential total pressures can be used to correlate the upstream separation criterion for a radial wall jet in a crosswind. This ratio is found to be independent of jet temperature differential but does not allow for relative size of the free stream boundary layer. Thus, as supported later by unpublished measurements, the crosswind becomes less effective in limiting the forward extend of the ground flow field as the free stream boundary layer height increases.

### 2.3.4 Region D- Recirculation and Entrainment Flow

·The flow behavior in the recirculation region is governed by considerations of hot gas buoyancy, mass entrainment, and turbulent mixing. A unified theoretical treatment of this flow field is not available although separate analysis of the buoyancy and entrainment effects may be made by application of the following methods.

By neglecting mass entrainment effects it may be shown that when the radial wall jet separates from the ground and rises as an annular convective jet, the ratio of its thickness to circumference is sufficiently small ( order of 1/100 ) to justify consideration of it as a two-dimensional convective jet. Using this representation analyses reported in Reference 11 and 45 show that the maximum convective velocity in the jet remains substantially invariant with axial distance and the thickness of the convective flow spreads at an included angle of about $25°$. Expressions for the decay and spread of the jet temperature differential are also derived.

If the convective flow due to hot gas buoyancy is omitted, then the steady state velocities in the recirculation region may be obtained from a potential flow approach with a distribution of sinks to represent the mass entrainment properties of the engine intake and jet exhaust flow. However, this method does not allow the temperature distribution to be obtained.

One approximate method for formulating the combined recirculation flow field consists of treating the convective jet by mass-entrainment and momentum-conservation techniques similar to those used to determine the characteristics of a jet in a crosswind as previously discussed in Section 2.3.1. This approach allows a prediction of the temperature distribution; however, due to the complexity of the flow field the resulting solution is not a simple prediction tool.

The effect of crosswinds on the recirculation flow can be simply treated by a superposition technique, whereby the crosswinds are added vectorially to the entrained velocities.

## 2.3.5 Region E- Intake Flow

Theoretical treatments of the three-dimensional flow field in the vicinity of an engine inlet are generally based on an application of potential flow theory. Since the flow is considered inviscid, such treatments cannot be used to predict temperature distributions which include the effects of turbulent mixing.

Simplified potential flow solutions, derived from a point sink model with a hemispherical control surface to represent the inlet face, give an adequate description of the flow field only for distances greater than a couple of intake diameters from the center of the intake face.

On the other hand, a mathematical model to account for the physical geometry of the intake and adjoining surfaces can be formulated by using source and sink distributions. Such an analysis (e.g. Reference 61) is usually complex and requires the use of a large high-speed digital computer to obtain a solution. However, as noted from References 62 and 63, further development of this complex method has enabled compressibility effects to be approximated and non-symmetrical inlet geometries to be analyzed. Thus, satisfactory predictions of the intake velocity distributions can be obtained, both with and without uniform crosswind effects.

The lack of any suitable theories for predicting temperature distributions in the plane of the engine intakes indicates that practical methods are limited by the availability of experimental measurements. Although the results of many experimental investigations are available (both large and small scale tests) it is found that the majority provide insufficient detail. Furthermore, the noted differences between small and large-scale measurements remain the subject of intensive investigation and suggest that suitable correlating parameters have not been determined. Thus, the methods developed in section 3 are based on large-scale test data wherever possible.

## 2.3.6 Region F- Interaction Flow

When multiple free jets exhaust along parallel axes there is a mutual interaction between the flows entrained by each jet. This mutual interaction results in forces which attract each jet towards a common axis and thus cause distortion of the jet profiles and curvature of the jet paths. In the absence of the ground plane the jets will eventually coalesce to form a single

20

equivalent jet.

A detailed theoretical treatment of such a flow field is limited by a lack of adequate knowledge on the turbulent transport properties in free shear flows, in addition to the geometric complexity of the problem. A simplified approach to the problem has been formulated by Alexander, et al. (Reference 64) who consider a straight forward superposition of the individual axisymmetric momentum distributions of each jet. A reasonable agreement between the analytical results and the experimental measurements was reported.

In practice, however, the coalescence of multi-jet flow in the free-jet region will either be negligible or at least incomplete before ground impingement takes place. Under these conditions the principal flow interaction phenomenom will usually be confined to the ground plane where the opposing wall jet flows meet. This effect causes a well known "fountain" flow of hot exhaust gases which are forced upwards along a vertical plane between multiple impinging jets. Although a qualitative understanding of the flow mechanism within the fountain is available, there are no systematic theoretical analyses or practical solutions for determining the flow characteristics within this region. Therefore, in this analysis, empirical techniques are developed to determine the fountain flow characteristics with and without crosswind effects on the basis of experimental data presented in References 65 through 67.

# SECTION 3

## FORMULATION OF PRACTICAL ENGINEERING METHODS

This section presents the derivation and application of analytical procedures which are used to predict the hot gas flow velocity and temperature distributions in the vicinity of both single and multi-nozzle configurations. The effect of cross-winds are also included.

A consideration of the range of physical parameters in this investigation dictates the need for retaining both compressibility and high temperature effects within close downstream proximity to the engine exhaust nozzles. Further downstream in the hot gas recirculation cycle these effects become less predominant and are usually negligible. Based on the momentum theories presented in many relevant flow investigations, and supplemented by a number of experimental observations, it is convenient to represent the hot gas flow field behavior in terms of total temperature and total/static pressure properties. Therefore, in the presentation of the following mathematical model, the flow field is described in terms of these parameters.

It should also be noted that the total pressure and temperature parameters normally represent the basic experimental variables in a gaseous flow and, therefore, direct comparisons can easily be made between the experiment and theoretical results. Direct measurement techniques for velocity (e.g. hot wire anemometers) are not very popular primarily because of their relative complexity and delicacy.

Where a value of the local flow velocity $(u)$ is required, this may be calculated from a knowledge of the locally-determined values of total pressure $(P_t)$, static pressure $(P)$, (generally assumed to be atmospheric), and total temperature $(T_t)$ using standard gas flow relationships, thus:

(a) For Isentropic Compressible Flow

$$(u)^2 = 2 \cdot \frac{\gamma}{\gamma - 1} \cdot G \cdot T_t \cdot \left[ 1 - \left( \frac{P_t}{P} \right)^{\frac{1-\gamma}{\gamma}} \right] \qquad (1)$$

(b) For Incompressible Flow

$$(u)^2 = 2 \cdot \left( \frac{P_t - P}{P} \right) \cdot G \cdot T_t \qquad (2)$$

Equation (1) yields a more accurate value of velocity under all conditions while equation (2), which is mathematically simpler,

22

is recommended for low flow velocities when $(P_t/P) < 1.1$ .

In formulating the analytical methods it is convenient to consider a single nozzle and top inlet configuration first. The flow field velocity and temperature distributions together with the flow boundaries are treated by considering each flow region A through F in sequential order. The mathematical model is then extended to include the effect of crosswinds and multi-nozzle configurations.

Following the common practice of the relevant technical literature, non-dimensional flow parameters are used through-out the analysis where possible and are denoted by a bar sub-script. These bar values represent the fractions of local differential total pressure and total temperature, measured above ambient conditions, divided by the corresponding jet exit values, thus:

$$\overline{\Delta P_t} = \left( \frac{P_t - P_a}{P_{tj} - P_a} \right)$$

or

$$\overline{\Delta T_t} = \left( \frac{T_t - T_a}{T_{tj} - T_a} \right) .$$

In addition, co-ordinates of points within the flow field are generally expressed as distances normalized by the jet nozzle diameter, thus:    $\overline{R} = R/D_j$ ,    $\overline{H} = H/D_j$

Since there is no well defined physical jet boundary, a jet pressure reference boundary is defined in terms of the dis-tance measured normal to the local flow axis or groundplane at which the value of the normalized total pressure differential is 0.25. Under incompressible flow conditions this is analogous to the widely used definition of the jet boundary as being the location at which the normalized velocity ratio is 0.5. For the purpose of analysis, a jet temperature reference boundary is also defined as the location where the normalized differential temperature ratio is 0.5.

It should be noted that neither of these reference bound-aries represent a physical flow boundary; they are introduced only for the purpose of defining the mathematical model. Some invest-igations (e.g. Reference 68) define a physical boundary at the point where the local velocity (u) is 1% of the maximum value on the flow axis i.e. (u) = $0.01(u_{max})$.

## 3.1 SINGLE NOZZLE CONFIGURATION

Presented in this section are practical engineering methods for predicting hot gas characteristics in the vicinity of a single-nozzle jet in ground effect. The analysis is developed for each flow region as discussed in Section 2.2, utilizing the

23

jet flow parameters defined above.

### 3.1.1 Region A- Free Jet Flow

The local total pressure and total temperature conditions within a free jet region can be expressed in terms of the pressure and temperature conditions along the jet axis and reference flow boundaries $(r_p)$ and $(r_t)$.

The analysis is of a semi-empirical nature and strongly relies upon the experimental data of References 7, 9, 17, 18 and 20. The analysis is based on the assumption that the static pressure throughout the free jet region is equivalent to the ambient static value. This assumption, which is made because of the difficulty and uncertainty of obtaining accurate measurements of the mean static-pressure value in a turbulent flow, is verified by the extensive measurements of Reference 17 and is found to be within acceptable limits of accuracy.

Examining the relevant test data it is noted that the decay of differential total pressure $(\Delta P_{tc})$ and total temperature $(\Delta T_{tc})$ along the jet axis can be uniquely expressed as functions of the two axial correlation parameters $(S_1)$ and $(S_2)$ respectively. Thus, using the nomenclature of Figure 5 these parameters are:

For total pressure decay

$$S_1 = \left(\frac{P_{tj}}{P_a}\right)^{-0.07} \cdot \left(\frac{T_{tj}}{T_a}\right)^{0.25} \cdot \frac{\overline{s}}{K_n \cdot \sqrt{C_D}} \qquad (3)$$

For total temperature decay

$$S_2 = \left(\frac{P_{tj}}{P_a}\right)^{-0.86} \cdot \left(\frac{T_{tj}}{T_a}\right)^{0.5} \cdot \frac{\overline{s}}{c_H} \qquad (4)$$

All flow parameters appearing in equations (3) and (4) are defined in the list of symbols.

The numerical constant $(K_n)$ accounts for variations in nozzle geometry and jet swirl. For a "sharp" nozzle such as shown in Figure 6 (a), the value of $(K_n)$ is unity. The corresponding value for a "blunt" nozzle, as shown in Figure 6 (b) is about 0.95 on the basis of test data of Reference 18. The nozzle configuration shown in Figure 6 (b) corresponds to a jet engine embedded in a large fuselage or a fan-in-a-wing configuration.
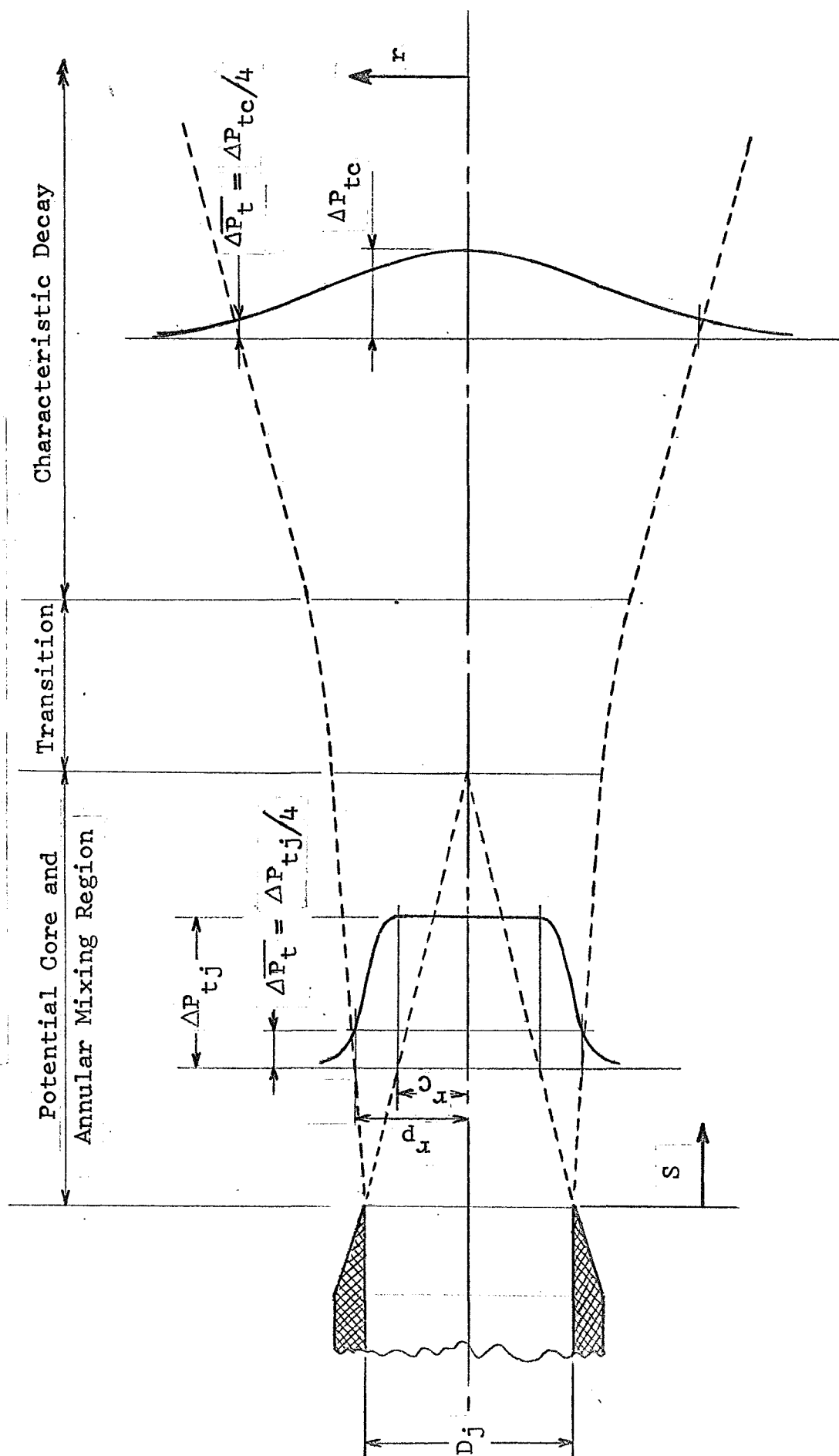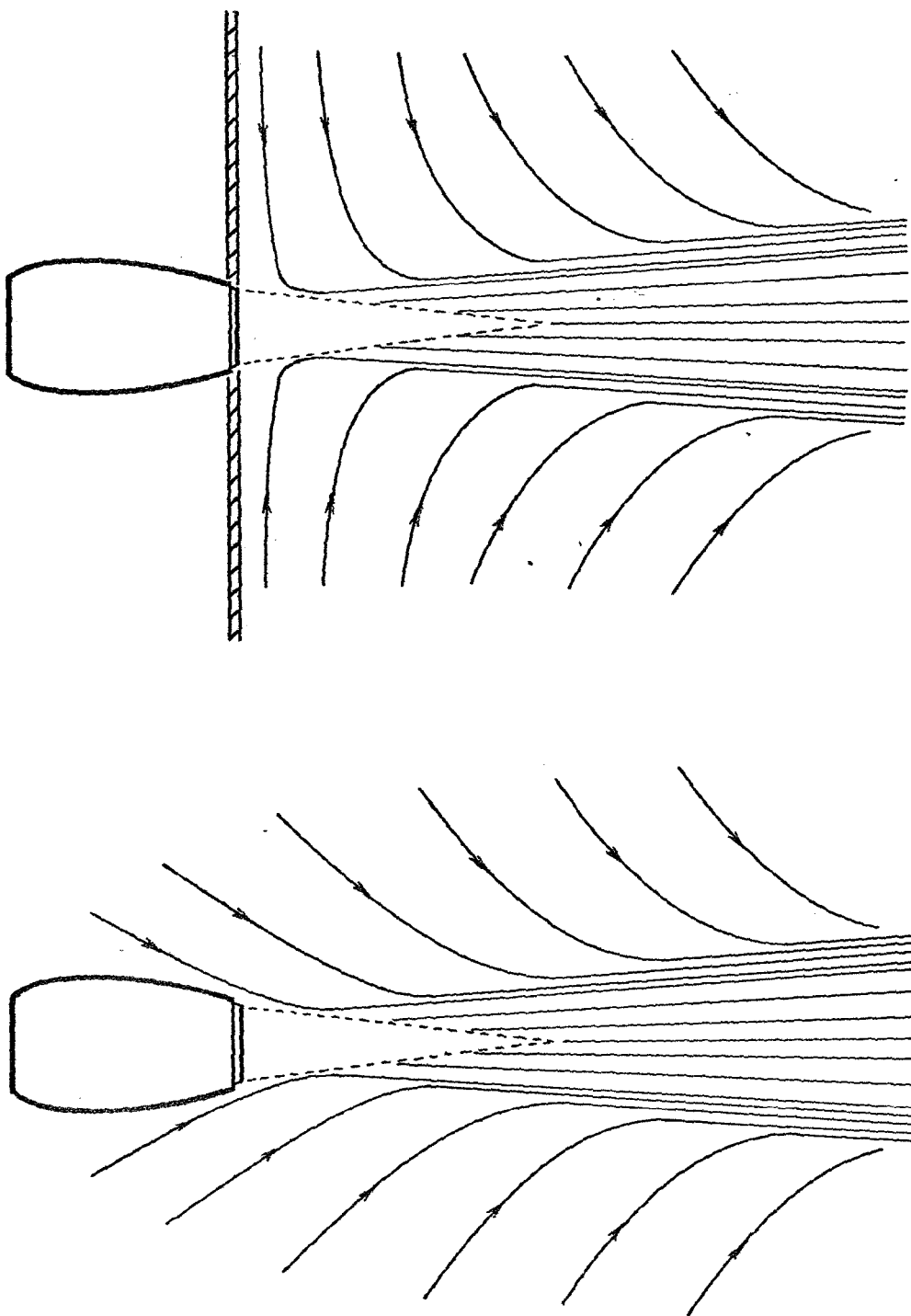
24

Figure 5.- Coordinate System for Free-Jet Decay in a Static Environment.

(a) Sharp Nozzle

(b) Blunt Nozzle

Figure 6.- Effect of Nozzle Geometry on Entrained Flowfield of a Free Jet.

26

The effect of an initial jet swirl, as would be produced by a jet engine operating at an off-design condition, is to intensify the turbulent jet mixing process and therefore the value of $K_n$ will be reduced below $K_n = 0.95$. However, the lack of explicit test data on jet swirl precludes an accurate quantitive assessment of this effect.

### 3.1.1.1  Potential Core Region

The potential core of the jet, shown in Figure 2, Region 1, is defined as the region where flow conditions are uniform and similar to those at the nozzle exit.

The non-dimensional core length $(\bar{S}_C)$, based on the total pressure decay is obtained from the correlation parameter $(S_1)$ given by equation (3) and the test data of Reference 41, thus:

$$\bar{S}_C = 4.87 \ K_n \ \sqrt{C_D} \ \left(\frac{P_{tj}}{P_a}\right)^{0.07} \left(\frac{T_{tj}}{T_a}\right)^{-0.25} \tag{5}$$

Also, the non-dimensional core radius $(\bar{r}_C)$ can be expressed as

$$\bar{r}_C = 0.945 - 0.194 \ (S_1) \tag{6}$$

Substituting equation (3) into equation (6) there follows:

$$\bar{r}_C = 0.945 - 0.194 \ \left(\frac{P_{tj}}{P_a}\right)^{-0.07} \left(\frac{T_{tj}}{T_a}\right)^{0.25} \frac{\bar{S}}{K_n \ \sqrt{C_D}} \tag{7}$$

Finally, the mean differential total pressure and total temperature within this region, given by $0 \leqslant r \leqslant r_C$, are obtained as

$$\Delta P_t = \Delta P_{tc} = \Delta P_{tj} \tag{8}$$

$$\Delta T_t = \Delta T_{tc} = \Delta T_{tj} \tag{9}$$

The velocity in this region is by definition uniform and can be calculated using equations (1), (8), and (9).

### 3.1.1.2  Annular Mixing Region

This region, as shown in Figure 2, Region 2, encompasses the potential core region and is characterised by turbulent mixing with the surrounding air.

The flow conditions along the jet axis for this region are the same as those for the potential core region and are given

by the values existing at the nozzle exit. By definition these are:

$$\overline{\Delta P_{tc}} = 1$$
$$\text{and} \quad \overline{\Delta T_{tc}} = 1 \qquad (10)$$

Because of turbulent mixing of the flows, there exists a radial decay of total pressure and temperature in this region. A number of relatively simple mathematical approximations to describe these radial pressure and temperature profiles have been developed, mostly from empirical studies. One of the more commonly used methods is that employing the Gaussian normal curve distribution, which, because it is mathematically simple and amenable to integral techniques, has been selected for the present analysis. Furthermore, the experimental data from a wide range of investigations such as those reported in References 9 and 57 clearly show that the pressure and temperature profiles in the mixing region of a free jet are essentially independent of downstream location, compressibility and temperature effects up to sonic conditions.

Thus the total pressure and temperature distributions within this region, given by $r_C < r \leqslant r_B$, can be expressed as:

$$\overline{\Delta P_t} = e^{-1.386 \left(\frac{r - r_C}{r_P - r_C}\right)^2} \qquad (11)$$

$$\text{and} \quad \overline{\Delta T_t} = e^{-0.693 \left(\frac{r - r_C}{r_t - r_C}\right)^2} \qquad (12)$$

where $(r_B)$ is a limiting value of the jet boundary up to which the Gaussian analytical representation is considered to be valid. This value is of the order of twice the jet pressure reference boundary radius $(r_P)$, i.e. $(r_B) \approx 2 \cdot (r_P)$.

The jet pressure reference boundary $(r_P)$ and the jet temperature reference boundary $(r_t)$ appearing in equation (11) and (12) respectively are derived using momentum techniques in Appendix A. These parameters can be uniquely defined in terms of the axial correlation functions $(S_3)$ and $(S_4)$ similar to those used in describing the jet centerline decay characteristics.

The axial correlation function $(S_3)$ for the jet pressure reference boundary $(r_P)$ is given by:

$$S_3 = \left(\frac{P_{tj}}{P_a}\right)^{-0.23} \cdot \left(\frac{T_{tj}}{T_a}\right)^{0.25} \cdot \overline{S} \qquad (13)$$

28

and $(S_4)$, for the temperature reference boundary ($r_t$) is given by:

$$S_4 = \left(\frac{P_{tj}}{P_a}\right)^{-0.43} \cdot \left(\frac{T_{tj}}{T_a}\right)^{0.25} \cdot \bar{S} \qquad (14)$$

For the Annular Mixing Region, satisfactory analytical expressions for both pressure and temperature reference boundaries are obtained by substituting the appropriate correlation functions $(S_3)$ and $(S_4)$ into the empirical boundary equation developed by Reference 38. Thus the equation for the normalized pressure reference boundary $(\bar{r}_p)$ is given by:

$$\bar{r}_p = \left(\frac{r_p}{r_j}\right) = 1.057 + 0.0285 \cdot (S_3) \qquad (15)$$

or by substituting equation (13) into equation (15), $(\bar{r}_p)$ becomes:

$$\bar{r}_p = 1.057 + 0.0285 \cdot \left(\frac{P_{tj}}{P_a}\right)^{-0.23} \cdot \left(\frac{T_{tj}}{T_a}\right)^{0.25} \cdot \bar{S} \qquad (16)$$

Similarly, the normalized temperature reference boundary $(\bar{r}_t)$ can be expressed as:

$$\bar{r}_t = \left(\frac{r_t}{r_j}\right) = 1.057 + 0.0285 \cdot (S_4) \qquad (17)$$

or by substituting equation (14) into equation (17) $(r_t)$ becomes:

$$\bar{r}_t = 1.057 + 0.0285 \cdot \left(\frac{P_{tj}}{P_a}\right)^{-0.43} \cdot \left(\frac{T_{tj}}{T_a}\right)^{0.25} \cdot \bar{S} \qquad (18)$$

The above relationships are applicable to a wide range of nozzle temperature and pressure ratios and yield good agreement with the available test data for values of the respective axial correlation function between 1 and 5. For the values of $(S_3)$ and $(S_4)$ between 0 and 1, i.e. immediately downstream of the nozzle, the jet boundaries can be assumed to be parallel and therefore can be approximated by:

$$\bar{r}_p = \bar{r}_t = 1.0 \qquad (19)$$

### 3.1.1.3  Transition Region

The transition region, as defined in Figure 2, Region 3, pertains to the flow field between the potential core and the characteristic decay regions. The length of this region (based on total pressure decay characteristics) is approximately 1.25 times that of the potential core $(\bar{S}_c)$.

The flow in this region is completely permeated by the turbulent mixing process. However, a stabilized shear flow decay pattern has not yet been fully developed.

For this reason the decay of total pressure and temperature along the jet axis can not be simply represented by the exponential decay functions which will be developed later for the characteristic decay region (Region 4). Although other mathematical formulations are possible the complexities of such effort are considered unwarranted for the present application. Therefore, the centerline decay characteristics and the jet reference boundaries in the transition region are herein obtained by fairing a curve to the appropriate test data between the potential core and the characteristic decay regions. These results will be discussed in more detail later in the text (See Section 3.1.1.5).

The radial distributions of total pressure and temperature within the transition region can be adequately represented by the Gaussian normal curve in terms of the centerline decay characteristics and the jet reference boundaries obtained from the experimental data as described above. The analysis is identical to that developed for the characteristic decay region presented below.

### 3.1.1.4 Characteristic Decay Region

This flow region, as defined in Figure 2, Region 4, extends from the transition region described above to the ground impingement region. As mentioned previously the flow in this region is completely mixed and it exhibits the decay characteristics of a fully developed shear flow. Therefore, it can be simply represented by exponential decay functions along the jet axis and Gaussian normal distribution functions along the jet radius.

Thus, utilizing the appropriate test data, the following semi-empirical relationships are developed for the decay of the normalized peak differential total pressure ( $\Delta \overline{P}_{tc}$ ) and total temperature ( $\Delta \overline{T}_{tc}$ ) along the jet centerline:

$$\Delta \overline{P}_{tc} = \left(\frac{S_1}{8.38}\right)^{-2.24} = \left[\left(\frac{P_{tj}}{P_a}\right)^{-0.07} \cdot \left(\frac{T_{tj}}{T_a}\right)^{0.25} \cdot \frac{S}{8.38. K_n \sqrt{C_D}}\right]^{-2.24} \quad (20)$$

and

$$\Delta \overline{T}_{tc} = \left(\frac{S_2}{6.3}\right)^{k_1} = \left[\left(\frac{P_{tj}}{P_a}\right)^{-0.86} \cdot \left(\frac{T_{tj}}{T_a}\right)^{0.5} \cdot \frac{S}{6.3. C_H}\right]^{k_1} \quad (21)$$

Experimental data from References 7, 9, 13, and 70 indicate that the temperature decay exponent $(k_1)$ varies with nozzle exit Mach number, as noted by Warren in Reference 7, and can be summarized by the following approximate variation:

30

| $(P_{tj}/P_a)$ | | | $k_1$ |
|---|---|---|---|
| 1.0 | $\rightarrow$ | 1.4 | $-1.15$ |
| 1.8 | $\rightarrow$ | 2.0 | $-1.40$ |

In the absence of a more complete experimental substantiation a linear interpolation of b over the range $1.4 < (P_{tj}/P_a) < 1.8$ is taken, thus

$$k_1 = -0.275 - 0.625 \cdot \left(\frac{P_{tj}}{P_a}\right) \qquad (22)$$

The radial distributions of total pressure and total temperature can now be expressed in terms of the centerline decay characteristics and the jet reference boundaries as follows:

$$\text{and} \qquad \overline{\Delta P_t} = \overline{\Delta P_{tc}} \cdot e^{-1.386 \ (r/r_p)^2} \qquad (23)$$

$$\overline{\Delta T_t} = \overline{\Delta T_{tc}} \cdot e^{-0.693 \ (r/r_t)^2} \qquad (24)$$

It should be noted that equations (23) and (24) are equally well applicable to the transition region described in Section 3.1.1 as well as the characteristic decay region provided that appropriate values are substituted for the centerline decay characteristics and the jet reference boundaries $(r_p)$ and $(r_t)$.

The analytical relationships for the jet reference boundaries applicable to the characteristic decay region are derived, using momentum techniques, in the appendix. The jet pressure reference boundary $(r_p)$ is derived in terms of the axial correlation parameter $(S_3)$ by considering a conservation of jet axial momentum. A similar treatment of the temperature reference boundary $(r_t)$ is not possible because of a lack of detailed knowledge on the interchange of thermal and turbulent energy. Thus in this case empirical techniques were used.

The final equations for the pressure and temperature reference boundaries are as follows:

$$\overline{r_p} = \left(\frac{r_p}{r_j}\right) = 0.109 \ (S_3)^{1.12} \qquad (25)$$

and

$$\overline{r_t} = \left(\frac{r_t}{r_j}\right) = 0.141 \ (S_3)^{1.12} \qquad (26)$$

Substituting equations (13) and (14) into equations (25) and (26) respectively there results:

$$\overline{r_p} = 0.109 \cdot \left[ \left(\frac{P_{tj}}{P_a}\right)^{-0.23} \cdot \left(\frac{T_{tj}}{T_a}\right)^{0.25} \cdot \overline{S} \right]^{1.12} \qquad (27)$$

31

and $\quad r_t = 0.141 \left[ \left(\dfrac{P_{tj}}{P_a}\right)^{-0.43} \cdot \left(\dfrac{T_{tj}}{T_a}\right)^{0.25} \cdot \bar{S} \right]^{1.12}$ 

$\hspace{11cm}$ (28)

### 3.1.1.5 Graphical Solution for Flow Characteristics in Region A (No Crosswinds)

The analytical relationships developed in the previous sub-sections have been evaluated and are presented graphically in Figures 7 through 11. These figures can be directly used to predict the flow characteristics of the entire Region A.

Specifically, Figure 7 presents the plot of the decay of the maximum total pressure $(\Delta P_{tc})$ along the jet axis as a function of the axial correlation parameter $(S_1)$. This figure was obtained by utilizing equations (10) and (20) for the potential core and the characteristic decay region, respectively, and by fairing the appropriate experimental data points for the transition region.

Similarly, the decay of the maximum total temperature $(\Delta T_{tc})$ along the jet axis for the entire flow field of Region A is plotted in Figure 8 as a function of the axial correlation parameter $(S_2)$. This figure was obtained using equations (10) and (21).

Also the variations of jet pressure reference boundary $(r_p)$ and the temperature reference boundary $(r_t)$ are presented in Figures 9 and 10, respectively, as functions of their corresponding axial correlation parameters $(S_3)$ and $(S_4)$. These figures were obtained using equations (15), (17), and (19) for the potential core region and equations (25) and (26) for the characteristic decay region. The corresponding values for the transition region were faired in using appropriate experimental data.

Finally, Figure 11 shows the variation of the normalized total pressure and total temperature profiles as a function of radial distance for the entire mixing zone of Region A. This figure was obtained using a set of equations (11), (23), and equations (12) and (24), respectively.

Thus, the flow characteristics of the entire Region A can be uniquely determined using either analytical expressions developed in Section 3.1.1 or the graphical solutions presented in this sub-section.

The above methods give a satisfactory account of compressibility effects for $(P_{tj}/P_a) \leq 2$ and temperature effects for $1 \leq (T_{tj}/T_a) \leq 3$. An extension of these methods to moderately expanded sonic jets, $(P_{tj}/P_a) > 2$, is not practical because substantial

32
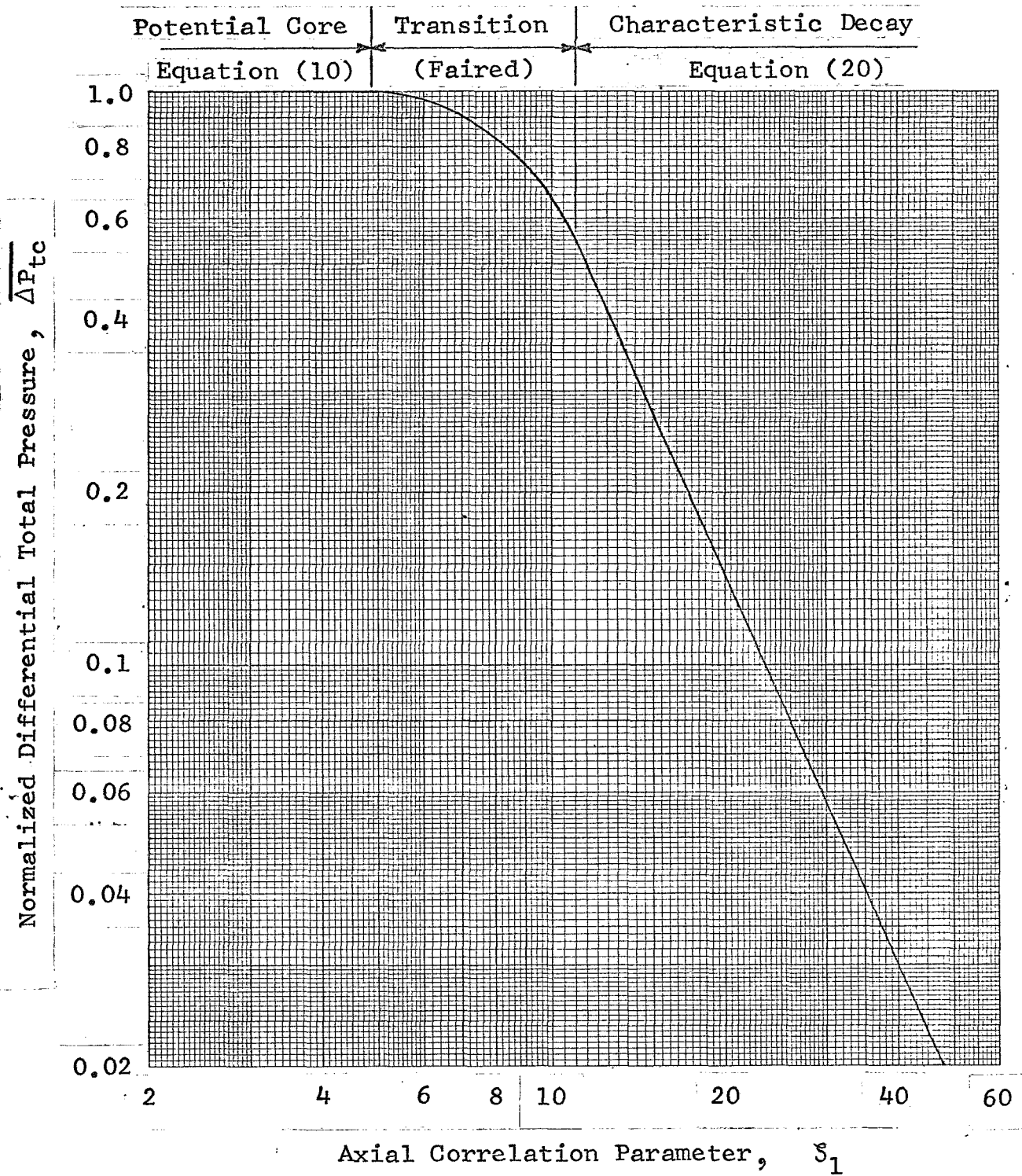
Figure 7.- Normalized Centerline Decay of Total Pressure for a Single Jet in Region A; No Crosswinds.
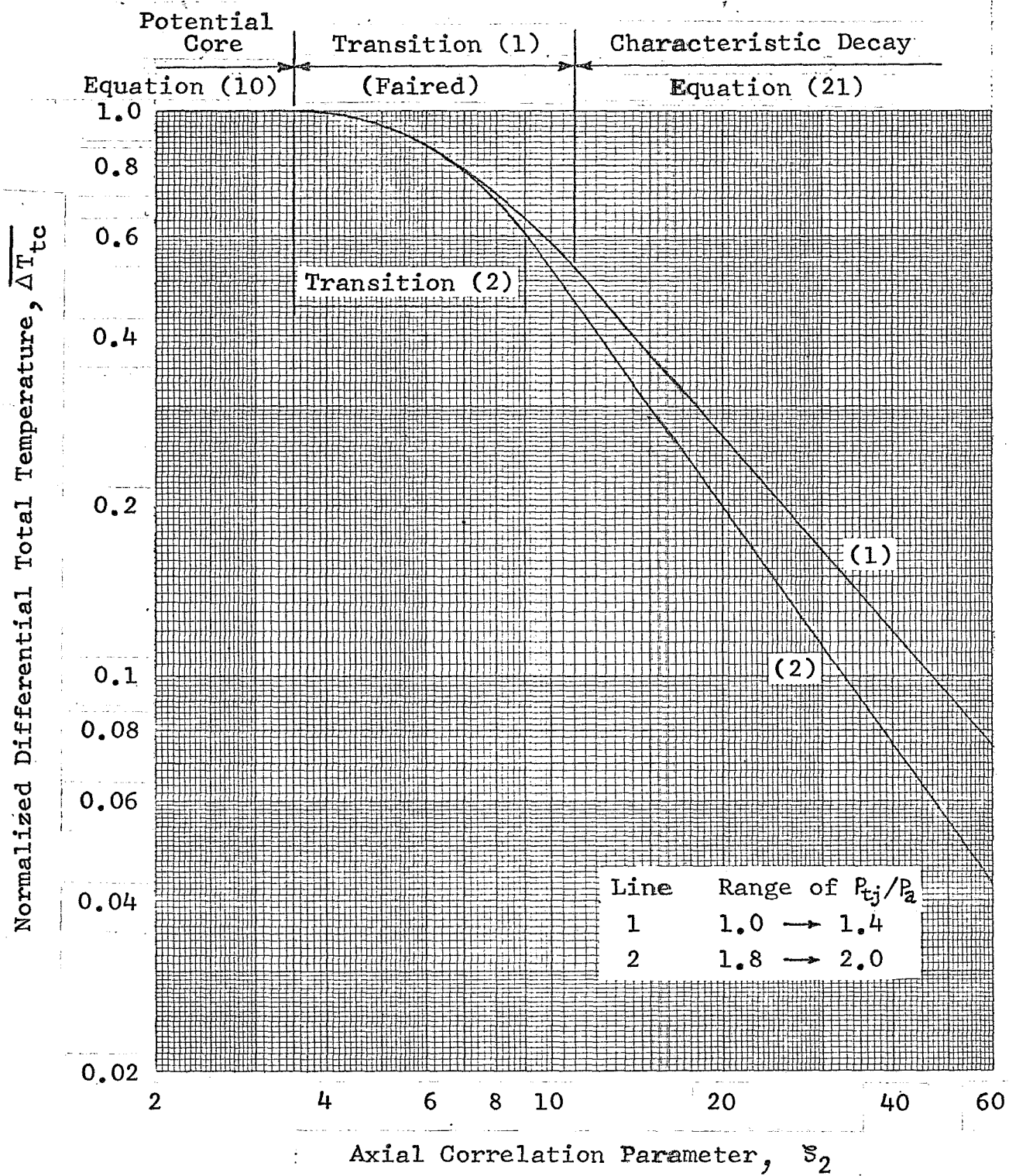
Figure 8.- Normalized Centerline Decay of Total Temperature for a Single Jet in Region A; No crosswinds.
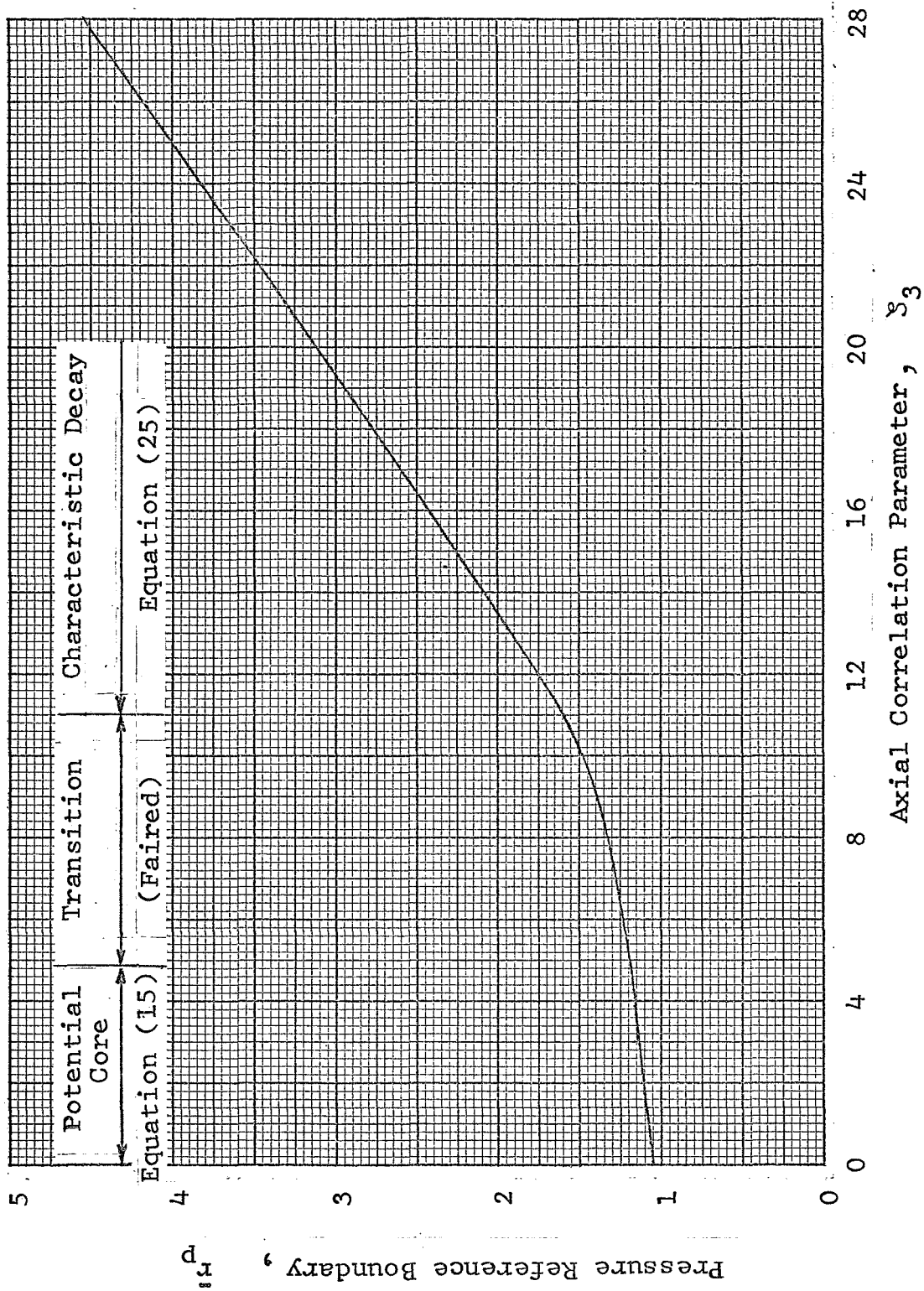
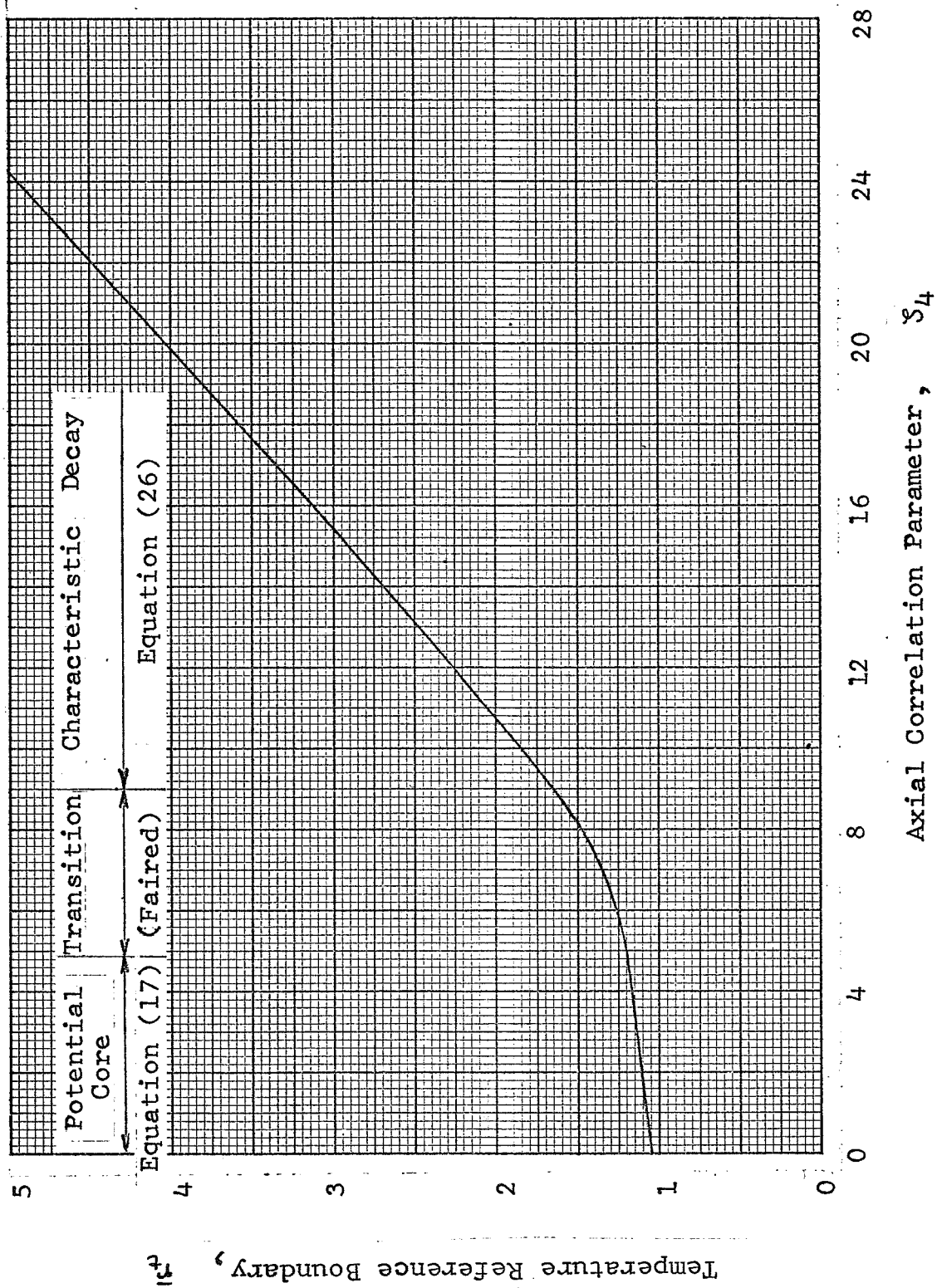Figure 9.- Pressure Reference Boundary Growth for the Free Jet.

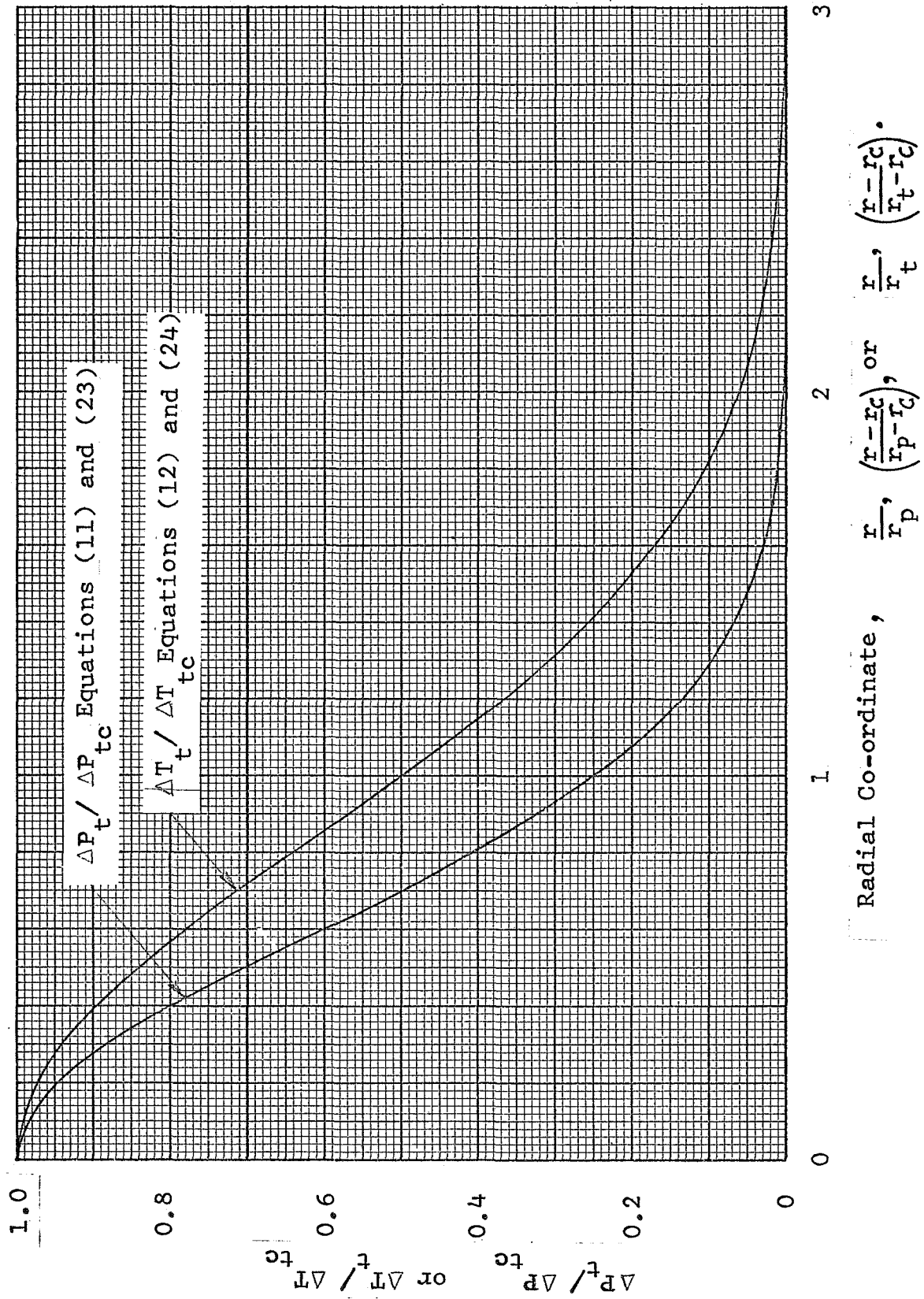Figure 10.- Temperature Reference Boundary Growth for the Free Jet.

36

Figure 11.- Normalized Mean Total-Pressure and Total-Temperature Profiles for the Turbulent Mixing Zone of a Single Jet in Region A

and non-uniform departures from subsonic flow behavior are evidenced by the available experimental data.

## 3.1.1.6  Effect of Crosswinds

When a free jet exhausts normal to a steady crosswind and is not appreciably affected by ground effect, it undergoes a cross sectional deformation as it is deflected downwind by the action of the turbulent mixing between the jet and crosswind.

An analysis of crosswind effects on typical jet configurations shows that the hot gas reingestion is only likely to be significant when jet path deflections (from the vertical) are less than about $15°$. Under most practical conditions the deflection of the jet path is generally much smaller and it is therefore valid to make the assumption that the length of the jet centerline path is nearly equal to the nozzle height. This enables the jet flow behavior to be described by the following methods.

A knowledge of the free-jet path prior to ground impingement is necessary in order to determine the ground flow and subsequent behavior. The jet path is normally defined by the line of local maximum dynamic pressure and as evidenced by experimental measurements it is essentially tangential to the local mean flow vector. The empirical expression for the jet path developed by Ivanov (Reference 11) is considered to be most appropriate because of the range of freestream-to-jet dynamic pressure ratios considered i.e. $(0.003 \leqslant (q_\infty/q_j) \leqslant 0.29)$. Using the nomenclature of Figure 12 Ivanov's expression is used in a modified form as follows:

$$\bar{x}_{wc} = (\mu)^{2.6} \cdot (\bar{z})^3 \tag{29}$$

The crosswind ratio $(\mu)$ is defined in terms of the ratio of differential total pressures as

$$\mu = \sqrt{\left( \Delta P_{t\infty} / \Delta P_{t_j} \right)} \tag{30}$$

The results obtained by Shandorov, as discussed in Reference 11, indicate that use of the parameter $(\mu)$ gives a satisfactory approximation for jet temperature variations in the range of $1 \leqslant (T_{t_j}/T_a) \leqslant 3$.

Differentiation of equation (29) leads to an expression for the jet path inclination, thus:

$$\theta_c = \cot^{-1} \left[ 3 \cdot (\mu)^{2.6} \cdot (\bar{z})^2 \right] \tag{31}$$
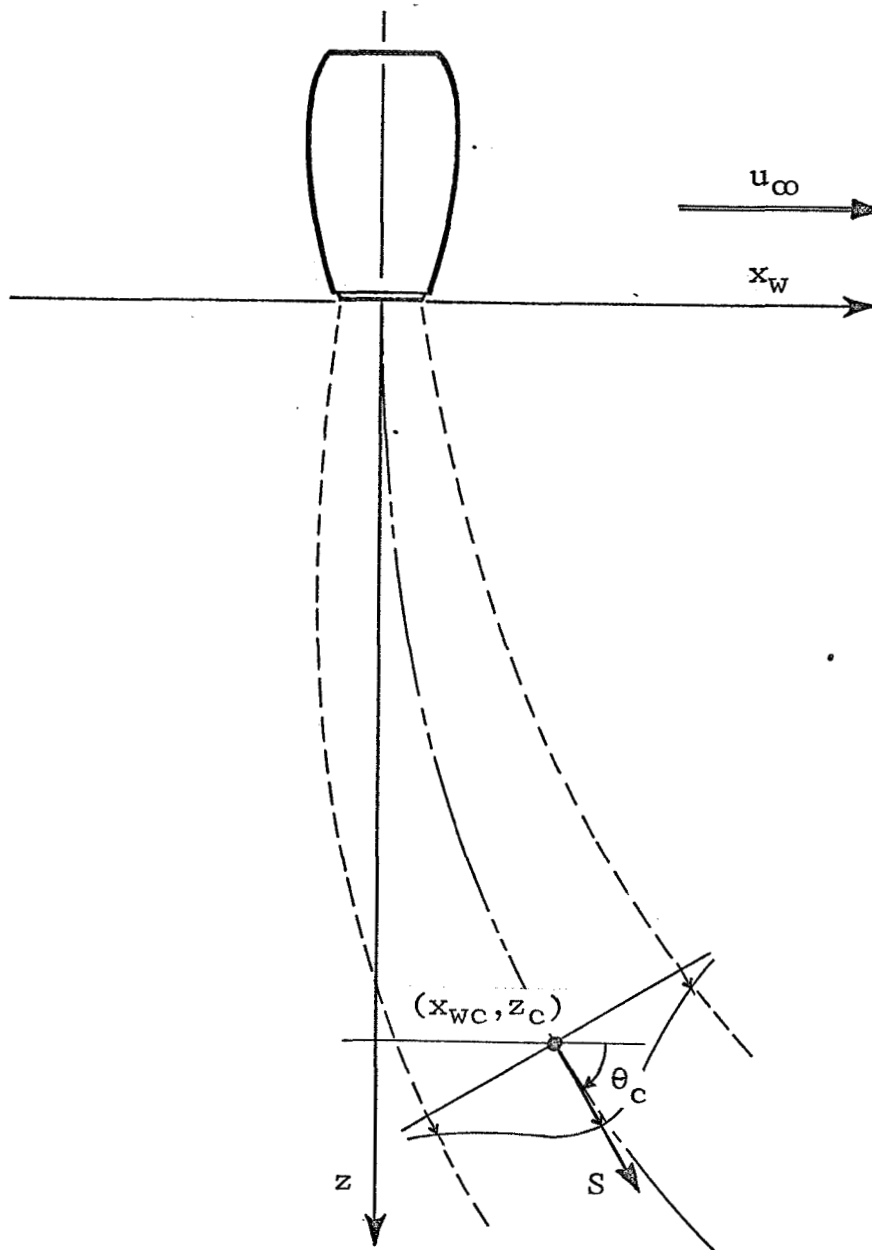
38

Figure 12.- Coordinate System for a Free Jet in a Crosswind.

Several analyses (notably that in Reference 34) show that, in addition to jet profile distortion, crosswinds promote an increase in the jet mass entrainment rate which results in more rapid decay and growth functions. For simplicity these considerations are disregarded and it is assumed that the effect of a crosswind is to distort the jet centerline path only. Therefore, the flow analyses developed for a straight jet in the previous sections are directly applicable to the wind-distorted jet provided that in this case the flow conditions are appropriately referenced to the curved jet centerline. In other words, all pressure, velocity and temperature profiles computed using the straight jet (no crosswinds) analysis are taken to be normal to the local inclination of the curved jet centerline.

### 3.1.2 Region B   Ground Impingement Flow

The ground impingement region, as defined in Figure 1, Region B, extends from the free jet region to the ground plane and is bounded laterally by the wall jet flow.

A review of the pertinent technical literature indicates that the flow in this region is amenable to a treatment of incompressible inviscid flow analyses since the intensity of the turbulent mixing between the jet and freestream is greatly reduced.

The analytical methods are developed for jet nozzle heights of no less than one jet diameter; i.e. $(\bar{H}j) \geq 1$. This limitation is imposed to exclude conditions where appreciable distortion of the nozzle exit flow distribution can occur as indicated by experimental results obtained for the normal impingement of incompressible jets (Reference 41).

In analyzing the jet-ground impingement characteristics it is important to recognize that the scale of the flow field must be related to the local jet diameter and flow profile properties close to the region of appreciable impingement influence. Since the influence of the ground on the impinging jet is most important at heights of less than approximately one local jet diameter it appears plausible that a reasonable correlation of the flow field behavior in the impingement zone can be obtained by reference to the properties exhibited by a free jet at the equivalent ground plane position.

The methods developed below can be used for predicting temperature and velocity distributions, ground stagnation conditions, and ground plane (radial) velocity and temperature variations.

40

## 3.1.2.1 Pressure Distributions

Although complex theories are available for predicting the flow field within the ground impingement region, it is more expedient to utilize the non-dimensional total pressure contours derived by Barnes and Sullivan (Reference 44) for an inviscid jet.

This data is presented in Figure 13 which shows the variation of the local differential total pressure within the ground impingement region (excluding the ground plane) as a fraction of the total differential pressure ($\Delta P_{tc}$) along the jet axis. This value of ($\Delta P_{tc}$) can be obtained directly from the free jet analysis by using the results of Figure 7 evaluated at an appropriate value of the axial correlation parameter $(S_1)$ corresponding to an equivalent jet axial distance. Using the nomenclature of Figure 14, this axial distance is given by:

$$\bar{S} = \bar{H}_j - \bar{H} \tag{32}$$

Furthermore, as indicated by the test data of References 17, 18, 20, and 41, the ground stagnation pressure ($\Delta P_{tg}$) can be closely approximated by the value occurring on the centerline of a free jet at an equivalent downstream location corresponding to the ground stagnation point. As shown in Figure 14, this ground stagnation point is located at the intersection of the vertical jet axis and the ground plane and is therefore given by:

$$\bar{S} = \bar{H}_j \tag{33}$$

For small values of nozzle height, for which the equivalent axial correlation parameter $(S_1) < 11$, the ground stagnation pressure ($\Delta P_{tg}$) can be obtained from Figure 7, using equations (3) and (33). For large values of nozzle height given by $(S_1) \ge 11$ the following analytical relationship for the dimensional value of ($\Delta P_{tg}$) is obtained by substituting equation (33) into equation (20), thus:

$$\Delta P_{tg} = \Delta P_{tj} \left[ \left( \frac{P_{tj}}{P_a} \right)^{-0.07} \cdot \left( \frac{T_{tj}}{T_a} \right)^{0.25} \cdot \frac{\bar{H}_j}{8.38 \, K_n \sqrt{C_D}} \right]^{-2.24} \tag{34}$$

As the flow in the ground impingement region is decelerated towards the ground there exists an appreciable rise in the static pressure. The rise in the static pressure differential ($\Delta P_c$) over the ambient value, along the jet centerline can be approximated by the Gaussian normal curve as follows:

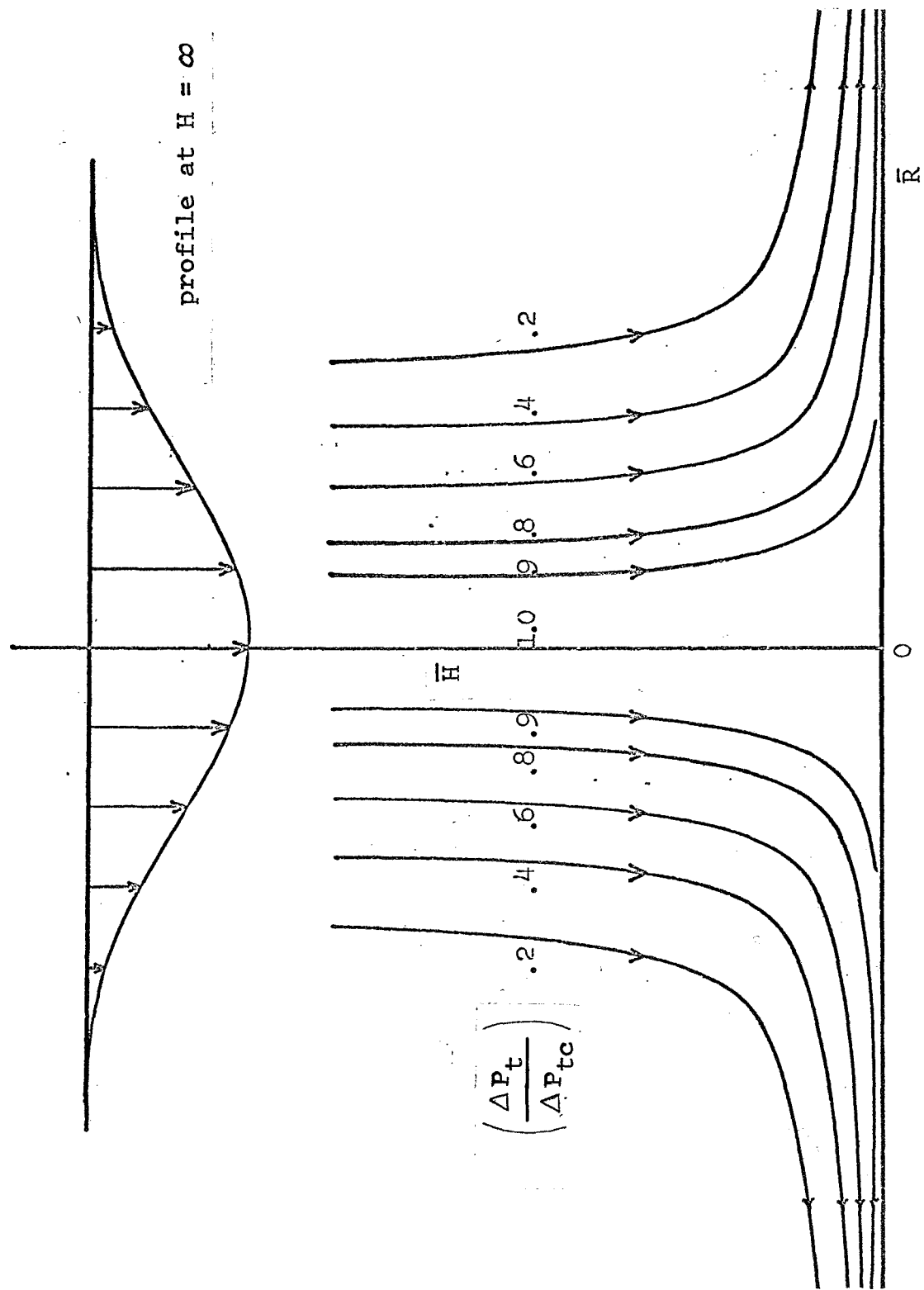$$\Delta P_c = \Delta P_{tg} \cdot e^{-3.466 \cdot (\bar{H})^2} \tag{35}$$

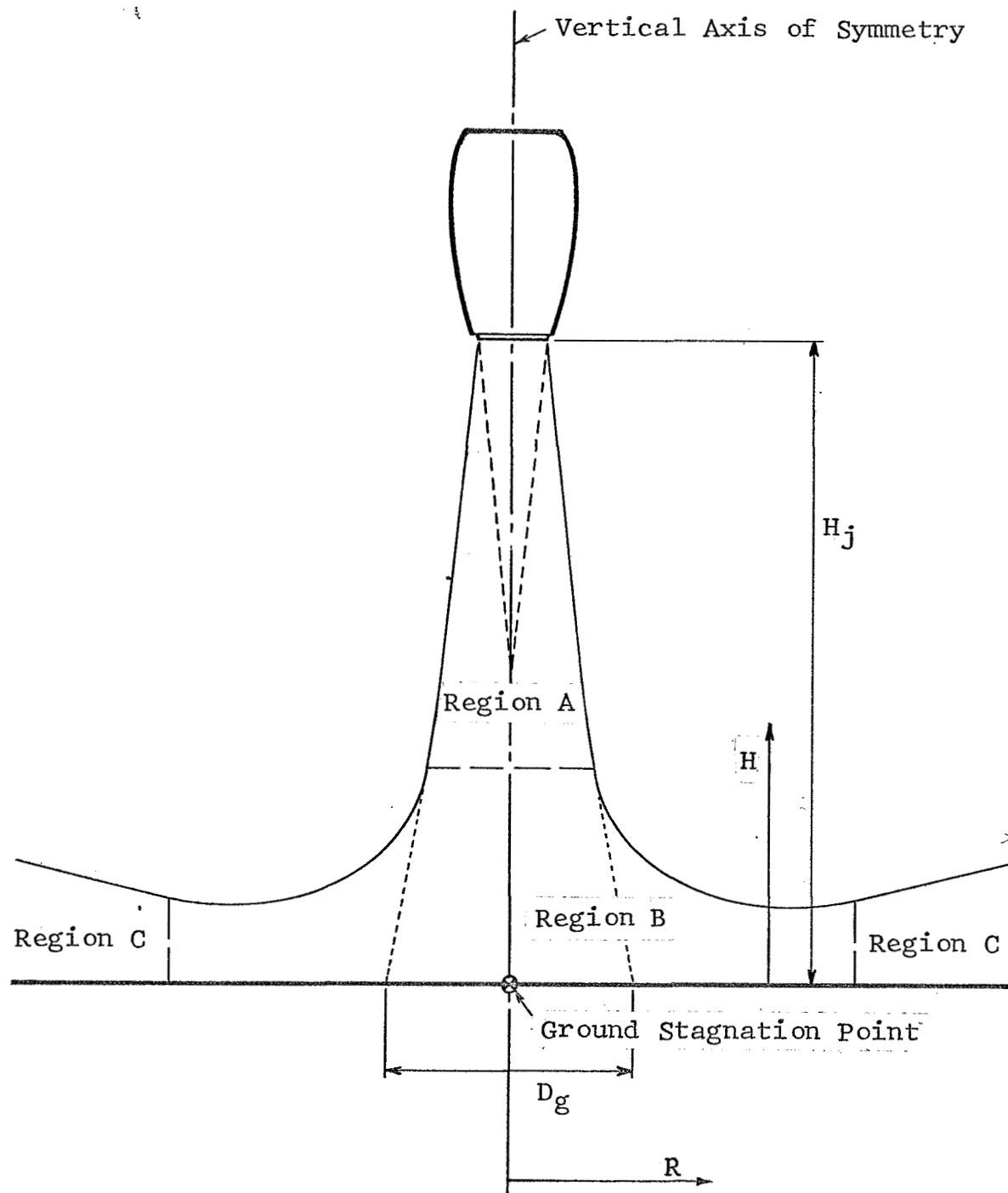Figure 13.— Streamlines for the Gaussian Jet Impinging on a Flat Plate.

Figure 14.- Coordinate System to Describe the Ground
Impingement Flowfield for a Vertical Jet
Exhausting Under Static Conditions.

where the dimensional value of the ground stagnation total pressure $(\Delta P_{tg})$ is obtained from equation (34) or Figure 7, whichever is applicable.

Figure 15 presents a comparison between the results obtained using equation (35) and the test data of Reference 41. Although this data is limited to incompressible isothermal flow it is considered that substantial deviation from this condition will not occur in this flow region. Thus, equation (35) or Figure 15 can be used to determine the static pressure variation along the jet centerline. These values can then be substituted in equation (1), instead of the ambient pressure values, to obtain velocity distributions within the ground impingement region. The total temperature variation required in equation (1) can be determined from the following sub-section.

### 3.1.2.2  Total Temperature Distribution

The total temperature distribution $(\overline{\Delta T_t})$ within the ground impingement region can be closely approximated using the free jet analysis presented in sub-sections 3.1.1.4 and 3.1.1.5.

For small values of nozzle heights corresponding to $(S_2) < 11$, the total temperature distributions $(\overline{\Delta T_t})$ within this region can be obtained from Figures 8, 10, and 11, using equations (4), (14) and (32). Also, the ground stagnation temperature $(\overline{\Delta T_{tg}})$ can be obtained from Figure 8 using equations (4) and (33). This graphical solution for $(\overline{\Delta T_t})$ and $(\overline{\Delta T_{tg}})$ is recommended for values of $(\overline{H_j})$ located in the equivalent free jet potential core or transition region.

For nozzle heights corresponding to $(S_2) \geqq 11$, the following analytical relationship is obtained for the total temperature distribution $(\overline{\Delta T_t})$, using equations (21) and (24), thus:

$$\overline{\Delta T_t} = \left[ \left( \frac{P_{tj}}{P_a} \right)^{-0.86} \cdot \left( \frac{T_{tj}}{T_a} \right)^{0.5} \cdot \frac{\overline{S}}{6.3 \cdot C_H} \right]^{k_1} \cdot e^{-0.693 \, (r/r_t)^2} \tag{36}$$

where $(k_1)$ and $(r_t)$ are given by equations (22), and (28), respectively.

Also, the ground stagnation temperature $(\overline{\Delta T_{tg}})$, for $(S_2) \geqq 11$ can be obtained by substituting $(\overline{H_j})$ for $(\overline{S})$ in equation (21), thus:

$$\overline{\Delta T_{tg}} = \left[ \left( \frac{P_{tj}}{P_a} \right)^{-0.86} \cdot \left( \frac{T_{tj}}{T_a} \right)^{0.5} \cdot \frac{\overline{H_j}}{6.3 \cdot C_H} \right]^{k_1} \tag{37}$$
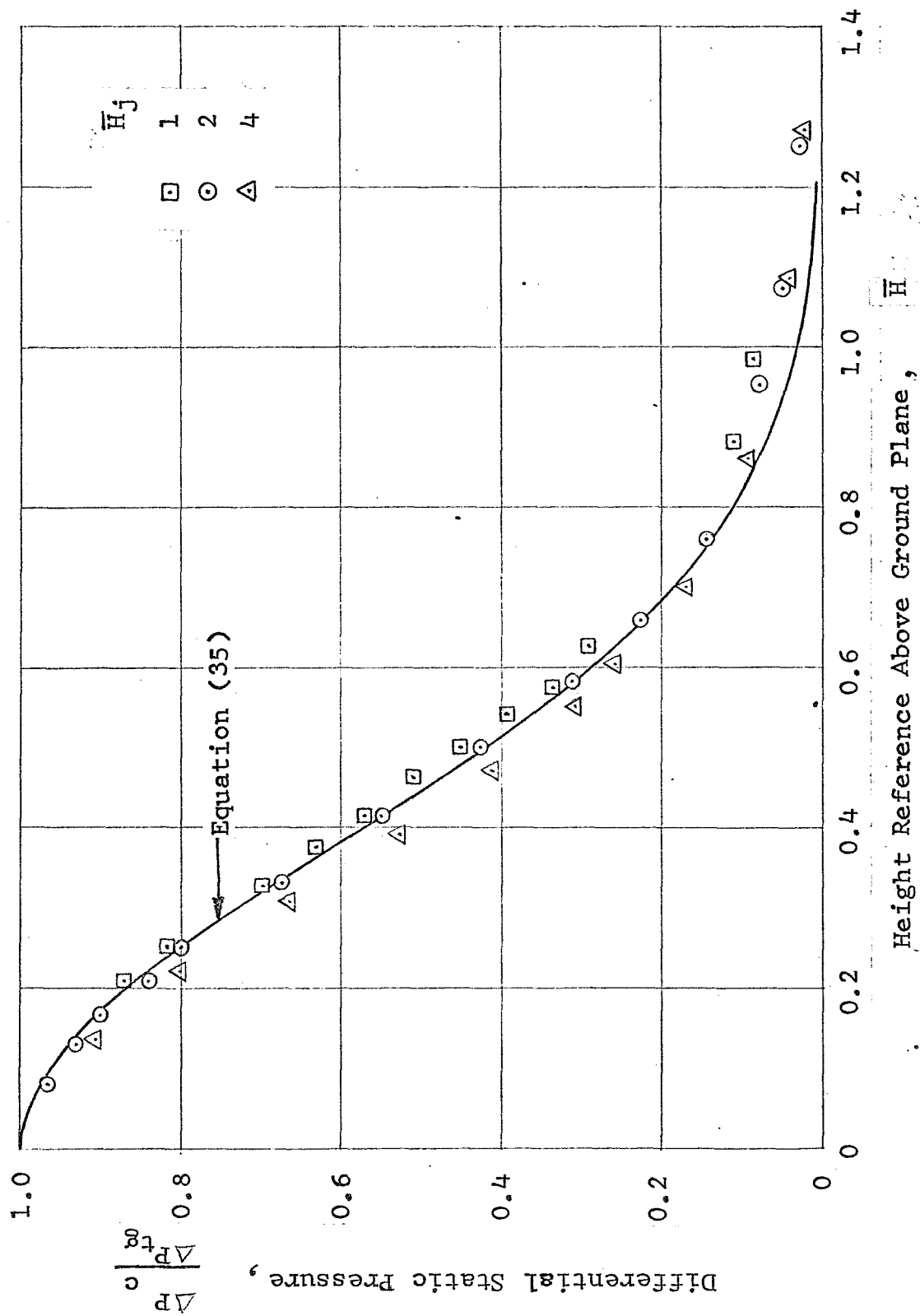
44

Figure 15.- Comparison Between Empirical Static Pressure Distribu-
tion on the Axis of a Vertically Impinging Jet in
Region B and Experimental Data from Reference 41.

### 3.1.2.3 Flow Conditions Along the Ground Plane

Close to the ground plane, the total pressure and temperature initially remain almost constant with increasing radius from the stagnation point (i.e. the point of intersection of jet axis with the ground). At a ground radius of about $0.4\,(D_g)$ where $(D_g)$ is the diameter of the equivalent free jet boundary at the ground plane, the total pressure commences a measurable decay which indicates a reappearance of the turbulent mixing process in the flow. This represents a transition zone of the ground impingement region and leads to a fully developed radial wall jet flow at a radius of about $2\,(D_g)$.

The variation of maximum total pressure $(\Delta P_{tw})$ along the ground plane in the impingement region for $(\bar{H}_j) \geq 4$ can be represented by the following equations:

For $\quad 0 \leq (R/D_g) \leq 0.4$

$$\Delta P_{tw} = \Delta P_{tg} \tag{38}$$

For $\quad 0.4 < (R/D_g) < 2.0 \tag{39}$

$$\Delta P_{tw} = \Delta P_{tg}\left(1.16 - 0.4\,(R/D_g)\right)$$

where $(\Delta P_{tg})$, the ground stagnation pressure, is obtained using the graphical solution of sub-section 3.1.1.5 or equation (34), whichever is applicable.

There is no test data to verify the applicability of equation (38) and (39) to small jet heights, $(\bar{H}_j) < 4$, although Reference 41 suggests a trend towards a reduction of the transition zone for small jet heights. However, based on the correlation of equations (38) and (39) with the available test data obtained from References 18, 20 and 43, as shown in Figure 16, it appears that the analytical representations should be adequate for predicting the ground plane peak total pressure for a wide range of practical jet heights.

The static pressure along the ground decays rapidly with radius from the stagnation point and reaches the atmospheric value in the fully developed wall jet region. For the case of vertical impingement, the close correspondence of the fully developed jet profile to the Gaussian curve suggests that the impingement theory of Barnes and Sullivan (Reference 44) may be utilized. Although their exact analysis of the decay of static pressure along the ground radial surface leads to a complex solution, it was shown that this decay can be adequately approximated by the Gaussian profile whose integrated surface loading equals the jet vertical momentum.

Using this result for the present study, the surface static pressure distributions can be expressed as follows:
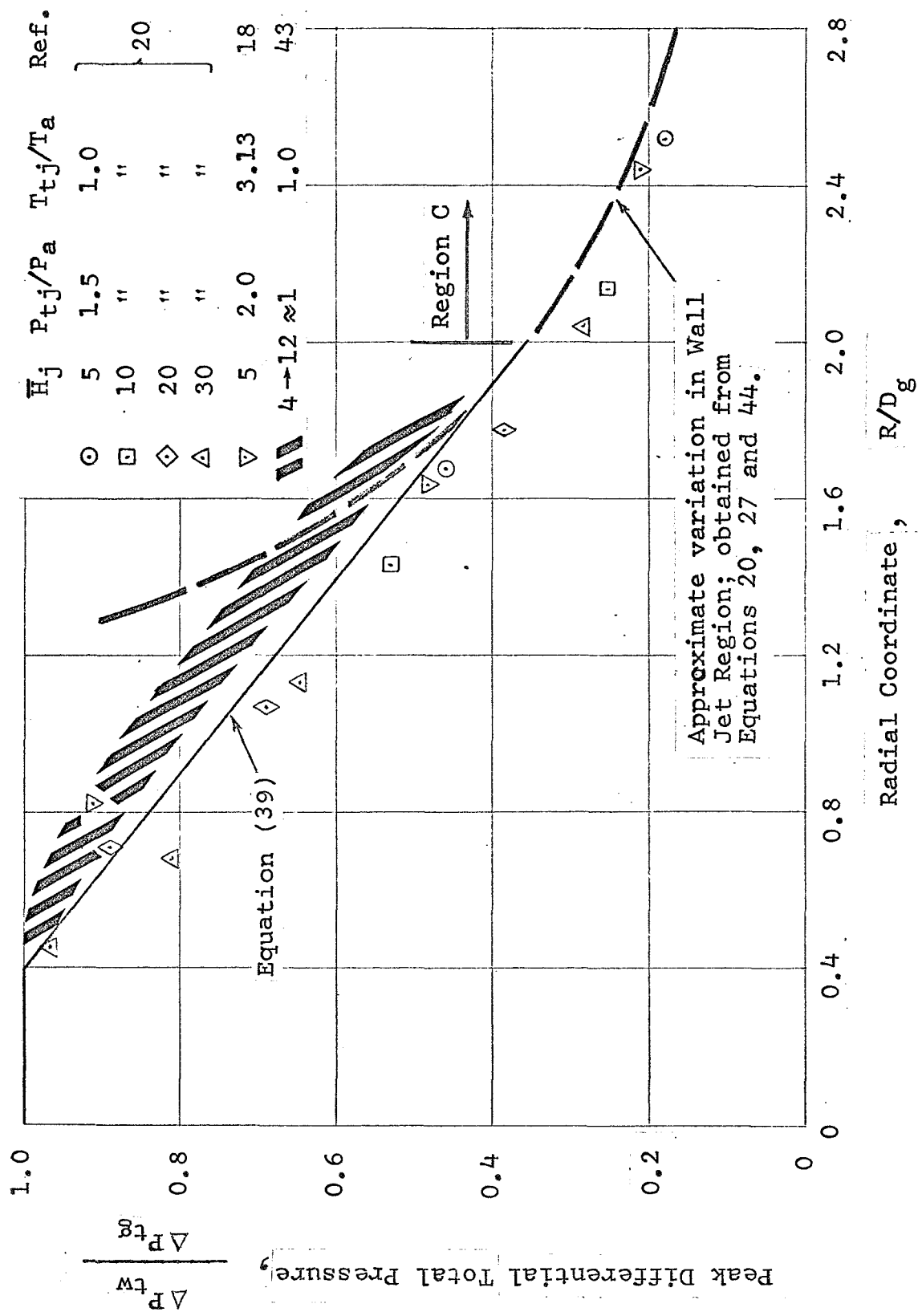
46

Figure 16.— Comparison Between Empirical Radial Variation of Peak Groundplane Total Pressure in Region B and Experimental Data of References 18, 20 and 43.

47

$$\Delta P_w = \Delta P_{tg} \cdot e^{-2.772 \, (R/D_g)^2} \tag{40}$$

Figure 17 presents a correlation of the analytical results obtained by equation (40) with the test data of Reference 17 for jet heights $\overline{H}_j > \overline{S}_c$.

If normal impingement occurs at jet heights where the potential core region intersects the ground plane, appreciable deviations from the ground static pressure distributions of fully developed jets are found. This is shown in Figure 18 which summarizes the data of Reference 41 at $\overline{H}_j = 1$, 2, and 4 for an isothermal incompressible jet, and compares the results with Equation (40). In the absence of more complete experimental data a simple linear interpolation of the data of Figure 18 is recommended to determine the decay characteristics at intermediate nozzle heights.

There is no adequate data on radial variation of ground plane total temperature. Therefore, the transition zone effects are omitted from the analytical model and the peak total temperature is assumed to be constant and equal to ground stagnation total temperature. Thus:

$$\overline{\Delta T_{tw}} = \overline{\Delta T_{tg}} \tag{41}$$

where $\left(\overline{\Delta T_{tg}}\right)$ is obtained from the graphical solution of subsection 3.1.1.5 or equation (37) whichever is applicable.

Equation (41) is considered applicable up to the beginning of the wall jet region.

3.1.2.4  Effect of Crosswinds

Under the influence of ambient crosswinds the deflection of the jet leads to the occurence of an oblique ground impingement as shown in Figure 19. The angle of impingement $(\theta_g)$ may be approximated by the value occurring at the equivalent ground plane position in a free jet and is obtained directly from equation 31 by substituting $\left(\overline{H}_j\right)$ for $\left(\overline{z}_c\right)$ thus:

$$\theta_g = \cot^{-1}\left[ 3 \cdot (\mu)^{2.6} \cdot \left(\overline{H}_j\right)^2 \right] \tag{42}$$

The analysis for pressure and temperature distributions within this region as affected by crosswinds is the same as that developed for a free jet in Section 3.1.1.6.

When oblique impingement occurs, the flow field in region B is asymmetric. There are no known experimental measurements that may be used to describe the oblique impingement flow field
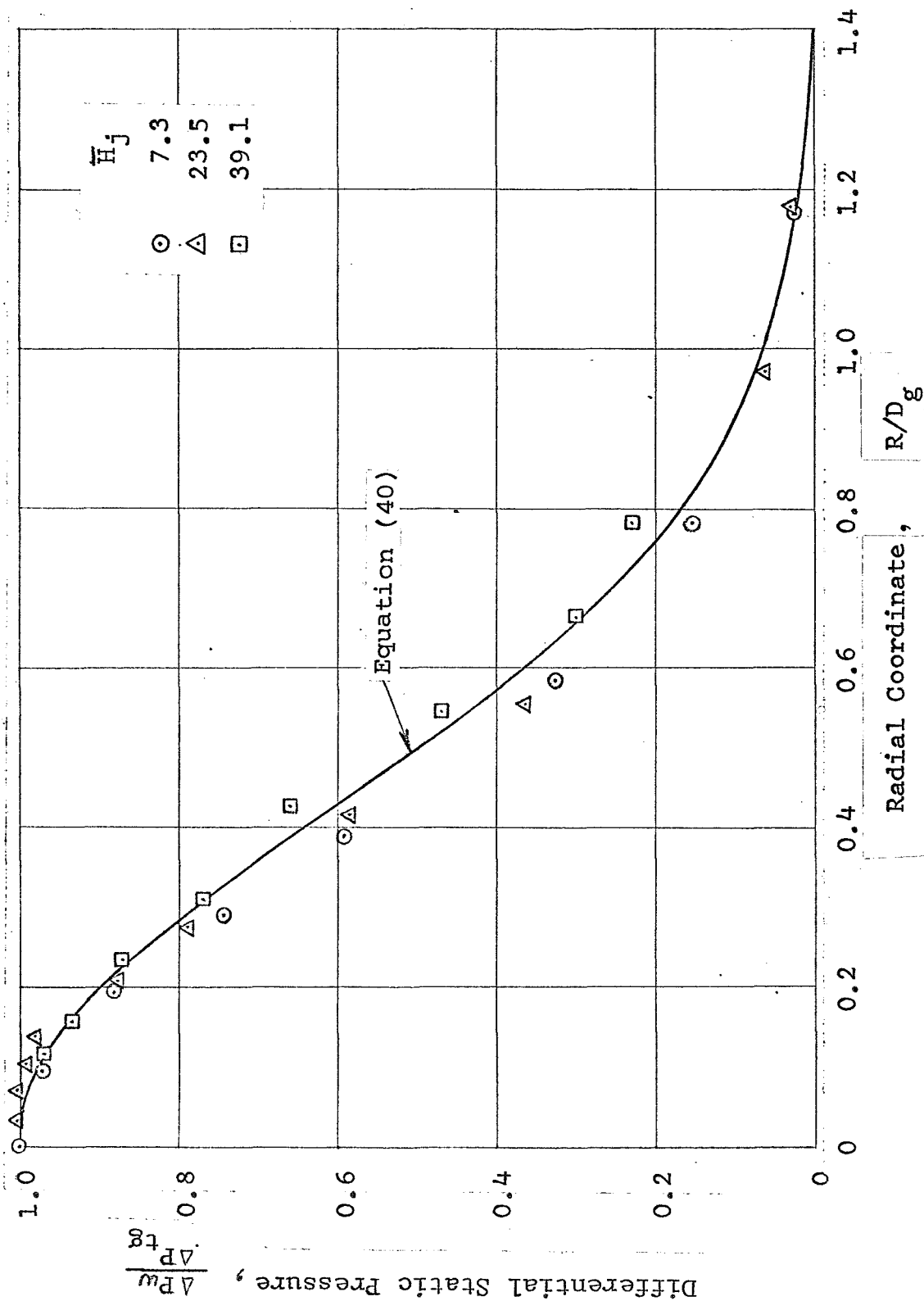
Figure 17.— Comparison Between Theoretical Radial Variation of Groundplane Static Pressure in Region B and Experimental Data of Reference 17.

49
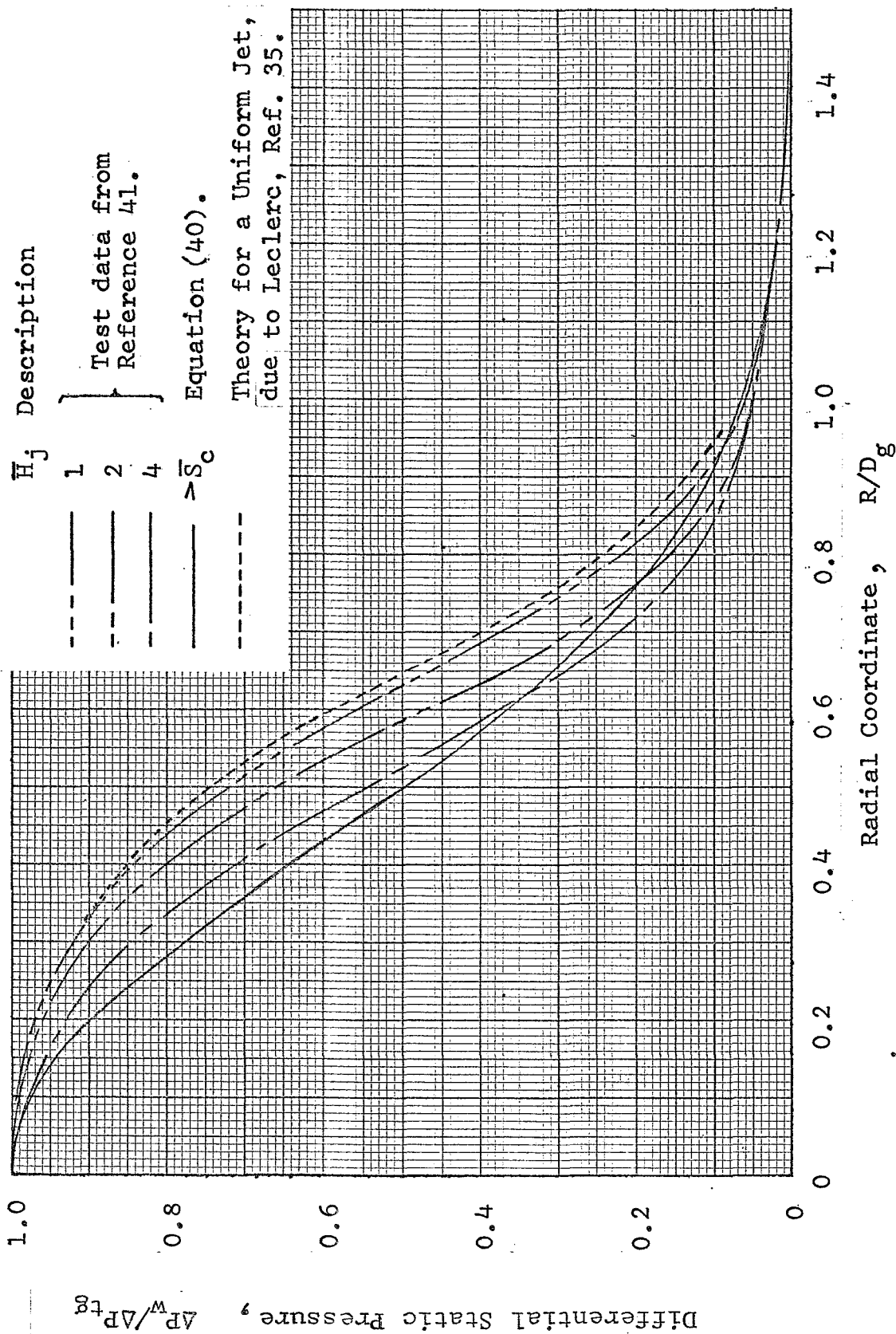
Figure 18.— Summary of Groundplane Static Pressure Distributions For A Vertically Impinging Jet.

50
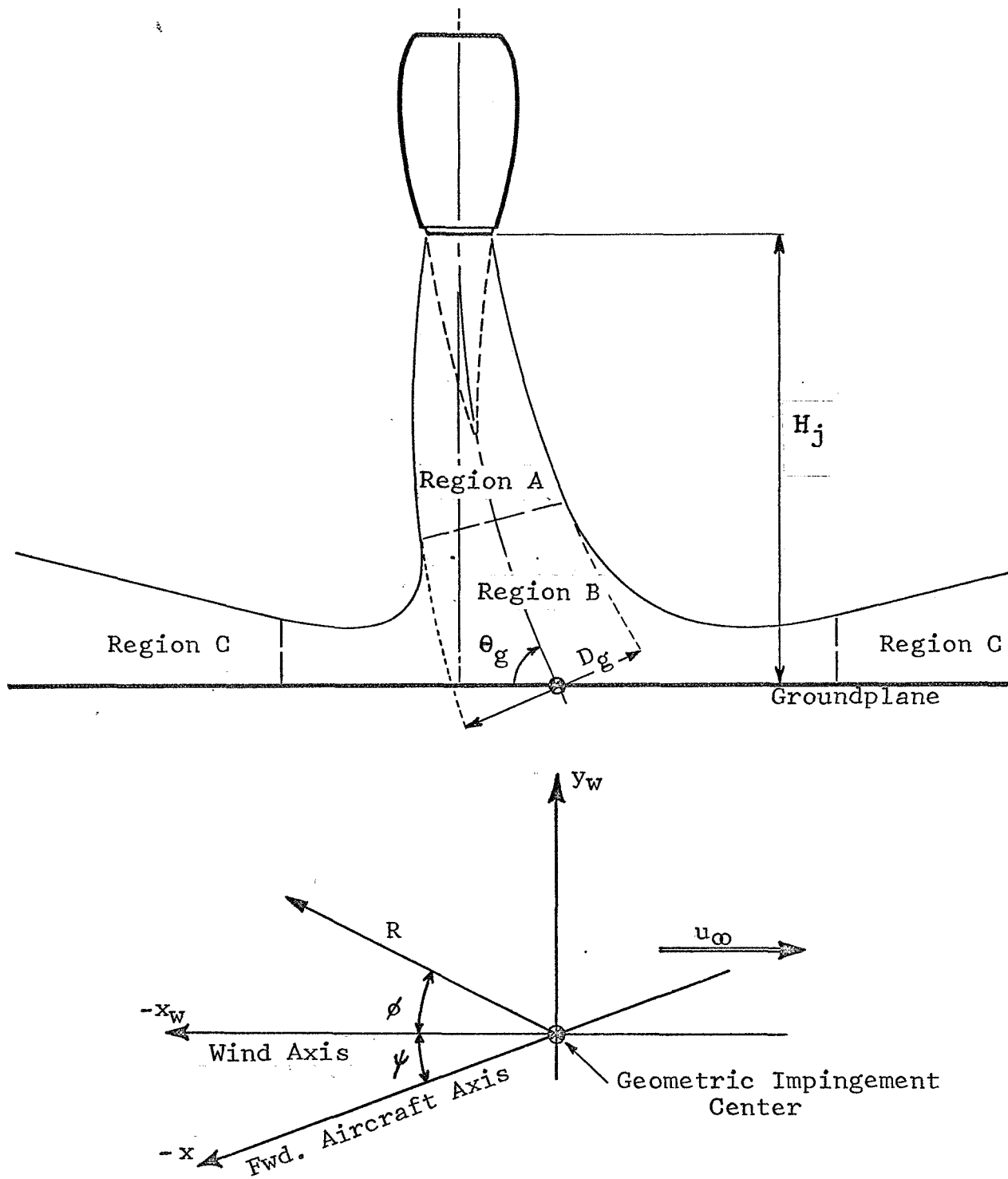
Figure 19.- Coordinate System to Describe the Ground Flow Field for a Single Jet With Crosswind Effects.

for a jet deflected by crosswinds. However, by making an analogy to the case of an inclined jet exhausting under static conditions, it is found from the data reported in Reference 60 that the location of the ground plane stagnation point is displaced upwind of the intersection of the jet path axis. For the small range of impingement angles considered $75° \leqslant (\theta_3) \leqslant 90°$ in the present analysis, this displacement remains small and is therefore neglected.

Other measurements reported in Reference 60 show that the value of the stagnation point pressure is essentially constant for the same range of impingement angles. Therefore the stagnation point pressure is obtained by the methods given for vertical (axisymmetric) impingement.

52

### 3.1.3 Region C- The Wall Jet Flow

The wall jet region, as shown in Figure 1, Region C, represents the radial ground flow extending from the ground impingement region to the flow separation and flow recirculation region.

Prediction methods developed for the radial wall jet region are based on the theoretical treatments reviewed in Section 2 with certain empirical modifications introduced in this section. The calculative methods given below consider the peak decay characteristics of total pressure and temperature, jet profiles, and reference flow boundaries in a similar manner to the treatment presented for other flow regions.

An important feature of the methods presented herein to describe the wall jet behavior is that only the jet nozzle flow parameters, nozzle height and ground impingement angle are required. Details of the flow characteristics in Regions A and B are not essential except in locating the position of fully established wall jet flow.

The static pressure throughout the wall jet region is assumed constant and equal to the ambient static value. Although this assumption is not strictly valid the analysis presented in Reference 69 indicates that the errors involved are negligible.

### 3.1.3.1 Total Pressure Distribution

The decay of peak differential total pressure resulting from a vertically impinging jet may be derived from the simple power expression given by the analytical investigations of References 53 and 54 for isothermal incompressible jets. By rewriting this expression in non-dimensional form, allowing for a variation of the nozzle discharge coefficient ($C_D$) on the basis of Abbott's investigation (Reference 55) and accounting for compressibility effects on the basis of observations made in References 56 and 70, the following relationship is obtained:

$$\left(\Delta \overline{P_{tw}}\right)^{1/2} = K_2 \cdot \sqrt{\overline{C_D}} \cdot \left(\overline{H_j}\right)^{\overline{k_2-1}} \cdot \left(\overline{R}\right)^{-k_2} \tag{43}$$

Substituting appropriate empirical values for $K_2$ and $k_2$ the effects of jet height variation $1 \leqslant \left(\overline{H_j}\right) \leqslant 36$ are found to be in good agreement with experimental data of both Reference 41 and 56. As noted by Abbott in Reference 56, the values of $\left(\Delta \overline{P_{tw}}\right)$ given by equation (43) are independent of temperature effects. This is further substantiated by the test data from References 18 and 20 for the temperature range $1 \leqslant \left(T_{tj}/T_a\right) \leqslant 3$.

53

A detailed review of available radial wall jet test data presented in References 18, 20, 41, and 54 through 57 was made to determine the most appropriate empirical values of $K_2$ and $k_2$. This information is summarized in Table I and is used to develop the following relationship for the decay behavior of the total differential pressure in the wall jet:

$$\left(\overline{\Delta P_{tw}}\right)^{1/2} = 1.26 \cdot \sqrt{C_D} \cdot \left(\overline{H_j}\right)^{0.08} \cdot \left(\overline{R}\right)^{-1.08} \tag{44}$$

The above equation is plotted in Figure 20 to show a comparison of the analytical results with large and small scale V/STOL model data obtained from References 71 and 65, respectively.

Extensive measurements obtained in References 17 and 60 indicate that the normalized total-pressure profiles in the wall jet region are essentially independent of nozzle height $\left(\overline{H_j}\right)$, nozzle pressure ratio $\left(P_{tj}/P_a\right)$, nozzle temperature ratio $\left(T_{tj}/T_a\right)$, radial coordinate $(\overline{R})$, and Reynolds number $(R_w)$. Furthermore, the pressure profile appears to be independent of whether the jet impinges obliquely or not. Figure 21 shows the mean experimental profile resulting from these measurements. The profile can be closely approximated by Glauert's theoretical curve for $R_w = 13,000$ (Reference 60) except in the outer region, $(h/h_p)>1$, where the recirculation flow field is approached. Glauert's profile is, however, defined by a complex expression which may be replaced by a simpler empirical representation utilizing separate expressions for the inner boundary layer (1/7th velocity power law) and outer free mixing zone (Gaussian profile). Thus the total differential pressure at any point within the wall jet can be expressed as follows:

For $0 \leq (h/h_p) \leq 0.17$

$$\left(\frac{\Delta P_t}{\Delta P_{tw}}\right) = \left(\frac{h}{0.17\, h_p}\right)^{2/7} \tag{45}$$

For $0.17 < (h/h_p)$

$$\left(\frac{\Delta P_t}{\Delta P_{tw}}\right) = e^{-2\cdot\left(\frac{h}{h_p}-0.17\right)^2} \tag{46}$$

where the peak total pressure $(\Delta P_{tw})$ close to the wall is given by equation (44). The height of the pressure reference boundary $(h_p)$ is given by the point on the outer profile where $\left(\Delta P_t/\Delta P_{tw}\right) = 0.25$ and can be obtained from the following analysis.

Expressions for the growth of the wall jet pressure boundary $(\overline{h_p})$ have been derived in the analyses of References 53 and 54 for isothermal incompressible jets and are presented in the following form:

$$\overline{h_p} = K_3 \cdot \left(\overline{H_j}\right)^{1-k_3} \cdot \left(\overline{R}\right)^{k_3} \tag{47}$$

54

Table I.- Summary of Test Data Applicable to the Wall Jet Region

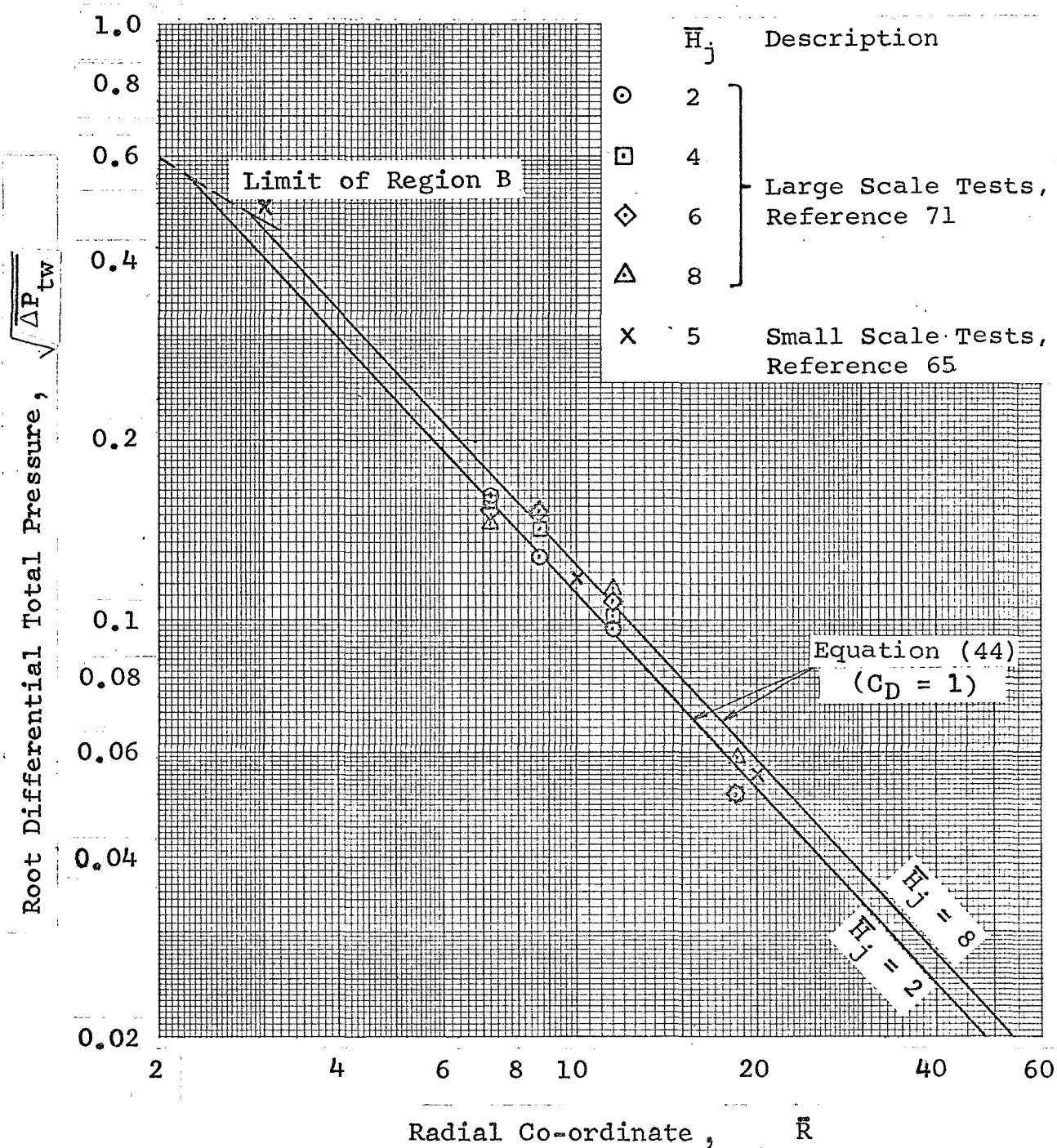| Reference | $K_2$ | $k_2$ | Test Conditions | | | | | | | |
|---|---|---|---|---|---|---|---|---|---|---|
| | | | $D_j''$ | $Pt_j/P_a$ | $Tt_j/T_a$ | $u_j$ | $C_D$ | $\bar{H}_j$ | $R_w \times 10^{-5}$ | $(\bar{R})_{max}$ |
| 18 | 1.21 | 1.13 | 3 | 2.0 | 1-3.13 | - | 0.98 | 5-30 | 2.2 | 9 |
| 20 | 1.27 | 1.09 | 3 | 1.5 | 1. | - | 0.98 | 5-30 | 1.6 | 9 |
| 41 | 1.43 | 1.12 | 12 | - | 1. | 120-190 | 0.98* | 1-4 | 0.8-1.3 | 4 |
| 54 | 1.49 | 1.10 | 1-3 | 1.08 | 1. | - | 0.611* | 8-24 | 0.1-0.5 | 69 |
| 55,56 | 1.26 | 1.08 | 1-2 | - | 1-2.18 | 350-1100 | 0.9 | 1-36 | 0.2-1.1 | 100 |
| 57 | - | 1.12 | 1. | 1. | 1. | - | - | - | 0.035 | 10 |
| 65 | - | - | 1.25 | 2.0 | 2. | - | - | 5 | 0.9 | 20 |
| 71 | - | - | 12.5 | 1.8 | 3. | - | - | 2-8 | 8. | 18 |

* Not measured experimentally

55

Figure 20.- Comparison Between Developed Wall Jet Peak
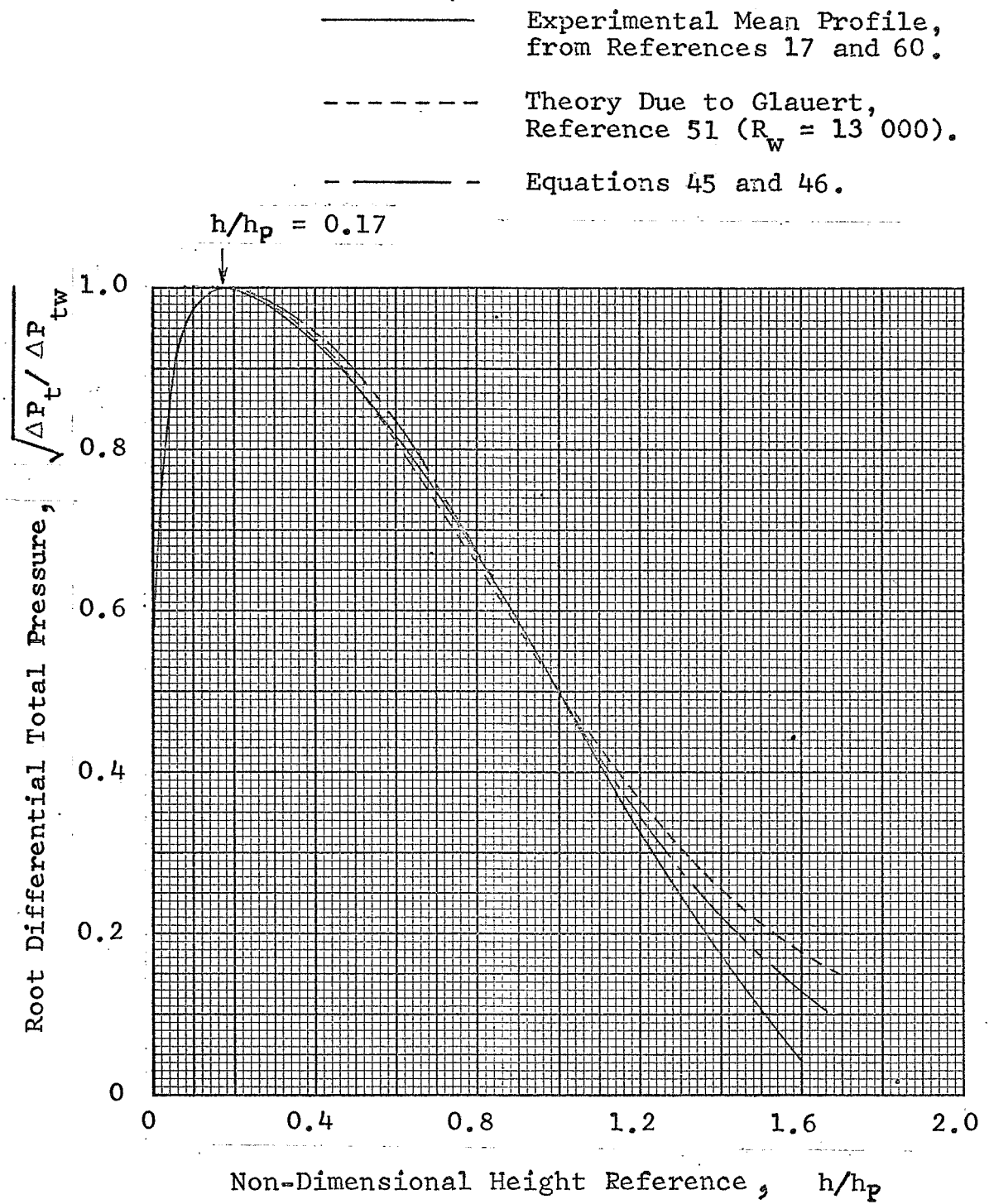Total-Pressure Decay and Test Data of
References 65 and 71.

Figure 21.- Root Differential Total Pressure
Profiles for The Wall Jet Region.

Good agreement with the test data of References 20, 41, and 54 is obtained by taking $k_3 = 0.9$. This value is significantly lower than the theoretical value of 1.01 given by Glauert. Although experimental data from different sources indicate appreciable variation of the constant $K_3$, the value of 0.098 (rounded off to 0.1) given in Reference 54 is used. Equation (47) can then be expressed as:

$$\bar{h}_p = 0.1.(\bar{H}_j)^{0.1}. (\bar{R})^{0.9} \tag{48}$$

Figure 22 shows that this equation results in fair agreement with large and small-scale data of References 71, 65 respectively.

Thus the total differential pressure $(\overline{\Delta P_t})$ at any point within the wall jet can be uniquely determined using equations (44), (45), or (46), and (48).

3.1.3.2 Total Temperature Distribution

In the absence of satisfactory theories, the total temperature characteristics $(\Delta T_t)$ are derived empirically from the data presented in References 18, 55, 56, and 71. From the preceeding analyses for Regions A and C, it is reasonable to expect the decay of total temperature differential to be functionally dependent on nozzle height $(\bar{H}_j)$, pressure ratio $(P_{t_j}/P_a)$, and heat discharge coefficient $(c_H)$. In addition, the heat sink properties of the ground may be important; however, there is insufficient data on such effects.

The model test data of Reference 55, which are used as the basis for predicting the peak total pressure decay in Region C, suggest the following simplified form of the peak total temperature decay.

$$\overline{\Delta T_{t\omega}} = K_4.(\bar{H}_j)^{-0.09} (\bar{R})^{k_4} \tag{49}$$

where the decay constant, $K_4$, is approximately 0.7 and the exponent, $k_4$, has the value 0.725. However, model and full-scale data of References 18 and 71, respectively, indicate that both $K_4$ and $k_4$ should be unity. Since the latter tests were made at more-representative nozzle pressure ratios ($1.7 \leq (P_{t_j}/P_a) \leq 2.0$) than those of References 55 and 56 ($(P_{t_j}/P_a) < 1.2$) the following expression for the decay of peak total temperature within the wall jet is recommended:

$$\overline{\Delta T_{t\omega}} = 1.0.(\bar{H}_j)^{-0.09}. (\bar{R})^{-1.0} \tag{50}$$

Figure 23 presents a good correlation of the results obtained from equation (50) with the test data of References 18, 65, and 71.

Unlike the pressure profile the total temperature profile of a wall jet does not possess the characteristic boundary
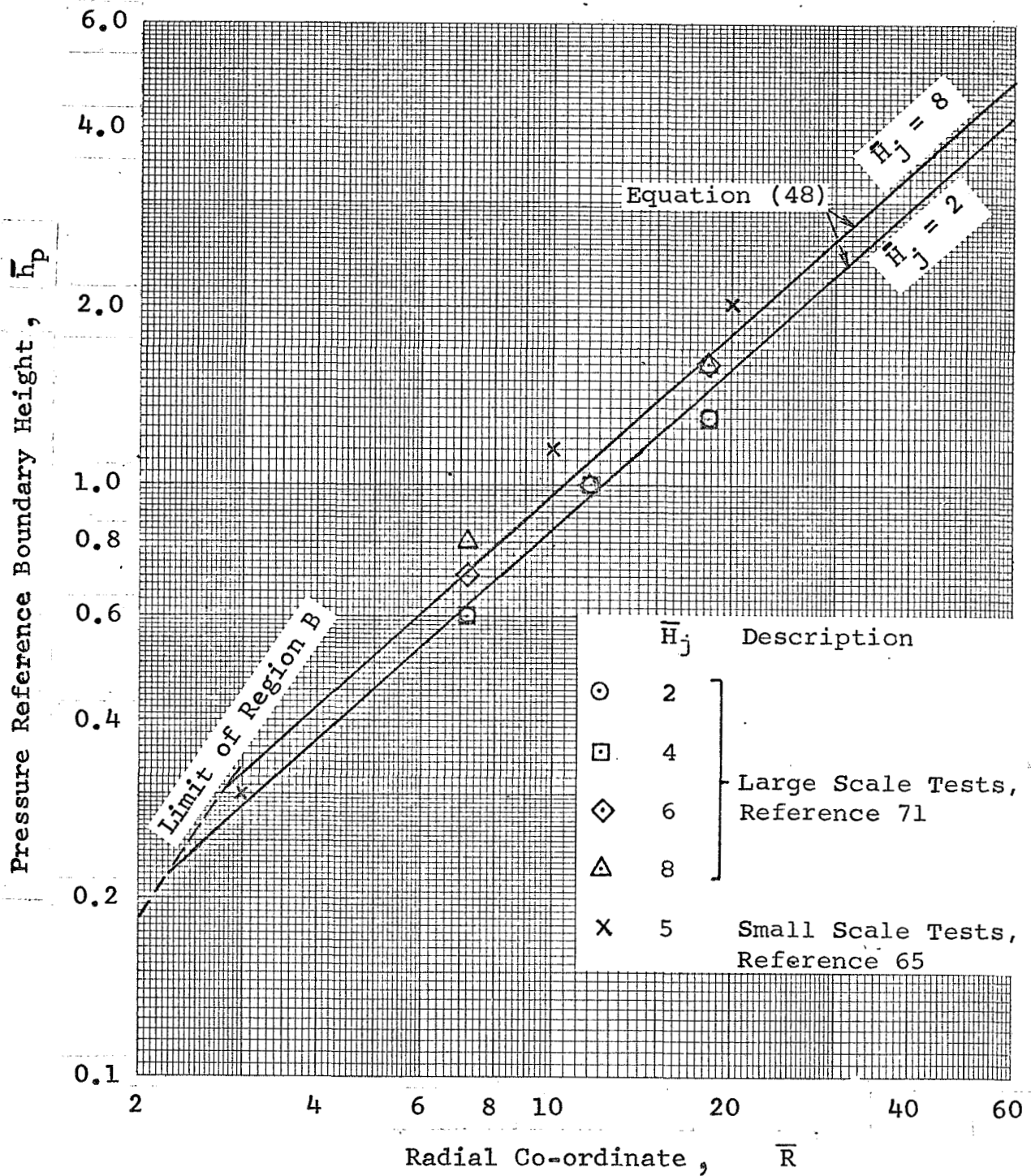
58

Figure 22.- Comparison Between Developed Wall Jet Pressure Reference Boundary Growth and Test Data of References 65 and 71.
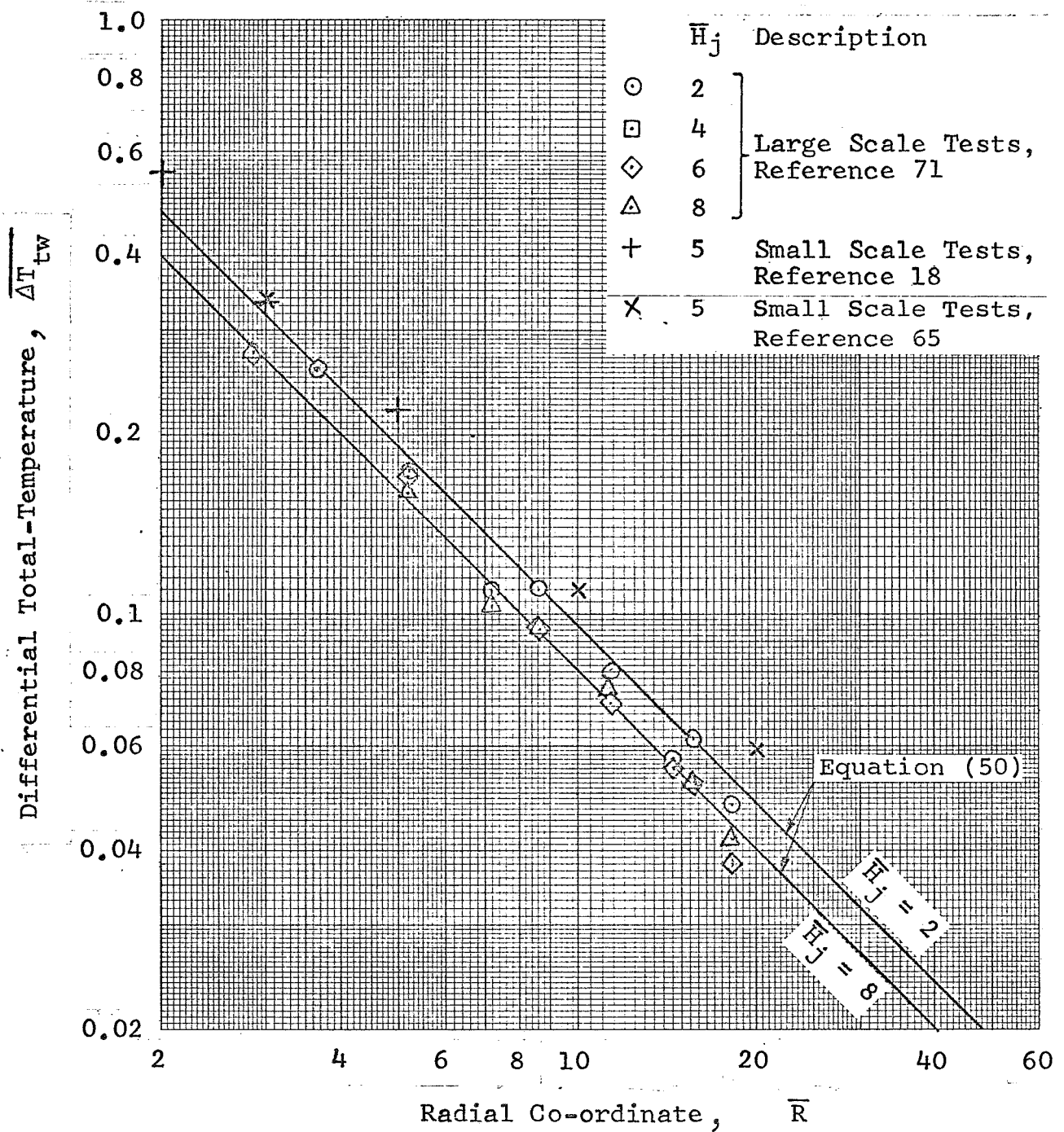
Figure 23.- Comparison Between Developed Wall Jet Peak Total-Temperature Decay and Test Data of References 18, 65 and 71.

60

layer shape. Although few detailed measurements of total temperature profiles have been made the available data indicates that the variation of differential total temperature may be reasonably well approximated by a Gaussian curve. This representation has been employed by Abbott in theoretical studies (Reference 56).

Heat transfer between the wall jet and the ground will, of course, cause departures from the Gaussian shape. The heat transfer will depend on the temperature differential between the ground and the wall jet flow, and also on the thermal properties of the ground.

Thus, the total differential temperature distribution within the wall jet can be represented by the following relationship:

$$\left(\frac{\Delta T_t}{\Delta T_{tw}}\right) = e^{-1.386 \left(h/h_t\right)^2} \tag{51}$$

where $\left(h_t\right)$ is the height of the temperature reference boundary given by the condition that $(\Delta T_t/\Delta T_{tw}) = 0.5$ and is determined from the following analysis:

Following the analysis of Reference 55, variation of the total temperature reference boundary ($\bar{h}_t$) may be obtained by assuming that it is related to the total pressure reference boundary ($\bar{h}_p$) by a factor varying between 1 and 1.4. Thus utilizing equation (48) there results:

$$\bar{h}_t = 1.4 \left(\bar{h}_p\right) = 0.14 \cdot \left(\bar{H}_j\right)^{0.1} \cdot \left(\bar{R}\right)^{0.9} \tag{52}$$

This relationship together with the experimental data of Reference 71 is plotted in Figure 24 which shows a reasonable correlation between the analytical and experimental results.

Thus the total temperature ($\Delta \bar{T}_t$) of any point within the wall jet region can be uniquely determined using equations (50), (51) and (52).

Finally, as in the case of other flow regions discussed previously, the local velocity distribution at any point within the wall jet region can now be established through equation (1) knowing the values of $(P_t)$ and $(T_t)$ determined in sub-section 3.1.3 and assuming $P = P_a$.

### 3.1.3.3 Ground Flow Separation Radius

Under static conditions the presence of a local jet temperature differential (above ambient) promotes natural buoyancy forces which counteract the radial momentum forces. When the two forces approach the same order of magnitude, the wall jet
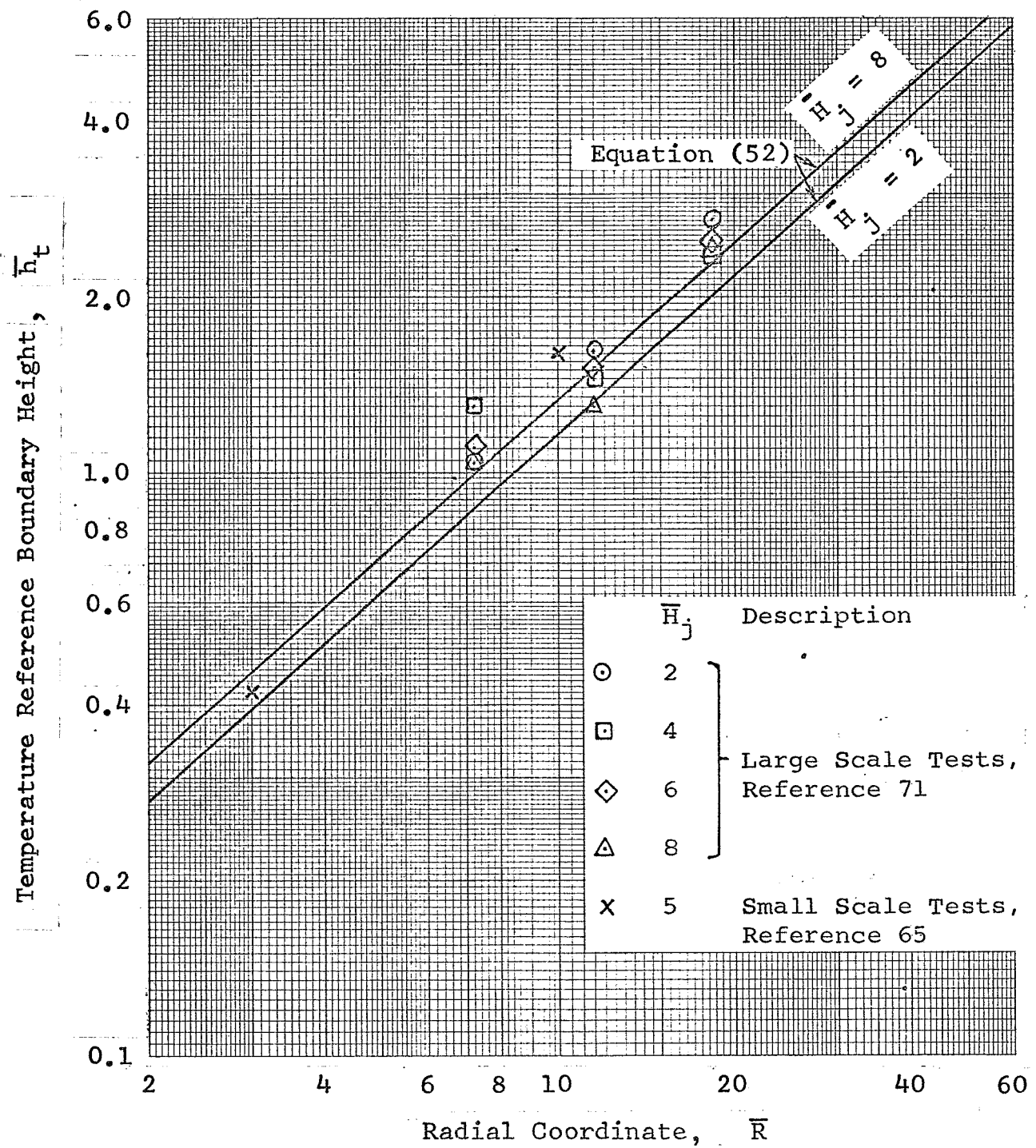
61

Figure 24.- Comparison Between Developed Wall Jet Temperature Reference Boundary Growth and Test Data of References 65 and 71.

flow separates and rises from the ground. Normally, in regions close to the impingement point, the wall jet momentum forces are much larger than those due to buoyancy. However, since local jet momentum decays at nominally twice the rate of the temperature differential $(\Delta T_{tw})$ a point is soon reached where the buoyancy forces approach the magnitude of the radial momentum forces.

Based on the experimental data obtained by Abbott (Reference 56) for $(P_{tj}/P_a) < 1.2$ and $(T_{tj}/T_a) < 2.7$ the following expression for the ground separation distance $(R_s)$ is obtained:

$$\bar{R}_s = 0.62 \cdot \left[ \frac{(u_j)^2}{g \cdot D_j} \cdot \frac{1}{(T_{tj}/T_a) - 1} \cdot \left(\frac{T_{tj}}{T_a}\right)^{-1/2} \right]^{1/2} \tag{53}$$

This expression is based on a simplified theoretical representation of the jet decay behavior discussed previously. By use of the incompressible Bernoulli's equation the above relationship can be represented as:

$$\bar{R}_s = 0.877 \left[ \frac{G \cdot T_a}{g \cdot D_j} \cdot \frac{(P_{tj}/P_a) - 1}{(T_{tj}/T_a) - 1} \cdot \left(\frac{T_{tj}}{T_a}\right)^{1/2} \right]^{1/2} \tag{54}$$

Abbott's analysis shows that a criterion for buoyant flow separation (no crosswinds) corresponds to a constant ratio (approximately 0.17) of the buoyancy pressure differential to the peak total pressure differential $(\Delta P_{ts})$ at the point of separation. This value can be obtained from equation (44) by substituting the value of $(R_s)$ for $(R)$, thus:

$$\left(\overline{\Delta P_{ts}}\right)^{1/2} = 1.26 \cdot \sqrt{C_D} \cdot \left(\bar{H}_j\right)^{0.08} \cdot \left(\bar{R}\right)^{-1.08} \tag{55}$$

Similarly, the peak differential total temperature $(\Delta T_{ts})$ at this same point can be obtained from equation (50), thus:

$$\overline{\Delta T_{ts}} = \left(\bar{H}_j\right)^{-0.09} \cdot \left(R_s\right)^{-1.0} \tag{56}$$

where, $\left(\bar{R}_s\right)$ in both of the above expressions is given by equation (54).

3.1.3.3   Effect of Crosswinds

Crosswinds affect not only the total pressure and temperature distributions within the wall jet region but also the ground separation radius.

The variation of peak total pressure $(\Delta P_{tw})$ as influenced by crosswinds can be directly obtained from equation (43) by

appropriately adjusting the empirical decay constants $K_2$ and $k_2$. These constants are derived from the test data of Reference 55 and are presented in Figure 25 as a function of the local jet turning angle $(\theta_t)$.

This angle is obtained from basic geometric considerations in terms of the ground impingement angle $(\theta_g)$, as given by equation (42), and the azimuth position $(\phi)$. Thus:

$$\theta_t = \cos^{-1}\left[ (-).\cos(\theta_g) . \cos(\phi) \right] \tag{57}$$

The peak total temperature $(\Delta T_{tw})$ can now be expressed in terms of the local jet turning angle $(\theta_t)$ as follows:

$$\overline{\Delta T_{tw}} = \left[ 2.109 - 0.0123.(\theta_t) \right] . (\overline{H_j})^{-0.09} . (\overline{R})^{-1.0} \tag{58}$$

Thus, having established the effect of crosswinds on the peak values of total pressure $(\Delta P_{tw})$ and temperature $(\Delta T_{tw})$, analyses of sub-sections 3.1.3.1 and 3.1.3.2 may be utilized to determine total pressure and total temperature distributions at any point within the wall jet region.

Also, the ground surface wind generally has a large effect on ground flow separation radius $(\overline{R_s})$. Specifically, it is found that the wall jet flow which propagates against the crosswind separates earlier than the flow in the downwind direction.

Physical considerations indicate that the flow separation would be expected to occur when the momentum of the wall jet approaches that of the crosswind. This is borne out by the experimental work of Abbott in Reference 55. Abbott conducted moving-model tests for a single engine in static ambient conditions and at small nozzle heights $((\overline{H_j}) < 6)$. Since crosswinds are defined relative to the model then these test conditions are representative of a stationary model in the presence of a uniform crosswind. Measurements of the upwind ground flow separation radius $(\overline{R_s})$ indicate that the flow separation was within $\pm$ 10% of the value given by

$$(\overline{\Delta P_{tw}})^{1/2} = 2.\mu \tag{59}$$

This criterion applied for the model test conditions of relative crosswind ratio $(0.01 \leq \mu \leq 0.08)$, nozzle pressure ratio $((P_{tj} / P_a) < 1.2)$, and nozzle temperature ratio $((T_{tj} / T_a) < 2.1)$, and was found to be in a good agreement with limited full-scale test data.
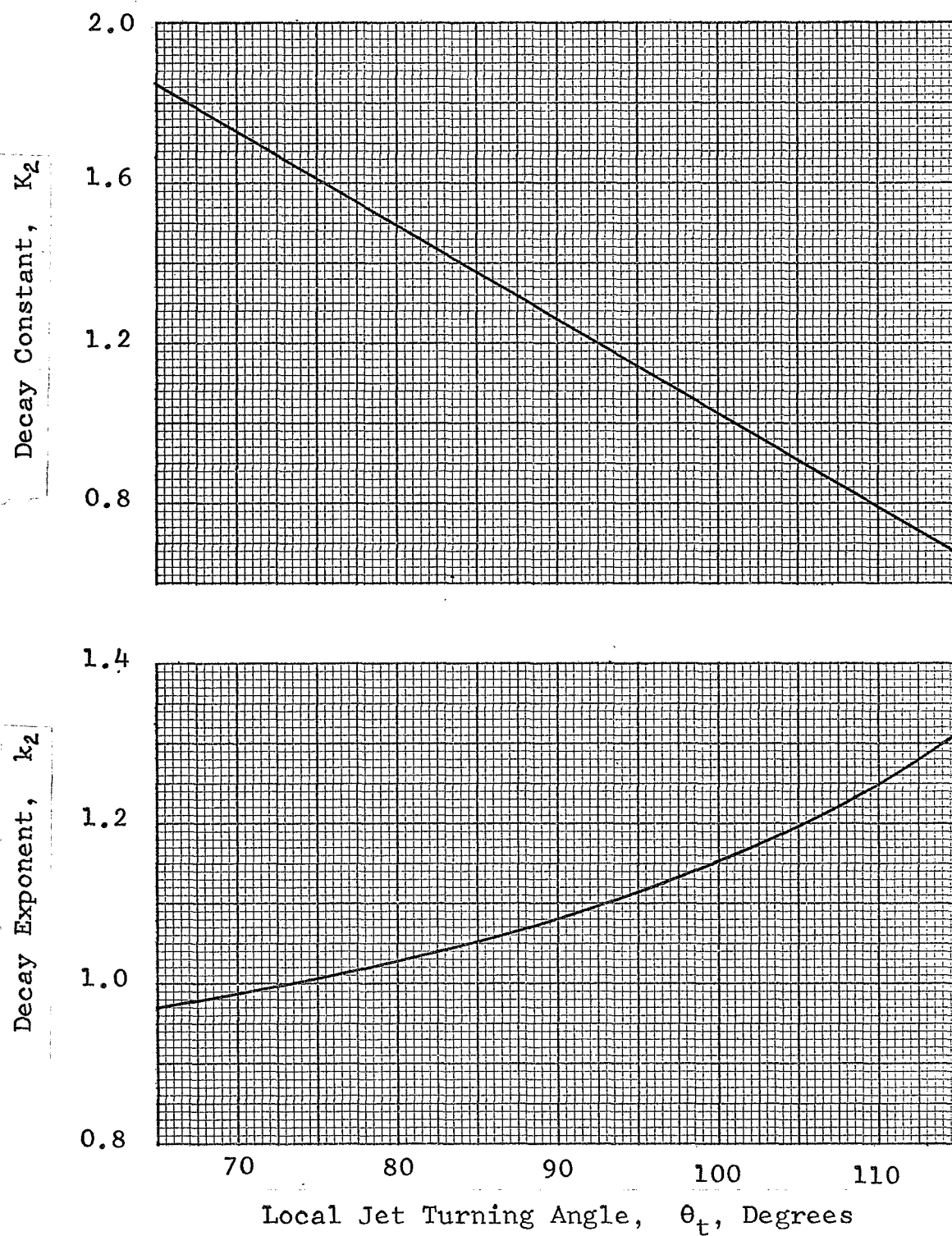
64

Figure 25.- Variation of Wall Jet Total-Pressure Decay Constant and Exponent With Local Jet Turning Angle, Obtained From Data of Reference 55.

Later experiments were conducted by blowing air past a stationary model in a wind tunnel. These tests covered the same range of relative crosswind ratios ($\mu$) as the moving-model experiments. It was found that the separation criterion for ($\Delta \overline{P_{t\omega}}$) could not be expressed as a simple linear function of ($\mu$). This is attributed to the presence of a boundary layer in the wind tunnel tests. Based on the reported data an approximate criterion for the ground flow separation is obtained as:

$$\left(\overline{\Delta P_{t\omega}}\right)^{1/2} = \left(\frac{2 \cdot \mu}{1 + 5 \cdot \mu}\right) \tag{60}$$

The above equation correlates with the experimental data within about $\pm$ 10% for crosswind ratios within the range $0.02 \leqslant (\mu) \leqslant 0.10$.

### 3.1.4 Region D- Far Field Recirculation Flow

This region, as shown in Figure 1, Region D, pertains to the flow outside the regions discussed previously, and is contained within the hot gas cloud boundaries with the exception of the engine intake flow.

The boundary of the recirculation region is defined by the envelope which represents the limit of significant temperature differential above the surrounding ambient value. Although there are few direct experimental measurements which are relevant to this investigation, it is possible to obtain a representative temperature envelope from experimental smoke injection studies since there is a general similarity between the dissipation processes for excess temperature and smoke density in a turbulent flow. In such studies, the smoke generating device is usually introduced either directly into the jet nozzle exhaust or into the radial ground flow.

Analytical approaches to a treatment of the flow within the boundaries of the recirculation and entrainment regions are discussed in the theoretical review of Section 2.5. Based on this discussion, it is clear that neither quantitative experimental data nor comprehensive analytical methods are available for reliable predictions of both mean velocity (or total pressure) and temperature distributions within this region.

A limited analysis for the flow characteristics within this region is postulated by neglecting the entrainment effect of the engine intake and exhaust flow. This analysis utilizes the concept of a "thin" annular convective jet which originates at a point where the

66

wall jet separates from the ground. By using the flow properties of the wall jet at separation to define the initial conditions for the convective jet, as shown in Figure 26, the two-dimensional analysis reported in Reference 11 is used as the basis for obtaining approximate vertical decay characteristics. Following the methods of Reference 11 it is convenient to treat the flow characteristics in Region D in terms of local velocities (instead of total pressures) and local total temperatures. This analysis is presented below.

### 3.1.4.1 Velocity Distributions

The analysis given in Reference 11 for a two-dimensional convective jet indicates that there is only a small variation of local peak velocity with increasing height. For practical heights considered in this analysis, this velocity is assumed to be independent of height and therefore can be expressed by the following relationship:

$$u_h = \left[ \frac{g \cdot D_j}{4 \cdot R_s} \cdot \left\{ 2 \cdot G \cdot \frac{(P_{tj}/P_a) - 1}{(T_{tj}/T_a)} \right\}^{1/2} \cdot \frac{(T_{tj}/T_a) - 1}{1} \right]^{1/3} \qquad (61)$$

Following the analysis of Reference 11, the lateral distribution of local vertical velocity (u) with the coordinate (b) measured along the radial vector (R) is given by:

$$u = u_h \left[ 1 - \left( \frac{b}{b_h} \right)^{3/2} \right]^2 \qquad (62)$$

The boundary ($b_h$) of the jet represents a finite limit to the lateral extent of the annular convective flow. Thus the outer limit of the recirculation region can be expressed as:

$$R_b = R_s + b_h \qquad (63)$$

Since the rising jet is conical then ($b_h$) can be defined by:

$$b_h = 0.22 \cdot \left( H + H_o \right) \qquad (64)$$

The value of (Ho), which is defined as the coordinate of the virtual origin of the convective jet measured below the ground (see Figure 26), is obtained by matching the known decay characteristics of the local peak temperature with the wall jet value at the separation point, thus:

$$H_o = \frac{0.021 \cdot \left( u_h \right)^2}{\Delta \overline{T}_{ts} \cdot \left( (T_{tj}/T_a) - 1 \right)} \qquad (65)$$

where $\left( \Delta \overline{T}_{ts} \right)$ is obtained from equation (56) and $u_h$ is given by equation (61).
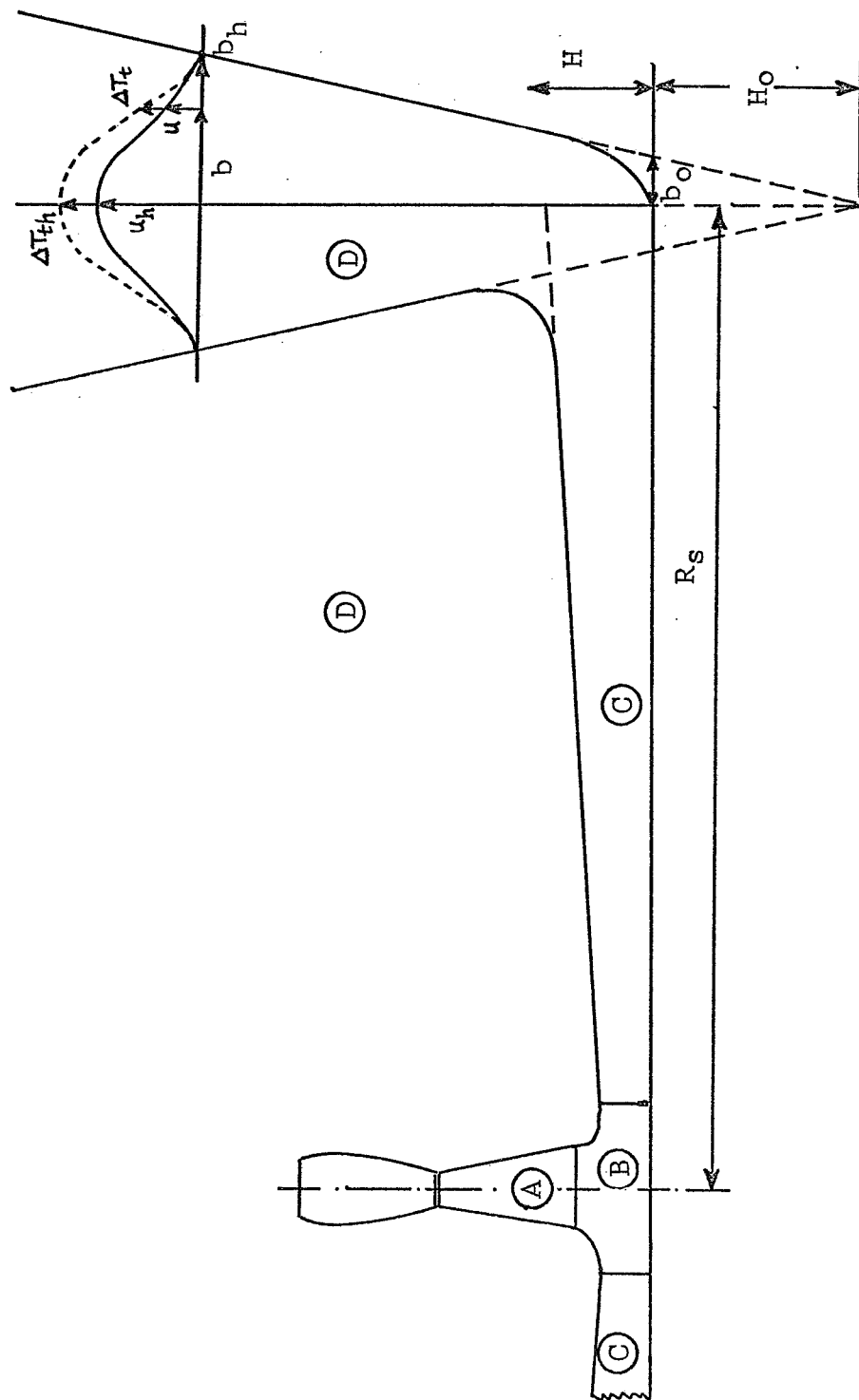
Figure 26.— Mathematical Representation of the Annular Convective Jet in the Recirculatory Region— Single Nozzle Configuration.

68

Although no specific methods can be readily obtained for calculating flow velocities outside the convective jet boundary and between the wall jet and free jet regions these velocities, as shown in Reference 68, are generally very small, within the range of 0 to 5 ft/sec. The flow field in this region is characterised by turbulent mixing and stationary eddies for which there are no usable theoretical methods or experimental data available at the present time.

### 3.1.4.2 Total Temperature Distributions

From the analysis presented in Reference 11 for a two-dimensional convective jet the variation of local peak total temperature ($\Delta T_{th}$) at any height (H) can be obtained as a function of the corresponding local peak velocity ($u_h$), thus:

$$\Delta T_{th} = \frac{0.021 \cdot (u_h)^2}{(H + H_o)} \cdot \frac{1}{(T_j/T_a) - 1} \tag{66}$$

where ($u_h$) and (Ho) are obtained from equations (61) and (65) respectively.

The lateral distribution of local total temperature ($\Delta T_t$) is then given by:

$$\Delta T_t = \Delta T_{th} \cdot \left[ 1 - \left(\frac{b}{b_h}\right)^{3/2} \right] \tag{67}$$

As discussed previously, there are no theoretical methods or experimental data to predict the temperature distribution within the recirculation region bounded by the convective jet flow, wall jet flow, and the free jet flow. In view of this fact, it is herein postulated that the temperatures within this closely bounded region will not exceed the maximum peak temperatures at the same height within the convective jet region. Therefore, equation (67) can be employed within reasonable limits. This postulation appears to be valid from the point of view that if the air mass entrainment was considered in the convective jet analysis, the jet would curve toward the intake. Thus, the temperature at any point under consideration would be more affected by the recirculatory flow from the convective jet.

### 3.1.4.3 Recirculation Flow Boundaries

Under zero wind conditions, the radial limit of the recirculation boundary can be approximated by equation (63). This envelope is equivalent to the section of a cone whose radius increases with height. A vertical boundary ($H_b$) to the convective flow is chosen by the condition that:

$$\overline{\Delta T_{th}} \quad = \quad 0.001 \tag{68}$$

Thus, for a typical jet where $(\Delta T_{tj})$ = 1000°F, the temperature at the boundary of the recirculating flow is no more than 1°F above ambient.

With crosswinds, the maximum vertical boundary ($H_b$) of hot gas cloud can be obtained from the experimental data obtained by Abbott in Reference 55.

Abbott has analyzed photographic records of the smoke boundary as affected by crosswinds. In accordance with his data the height of the flow boundary at a location where it intersects the jet centerline can be approximated by the following expression:

$$H_b \quad = \quad 0.5 \left( R_b \right) \tag{69}$$

where $(R_b)$ is the upwind radial flow boundary given by equation (63).

3.1.5   Region E- Engine Intake Flow

This region, as shown in Figure 1, Region E, pertains to flow conditions at and in close proximity to the engine intake.

The intakes of V/STOL lift engines act as sinks which draw in the surrounding air from all directions. Simple analyses show that the inlet sink strength is small compared to the entrainment properties of the exhaust flow. Thus the entrained inlet flow is drawn only from a localised region within a few diameters of the inlet face.

The inlet sink effect causes a rapid acceleration of the entrained air mass as it approaches the inlet plane, with a consequent streamtube contraction and with a reduced intensity of the turbulent mixing process. Thus relatively hot gases in the surrounding recirculation region can be induced into the inlet plane without much dissipation taking place.

As indicated by some of the experimental measurements, inlet flow characteristics exhibit a random time dependency, with strong temperature fluctuation typical of those due to large scale turbulence. This makes the evaluation of time-average behavior very difficult as evidenced by poor test repeatability in some cases. Furthermore, substantial differences in the measurements of intake temperature rise (ITR) have been recorded by various investigators for tests of similar configurations under similar flow conditions but at different

70

geometric scale.

The question of model scaling effects is presently the subject of an intensive investigation to determine valid correlation parameters (References 72, 73 and 74). To formulate an effective mathematical model for the hot gas ingestion flow it is necessary to achieve geometric, kinematic, and dynamic similarity. It is, however, not practical to achieve similarity of both inertial-to-viscous and inertial-to-gravitational forces at different geometric scale. Thus it is generally assumed that one force ratio is dominant and the other can be neglected. The discussion in Reference 73 indicates that limited success with each scaling technique has been obtained from independent studies although correct scaling methods are not yet sufficiently well defined.

In addition to the scaling problems there is a strong dependency of intake flow characteristics on airframe/intake configuration. There are two principal types of engine inlet installations, each of which exhibits marked differences in ingestion behavior. These are the top-inlet and the side-inlet configurations, as shown in Figure 27. The first type pertains to vertically-mounted engines having inlets flush with the upper surface of the installation (either pod or fuselage), while the second configuration is typified by a pair of scoop intakes on the fuselage sides usually well forward of the exhaust nozzles, as appropriate to a horizontal engine layout.

Due to the complexity of the intake flow behavior as discussed above and in view of insufficient experimental data there are no comprehensive analytical methods for reliable prediction of the flow characteristics within this region. Hence, resort must be made to semi-empirical or totally empirical solutions to obtain pressure, velocity and temperature distributions within the engine intakes. These methods are presented below.

### 3.1.5.1  Intake  Pressure and Velocity Distributions

In reviewing the existing analytical approaches (Section 2) it was found that methods to calculate the pressure and velocity distributions for arbitrary inlet/airframe configurations were complex and limited to simplified representations. While a trial-and-error method such as given by Reference 61 represents a useful design tool for intakes operating under both static and crosswind conditions, it does not allow a rapid and accurate assessment of the flow behavior for any given intake geometry. Since the design of efficient intakes (minimum velocity distortion and no flow separation) is in itself an art, it is considered to be outside the scope of hot gas ingestion studies. Therefore, methods presented below are restricted to an approximate estimate of mean total pressure and velocity values on the assumption of an ideal intake efficiency.
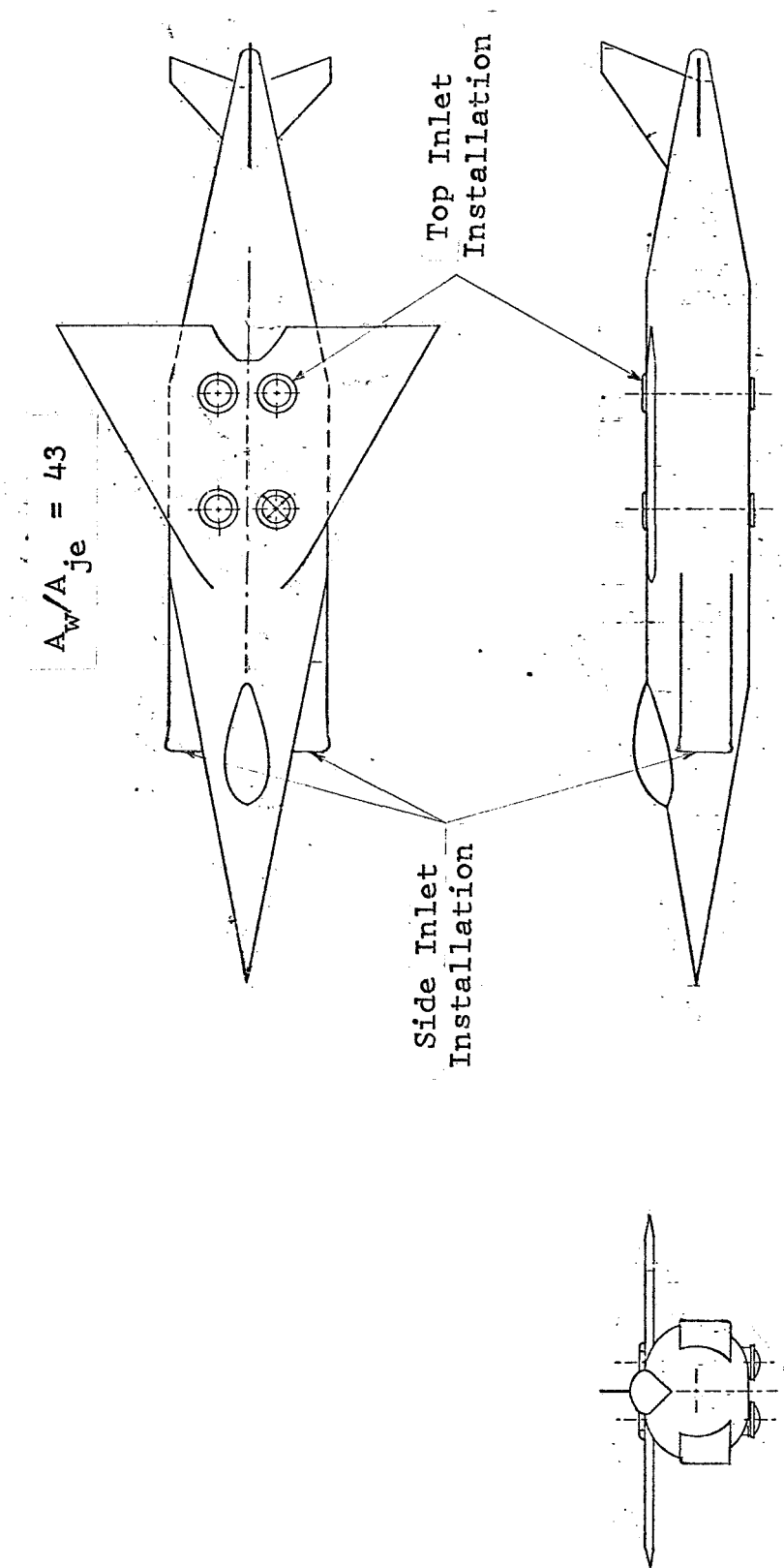
71

Figure 27.— Typical Arrangement of Top-Inlet and Side-Inlet Installations, From Reference 79.

By neglecting effects due to the intake boundary layer and flow separation the total pressure ($P_{ti}$) in the intake reference plane is essentially constant and equivalent to the free-stream total pressure ($P_{t\infty}$), thus:

$$P_{ti} = P_a + \Delta P_{t\infty} \tag{70}$$

where ($\Delta P_{t\infty}$) represents the total pressure head of any cross-wind velocity. Since this value is small in comparison with the absolute pressure ($P_a$) it can be neglected.
Given the total engine inlet cross-section area ($A_i$) the mean inlet static pressure ($P_i$) is derived by equating the engine inlet and exhaust flows (neglecting fuel addition) and can be expressed to first order by:

$$P_i = P_{ti} - \Delta P_{tj} \cdot \left(\frac{A_j}{A_i}\right) \cdot \left(\frac{T_a + (ITR)_{mean}}{T_{tj}}\right) \cdot \left(\frac{P_a}{P_i}\right) \tag{71}$$

where the value of ($P_{ti}$) is obtained from equation (70).
The ratio ($P_a/P_i$) in equation (71) is initially assumed to be unity, then the solution for ($P_i$) is obtained through an iterative calculation procedure.

The mean idealised inlet velocity ($u_i$) is now obtained from equation (1), where the mean inlet total temperature ($T_{ti}$) is given by:

$$T_{ti} = T_a + (ITR)_{mean} \tag{72}$$

where mean ITR is obtained from sub-section 3.1.5.2 given below.

### 3.1.5.2   Intake Temperature Distributions

For a single engine configuration without crosswinds, the mean inlet temperature rise (ITR) sensed at the intake plane is generally small with a relatively flat distribution. This ITR is considered to be due to recirculation of the separated ground flow which rises upwards under buoyancy forces and is induced into the intake by the entrainment process. Since the ground flow separation point is normally well outside the aircraft planform limits the effects of airframe/engine geometry in this case are normally minimal.

Because of this relatively simple mathematical model of the recirculating flow, the mean ITR can be estimated from equation (66), knowing the ground flow separation radius ($\bar{R}_s$) from equation (54).

For typical lift engine parameters ($D_j$ = 1 ft., $P_{tj}/P_a$ = 1.8, $T_{tj}/T_a$ = 1200°F) a mean ITR of the order of 8°F is predicted using these equations. A wide selection of experimental data for both large- and small-scale tests (References 71, and 75 through 78) show that measured mean ITR is in fair agreement with the predictions of equation (66). These test data also confirm an insensitivity of the measured ITR to aircraft configuration and nozzle height variations, as expected on the basis of the flow model.

Large scale experimental data in Reference 71 show that instantaneous ITR distributions exhibit random fluctuations with peak values approaching twice the mean ITR level.

In the presence of crosswinds, the forward extent of the recirculation region is reduced. A consequent decrease in the mean-path length of the recirculating exhaust flow directly upstream of the nozzle leads to an increased ITR with a distributional bias towards the upwind side. This trend is somewhat modified by a decreasing recirculation boundary height above the inlet, which implies a height limit for the hot gas ingestion that is largely dependent on the relative crosswind speed. The possibility of recirculating flow being trapped under the wing is also recognized to have an effect on ITR.

The above considerations of crosswind effects preclude development of a reliable mathematical model and therefore large scale test data from References 79 and 80 are herein utilized to show typical variations of ITR for a single nozzle/inlet configuration. These data, which are considered representative for a wide range of single nozzle top-intakes, are presented in Figure 28, for the typical aircraft top-inlet configuration shown in Figure 29.

Side-inlet configurations are characterized by forward-facing intakes usually located well ahead of both the wing and the engine nozzles. This location is usually dictated by a horizontal engine mounting. In addition, it is desirable to locate the inlets well away from the recirculatory flow patterns generated by wing/fuselage configurations and/or multi-nozzle arrangements.

Side-inlet configurations are, however, susceptible to an entrainment of the local groundflow under static ambient conditions. This is attributed to the sink effect of the inlet

74
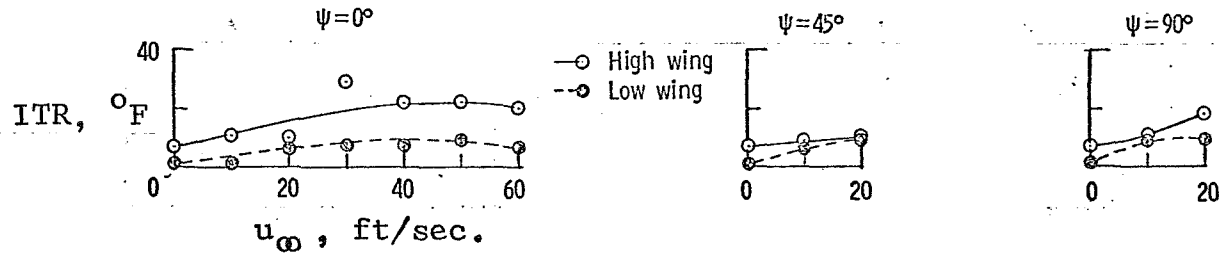
(a) Effect of Wing Location.
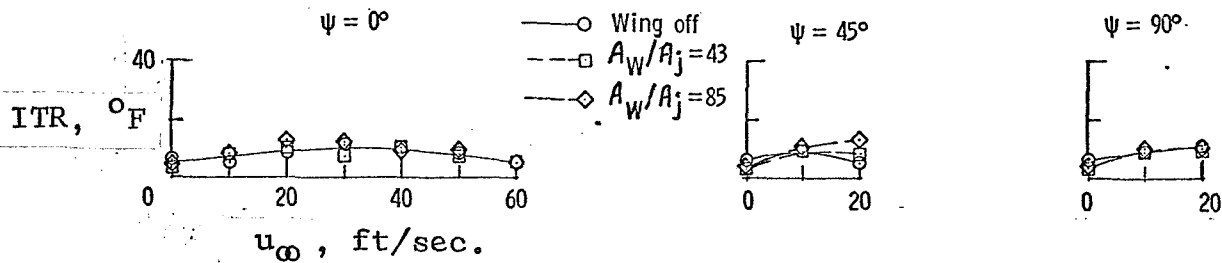


(b) Effect of Wing Size.
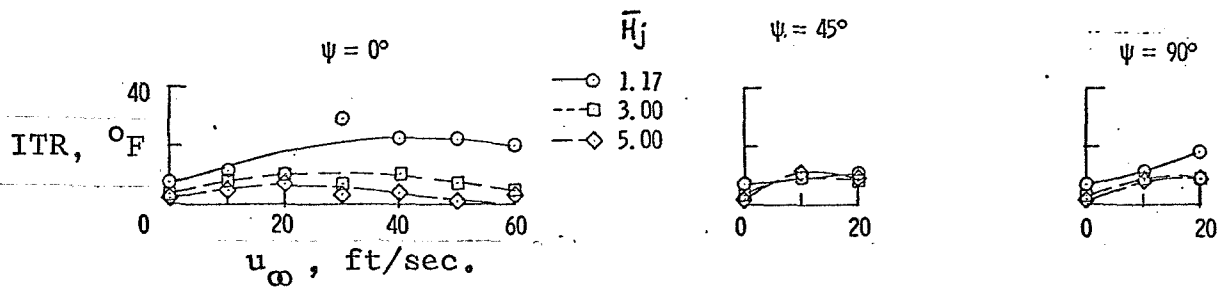


(c) Effect of Nozzle Height.

Figure 28.— Variation of Average Inlet Air Temperature Rise
with Windspeed for the Single-Nozzle Configuration
of Figure 29 with Top Inlets.

75

Large Delta Wing    $A_w/A_{je} = 86$

Small Delta Wing    $A_w/A_{je} = 43$
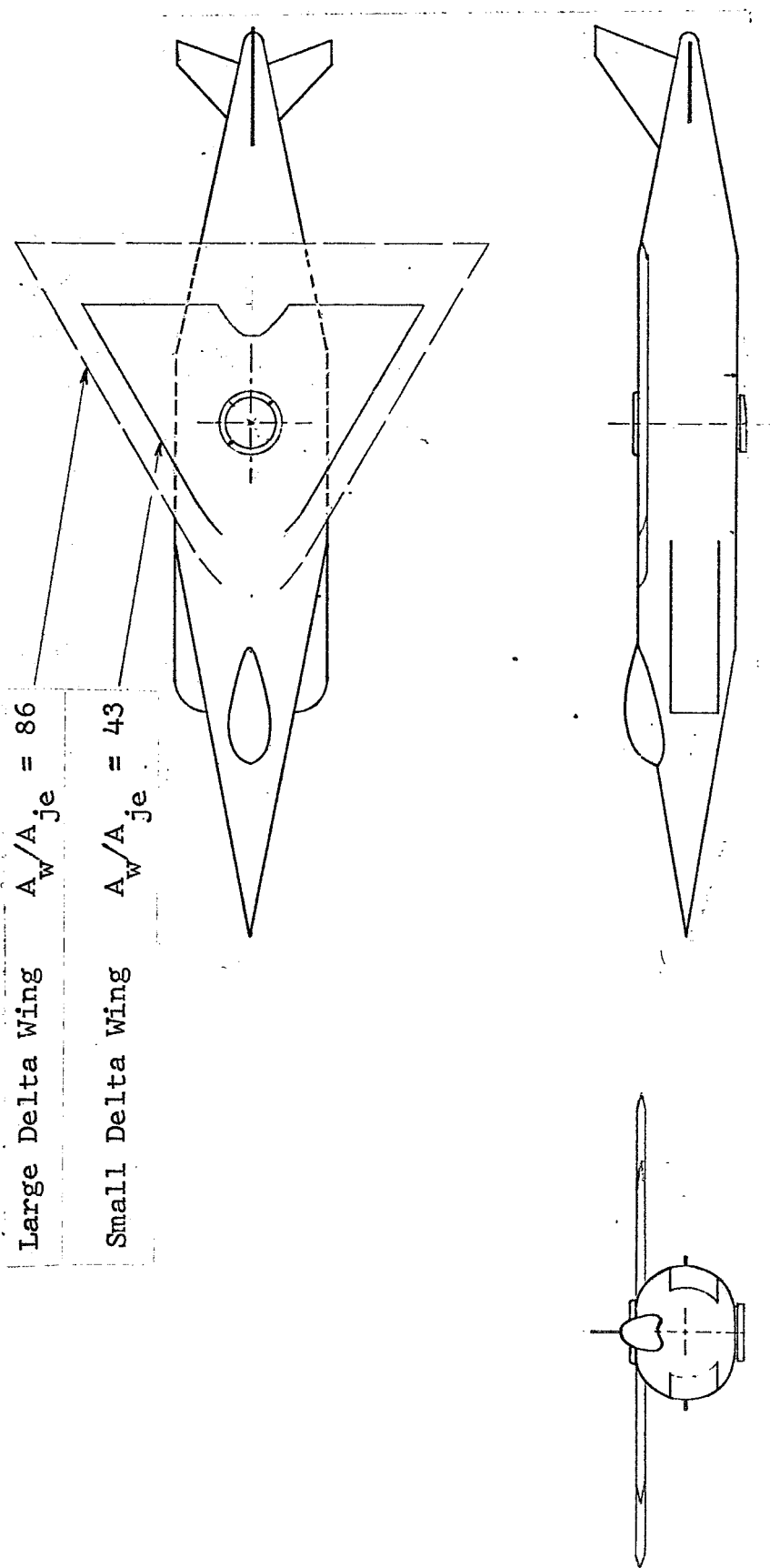
Figure 29.- Large-Scale Single-Nozzle Configurations from References 79, 80; Shown With Wing in High Position.

flow when the inlets are in close proximity to the ground and is expected to diminish with increasing inlet height. The variation of mean ITR with height for a large scale model (Refrences 79, 80) of a single nozzle configuration such as shown in Figure 29 is not very pronounced as compared to multi-engine nozzle configurations which will be discussed later. This sensitivity of ITR to height for no crosswinds can be depicted from Figure 30 which shows the mean ITR varies from 35°F to about 15°F as nozzle height ($\overline{H_j}$) increases from 1.17 to 5.0.

In the presence of ambient crosswinds, side inlets are prone to higher ITR as compared to that at static conditions (See Figure 30 ) and appreciably higher than for the top-inlet configurations as presented in Figure 28. This is caused by an earlier separation of the ground flow as affected by crosswinds and a direct blow-back of the relatively hot gases into the side inlets before the flow recirculation boundary retreats to a point below or aft of the inlet plane. Therefore, ITR for side inlet usually reaches a maximum value at some intermediate wind speed and then reduces with further increases in wind velocity. The maximum value of ITR for a typical side inlet single nozzle configuration operating at a nozzle height of about 1.17 is approximately 160°F for a wind speed of about 40 ft/sec.

Although it is recognised that the variation in ITR for generalised side inlet configurations will be somewhat affected by airframe/wing/nozzle geometry, the trends exhibited by Figure 30 can be used for first order estimates. These test data are presented instead of anlytical methods which are extremely complex to develop at the present time.

### 3.1.6 Region F- Fountain Flow

This flow region, as defined in Figure 1 Region F is associated only with multi-nozzle configurations. The methods for predicting the flow characteristics in this region are presented in the next section dealing with multi-nozzle configurations.
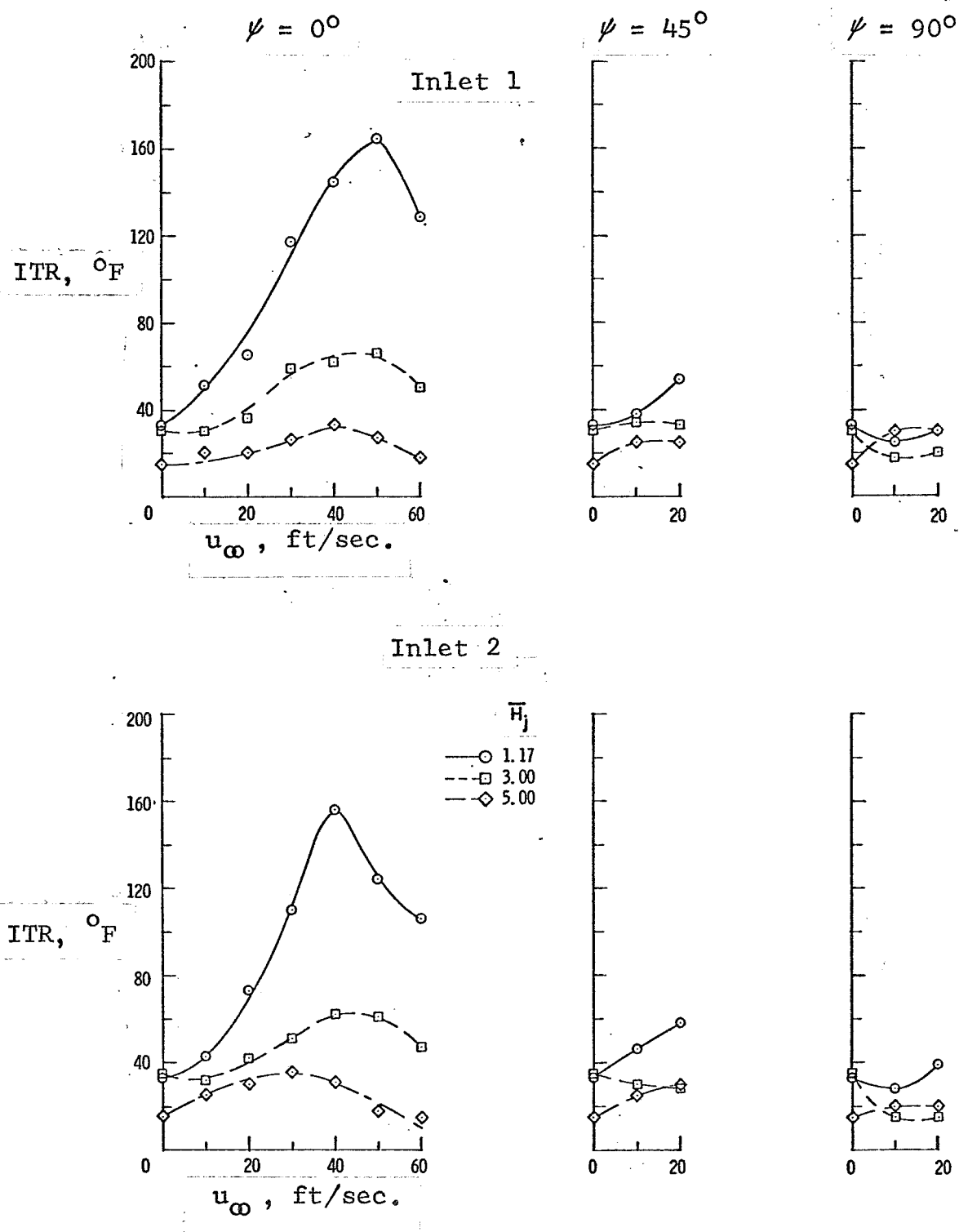
Figure 30.- Effect of Nozzle Height on the Variation of Average
Inlet-Air temperature Rise With Windspeed for the
Single-Nozzle Configuration of Figure 29 with Side
Inlets and High Wing. $A_w/A_{je} = 43$.

## 3.2  MULTI-NOZZLE CONFIGURATIONS

This section presents the formulation of engineering methods
to predict the flow field velocity and temperature distributions
for various engine arrangements having either 2 nozzles in line
or 4 nozzles in rectangular configuration.  It is assumed that
the geometry and exhaust flow conditions for each nozzle are iden-
tical since this can, under certain circumstances, have a critical
influence on the flow field behavior.

An important distinction must first be made between two
basic classes of multi-nozzle configurations.  These are defined
as being of either the "closed" or "open" type.  Examples of
the "closed" type are represented by closely-spaced in-line or
clustered nozzle arrangements in which the individual nozzle
exhaust flow fields partially (or even totally) coalesce before
the ground impingement.  The subsequent flow field characteristics
are then generally related to those exhibited by the single jet
arrangement and as such they can be analytically treated using
the methods developed in Section 3.1.

The "open" type nozzle configuration corresponds to a
significantly larger spacing between the exhaust nozzles whereby
the individual jets do not merge prior to ground impingement.
In this case there exists a mutual flow interference between in-
dividual ground jets.  Of particular importance is the flow inter-
action between two or more opposing wall jet flows which give
rise to a well known "fountain" flow phenomenon.  The "fountain"
flow is created by a strong flow of relatively undiluted engine
exhaust gases which surge upwards between the nozzles in
the immediate vicinity of the aircraft structure as shown sche-
matically in Figure 31.  It is widely recognized that this is a
more serious problem than that due to the far-field recirculation
behavior of either the single nozzle or "closed" multi-nozzle
configurations.

As noted in the theoretical review (Section 2.3), approximate
methods exist for predicting the engine spacing at which the
fountain effect should occur.  However, no comprehensive methods
are presently available for predicting velocity and temp-
erature distributions in the fountain when it does occur. . In
the following analysis of fountain behavior approximate methods
based on the available experimental evidence are given for
fountain velocities and temperatures.

Approximate criteria that establish the presence of a
measurable fountain effect of two-jet and rectangular (square)
four-jet nozzle configurations are obtained from model test
results reported in References 65, 66 and 78.  As noted by
Skifstad (Reference 67) the data of Reference 66
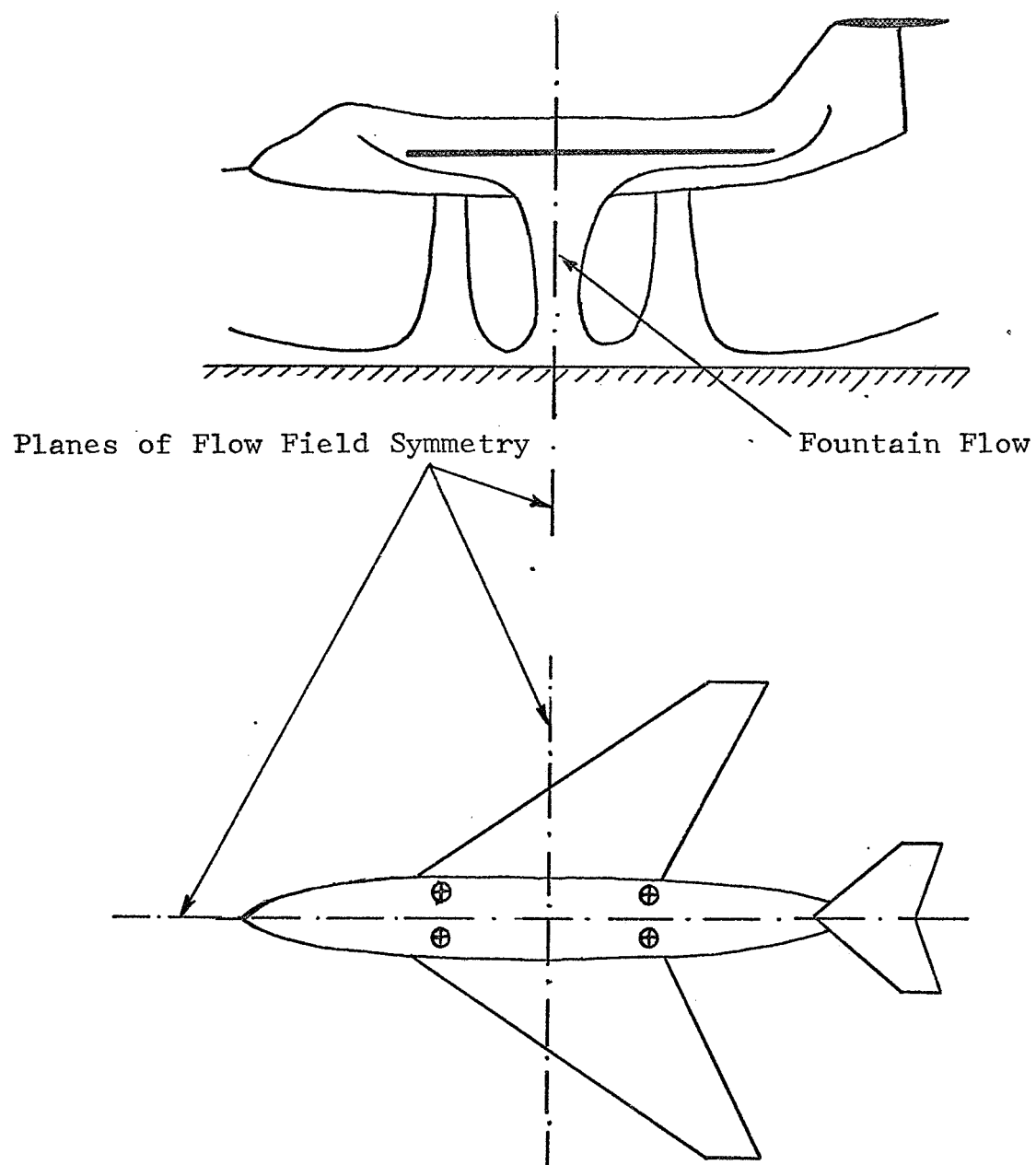show that the fraction of the jet momentum occurring in the

Planes of Flow Field Symmetry

Fountain Flow

Figure 31.- Schematic Representation of the Interaction Flow
for a 4-Nozzle Configuration- No Crosswinds.

80

fountain can be related to the nozzle height-to-separation ratio. Figure 32 summarizes the approximate threshold boundaries of the fountain existence in terms of the normalised maximum separation distance and nozzle height for a two-nozzle configuration and also for four nozzles in a square arrangement. For the four nozzle configuration, the maximum nozzle separation distance is that between a diagonally opposite pair. The boundary for the two-nozzle configuration is also in reasonable agreement with the test data of References 65 and 78.

It is observed from Figure 32 that to avoid the fountain effect for a given nozzle height and diameter, the spacing for square arrangement of four nozzles is about 2/3 of that required for two nozzles. In the general case of rectangular arrangements of four nozzles it is expected that the fountain threshold boundary would lie between the limits of the square and the two nozzle arrangements. However, direct experimental validation of this effect is not available at the present time.

The analytical methods for flow characteristics of multi-nozzle configurations are herein presented in a similar manner to those developed for a single nozzle configuration discussed in Section 3.1. Only the methods for the flow regions which are affected by multi-jet configurations are discussed in detail. Other flow regions are treated by a single jet analysis and therefore the methods of Section 3.1 can be directly applied.

## 3.2.1 General Considerations of Multi-Jet Flow Field

As pointed out in Section 2 a detailed analysis of the flow field in vicinity of multi-nozzle configurations is generally precluded by a lack of adequate theoretical and experimental data.

An approximate method, suggested by Alexander (Reference 64) yields reasonable results for multiple parallel circular jets for which the interaction effects are relatively small. This method consists of superposition of the local momentum crossection profiles for each individual jet at any given downstream coordinate. By making the approximation that flow distributions of momentum and differential total pressure are similar, the differential total pressure profiles downstream of a multi-nozzle configuration are obtained by a simple linear addition of the individual profiles for each nozzle. The latter profiles are obtained from the free jet single-nozzle analysis presented in Section 3.1.1.

For parallel multi-jets which coalesce at some downstream distance, the resulting flow approximates that of an equivalent single nozzle jet with the same total momentum. This behavior is confirmed by the results of various experimental investigations such as those presented in References 18, 20, and 81. It is
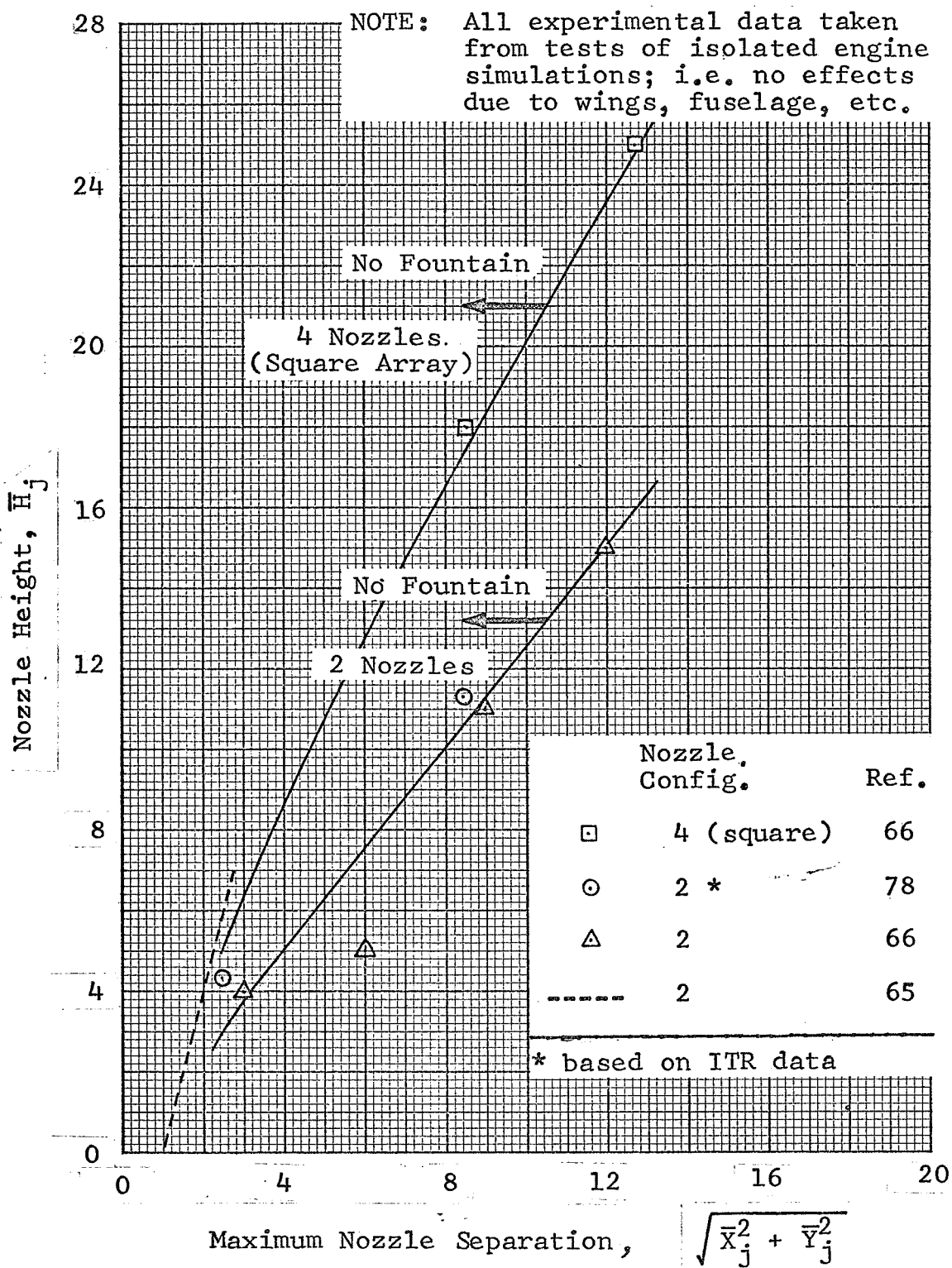
Figure 32.— Approximate Limits of Hot Gas Fountain for 2 Nozzle Configurations and 4 Nozzles in a Square Arrangement.

therefore possible to obtain an approximation for the flow field far downstream in terms of a single jet with an effective diameter $\left(D_{je}\right)$, defined as the diameter of the circle whose area is equal to the total nozzle area of two or more nozzles, thus:

$$D_{je} = \sqrt{\frac{4}{\pi} \cdot A_{je}} \tag{73}$$

Once the effective jet diameter $(D_{je})$ has been established the flow characteristics in the vicinity of coalesced multi-jets can be determined using the single jet analysis presented in Section 3.1.

The flow characteristics in the ground impingement region (Region B) are greatly affected by the nozzle separation-to-height ratio. When this ratio is large the flow from each nozzle will be confined to isolated ground impingement zones, which can be treated individually using the single jet analysis of Section 3.1. On the other hand, when this ratio is small (say less than 0.2), the jets will coalesce prior to ground impingement and again the single jet analysis can be employed utilizing the concept of an equivalent jet diameter given by equation (73). For intermediate nozzle separation-to-height ratios, when mutual flow interaction effects are large, there are no usable methods for predicting the flow characteristics within the ground impingement region of multi-jet configurations.

The flow field in the wall jet region of multi-nozzle configurations is dependent on the particular flow conditions which exist in the ground impingement zone discussed above.

In general, the flow characteristics within the wall jet (Region C), the recirculation flow (Region D) and engine intake (Region E) away from the interaction plane (Region F) can be approximated using the isolated, or the equivalent single jet analysis whichever is applicable.

The methods for determining flow characteristics within the interaction plane (Region F) for multi-nozzle jet configurations are presented below.

83

## 3.2.2  Region F-  Interaction Plane Flow

The flow mechanism of mutually opposing wall jets is analogous to a reverse of the ground impingement flow. In this case, however, the flow is confined to a relatively thin vertical wall known as the interaction plane instead of the ground plane.

Conceptually, the flow at any point within this region can be represented as a continuation of the radial ground flow deflected along the vertical plane at the same angle as if the interaction plane was flat or entirely removed. This flow mechanism is described in detail in Reference 68 and is schematically represented in Figure 33.

To facilitate analytical treatment, the flow within the interaction plane as shown in Figure 33 can be sub-divided into three distinct sub-regions.

(a)  Ground flow of the interaction plane, where the flow is predominantly horizontal and parallel to the ground.

(b)  Radial flow, where the flow is in a radial direction within the vertical plane.

(c).  Fountain flow of the interaction plane, where the flow is predominantly vertical and perpendicular to the ground.

Practical engineering methods for predicting flow characteristics within these sub-regions are presented below.

## 3.2.2.1  Ground Flow

This sub-section presents analytical methods for predicting flow characteristics along the ground in the interaction plane.

## 3.2.2.1.1  Pressure and Temperature Distributions

The static pressure ($\Delta P_w$) along the ground within the interaction plane is obtained as a normal component of the total pressure assuming no cross-flow through the interaction plane. Thus using the nomenclature of Figure 33 there results:

$$\overline{\Delta P_w} = \overline{\Delta P_{tw}} \cdot sin^2(\beta) \tag{74}$$

where $\left(\overline{\Delta P_{tw}}\right)$ is given by equation (44). The results obtained from equation (74) are compared with the experimental data from Reference 65 as shown in Figure 34. This figure indicates that the predicted values are in a good agreement with the test data except close to the stagnation point where they are consistently high. The differences are shown to be greatest for the smaller
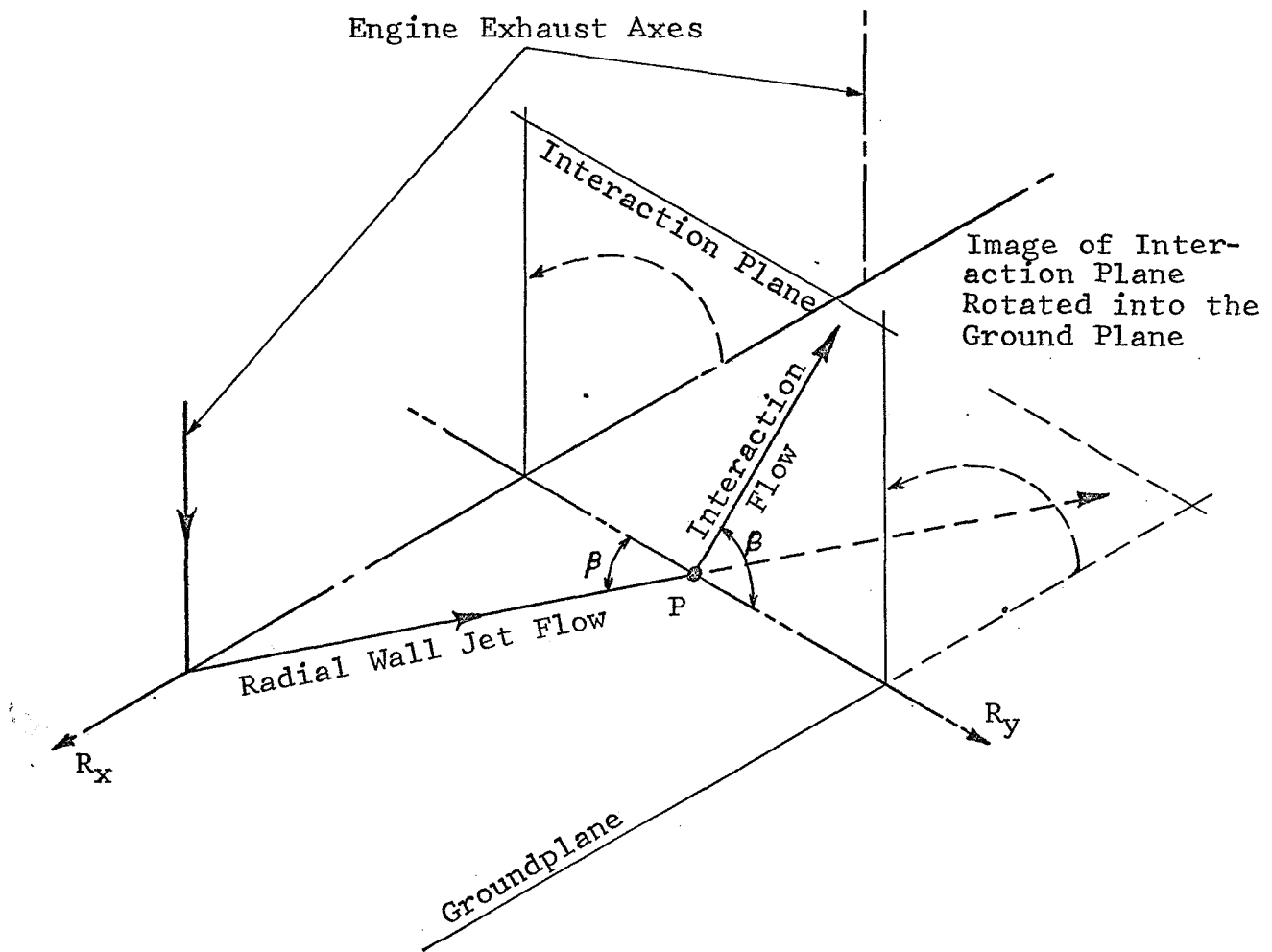
84

Figure 33.- Schematic Representation of the Flow in the
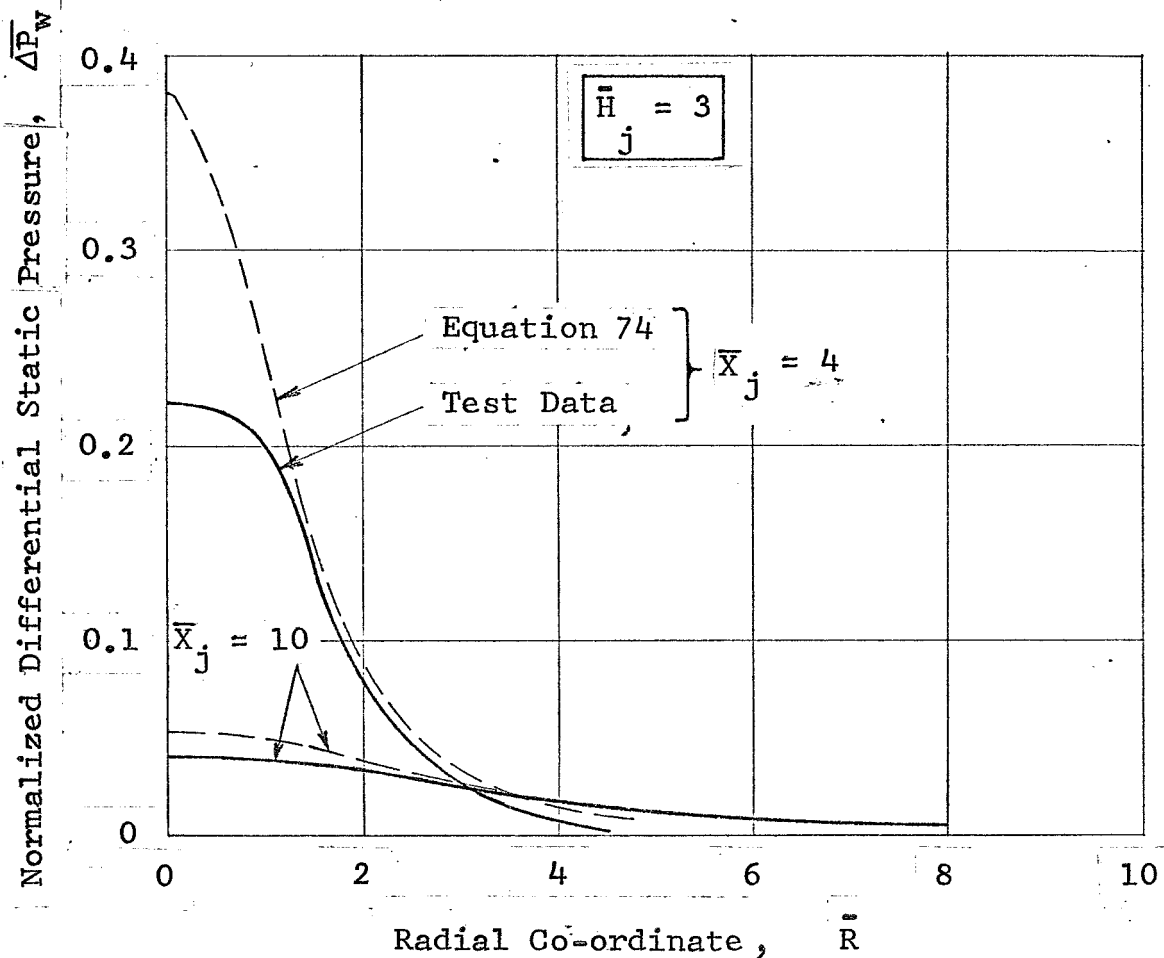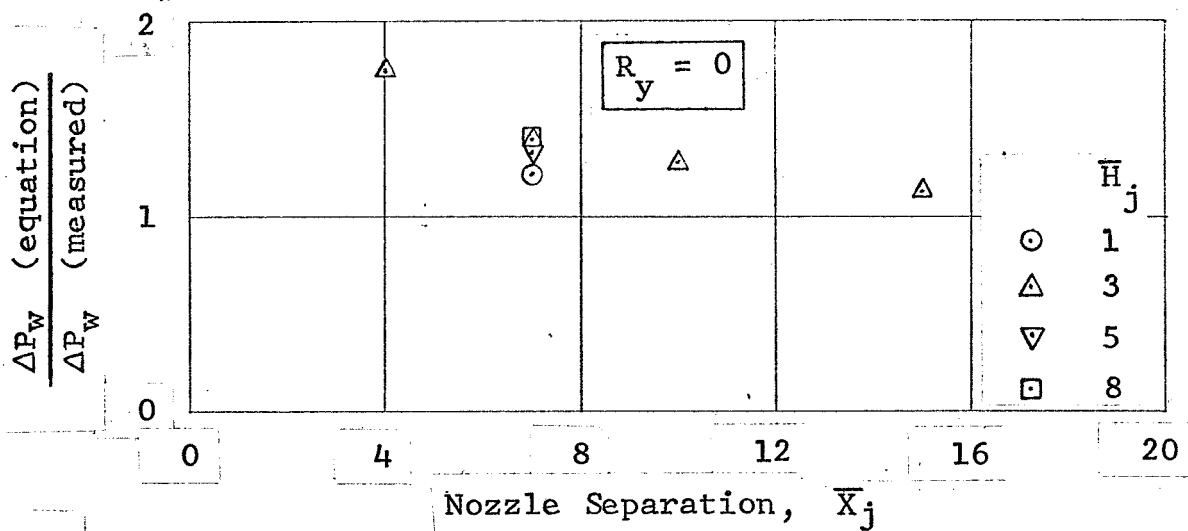Interaction Plane Between Two Jets.

Figure 34.- Comparison Between Analytical Peak Differential Static Pressure Along the Interaction Plane and Experimental Data of Reference 65 for a Pair of Jets.

nozzle separation-to-height ratios.

Although the flow in the interaction plane within small lateral distances of the stagnation point (the fountain effect) is predominantly vertical, at greater lateral distances, experimental observations suggest a more rapid change in the flow vector from vertical to horizontal, than indicated by the mathematical model. The experimental results of References 71 and 78 show that the interaction flow away from the fountain exhibits characteristics similar to a wall jet and may be treated as such. The theoretical results obtained from the wall jet analysis (Section 3.1.3) are compared with the corresponding test data and are presented in Figures 35 and 36 which show the decay of peak total pressure and total temperature, respectively in the far-field interaction plane for 2-nozzle configurations. It can be noted from these figures that while peak total pressure values at any point are close to those predicted by considering an isolated wall jet flow field (Equation 44) this is not true of the temperature decay. Based on the full scale data of Reference 71 the far-field interaction plane peak temperature differential is nearly twice that predicted for the isolated wall jet.

Furthermore, experimental measurements reported in References 71 and 78 indicate that the pressure reference boundaries may also be computed using the isolated wall jet while the corresponding temperature boundaries are comparatively much larger. Therefore, appropriate empirical modifications of temperature relationships are recommended. However, the available experimental data is inadequate to verify such modifications at the present time.

3.2.2.1.2  Interaction Plane Flow Boundaries

The methods for predicting the ground flow separation radius and the vertical boundary of the interaction plane are the same as those developed for a single jet (Section 3.1.3). In this case, however the effective jet diameter ($D_{je}$) as given by equation (73) should be utilized where appropriate.

Comparison of these prediction methods with the available experimental data is limited to crosswind effects on small scale models as given in References 72 and 73. Figure 37 shows a correlation between the analytical and experimental results for a 2-nozzle configuration. As can be noted from this figure only a fair correlation is obtained, with large discrepancies evident for strong crosswind conditions. The predicted ground flow boundary generally represents an upper limit to the measured separation and the effect of a change in the ambient wind vector is within the scatter of experimental data.
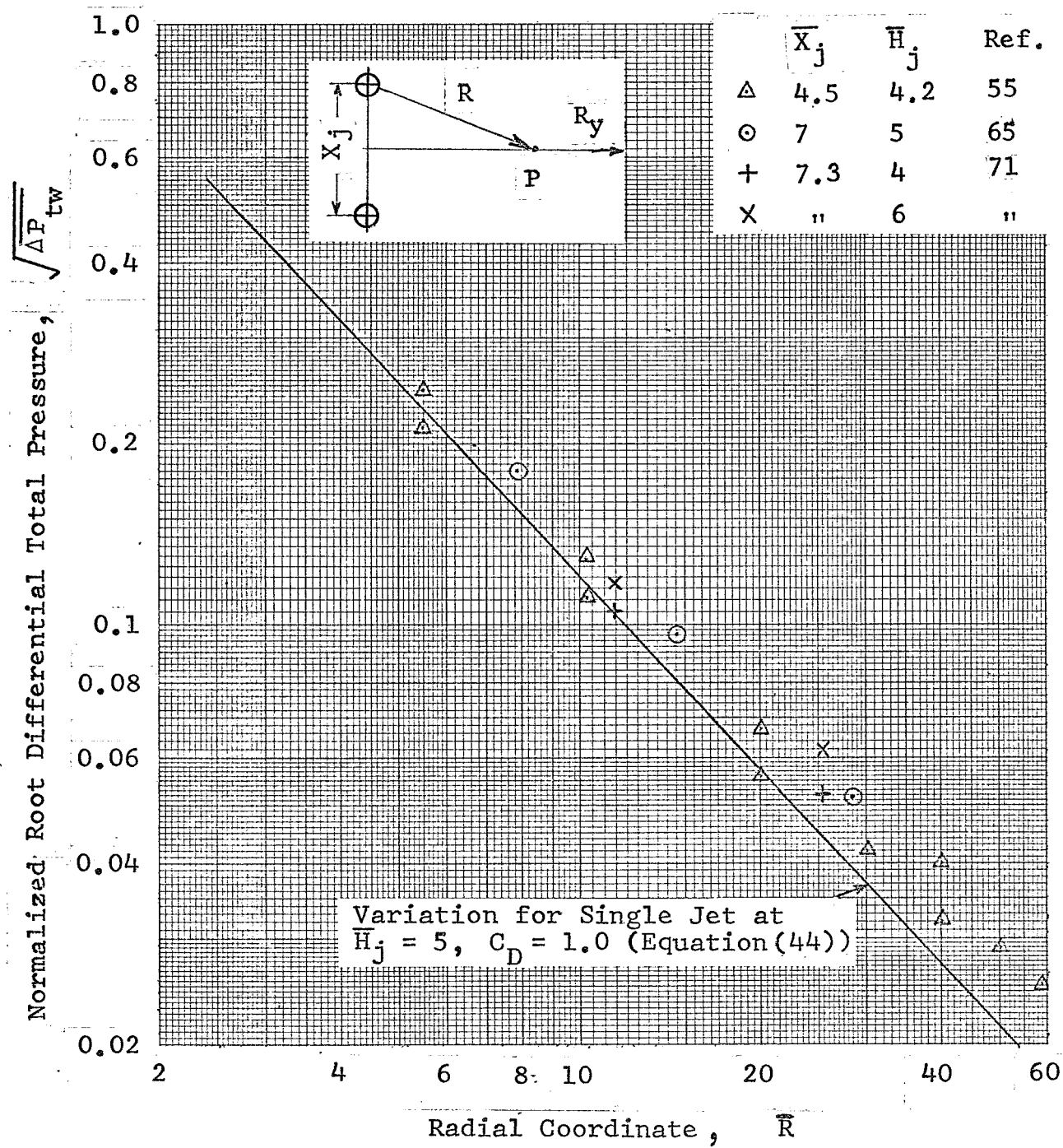
Figure 35.- Variation of Peak Total Pressure Along the Interaction Plane; No Crosswinds.
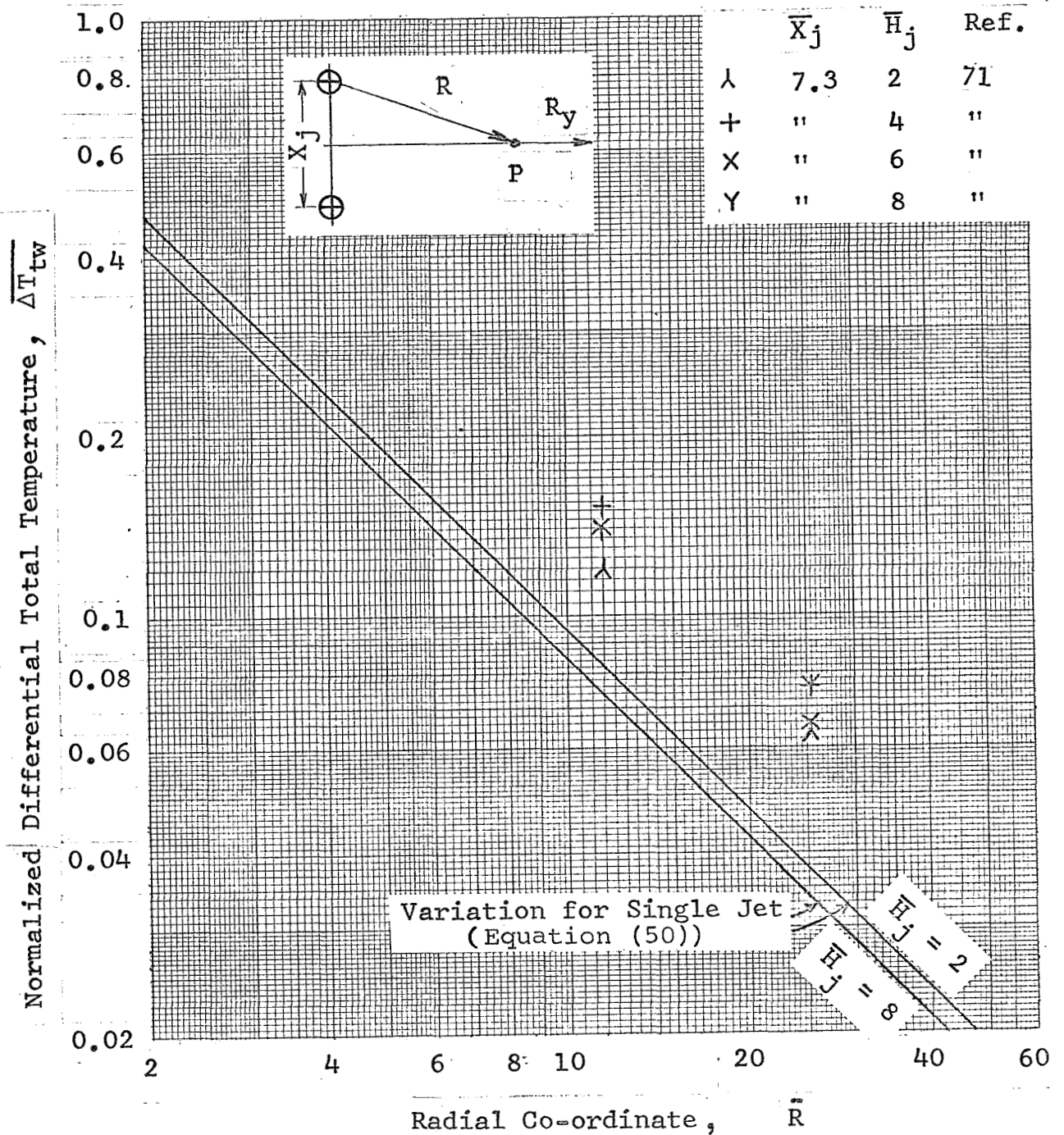
Figure 36.- Variation of Peak Total Temperature Along the Interaction Plane; No Crosswinds.
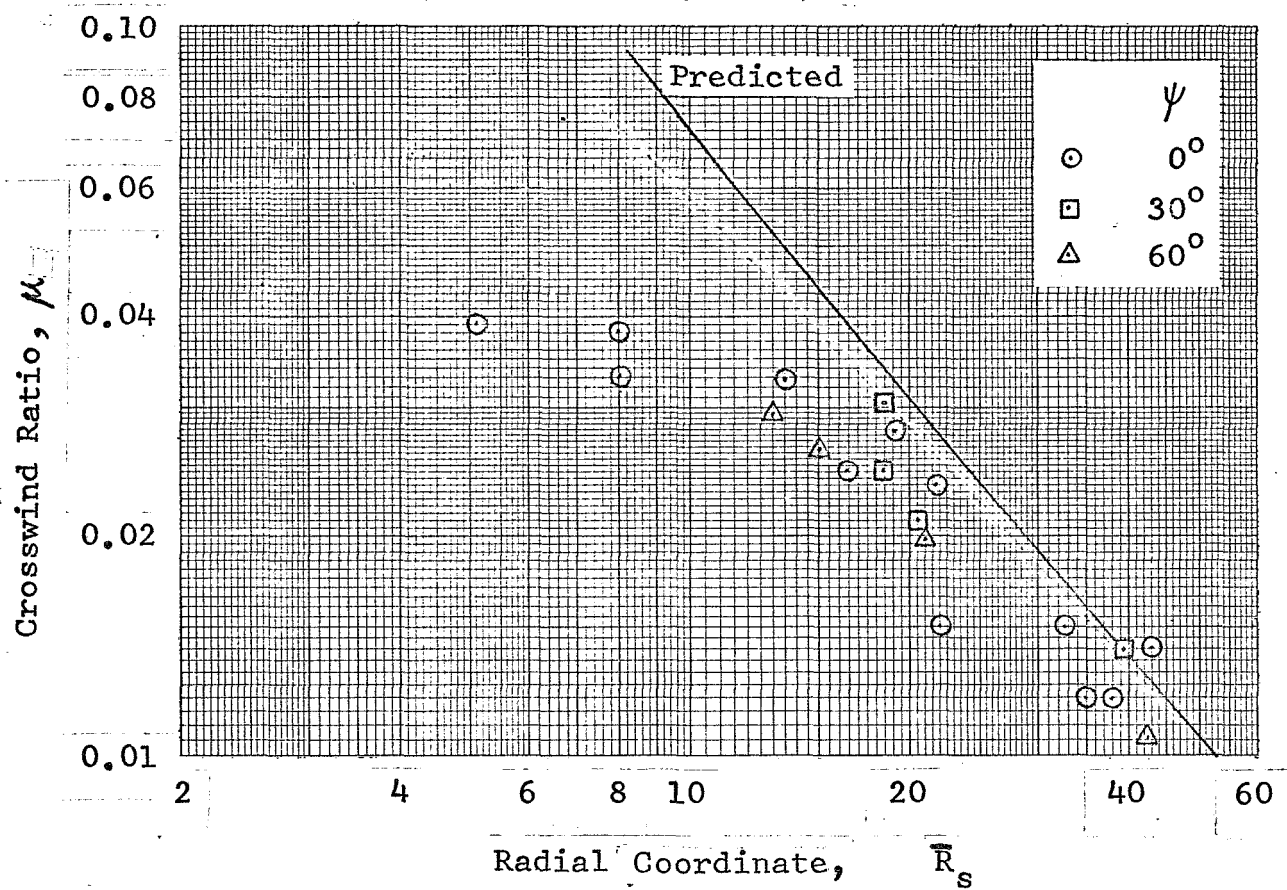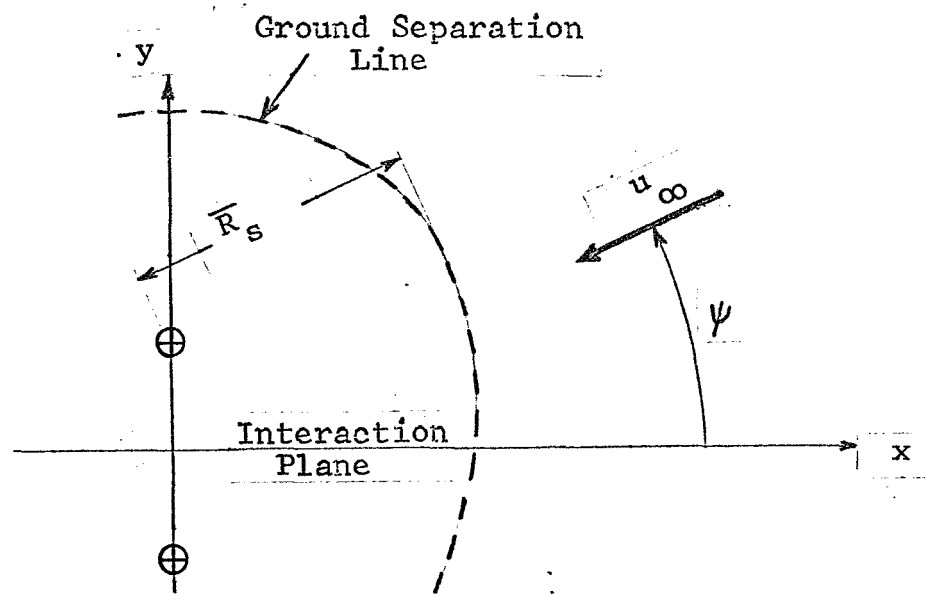
Figure 37.- Variation of Ground Separation Radius With Crosswind
Ratio for Two Isolated Jets, from Reference 72.

Figure 38 shows a similar comparison for a 4-nozzle configuration where the crosswind ratio $(\mu)$ has been used to allow for variations in nozzle pressure ratio. This is similar to the correlation obtained by Ryan (Reference 73) using the corresponding dynamic pressure ratio. Again there is a substantial scatter in the experimental data and a small effect due to a change in the wind vector.

An approximate method for predicting the height of the hot gas boundary of the interaction plane is based on the smoke cloud data of Abbott (Reference 55), whose results indicate, approximately, that

$$\overline{H}_b = \overline{R}_s \tag{74}$$

The above relationship is applicable to wind conditions along the interaction plane. For no crosswinds, since the separation radius is shown to be larger, the boundary height is expected to increase. On the other hand, when the crosswind vector is normal to the interaction plane the single jet analysis can be utilized for this purpose.

### 3.2.2.2 Radial Flow

As mentioned previously, the radial flow within the interaction plane can be treated as if the ground flow continued at the same angle if the interaction plane was removed. Thus the total pressure, total temperature, and the corresponding local velocity at a point in the interaction plane at some distance away from the ground and the fountain flow can be considered to be the same as those within the wall jet of a single nozzle at the same total distance from the jet axis.

### 3.2.2.3 Hot Gas Fountain Flow

The turbulent nature of the hot gas fountain renders a theoretical treatment of the flow in this region extremely difficult. A satisfactory solution would require a detailed knowledge of the entrainment behavior of the neighboring flows together with an account of hot gas buoyancy effects which may be appreciable. No complete theoretical analysis of the subject is known to have been reported.

Important experimental studies aimed at an understanding of the hot gas fountain phenomena have been limited to small scale investigations such as reported in References 65, 66, and 78. However, even these do not provide sufficient data to substantiate comprehensive quantitative prediction methods. In addition, the problem of relating geometric scale changes is
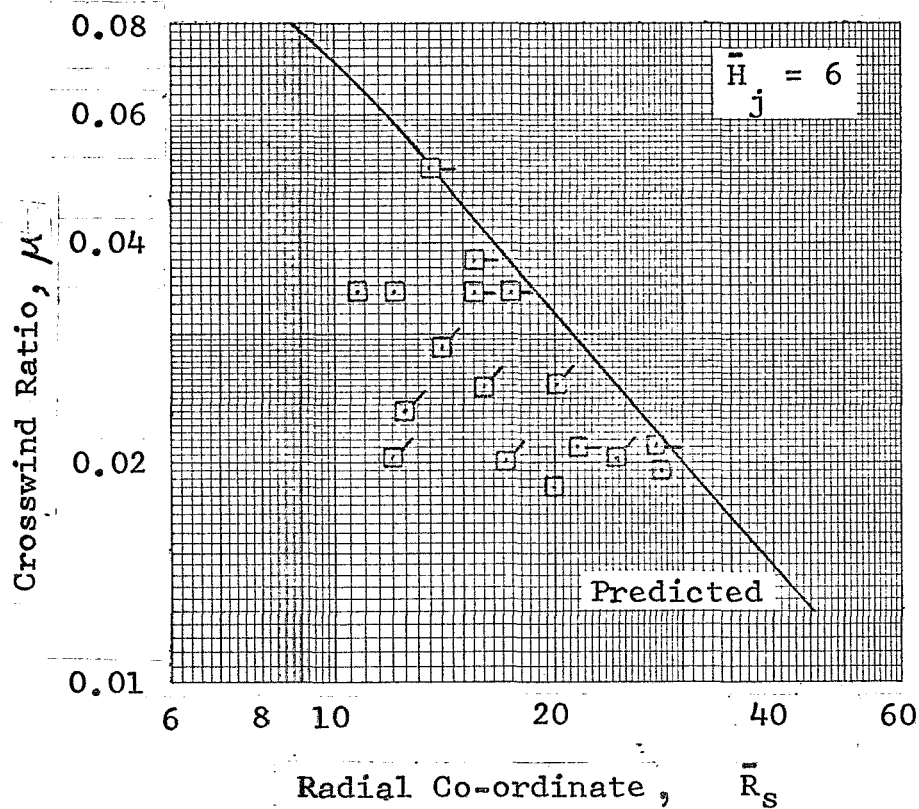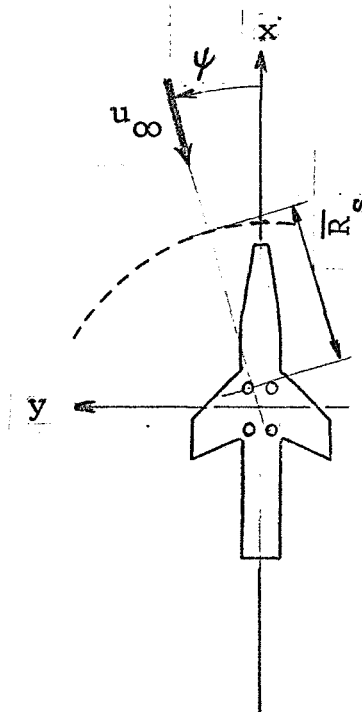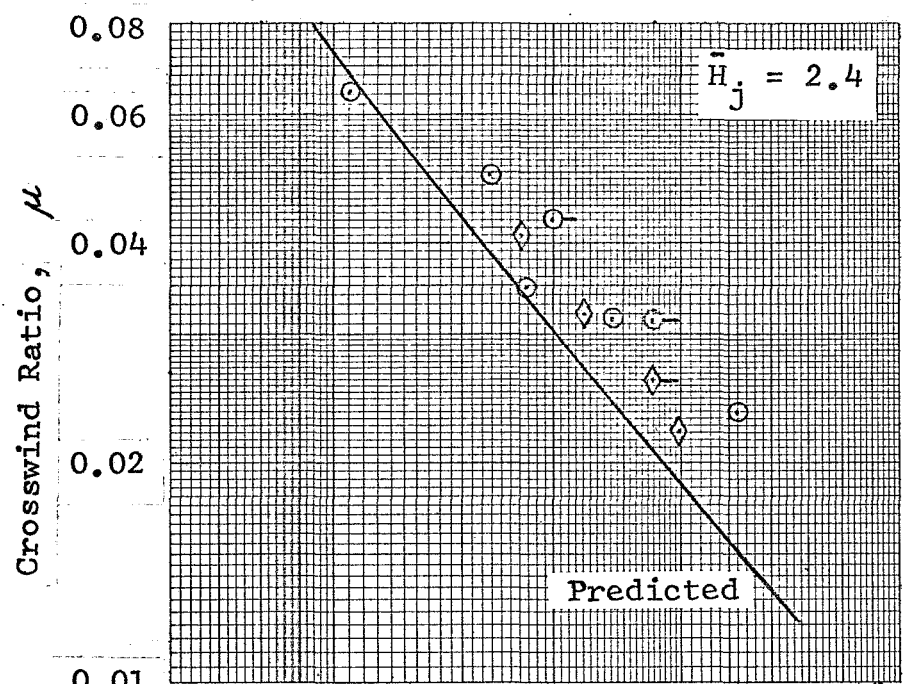
Figure 38.- Variation of Experimental Ground Separation Radius with Crosswind Ratio for a 4-Nozzle Configuration from References 72 and 73.

92

hampered by a lack of knowledge on the relative importance of buoyancy forces in the hot gas fountain.

### 3.2.2.3.1 Velocity and Temperature Distribution

An indication of the peak velocity and total temperature in the fountain produced by a pair of isolated engines (no fuselage or wings) is obtained from the small-scale data reported in Reference 65. Figures 39 and 40 respectively present the peak velocity and temperature at a height representative of the engine inlet for top-inlet configurations. These figures show the effect of variation of nozzle height and nozzle separation distance for the flow conditions specified by $\left(P_{t_j}/P_a\right) = 1.8$, $\left(T_{t_j}\right) = 500^\circ F$. The boundaries of unstable and fully developed fountain flow are also indicated. Velocities at other conditions can be approximated by use of the following equation

$$ u_f = u_f^* \sqrt{\frac{\left(P_{t_j}/P_a\right) - 1}{0.8}} \tag{75} $$

This equation is obtained assuming that the fountain differential total pressure is proportional to the jet total pressure $(\Delta P_{t_j})$ and also that the fountain density is constant. The validity of equation 75 is substantiated by the test data of Reference 65.

The differential total temperature shown in Figure 40 is presented in non- dimensional form since it appears to be proportional to the jet total temperature $(\Delta T_{t_j})$ and reasonably independent of nozzle pressure ratio, $(P_{t_j}/P_a)$. Reference 65 also indicates that the thickness of the fountain boundary defined by 50% reduction of peak velocity is of the order of three nozzle diameters.

At relatively low heights (as shown in Figures) 39 and 40, and also at low pressure ratio $((P_{t_j}/P_a) = 1.2)$ the fountain exhibits a random instability as it is deflected toward either engine. Additional departure from flow symmetry is evidenced by a critical sensitivity to crosswinds, small assymmetries in nozzle inclination, and nozzle pressure ratio imbalance.

$$P_{tj}/P_a = 1.8$$

$$T_{tj} = 500 \, {}^{\circ}F$$

$$\bar{H}_i = \bar{H}_j + 4.5$$
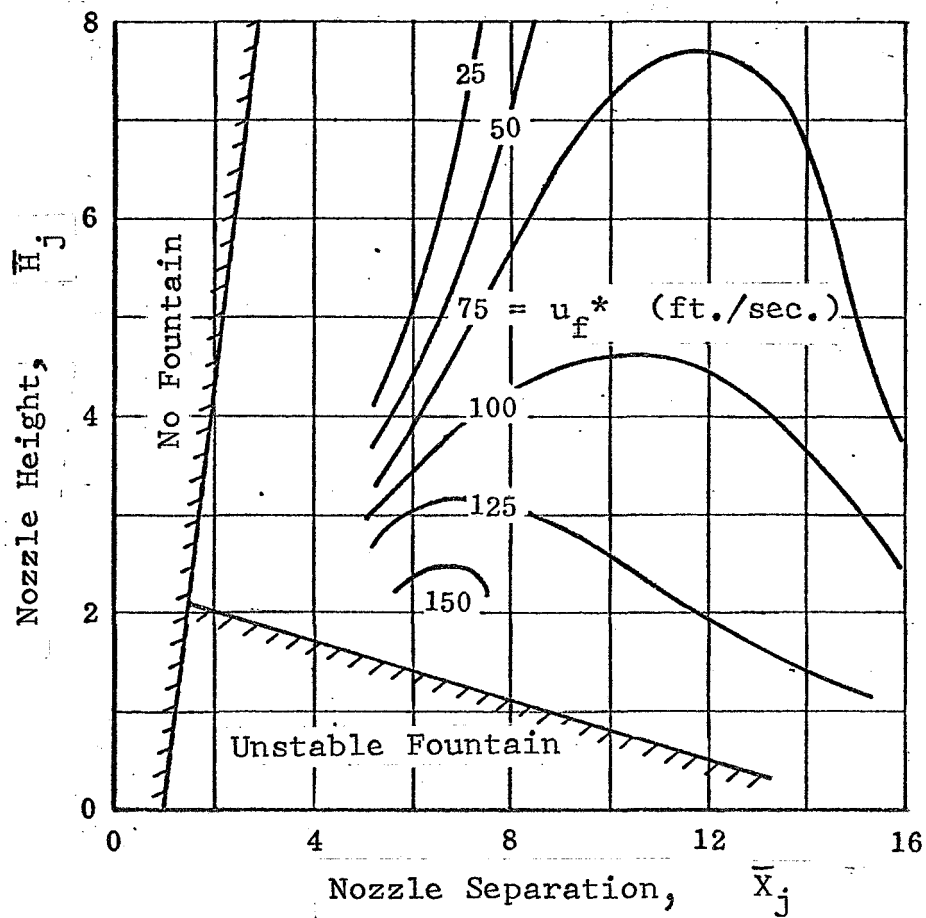


Figure 39.— Map of Maximum Fountain Velocities at the Intake Plane Versus Nozzle Height and Separation for the Small – Scale Isolated 2-Nozzle Configuration of Reference 65.

94

$$P_{tj}/P_a = 1.8$$

$$T_{tj} = 500\ ^\circ F$$

$$\overline{H}_i = \overline{H}_j + 4.5$$
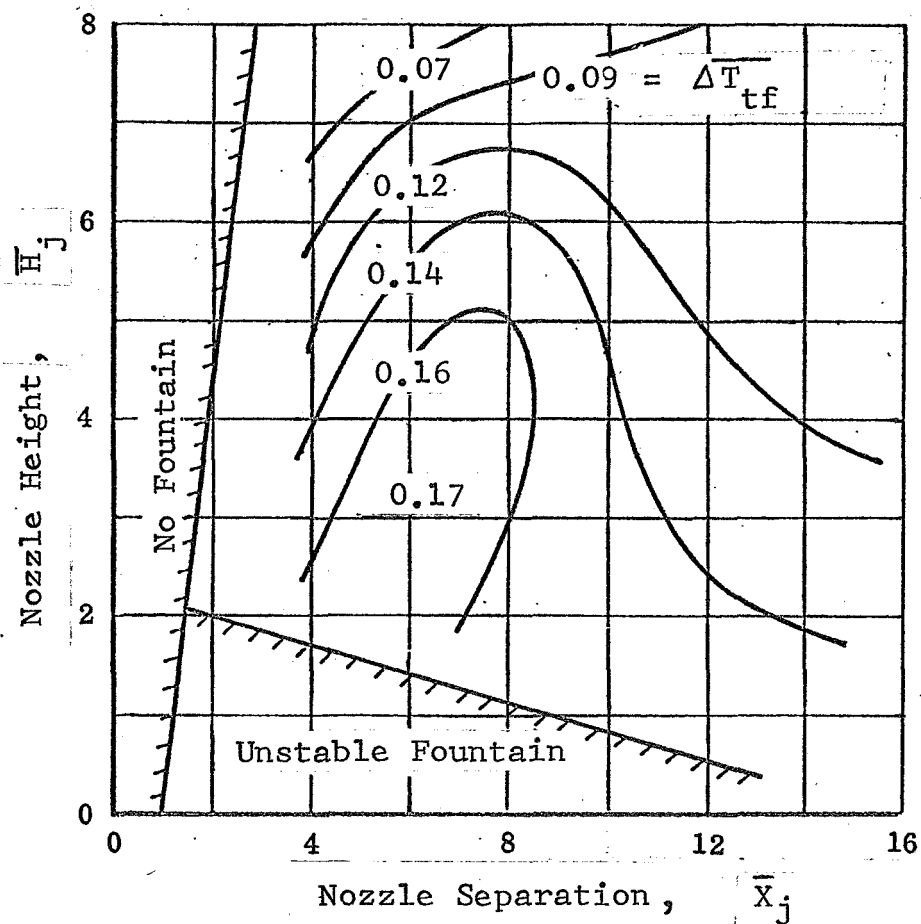
Figure 40. - Map of Peak Fountain Total Temperature at the Intake Plane Versus Nozzle Height and Separation for the Small-Scale Isolated 2- Nozzle Configuration of Reference 65.

### 3.2.3 Effect of the Interaction Plane Flow on Engine Intakes

The methods for evaluating inlet velocity and temperature distributions with no interaction plane effects are discussed and presented in Section 3.1.5 for a single nozzle configuration. These methods are considered to be generally applicable to multi-nozzle configurations, especially for the purpose of predicting inlet velocity or total pressure distributions, but have to be substantially modified to determine inlet temperature rise (ITR). Therefore, the discussion of these methods will not be duplicated, but only major differences and modifications of the methods as affected by the interaction flow and inlet air-frame configurations is presented in this section.

#### 3.2.3.1 Intake Pressure and Velocity Distributions

The average values of intake pressure and velocity distributions for multi-nozzle configurations with and without cross-winds can be obtained using engineering methods presented in sub-section 3.1.5.1.

#### 3.2.3.2 Intake Temperature Distribution

#### 3.2.3.2.1 Top-Inlet Configurations

For multi-nozzle configurations which give rise to the hot gas fountain effect (sub-section 3.2.2.3), the far-field re-circulation effect on ITR (described in sub-section 3.1.5.2) is less predominant than that of the near-field flow from the fountain. The magnitude and spacial distribution of ITR can be greatly affected by a particular placement of inlets with regard to airframe structure (fuselage, wings, etc.) which may deflect the hot fountain gases directly into the intakes. Furthermore, the crosswinds may deflect the fountain especially if it is unstable, and can have a critical influence on ITR values.

Although there are no systematic methods which can account for the effects discussed above, the maximum (time-average) value of ITR can be obtained from the fountain temperature characteristics presented in Figure 40.

The presence of large obstructions (such as wings) in the direct fountain flow path will result in an increased flow path length, and the additional turbulent mixing with cooler gases along the elongated path therefore should not cause an increase of ITR values above the maxima indicated by Figure 40.

Examining mean ITR measurements from small-scale tests (Reference 73) for a four-nozzle top inlet configuration similar to that shown in Figure 27, it is noted that a unique relationship may exist between the mean ITR (as a ratio to $(\Delta T_{tj})$) and the

96

crosswind ratio $(\mu)$. This relationship is shown in Figure 41 which presents a plot of non-dimensionalized ITR values versus crosswind ratios for wide variations in $(T_{tj})$, $(P_{tj}/Pa)$, and $(U_\infty)$. The boundaries shown in this figure enclose a majority of the test data including experimental scatter and are reasonably consistent with the published repeatability of ITR measurements. This method of presentation appears to be superior to the separate correlations attempted by Ryan (Reference 73) using either the ratio $(U_\infty/U_j)$, or using a buoyancy parameter obtained from Abbott's analysis (Reference 55).

Figure 41 also contains large scale data obtained from References 79 and 80. Although this data, when plotted in the non-dimensional form of mean $\overline{ITR}$ versus crosswind ratio $(\mu)$ follows a similar trend as the small-scale data of Reference 73 there is a distinct difference in magnitudes of $\overline{ITR}$. The indicated increase in $\overline{ITR}$ for the large scale data is attributed to the scaling effects which, because of insufficiency of the latter type of data, can not be completely evaluated at the present time.

Experimental measurements of the ITR distribution on large scale models where the fountain effect is present (References 79, 80) show substantial random variations. In general, there is a mean distributional bias which is attributed to the particular flow characteristics of the fountain. Figures 42 and 43 show typical ITR time history variations for the large-scale four-nozzle top inlet configuration under both static and ambient crosswind conditions.

The test data of References 79 and 80 is also utilized to illustrate the effect of airframe/ wing/ inlet geometry on ITR. This effect can be seen from Figures 44 and 45 which summarize typical variations in ITR as affected by nozzle height, using size and location with and without crosswinds for the four-nozzle top inlet configuration shown in Figure 27.

Also, Figures 46 and 47 show similar geometric effects for a two-nozzle top inlet configuration based on the test data of Reference 81.

## 3.2.3.2.2  Side-Inlet Configurations

Detailed measurements of ITR for the large-scale side inlet models, (References 79, 80) show that severe temperature gradients can occur for all exhaust nozzle configurations. It is noted that ITR gradients are predominantly vertical with the highest temperature at, or close to, the lowest part of the intake duct. In addition, the mean ITR is sensitive to nozzle height for a given configuration under static conditions while being relatively independent of wing size and location. Under the influence of crosswinds (at $\psi \neq 0°$) ITR generally increases to a peak before being progressively reduced and eliminated altogether
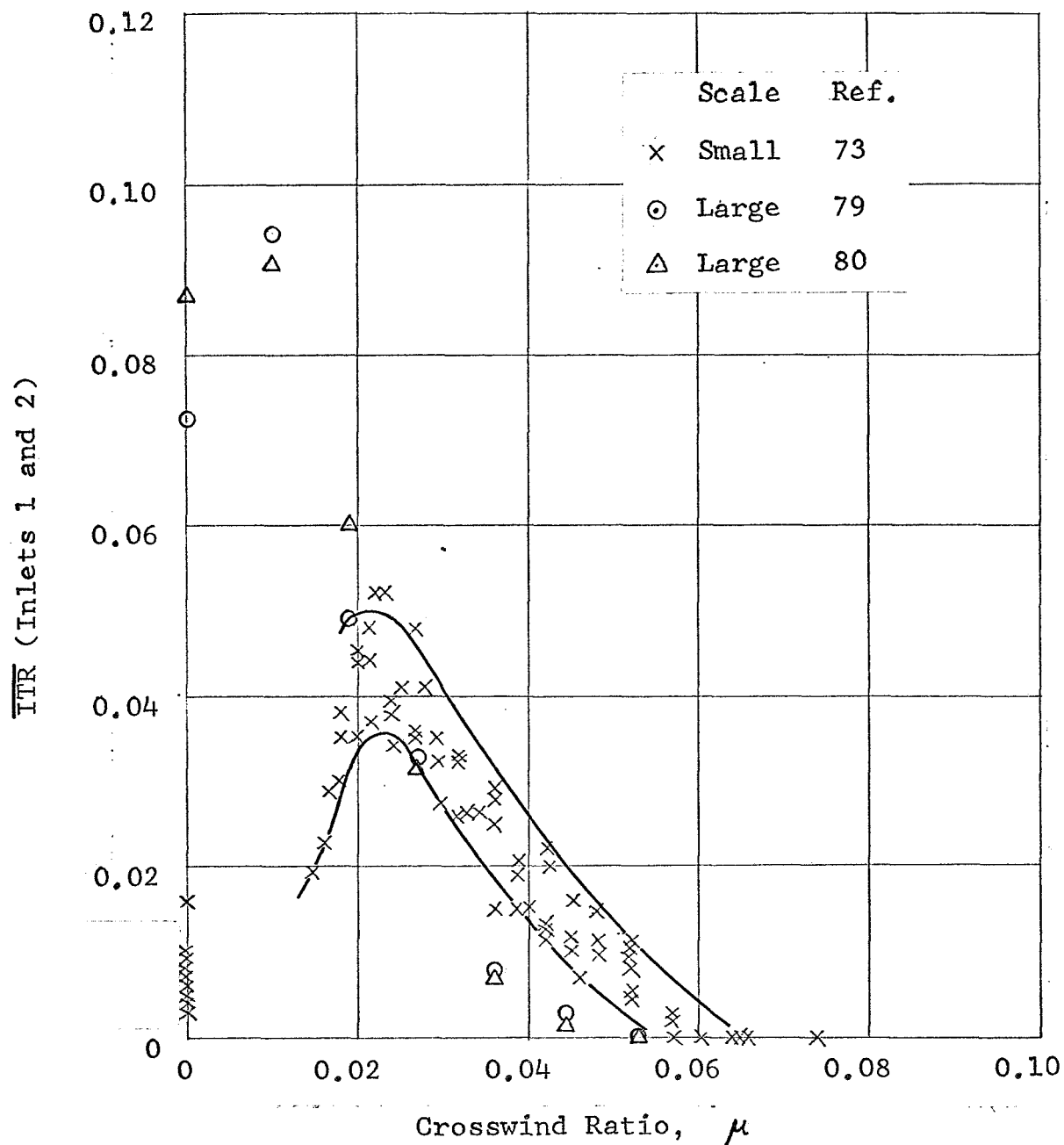
(a) Average Conditions in Forward Inlets.

Figure 41 .- Comparison Between Large and Small Scale Test Data on Mean $\overline{ITR}$ Versus $\mu$ for a Top-Inlet Four-Nozzle Configuration With a High Delta Wing. $\psi = 0°$, $\overline{H}_j = 6$.
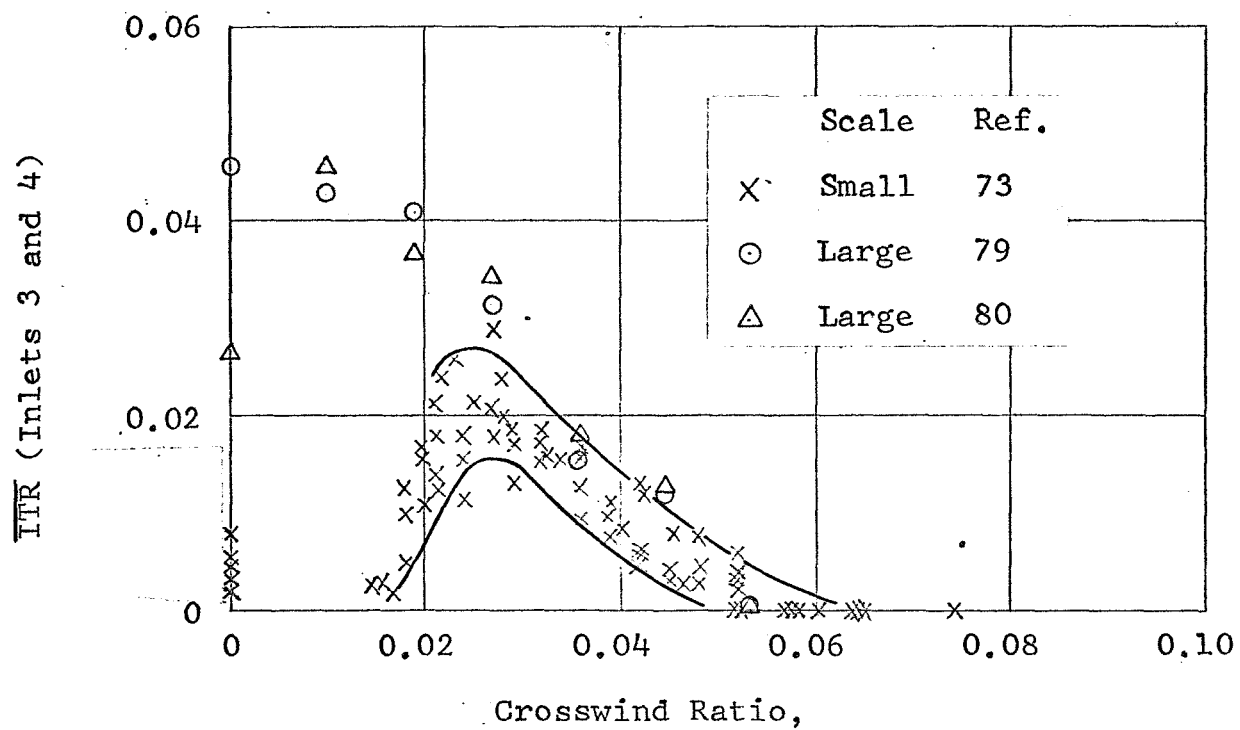
(b)   Average Conditions in Rear Inlets

Figure 41.- Concluded.

Figure 42.— Typical Time History of Inlet-Air Temperature Rise for the Four-Nozzle Configuration of Figure 38 With Top Inlets. $\bar{H}_j = 6$, $\psi = 0^\circ$, $u_\infty = 0$. ft/sec. (Reproduced from Reference 80).

Figure 42.- Concluded.

101

Figure 43.- Typical Time History of Inlet-Air Temperature Rise for the Four-Nozzle Configuration of Figure 38 with Top Inlets. $\overline{H}_j = 6$, $\psi = 0°$, $u_\infty = 20$ ft/sec. (Reproduced from Reference 80).

Figure 43.- Concluded.

Figure 44.— Effect of Nozzle Height and Wing Location on the Variation of Average Inlet-Air Temperature Rise With Windspeed for the Four-Nozzle Configuration of Figure 27 With Top Inlets. $A_w/A_{je}$ = 43.

104

Figure 45.— Effect of Wing Size on the Variation of Average Inlet-Air Temperature Rise With Windspeed for the Four-Nozzle Configuration of Figure 27 With Top Inlets. $\overline{H}_j = 6$.

Figure 46.- Effect of Wing Size on the Variation of Mean ITR with $\overline{H}_j$ for a Large-Scale Two-nozzle Configuration at $\overline{\overline{S}}_j = 4.88$, from Reference 81.
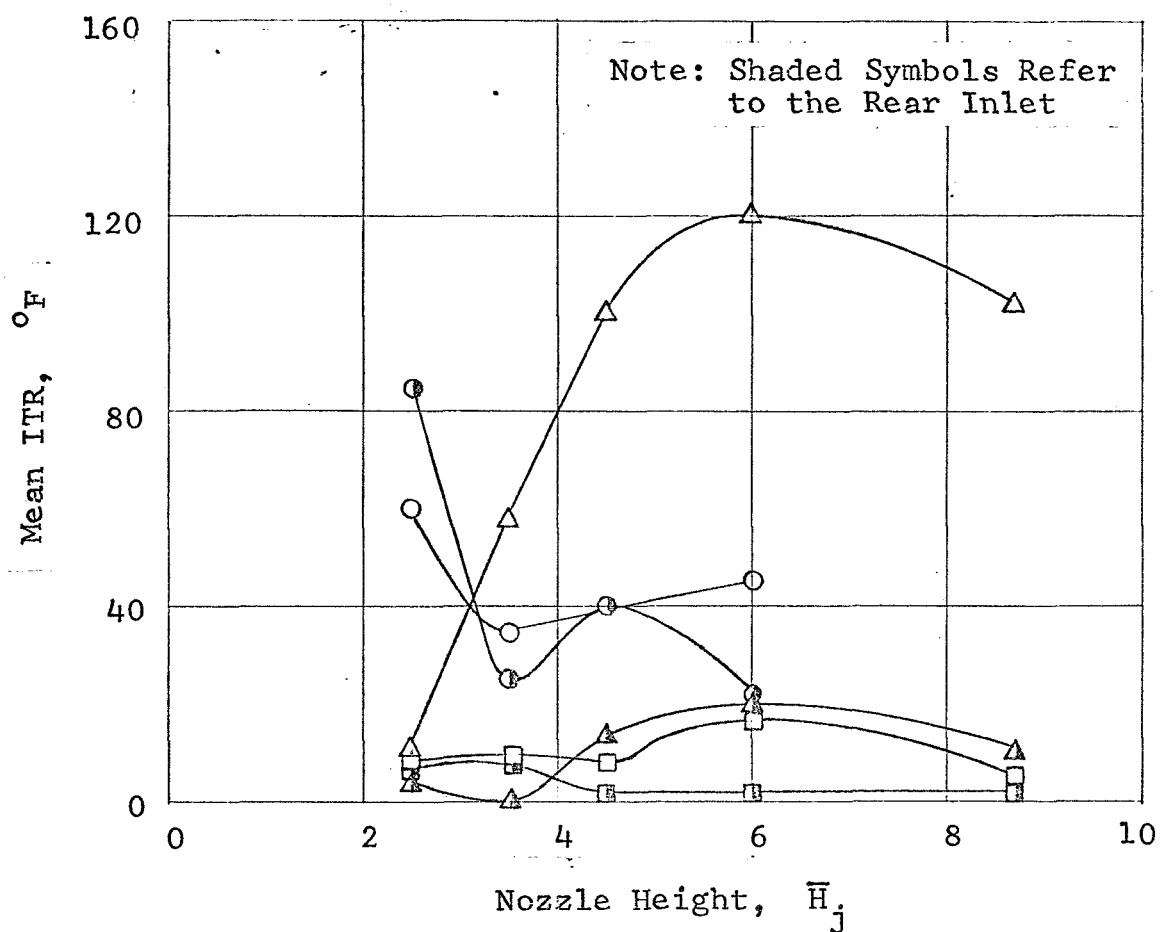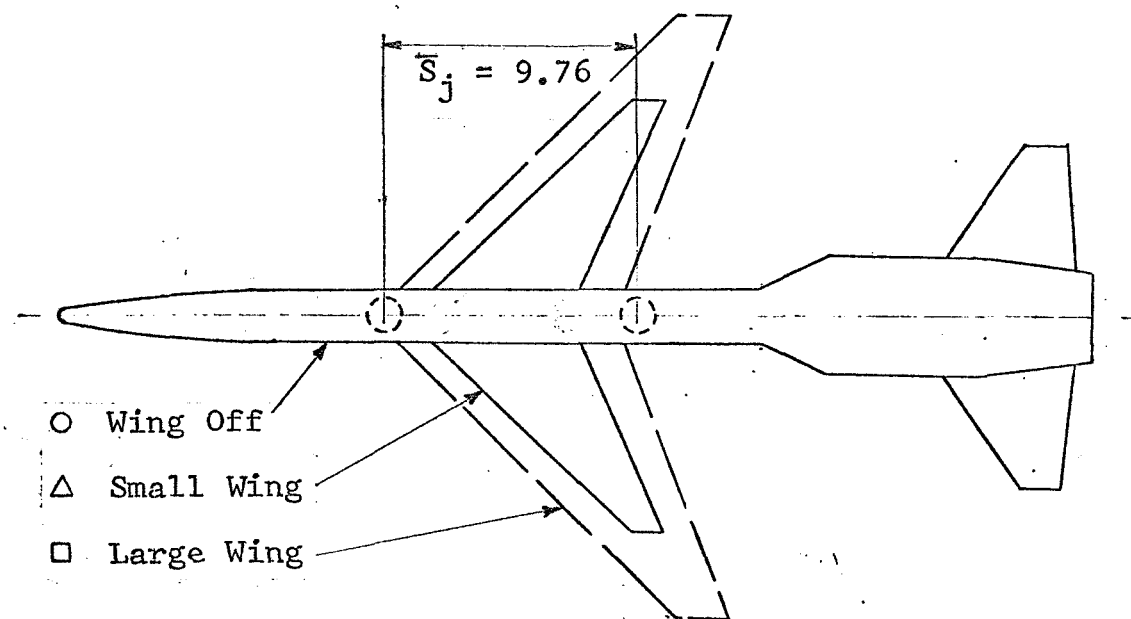
Figure 47.- Effect of Wing Size on the Variation of Mean ITR with $\overline{H}_j$ for a Large Scale Two-Nozzle Configuration at $\overline{S}_j = 9.76$, from Reference 81.

107

at higher forward speeds.

These characteristics suggest that side inlet configurations having the engine inlets well forward of the nozzles are susceptible to ingestion of the local groundflow passing underneath. An inspection of the experimental data of References 79 and 80 indicates that the maximum local time-average ITR is experienced at the lowest nozzle heights and approaches the value of the peak temperature in the wall jet or interaction plane groundflow. However, the vertical ITR distribution was not found to have any direct relationship to the temperature profile of the local undistrubed groundflow.

In the presence of ambient crosswinds originating along the $\psi = 0°$ azimuth the value of the crosswind ratio at which ITR is reduced to zero is in general agreement with that predicted by the analytical methods. This is the point where the forward extent of the hot gas recirculation boundary passes behind the intake plane. Due to the turbulent nature of the flow field, however, there is no clearly defined boundary although the experimental data show ingestion to be highly sporadic with rapidly lengthening time intervals during which no ingestion occurs.

On the basis of small-scale tests on a four-nozzle side inlet configuration similar to that shown in Figure 27, the non-dimensional experimental data for ITR from Reference 73 can be uniquely presented as a function of the crosswind ratio for a wide range of nozzle conditions. This relationship, which is similar to that presented for top inlets is shown in Figure 48.

Side-inlet configurations exhibit large and random fluctuations in the ITR distribution. This is accompanied by a general increase in mean ITR towards the edge nearest to the ground, as mentioned previously. Figures 49 and 50 present typical side-inlet ITR time histories, under static and crosswind conditions respectively, taken from Reference 80 for the large scale four-nozzle configuration shown in Figure 27.

The effect of airframe/ wing/ inlet geometry with and without crosswinds for typical side-inlet configurations is shown in Figures 51 and 52.

As in the case of top-inlets these data can be used to obtain qualitative trends of ITR as affected by geometry of typical full-scale V/STOL aircraft configurations.

108
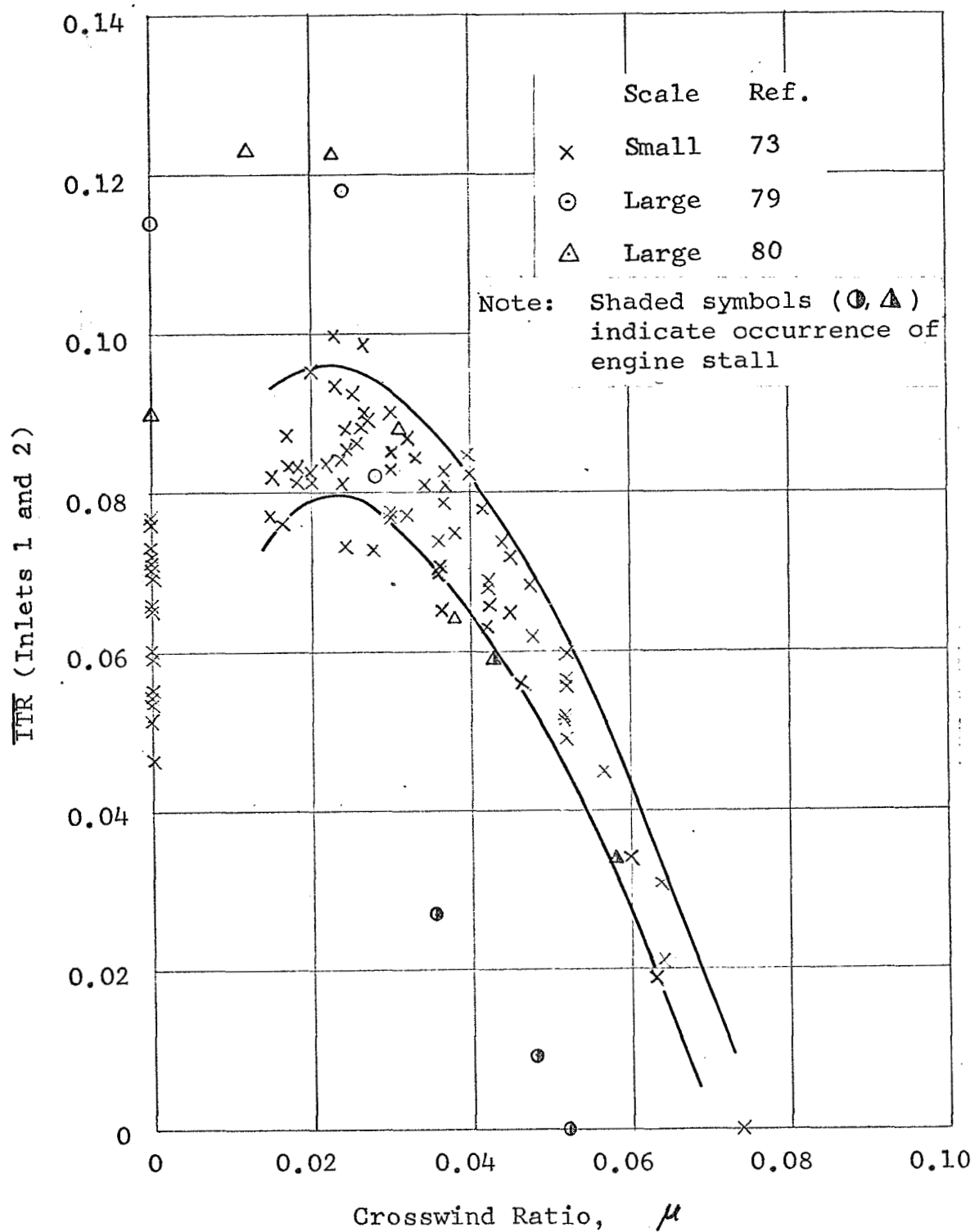
Figure 48.- Comparison Between Large and Small Scale Test Data on Mean $\overline{ITR}$ Versus $\mu$ for a Side-Inlet Four-Nozzle Configuration With a High Delta Wing. $\psi = 0°$, $\overline{H}_j = 2.4$.
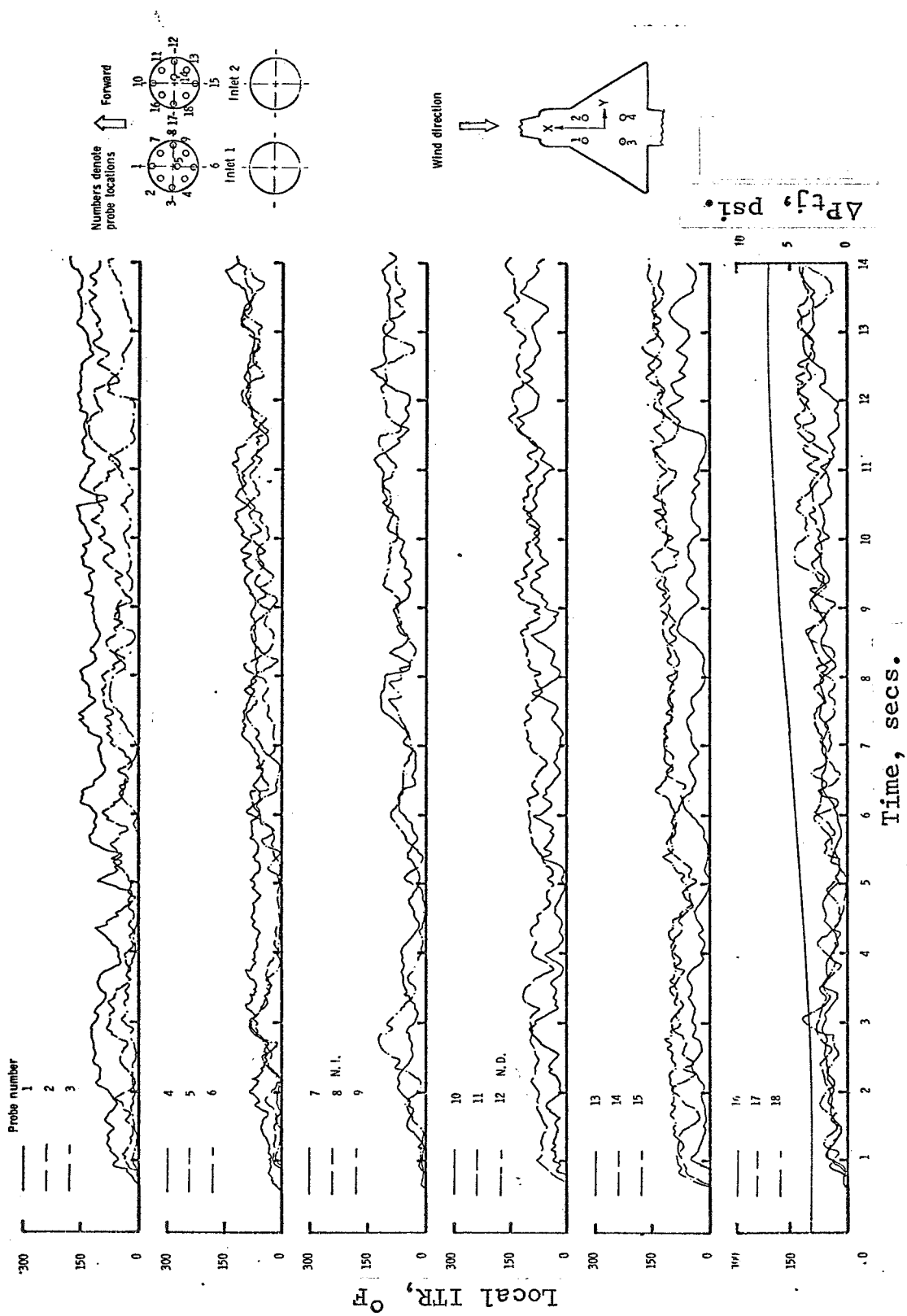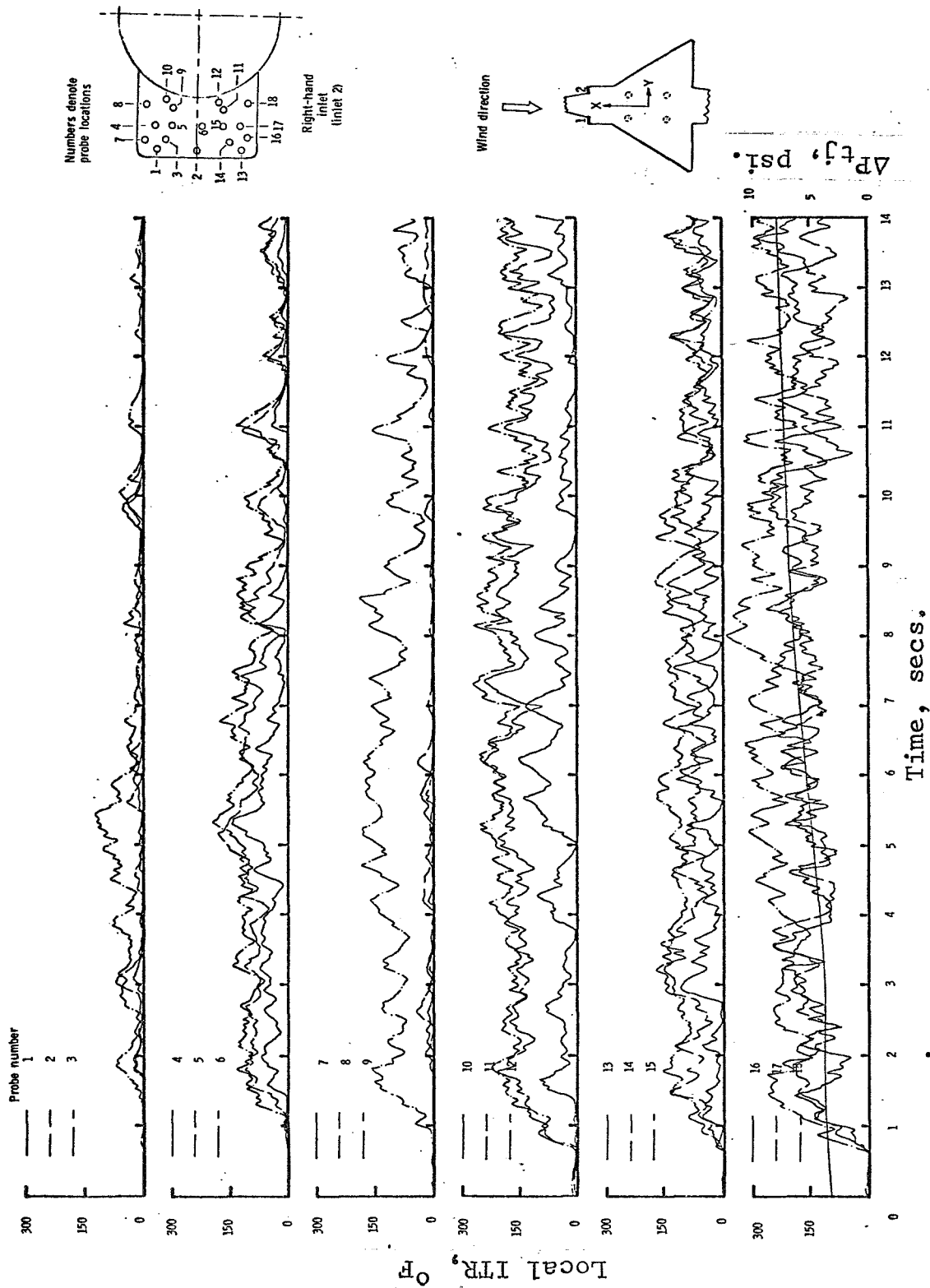
Figure 49.- Typical Time History of Inlet-Air Temperature Rise for the Four-Nozzle Configuration of Figure 27 with Side Inlets. $\bar{H}_j = 2.34$, $\psi = 0$, $u_\infty = 0$ ft/sec. (Reproduced from Reference 79).
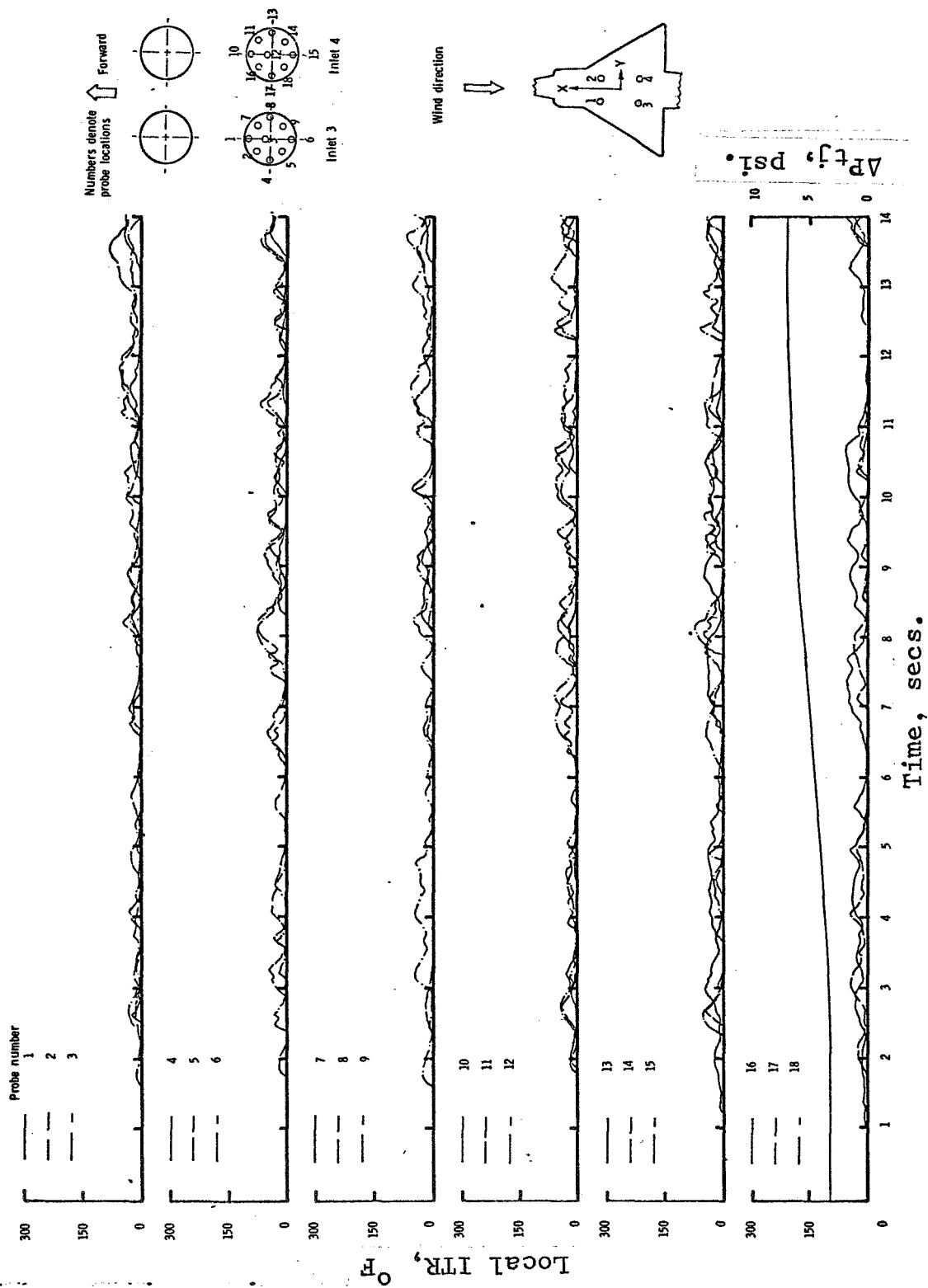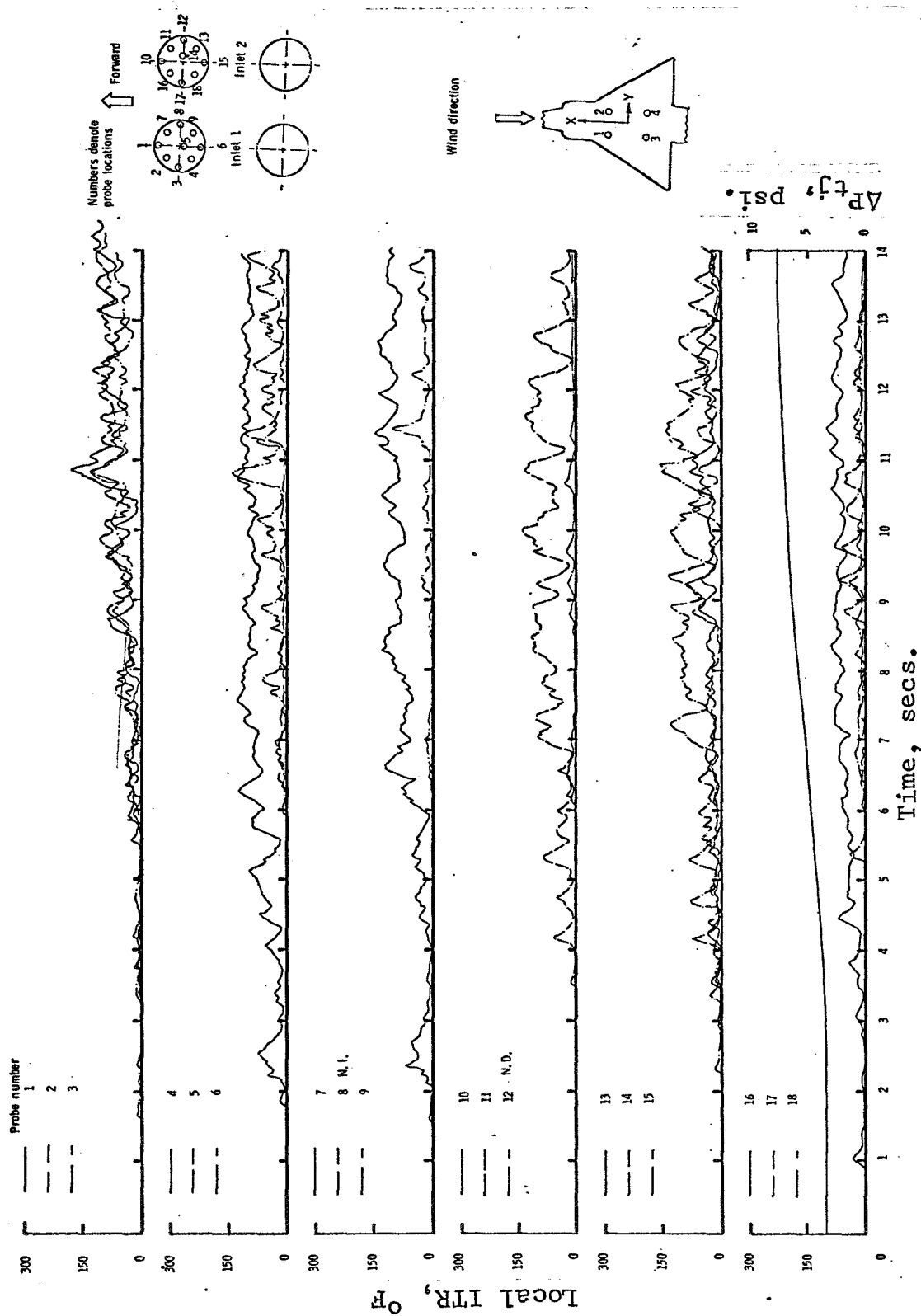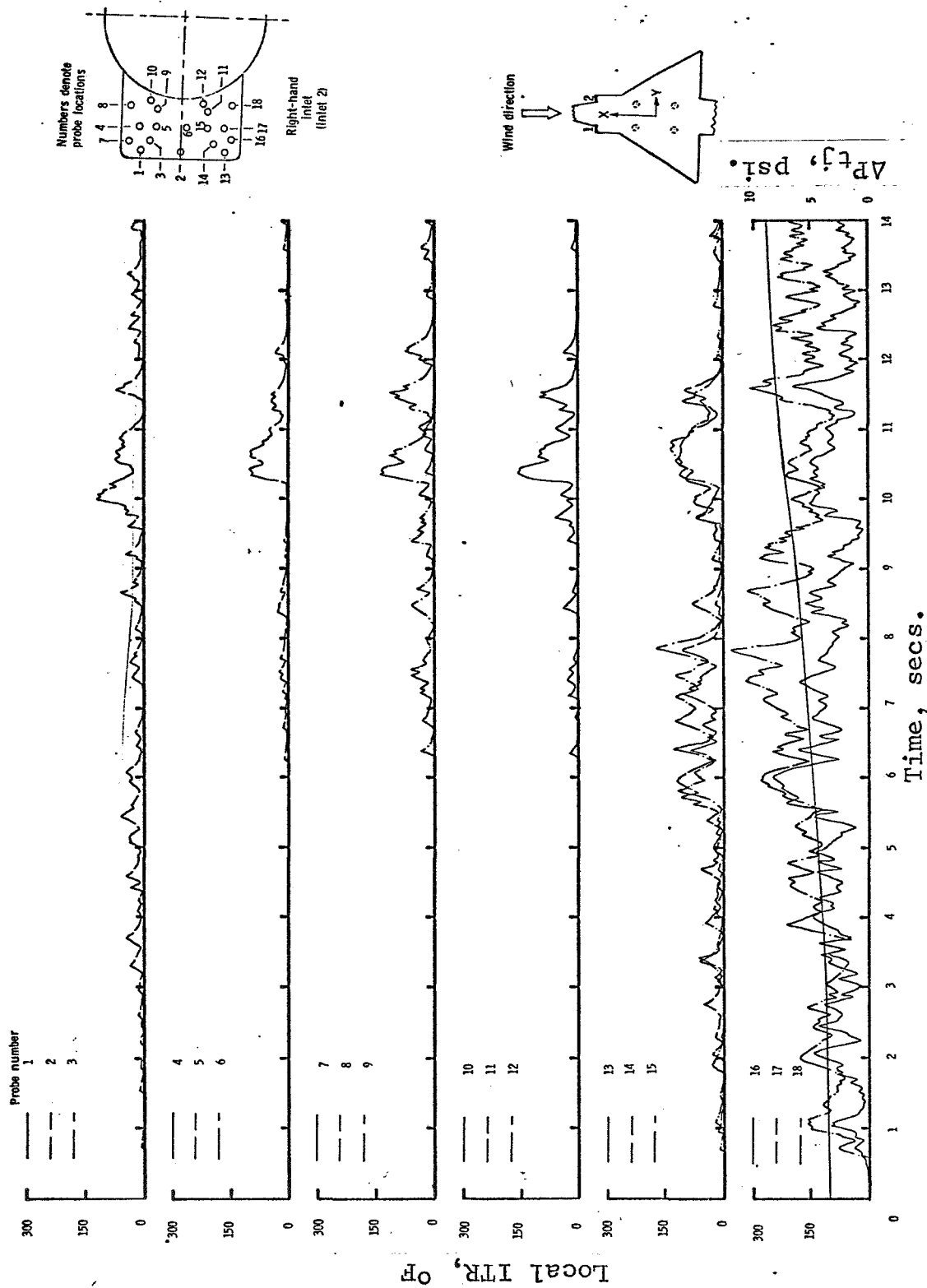
Figure 50.— Typical Time History of Inlet-Air Temperature Rise for the Four-Nozzle Configuration of Figure 27 with Side Inlets. $\overline{H}_j = 2.34$, $\psi = 0°$, $u_\infty = 30$ ft/sec. (Reproduced from Reference 79).
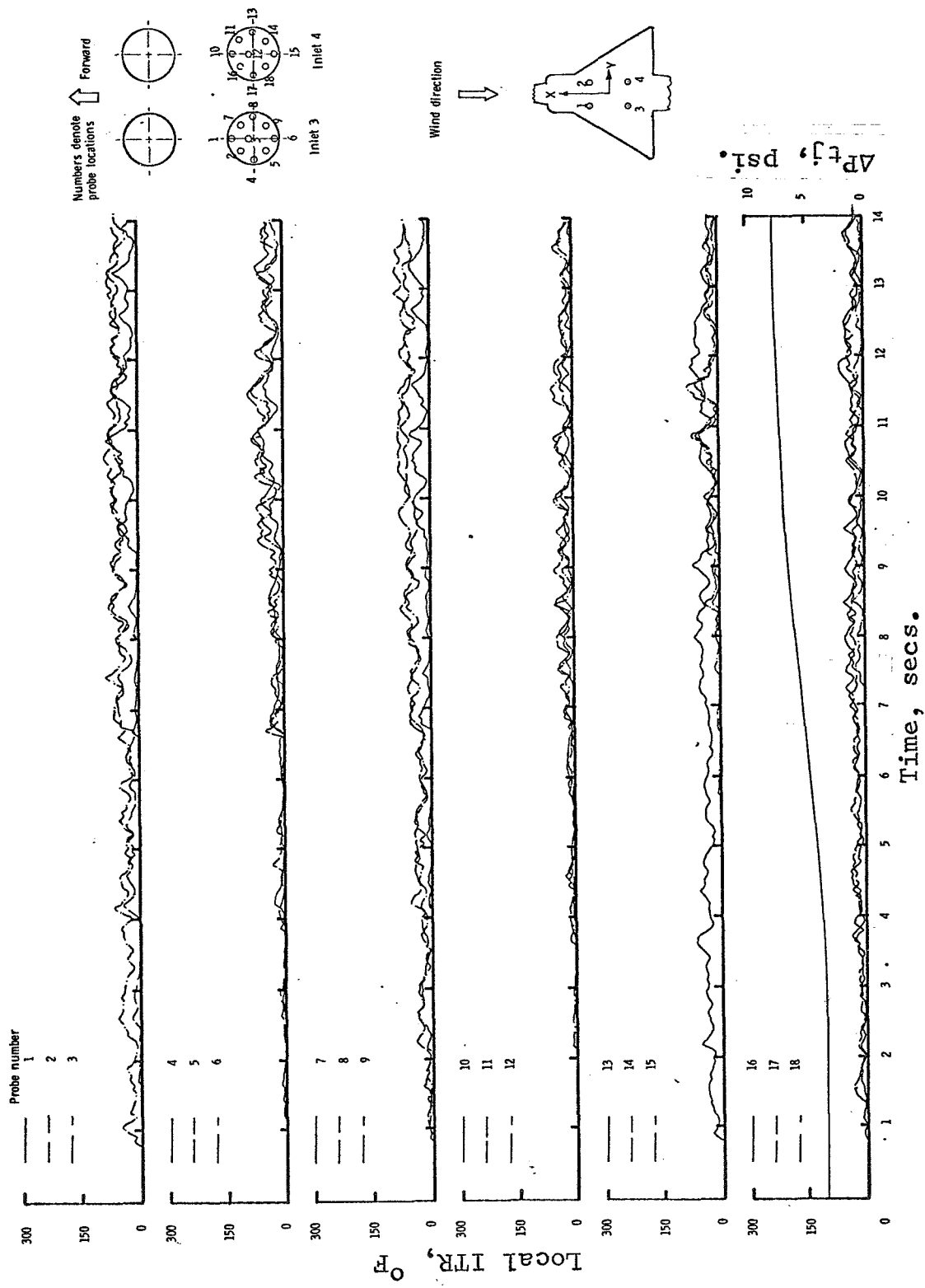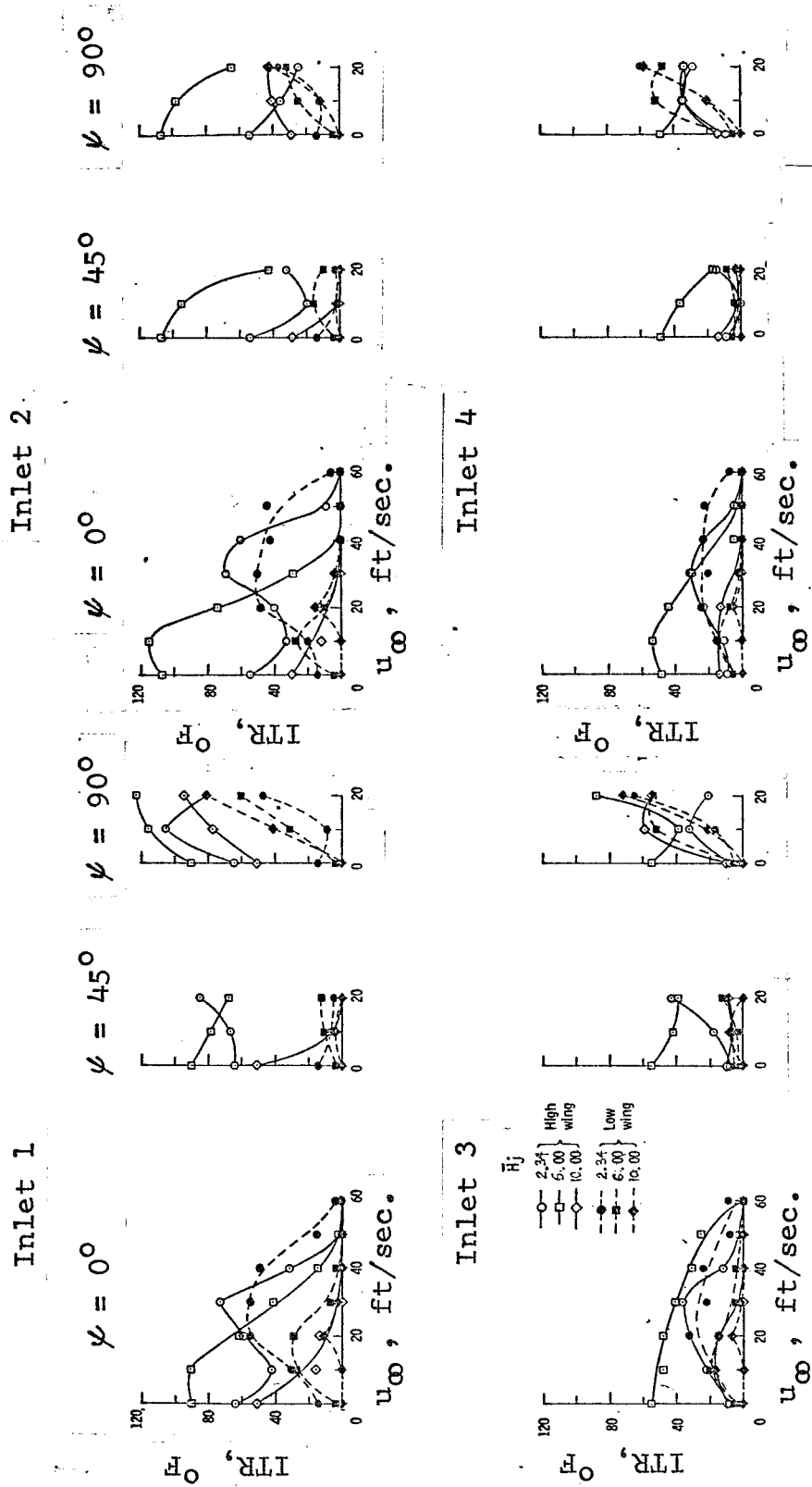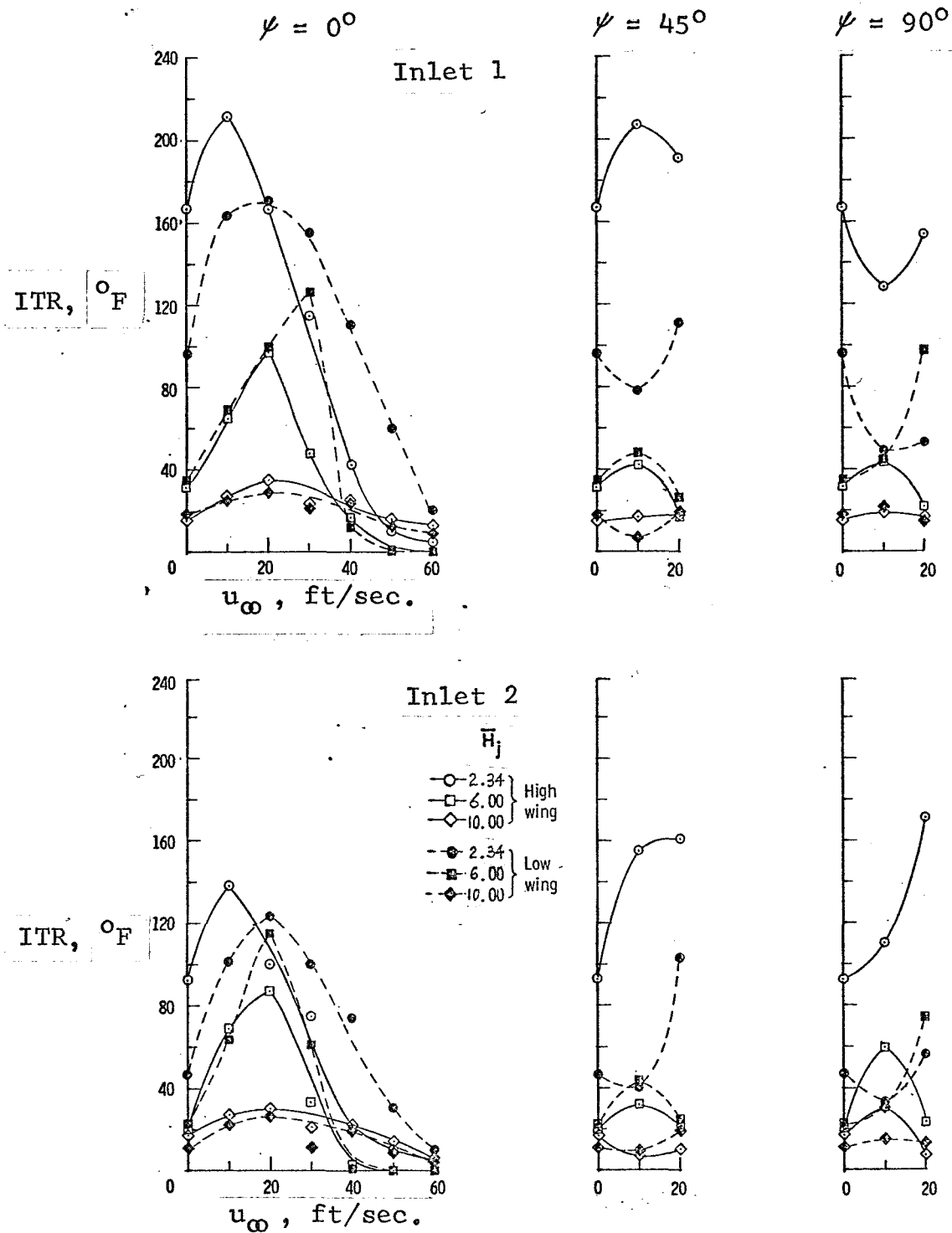
Figure 51.- Effect of Wing Location on the Variation of Average Inlet-Air Temperature Rise With Windspeed for the Four-Nozzle Configuration of Figure 27 with Side Inlets. $A_w/A_{j_e} = 43$.
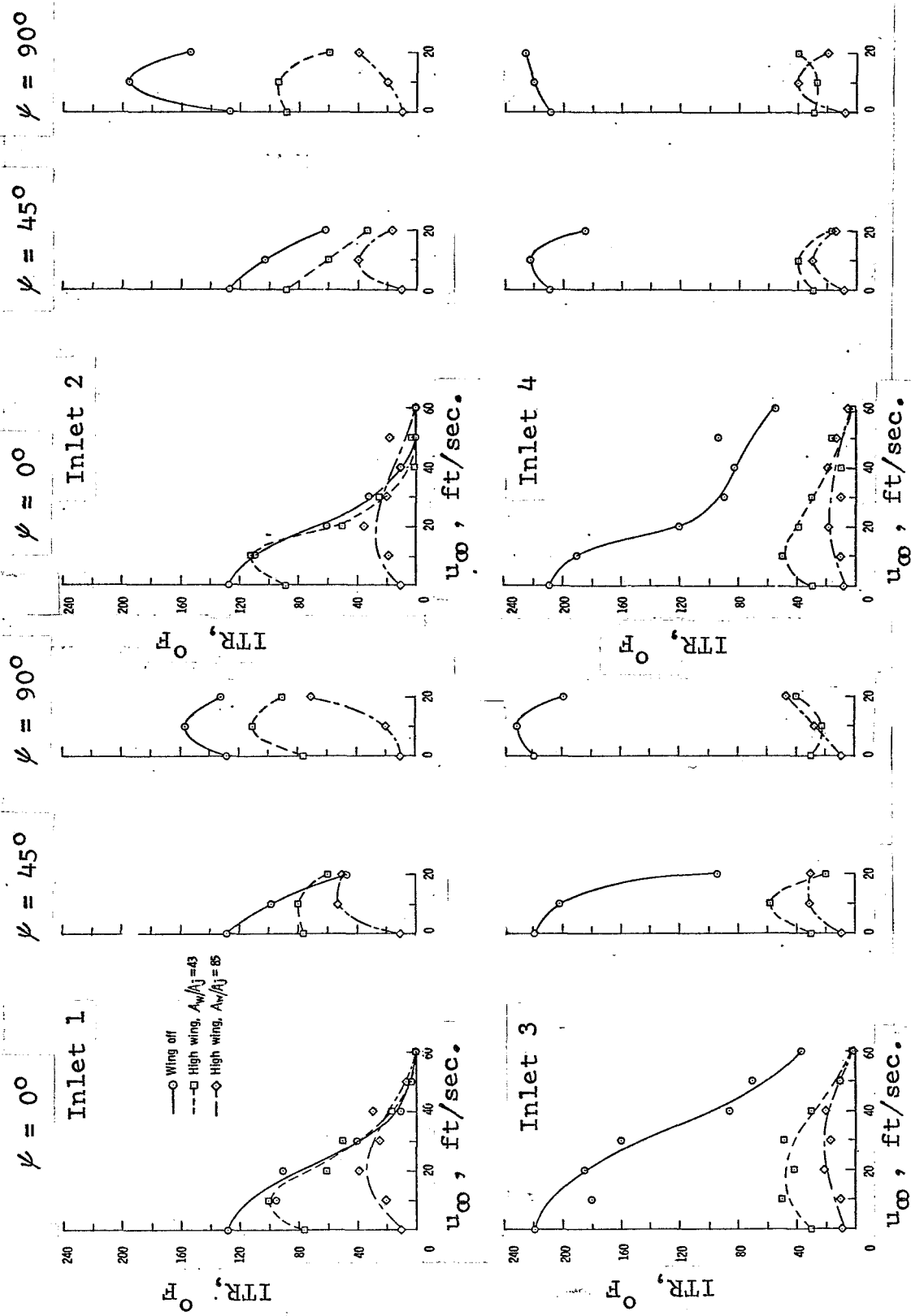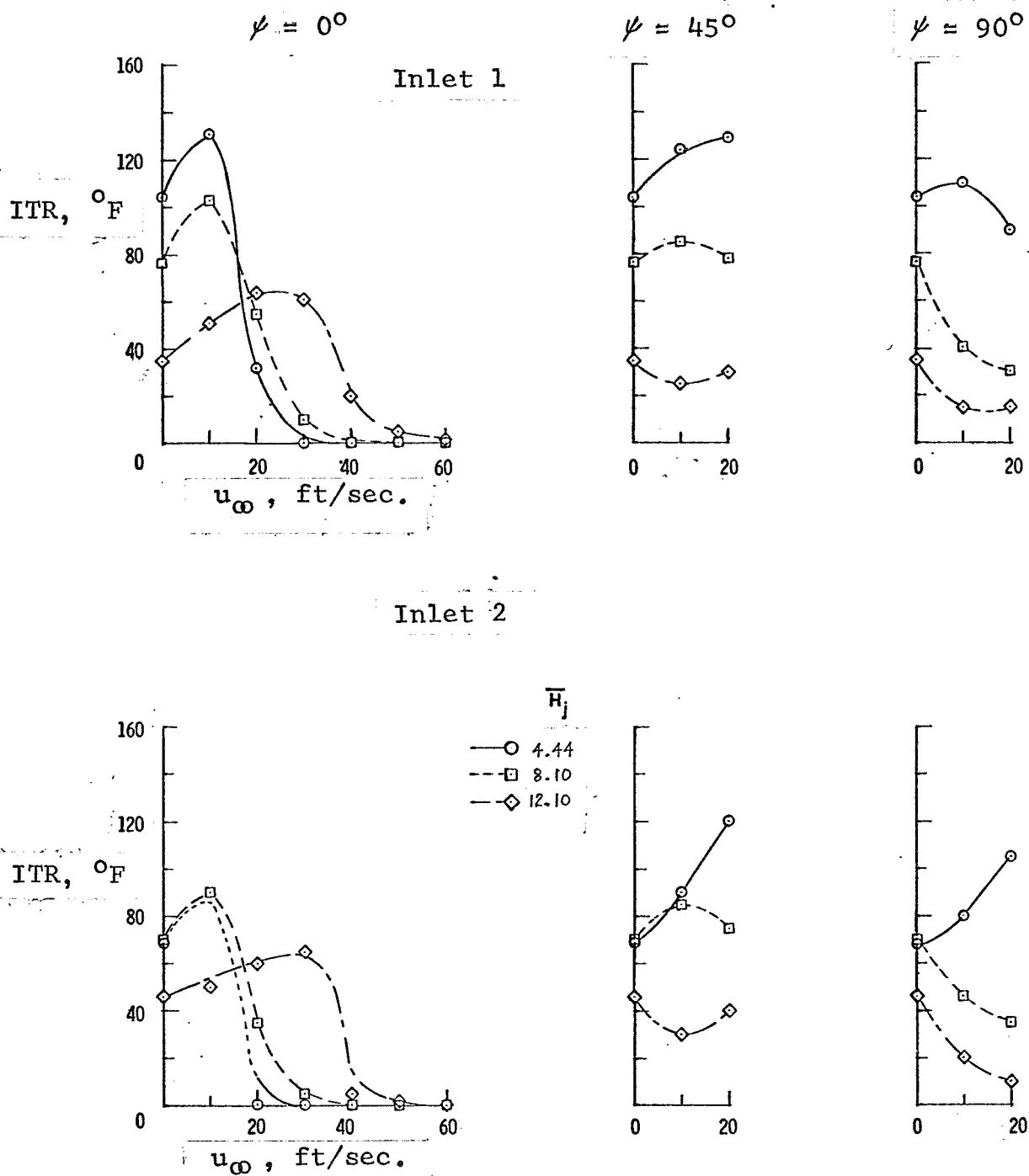
Figure 52.- Effect of Nozzle Height on the Variation of Average Inlet-Air Temperature Rise with Windspeed for the Four-Nozzle Configuration of Figure 53 with Side Inlets. High Delta Wing; $A_w/A_{j_e}$ = 43.
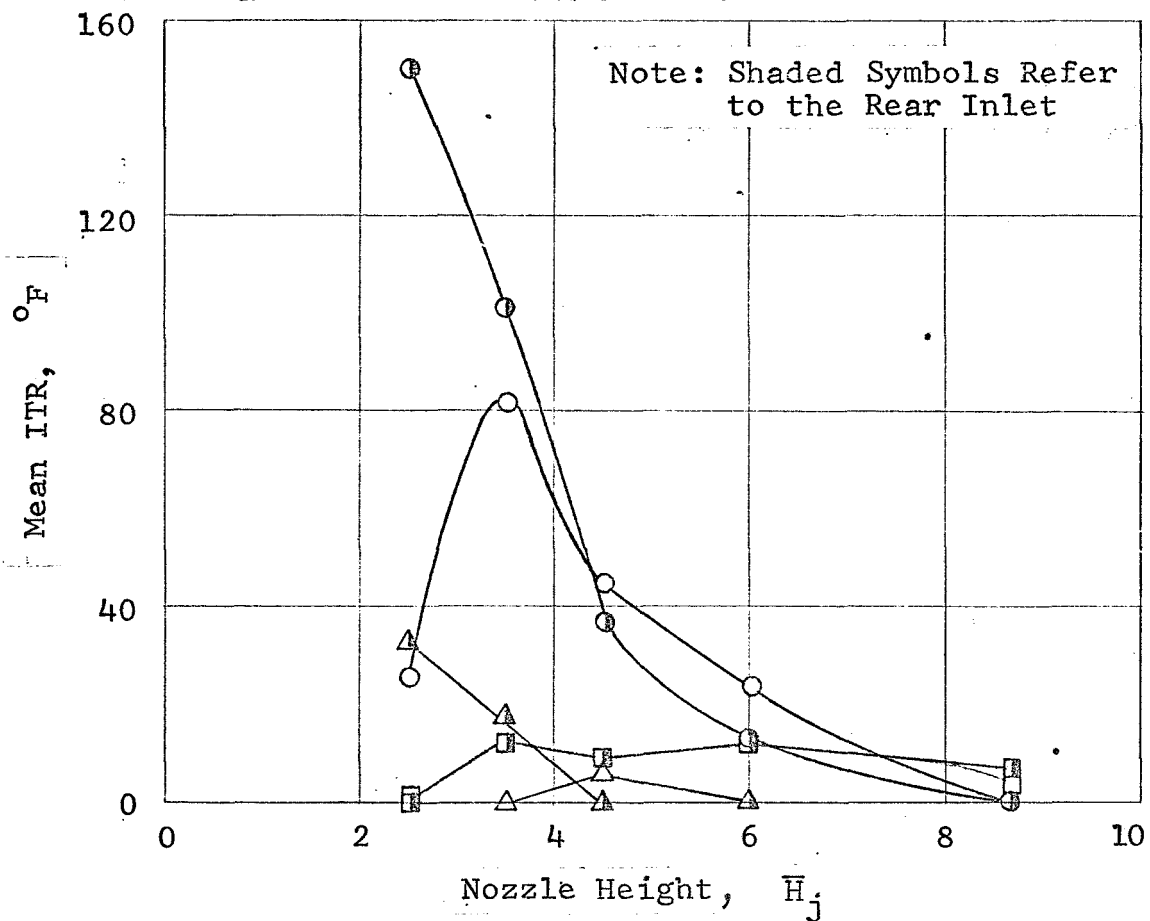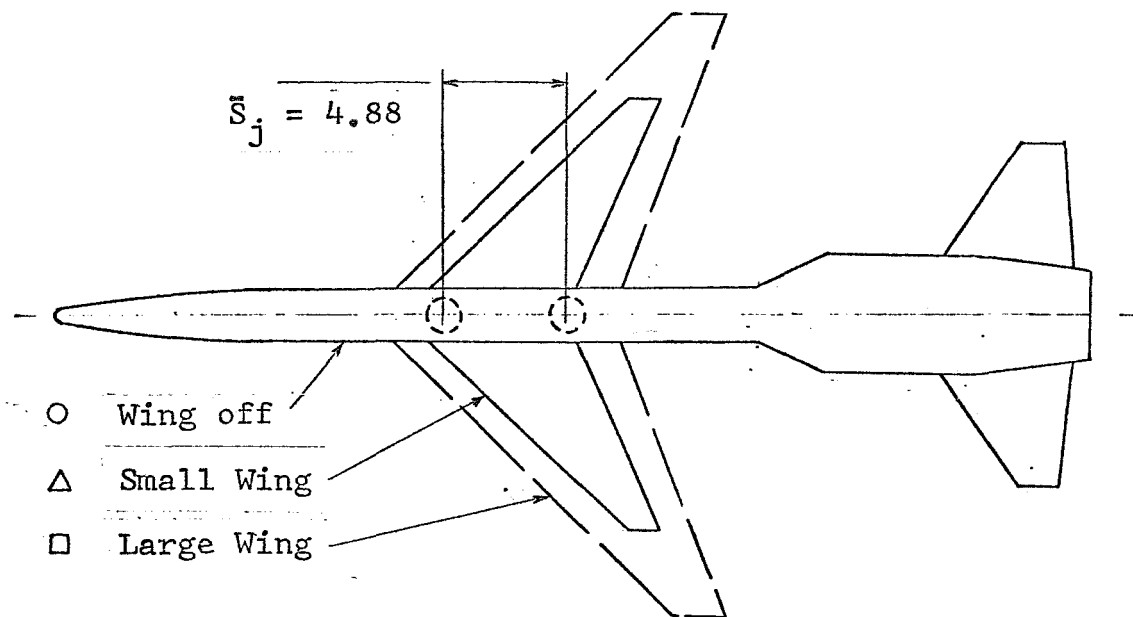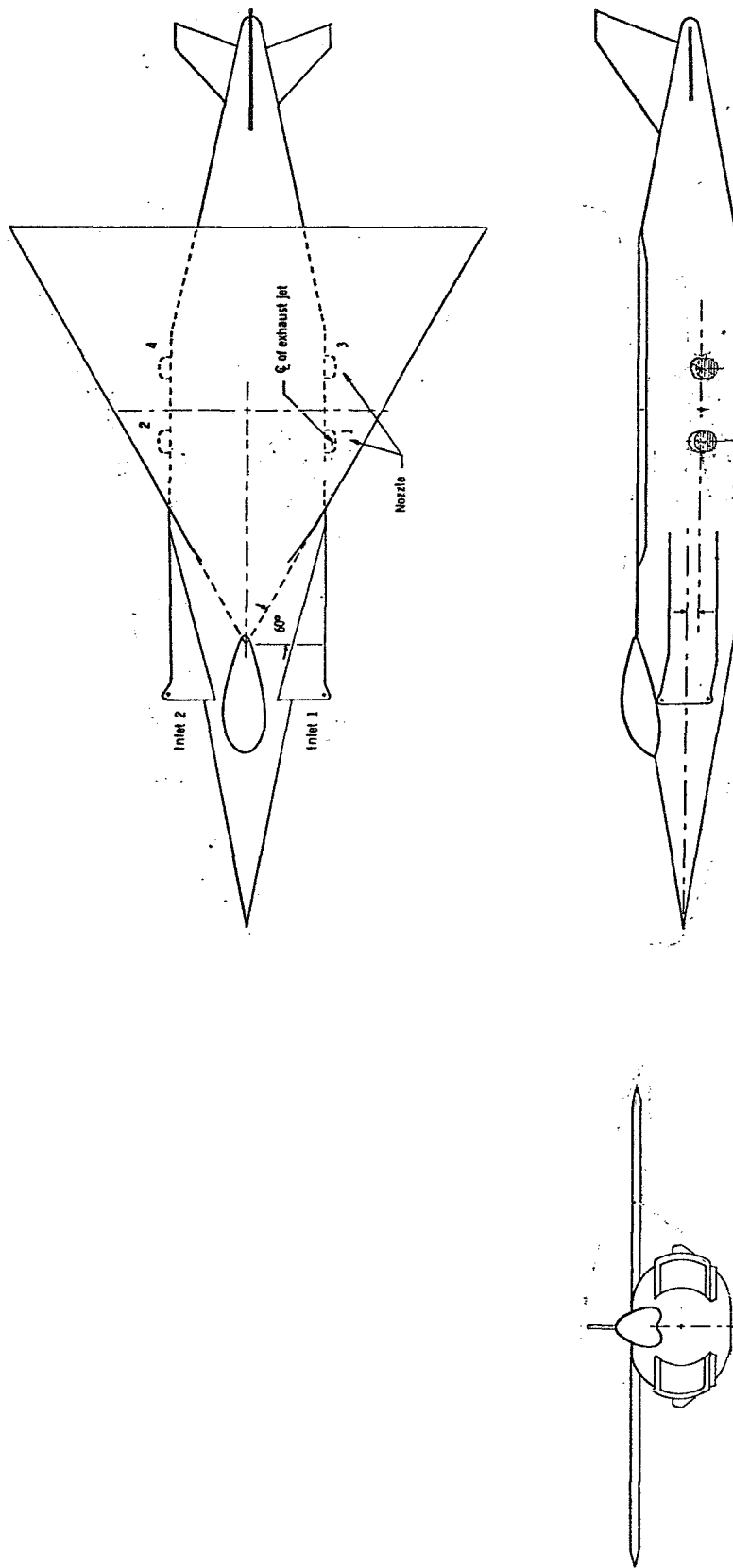
Figure 53.– Large-Scale Four-Nozzle Configuration Representative of the Hawker P.1127 Aircraft, from Reference 80.

114

SECTION 4

DESIGN PROCEDURES

The engineering methods developed in Section 3 are intended
to serve as a guide in the preliminary design of single-, two-,
and four-nozzle (rectangular arrangement) configurations of
V/STOL aircraft powered by jet lift engines operating in close
proximity to the ground. The design procedures are adequate to
predict the principal time-average velocity and temperature
distributions in the hot gas flow field due to circular engine
nozzles which are aligned vertically and have identical flow
characteristics, without swirl. The methods are considered
applicable to the wide range of design parameters as follows:

(1)   Exhaust Nozzle Height $(\overline{H}_j)$ = 1 to 30
(2)   Nozzle Stagnation Pressure Ratio $(P_{tj}/P_a) \leq 2$
(3)   Nozzle stagnation Temperature Ratio $(T_{tj}/T_a) \leq 3.2$
(4)   Crosswind Ratio $(\mu) < 0.1$

The following design procedures are presented to illustrate
application of the methods developed in the previous sections
to practical engineering problems. These procedures pertain to
single and multi-nozzle configurations with and without crosswinds.

4.1   SINGLE-NOZZLE CONFIGURATION (NO CROSSWINDS)

Determine the following design parameters:      .

(a)   Nozzle diameter $(D_j)$
(b)   Total pressure at the nozzle exit, $(P_{tj})$
(c)   Total temperature at the nozzle exit, $(T_{tj})$
(d)   Jet mass discharge coefficient $(C_D)$
(e)   Total heat discharge coefficient $(C_H)$
(f)   Ambient pressure (Pa) and temperature (Ta)

The hot gas flow characteristics in the vicinity of a single-
nozzle configuration operating in ground proximity can be deter-
mined considering isolated flow regions as discussed in Sections
2 and 3. Thus:

4.1.1 Region A-  Free Jet Flow

(a)   For selected values of the axial coordinate (S) radial
coordinate (r) and nozzle height ($H_j$), calculate

$$\overline{S} = S/D_j \tag{76}$$

$$\overline{r} = 2r/D_j \tag{77}$$

$$\overline{H}_j = H_j/D_j \tag{78}$$

(b)  Using the nozzle height $(\bar{H}_j)$ from step (a), determine axial limit of the free jet flow:

$$(\bar{S})_{max} = (\bar{H}_j - 1) \qquad (79)$$

(c)  Obtain the local total pressure $(P_t)$ at any point $(\bar{S}, \bar{r})$ in the free jet region as follows:

(i)  calculate $(S_1)$ from:

$$S_1 = \left(\frac{P_{tj}}{P_a}\right)^{-0.07} \left(\frac{T_{tj}}{T_a}\right)^{0.25} \frac{\bar{S}}{K_n \sqrt{C_D}} \qquad (80)$$

where $K_n = 1$ for a sharp nozzle, or $K_n = 0.95$ for a blunt nozzle (See Figure 6.)

(ii)  If $(S_1) \leqslant 4.87$, calculate $(\bar{r}_c)$ from:

$$\bar{r}_c = 0.945 - 0.194 (S_1) \qquad (81)$$

and, if $(\bar{r}) \leqslant (\bar{r}_c)$, the value of $(P_t)$ is given by:

$$P_t = P_{tj} \qquad (82)$$

(iii)  If $(S_1) \leqslant 4.87$ and $\bar{r} > \bar{r}_c$, calculate $(S_3)$ from:

$$S_3 = \left(\frac{P_{tj}}{P_a}\right)^{-0.23} \cdot \left(\frac{T_{tj}}{T_a}\right)^{0.25} \cdot \frac{\bar{S}}{K_n} \qquad (83)$$

Then, enter Figure 9 and obtain the value of $(\bar{r}_p)$ corresponding to $(S_3)$ and calculate $(P_t)$ from:

$$P_t = P_a + (P_{tj} - P_a) \cdot e^{-1.386 \left(\frac{\bar{r} - \bar{r}_c}{\bar{r}_p - \bar{r}_c}\right)^2} \qquad (84)$$

(iv)  If $(S_1) > 4.87$ enter Figure 7 and obtain the value of $(\Delta \bar{P}_{tc})$ corresponding to $(S_1)$, calculated from step (c) (i)

Also, enter Figure 9 and obtain the value of $(\bar{r}_p)$ corresponding to $(S_3)$, calculated from step (c) (iii).

Then, calculate $(P_t)$ from:

$$P_t = P_a + \overline{\Delta P_{tc}} \cdot (P_{tj} - P_a) \cdot e^{-1.386 \left(\bar{r}/\bar{r}_p\right)^2} \qquad (85)$$

(d)  Obtain the local total temperature (Tt) at any point $(\bar{S}, \bar{r})$ in the free jet region as follows:

116

(i) Calculate $(S_2)$ from:

$$S_2 = \left(\frac{P_{tj}}{P_a}\right)^{-0.86} \cdot \left(\frac{T_{tj}}{T_a}\right)^{0.5} \cdot \frac{\bar{S}}{C_H} \tag{86}$$

(ii) If $(S_1) \leq 4.87$, calculate $(\bar{r}_c)$ from step (c) (ii) above

Then, if $\bar{r} < \bar{r}_c$, the value of $(T_t)$ is given by:

$$T_t = T_{tj} \tag{87}$$

(iii) If $(S_1) \leq 4.87$ and $\bar{r} > \bar{r}_c$, calculate $(S_4)$ from:

$$S_4 = \left(\frac{P_{tj}}{P_a}\right)^{0.43} \cdot \left(\frac{T_{tj}}{T_a}\right)^{0.25} \cdot \bar{S} \tag{88}$$

Then enter Figure 10 and obtain the value of $(\bar{r}_t)$ corresponding to $(S_4)$ and calculate $(T_t)$ from:

$$T_t = T_a + (T_{tj} - T_a) \cdot e^{-0.693 \left(\frac{\bar{r} - \bar{r}_c}{\bar{r}_t - \bar{r}_c}\right)^2} \tag{89}$$

(iv) If $(S_1) > 4.87$, enter Figure 8 and obtain the value of $(\Delta T_{tc})$ corresponding to $(S_2)$, calculated from step (d) (i).

Also, enter Figure 10 and obtain the value of $(\bar{r}_t)$ corresponding to $(S_4)$, calculated from step (d) (iii).

Then, calculate $(T_t)$ from:

$$T_t = T_a + \Delta T_{tc} \cdot (T_{tj} - T_a) \cdot e^{-0.693 \left(\bar{r}/\bar{r}_t\right)^2} \tag{90}$$

(e) Obtain the local velocity $(u)$ at any point $(\bar{S}, \bar{r})$ in the free jet region as follows:

(i) Assume the static pressure $(P)$ is constant and given by:

$$P = P_a \tag{91}$$

(ii) If $(P_t/P) \leq 1.1$, calculate the jet velocity on the basis of incompressible flow assumptions from:

$$u = \sqrt{2 \cdot G \cdot T_t \left( \frac{P_t - P}{P} \right)} \tag{92}$$

(iii)  If $(P_t/P) > 1.1$ calculate the jet velocity on the basis of compressible flow assumptions using:

$$u = \sqrt{2 \cdot \left( \frac{\gamma}{\gamma - 1} \right) \cdot G \cdot T_t \cdot \left[ 1 - \left( \frac{P_t}{P} \right)^{\frac{1-\gamma}{\gamma}} \right]} \tag{93}$$

where the values for $(\gamma)$ and $(G)$ are the gas properties for the ambient air; i.e. approximately, $(\gamma) = 1.4$ and $(G) = 1716$ ft. lb./ slug mol. $^{\circ}$R.

118

## 4.1.2 Region B- Ground Impingement Flow

(a) Calculate the vertical limit $(H)_{max}$ of Region B as:

$$(H)_{max} = D_j \qquad (94)$$

(b) Calculate the radial limit $(R)_{max}$ of Region B as follows:

(i) Utilize the procedures given under section 4.1.1 step (c) to obtain the value of $(\bar{r}_p)$ for $(\bar{S}) = (\bar{H}_j)$

(ii) Calculate the ground impingement reference diameter $(Dg)$ from:

$$D_g = \frac{\bar{r}_p \cdot D_j}{2} \qquad (95)$$

(iii) Finally, calculate

$$(R)_{max} = 2 \cdot (D_g) \qquad (96)$$

(c) Calculate the value of the ground stagnation pressure $(P_{t_g})$ as follows:

(i) Given the nozzle height $(H_j)$ and nozzle diameter $(D_j)$, calculate:

$$\bar{H}_j = H_j / D_j \qquad (97)$$

(ii) Utilize the procedures given in section 4.1.1 ($c$) to obtain $(P_t)$ by putting:

$$\bar{S} = \bar{H}_j \qquad (98)$$

$$\bar{r} = 0 \qquad (99)$$

(iii) Then, obtain:

$$P_{t_g} = P_t \qquad (100)$$

(d) Calculate the value of the ground stagnation temperature $(T_{t_g})$ as follows:

(i) Using the value of $(\bar{H}_j)$ from step (a)(i), utilize the procedures given in section 4.1.1 ($d$) to obtain $(T_t)$ by putting:

$$\bar{S} = \bar{H}_j \qquad (101)$$

$$\bar{r} = 0 \qquad (102)$$

119

(ii)  Obtain:

$$T_{tg} \quad = \quad T_t \tag{103}$$

(e)  Calculate the flow conditions in the vertical region of the impinging flow, as shown by Figure 13, as follows:

(i)  Given the local height (H) and radius (R) referenced to the ground stagnation point, calculate:

$$\bar{H} = H/D_j \tag{104}$$

$$\bar{R} = R/D_j \tag{105}$$

(ii)  Utilize the procedures given under section 4.1.1 (c), (d) to obtain (Pt) and (Tt) by putting:

$$\bar{S} = \bar{H}_j - \bar{H} \tag{106}$$

$$\bar{r} = 2.(\bar{R}) \tag{107}$$

(iii)  Calculate the local static pressure (P) from:

$$P = P_a + \left(P_{tg} - P_a\right) e^{-3.466\,(\bar{H})^2} \tag{108}$$

(iv)  Finally, calculate the local velocity (u) from step (e) of section 4.1.1, using the values of (Pt), (P) and (Tt) obtained above.

(f)  Calculate the flow conditions along the ground plane, as shown in Figure 13, as follows:

(i)  Given the value of (Dg) from step (b) (ii) above calculate the peak ground plane total pressure (Ptw) as follows:

$$For \quad 0 \leqslant \left(\frac{R}{D_g}\right) \leqslant 0.4$$

$$P_{tw} = P_{tg} \tag{109}$$

For $0.4 < \left(\frac{R}{D_g}\right) < 2$

$$P_{tw} = \left(P_{tg} - P_a\right)\left(1.16 - 0.4\left(\frac{R}{D_g}\right)\right) \tag{110}$$

120

(ii). Calculate the peak ground plane total temperature
(Ttw) from:

$$T_{tw} = T_{tg} \tag{111}$$

(iii) Calculate the ground plane static pressure
($P_w$) as follows:

For $\overline{H}_j < 4$, enter Figure 18 and interpolate between
the curves to obtain ($\Delta P_{tw}/\Delta P_{tg}$) corresponding to the
value of ($R/D_g$). Then obtain:

$$P_w = P_a + \left(\Delta P_w/\Delta P_{tg}\right)\left(P_{tg} - P_a\right) \tag{112}$$

For $\overline{H}_j \geq 4$, calculate ($P_w$) from:

$$P_w = P_a + \left(P_{tg} - P_a\right) e^{-2.772 \left(R/D_g\right)^2} \tag{113}$$

(iv) Finally, calculate the peak ground plane velocity
($U_w$) from step (e) of section 4.1.1 by using the values
of (Ptw), (Pw) and (Ttw) obtained above.

## 4.1.3 Region C- Radial Wall Jet

(a) For selected values of the height coordinate (H) and radial coordinate (R) referenced to the ground plane stagnation point, obtain the non-dimensional values $(\overline{H}) = H/D_j$ and $(\overline{R}) = R/D_j$.

(b) Compute the radial location at which the wall jet begins:

$$(\overline{R})_{min} = 2 \left(\overline{D_g}\right) \tag{114}$$

where $\overline{D}g$ is obtained from step (b), section 4.1.2

(c) Obtain the radial location at which the wall jet ends. This is given by the non-dimensional radius $(\overline{R}_s)$ at which the wall jet will separate from the ground due to buoyancy, thus:

$$\overline{R}_s = 0.877 \sqrt{\frac{G \cdot T_a}{g \cdot D_j} \cdot \frac{(P_{tj}/P_a) - 1}{(T_{tj}/T_a) - 1} \cdot \left(\frac{T_{tj}}{T_a}\right)^{1/2}} \tag{115}$$

(d) Obtain the local total pressure (Pt) at any point $(\overline{H}, \overline{R})$ within the radial wall jet region as follows.

(i). Calculate the non-dimensional value of the peak total pressure $(\Delta\overline{P_{tw}})$ from:

$$\Delta\overline{P_{tw}} = 1.59 \cdot \left(c_{Dj}\right) \cdot \left(\overline{H_j}\right)^{0.16} \cdot \left(\overline{R}\right)^{-2.16} \tag{116}$$

(ii) Determine $(\overline{h}_p)$ from:

$$\overline{h}_p = 0.1 \cdot \left(\overline{H_j}\right)^{0.1} \cdot \left(\overline{R}\right)^{0.9} \tag{117}$$

(iii) Compute the height at which the peak total pressure occurs, thus:

$$\overline{H} = 0.17 \left(\overline{h_p}\right) \tag{118}$$

(iv) Obtain the dimensional value of the peak total pressure from:

$$P_{tw} = P_a + \left(\Delta\overline{P_{tw}}\right) \cdot \left(P_{tj} - P_a\right) \tag{119}$$

where $\left(\Delta\overline{P_{tw}}\right)$ is given in step (d) (i) above.

(v)   If $\bar{H} \leqslant 0.17$ $(\bar{h}_p)$ calculate the local total pressure $(P_t)$ from:

$$P_t = P_a + \left(\overline{\Delta P_{tw}}\right). \left(P_{tj} - P_a\right). \left[\frac{\bar{H}}{0.17(\bar{h}_p)}\right]^{2/7} \qquad (120)$$

(vi)   If $\bar{H} > 0.17$ $(\bar{h}_p)$ calculate the local total pressure $(P_t)$ from:

$$P_t = P_a + \left(\overline{\Delta P_{tw}}\right). \left(P_{tj} - P_a\right). e^{-2.0\left(\frac{\bar{H}}{\bar{h}_p} - 0.17\right)^2} \qquad (121)$$

(e)   Obtain the local total temperature $(T_t)$ at any point $(\bar{H}, \bar{R})$ within the radial wall jet region as follows:

(i)   Calculate $(\overline{\Delta T_{tw}})$ from:

$$\overline{\Delta T_{tw}} = \left(\bar{H}_j\right)^{-0.1}. \left(\bar{R}\right)^{-1.0} \qquad (122)$$

(ii)   Determine the local value of peak total temperature $(T_{tw})$ at any given value of $(\bar{R})$ as that occuring at the ground surface, thus:

$$T_{tw} = T_a + \left(\overline{\Delta T_{tw}}\right). \left(T_{tj} - T_a\right) \qquad (123)$$

(iii)   If $\bar{H} \neq 0$, obtain $(T_t)$ from:

$$T_t = T_a + \left(\overline{\Delta T_{tw}}\right). \left(H_j - T_a\right). e^{-0.354\left(\bar{H}/\bar{h}_p\right)^2} \qquad (124)$$

(f)   Finally, calculate the local velocity $(u)$ at any point $(\bar{H}, \bar{R})$ within the radial wall jet region from step (e) of Section 4.1.1

using the values of total pressure and temperature obtained in (d) and (e) above and assuming $(P) = (P_a)$.

## 4.1.4 Region D- Recirculation Flow

(a) For selected values of the height coordinate (H) and radial coordinate (R) referenced to the ground plane stagnation point, obtain the non-dimensional values $\bar{H} = H/D_j$ and $\bar{R} = R/D_j$ .

(b) Obtain the peak vertical velocity ($u_h$) in the convective flow from :

$$u_h = \left[ \frac{g \cdot D_j}{4 \cdot \bar{R}_s} \frac{(T_{tj}/T_a) - 1}{1} \left\{ 2 \cdot G \cdot \frac{(P_{tj}/P_a) - 1}{(T_{tj}/T_a)} \right\}^{1/2} \right]^{1/3} \quad (125)$$

where $\bar{R}_s$ is given in step (c) of Section 4.1.3

(c) Calculate the peak total temperature ($T_{th}$) in the convective flow as follows:

(i) Calculate ($\overline{\Delta T_{ts}}$) from :

$$\overline{\Delta T_{ts}} = \left(\bar{H}_j\right)^{-0.1} \cdot \left(\bar{R}_s\right)^{-1.0} \quad (126)$$

where $(\bar{R}_s)$ is given in step (b) above.

(ii) Calculate ($\bar{H}_o$) from :

$$H_o = \frac{0.021 \ (u_h)^2}{(\overline{\Delta T_{ts}}) \cdot ((T_{tj}/T_a) - 1)} \quad (127)$$

(iii) Determine ($T_{th}$) from :

$$T_{th} = T_a + \frac{0.021 \ (u_h)^2}{(H + H_o)} \quad (128)$$

(d) Obtain the limiting radial boundary ($R_b$) of the recirculating gases using:

$$R_b = R_s + 0.22 \ (H + H_o) \quad (129)$$

(e) Obtain the limiting height ($H_b$) of the recirculating gases from the condition :

$$T_{th} = T_a + 0.001 \ (T_{tj} - T_a) \quad (130)$$

(f) Finally, compute ($H_b$) from :

$$H_b = \frac{21 \cdot (u_h)^2}{(T_{tj} - T_a)} - H_o \quad (131)$$

## 4.1.5  Region E-  Intake Flow

(a)  Given the inlet height (Hi) above the ground plane, the mean inlet total temperature rise (ITR) can be estimated as follows:

(i)  Obtain $\overline{Hi}$ = Hi/Dj

(ii)  Then calculate (ITR) mean from :

$$\left(ITR\right)_{mean} = \frac{0.021 \ \left(u_h\right)^2}{\left(H_i + H_o\right)} \tag{132}$$

(b)  The ideal mean inlet velocity ($u_i$) is obtained as follows:

(i)  Given the total inlet area (At), calculate an initial value of the inlet mean static pressure (P$_i$) from :

$$P_i = P_a - \left(P_{tj} - P_a\right)\cdot\left(\frac{A_i}{A_j}\right)\cdot\left(\frac{T_a + \left(ITR\right)_{mean}}{T_{tj}}\right)\cdot\left(\frac{P_a}{P_i}\right) \tag{133}$$

where the ratio (P$_a$/P$_i$) is initially taken to be unity, and the final value (P$_i$) is obtained through an iteration procedure.

(ii)  Now obtain ($u_i$) from step (e) of section 4.1.1 by putting $P_t$ = $P_a$, P = P$_i$ , and $T_t$ = $T_{ti}$ = ($T_a$ + ITR)

## 4.2  SINGLE-NOZZLE CONFIGURATION (WITH CROSSWINDS)

Determine the following design parameters in addition to those obtained in Section 4.1:

(a)  Crosswind velocity ($u_\infty$)
(b)  Crosswind vector ($\psi$)

Design procedures to account for crosswind effects on the flow field due to a single-nozzle configuration are based on the "no crosswind" methods given in Section 4.1, with appropriate modification as detailed below.  Thus:

### 4.2.1  Region A-  Free Jet Flow

(a)  Calculate the jet centerline path as follows:

(i)  Compute ($\Delta P_{t\infty}$) from:

$$\Delta P_{t\infty} = \frac{1}{2} \cdot \frac{P_a}{G \cdot T_a} \cdot \left(u_\infty\right)^2 \tag{134}$$

(ii)  Calculate the crosswind ratio ($\mu$) using:

$$\mu = \sqrt{\Delta P_{t\infty} \Big/ \left(P_{tj} - P_a\right)} \tag{135}$$

(iii)  Determine the coordinates of the jet centerline from

$$\overline{x}_{wc} = \left(\mu\right)^{2.6} \cdot \left(\overline{z}_c\right)^3 \tag{136}$$

(iv)  Then calculate the jet centerline path inclination ($\theta_c$) using:

$$\theta_c = \cot^{-1}\left[ 3 \cdot \left(\mu\right)^{2.6} \cdot \left(\overline{z}_c\right)^2 \right] \tag{137}$$

(b)  For selected values of the jet axial coordinate ($S$), radial coordinate ($r$) measured normal to the local jet axis and nozzle height ($H_j$) the local flow conditions are obtained by following the procedures given under Section 4.1.1 using the substitution:

$$\overline{z}_c = S \tag{138}$$

All flow profiles thus obtained must be referred to the curved jet centerline determined above.

126

## 4.2.2  Region B-  Ground Impingement Flow

To account for wind effects in the ground impingement region the methods detailed in Section 4.1.2 are fully applicable provided that all flow profiles are referred to the curved jet centerline as obtained in Section 4.2.1.

## 4.2.3  Region C-  Wall Jet Flow

In order to determine the effect of crosswinds in the wall jet region the procedures detailed in Section 4.1.3 are modified as follows:

(a)  Determine the radial location at which the wall jet begins (measured from the ground impingement point of the curved jet), using equation (114).

(b)  Calculate the downwind ground separation radius ($R_5$) using equation (115).

(c)  Also, compute the upwind (minimum) separation radius ($R_5$) using the criterion:

$$\overline{\Delta P_{tw}} = \left( \frac{2 \cdot \mu}{1 + 5 \cdot \mu} \right)^2 \tag{139}$$

where the value of ($\mu$) is obtained from Section 4.2.1, step (a) (ii) and ($\overline{\Delta P_{tw}}$) is determined below.

(d)  Re-calculate the peak total pressure ($\overline{\Delta P_{tw}}$) using Section 4.1.3, step (d), as follows:

(i)  Compute the ground impingement angle ($\theta_g$) using:

$$\theta_g = \cot^{-1} \left[ 3 \cdot (\mu)^{2 \cdot 6} \cdot (\overline{H}_j)^2 \right] \tag{140}$$

(ii)  For a given azimuthal angle ($\phi$) between the wall jet vector and the upwind axis determine the ground turning angle ($\theta_t$) from:

$$\theta_t = \cos^{-1} - \cos(\theta_g) \tag{141}$$

(iii)  Use the value of ($\theta_t$) in Figure 25 to find the values of ($K_2$) and ($k_2$), and thus calculate ($\overline{\Delta P_{tw}}$) from:

$$\Delta P_{tw} = K_2 \cdot \sqrt{C_D} \cdot (\overline{H}_j)^{k_2} \cdot (\overline{R})^{-(1 + k_2)} \tag{142}$$

(e)  Re-calculate the peak total temperature ($\overline{\Delta T_{tw}}$) using Section 4.1.3, step (e), thus:

$$\overline{\Delta T_{tw}} = \left[ 2.109 - 0.0123 (\theta_t) \right] \cdot (\overline{H}_j)^{-0.1} \cdot (\overline{R})^{-1} \tag{143}$$

127

where $\left(\theta_t\right)$ is obtained in step (c)(ii) above.

## 4.2.4  Region D-  Recirculation Flow

In the presence of crosswinds a realistic mathematical model for the recirculating flow is not available, although at low crosswind speeds the flow will approximate that given for the no-wind case in Section 4.1.4.

With winds it is, however, possible to obtain essential hot gas boundary characteristics as follows:

(a)  Obtain the upwind radial limit $\left(R_b\right)$ of the hot gases as the value of the wall jet separation radius $\left(R_s\right)$ given by the methods in Section 4.2.3 step (a).

(b)  Calculate the approximate height $\left(H_b\right)$ of the boundary at a point directly above the engine nozzles from

$$H_b \;=\; 0.55 \;\left(R_b\right) \tag{144}$$

## 4.2.5  Region E-  Intake Flow

(a)  For a top-inlet configuration, a representative mean inlet temperature rise (ITR) can be estimated as follows:

(i)  Given $\left(U_\infty\right)$, enter Figure 28 and read off a typical ITR value for an appropriate configuration.

(ii)  Calculate the normalized value of ITR from

$$\overline{ITR} \;=\; \left(ITR / 1100\right) \tag{145}$$

(iii)  Finally, calculate the corrected value of ITR from:

$$\left(ITR\right)_{corr.} \;=\; \overline{ITR} \cdot \left(T_{t_j} - T_a\right) \tag{146}$$

(b)  For a side-inlet configuration, a representative mean ITR can be estimated by repeating step (a) above using Figure 30.

(c)  Having obtained the mean ITR from either step (a) or (b) above, calculate the mean inlet velocity using the procedure given by Section 4.1.5 step (b).

## 4.3  MULTI-NOZZLE CONFIGURATION (NO CROSSWINDS)

Determine the following design parameters in addition to

128

those given in Section 4.1.

 ·(a)  Longitudinal nozzle separation distance ($X_j$)

 (b)  Lateral nozzle separation distance ($Y_j$)

These dimensions are used to define both two-nozzle and four-nozzle (rectangular) configurations.  For a two-nozzle configuration either $(X_j)$ or $(Y_j)$ will be zero.

The hot gas flow characteristics can now be determined as follows:

### 4.3.1  Region A-  Free Jet Flow

(a)  Utilize the design procedures given for the single-nozzle configuration in Section 4.1.1 to calculate the isolated vertical flow fields under each nozzle. Since the flow from two or more nozzles may coalesce, calculate the combined flow as follows:

(i)  For a given value of ($S$) obtain the value of ($S_1$) from equation (80).

(ii)  If $(S_1) < 4.87$, compute the value of ($\bar{r}_C$) from equation (81) and then determine the effective boundary radius ($r_B$) of each jet from

$$r_B = \frac{D_j}{2} \cdot \left[ 2 \cdot \bar{r}_P - \bar{r}_C \right] \qquad (147)$$

where $(r_P)$ is obtained as follows:

(iii)  For a given downstream location ($S$) calculate the value of ($S_3$) from equation (83), then enter Figure 9 and obtain the corresponding value of ($\bar{r}_P$).

(iv)  If $(S_1) \geqslant 4.87$, obtain the effective boundary radius ($r_B$) of each jet directly from

$$r_B = D_j \cdot \bar{r}_P \qquad (148)$$

(v)  Now determine, from geometrical considerations, the extent of any jet coalescence by the overlap area of the isolated flow boundaries ($r_B$) for each jet.

(vi)  The combined total pressure ($P_t$) at any point where ($n$) jets are coalescing is obtained from

$$P_t = P_a + \sum_{m=1}^{n} \cdot \left( P_{t_{(m)}} - P_a \right) \qquad (149)$$

129

where $\left(P_{t_m}\right)$ are the values obtained by the isolated jet analyses.

(vii) The corresponding value of the combined total temperature $\left(T_t\right)$ can be estimated as a weighted average from :

$$T_t = T_a + \sqrt{\sum_{m=1}^{n} \cdot \left(T_{t_{(m)}} - T_a\right)^2} \qquad (150)$$

## 4.3.2 Region B- Ground Impingement Flow

(a) The ground impingement flow behavior for both two-nozzle and four-nozzle (rectangular) configurations can be evaluated by reference to the single-nozzle procedures given in Section 4.1.2 if certain geometric conditions are satisfied.

(b) For a two-nozzle configuration, obtain the flow characteristics as follows:

(i) From Figure 32 determine if the hot gas fountain effect is present for the given values of $\bar{H}_j$ and either $\bar{X}_j$ or $\bar{Y}_j$ (whichever is not zero).

(ii) If the fountain is present, there are two isolated impingement regions. These are both treated by direct reference to the procedures given in Section 4.1.2.

(iii) If the nozzle separation-to-height ratio satisfied the condition that

$$\sqrt{\left(\bar{X}_j\right)^2 + \left(\bar{Y}_j\right)^2} \leqslant 0.2 \cdot \bar{H}_j \qquad (151)$$

then the flow in region A is assumed to have totally coalesced prior to ground impingement. Now obtain the impingement behavior as that due to a single equivalent jet whose diameter $\left(D_{je}\right)$ is given by

$$D_{je} = D_j \cdot \sqrt{2} \qquad (152)$$

(c) For a four-nozzle (rectangular) configuration, determine the flow behavior as follows:

(i) From Figure 32 determine if the hot gas fountain is present for the given values of $\bar{H}_j$ and $\sqrt{\left(\bar{X}_j\right)^2 + \left(\bar{Y}_j\right)^2}$.

(ii)  Also determine from Figure 32 if the hot gas
fountain effect is present for isolated jet pairs whose
separation distance is given by either $\overline{X_j}$ or $\overline{Y_j}$ .

(iii)  If the fountain is present under all conditions
indicated above then there are four isolated impinge-
ment regions which can be treated by direct reference
to the procedures given in Section 4.1.2.

(iv)  If either of the jet pairs satisfy the condition
that their separation-to-height ratio is $\leqslant 0.2$ (either
$(\overline{X_j}/\overline{H_j})$ or $(\overline{Y_j}/\overline{H_j})$) then there are only two impinge-
ment regions, which are both treated by substituting
the equivalent diameter

$$ \mathcal{D}_{je} = \mathcal{D}_j \cdot \sqrt{2} \tag{153} $$

in the procedures given in Section 4.1.2.

(v)  If both of the jet pairs satisfy the condition
that their separation-to-height ratio $((\overline{X_j}/\overline{H_j})$ and
$(\overline{Y_j}/\overline{H_j})$ is $\leqslant 0.2)$ then only one impingement region
results.  This is considered by substituting the
equivalent diameter $(\mathcal{D}_{je}) = 2 \cdot (\mathcal{D}_j)$  in the procedures
given in Section 4.1.2.

## 4.3.3  Region C-  Wall Jet Flow

The wall jet flow extending radially outwards from each
ground impingement region is treated by reference to the design
procedures given in Section 4.1.3 for the single-nozzle config-
uration.  It is, however, necessary to substitute either the
isolated or equivalent nozzle diameter as appropriate to the
analysis of ground impingement characteristics given in Section
4.3.2 above.

It should be noted that the wall jets resulting from two
or more impingement regions will meet at the vertical interaction
plane(s).  The design procedures for determining the flow char-
acteristics in close proximity or at the interaction planes are
given in Section 4.3.6.

## 4.3.4  Region D-  Recirculation Flow

The characteristics of the far field recirculation flow are
obtained by direct reference to the methods given in Section
4.1.3 for the single-nozzle configuration.  Since these character-
istics depend on the conditions in the wall jet at the separation
point then it is essential to use the nozzle diameter appropriate
to the analysis of ground impingement, as given in Section 4.3.2
above.

131

## 4.3.5  Region E- Intake Flow

(a) Determine the mean inlet total temperature rise (ITR) for top-inlets of multi-nozzle configurations as follows:

(i)  From the methods given in Section 4.3.2 step (b), determine if the hot gas fountain is present.

(ii)  If no fountain exists, use the procedure given in Section 4.1.5 step (a) to calculate the value of ITR.

(iii)  If the fountain is present, obtain a typical ITR value from interpolation of appropriate graphical data presented in Figures 44 through 47 under Section 3.2.3.2.1 for large scale models.  Since all data is for a nominal nozzle temperature differential of about $1100^\circ$ R then calculate the normalized value of ITR from:

$$\overline{ITR} = \left( ITR / 1100 \right) \qquad (154)$$

and finally obtain the corrected ITR value from

$$\left( ITR \right)_{corr.} = \overline{ITR} \left( T_{t_j} - T_a \right) \qquad (155)$$

(b) Determine the mean inlet total temperature rise (ITR) for side-inlets of multi-nozzle configurations as follows:

(i)  From the methods given in Section 4.3.2 step (b), determine if the hot gas fountain is present.

(ii)  If no fountain exists, use Figure 30 to obtain a typical ITR value.  Then calculate the value of $(\overline{ITR})$ from equation (154) and use this value to obtain the corrected ITR value from equation (155).

(iii)  If the fountain is present, obtain a typical ITR value from interpolation between the appropriate graphical data presented in Figures 51, 52 Section 3.2.3.2.2.  Then perform the same calculation procedure as in step (a)(iii) above to obtain the corrected ITR value.

(c) Having obtained the mean ITR from either step (a) or (b) above, calculate the mean inlet velocity using the design procedures given in Section 4.1.5 step (b).

132

## 4.3.6  Region F-  Interaction Plane Flow

(a)  Determine the flow characteristics along the ground in the interaction plane by using the design procedures presented in Sections 4.1.3 and 4.3.3, modified as follows:

(i)  Obtain the peak total pressure ( $P_{tw}$) near the ground in the interaction plane as the value obtained by considering either of the mutually impinging wall jets as isolated jets.

(ii)  Calculate the ground static pressure ( $P_w$) in the interaction plane from

$$P_w = P_a + \overline{\Delta P_{tw}} \cdot \left( P_{tj} - P_a \right) \cdot \sin^2\left(\beta\right) \quad (156)$$

where $(\beta)$ is the angle between the local wall jet flow and the impingement plane as shown in Figure 33.

(iii)  On the basis of test data presented in Figure 36 obtain the corresponding peak total temperature ($\Delta T_{tw}$) as twice the value of the isolated wall jet flow.

(iv)  Finally, calculate the peak velocity ($u_w$) near the ground in the interaction plane from the methods given under Section 4.1.1 step (e) by using the values of ( $P_{tw}$), ( $P_w$ ) and ($T_{tw}$) obtained above.

(b)  Determine radial flow characteristics within the interaction plane as if the flow continued with the interaction plane removed.  Thus the total pressure, total temperature and velocity at a point in this portion of the interaction plane is obtained by utilizing the design procedures given in Section 4.1.3 steps (d) through (f).

(c)  Determine the peak values of velocity and total temperature in the vertical fountain between any one pair of jets as follows:

(i)  Given the values of nozzle spacing (either $\overline{X_j}$ or $\overline{Y_j}$ ) and nozzle height ( $\overline{H_j}$), enter Figure 39 and obtain a value of ( $u_f^*$).

Then calculate the peak fountain velocity ($u_f$), from :

$$u_f = u_f^* \cdot \sqrt{\frac{P_{tj} - P_a}{0.8 \cdot P_a}} \quad (157)$$

(ii) Also, enter Figure 40 and obtain a value of
$(\overline{\Delta T_{tf}})$. Then, calculate the corresponding peak
fountain temperature $(T_{tf})$ from

$$T_{tf} = T_a + \overline{\Delta T_{tf}} \cdot \left(T_{tj} - T_a\right) \qquad (158)$$

## 4.4  MULTI-NOZZLE CONFIGURATION (WITH CROSSWINDS)

Design parameters required for calculation of the hot gas
flow characteristics for a multi-nozzle configuration operating
in crosswinds are already defined in Sections 4.1 through 4.3
above.

The effect of crosswinds on flow characteristics within
each flow region of multi-nozzle configurations can be determined
as follows:

### 4.4.1  Region A-  Free Jet Flow

The free jet flow behavior can be obtained directly from
the methods given in Section 4.2.1 with allowance for coalescing
jets made on the basis of methods given in Section 4.3.1.

### 4.4.2  Region B-  Ground Impingement Flow

The ground impingement flow field characteristics, as affected
by crosswinds can be directly obtained from the design procedures
given in Section 4.3.2 for a multi-nozzle configuration, provided
that all flow profiles are referred to the centerline of the
curved jet defined by $(\theta_c)$ given by equation (136).

### 4.4.3  Region C-  Wall Jet Flow

The effect of crosswinds on the flow characteristics within
the wall jet flow can be obtained by using the design procedures
given in Section 4.2.3. If appropriate, the equivalent jet
diameter $(D_{je})$ can be obtained from Section 4.3.3.

### 4.4.4  Region D-  Recirculation Flow

The effect of crosswinds on the flow characteristics in the
recirculation region is obtained in a manner similar to that for
a single-nozzle (Section 4.2.4) with the following modifications:

(a)  When the crosswind velocity is not along an interaction
plane, use the design procedures given in Section 4.2.4.

(b)  When the crosswind velocity lies along an interaction
plane, the design procedures given in Section 4.2.4
are followed with the exception that equation (144) is
replaced by :

$$H_b \approx R_b \qquad (159)$$

134

## 4.4.5  Region E-  Intake Flow

(a)  Determine the mean inlet total temperature rise (ITR) for top-inlets of multi-nozzle configurations as follows:

(i)  From the methods given in Section 4.3.2 step (b), determine if the hot gas fountain is present.

(ii)  If no fountain exists, use the design procedure given in Section 4.2.5 step (a) to obtain a typical value of ITR.

(iii)  If the fountain is present determine a typical value of ITR from interpolation of graphical data (Figures 44 and 45) given in Section 3.2.3.2.1, if appropriate.  Then using equations (154) and (155) given in Section 4.3.5 step (a) (iii) calculate the corrected value of ITR.

(b)  Determine the mean inlet total temperature rise (ITR) for side-inlets of multi-nozzle configurations as follows:

(i)  Repeat step (a) (i) above

(ii)  If no fountain exists, use Figure 30 to obtain a typical ITR value.  Then using equations (154) and (155) given in Section 4.3.5 step (a) (iii) calculate the corrected value of ITR.

(iii)  If the fountain is present, obtain a typical estimate of ITR from interpolation of the graphical data (Figures 51 or 52) given in Section 3.2.3.2.2, if appropriate.  Then using equations (154) and (155) given in Section 4.3.5 step (a) (iii) calculate the corrected value  of ITR.

(c)  Having obtained the mean ITR from either step (a) or (b) above, calculate the mean inlet velocity using the design procedures given by Section 4.1.5 step (b).

## 4.4.6  Region F-  Interaction Plane Flow

(a)  When the crosswind vector is along the interaction plane determine the flow characteristics as follows:

(i)  Calculate the upwind separation radius of the flow along the ground, measured from the stagnation point within the interaction plane, as the value of $(R_s)$ obtained on the basis of design procedures given in Section 4.2.3 step (b).

(ii)  Determine the flow characteristics along the ground in the interaction plane by using the design procedures presented in Section 4.2.3 and 4.3.3 in a manner similar to that detailed in Section 4.3.6.

(iii)  Determine the radial flow characteristics by reference to the procedures given in Section 4.3.6 step (b) by using the wall jet characteristics obtained from Section 4.2.3 steps (c) and (d).

(iv)  Obtain the fountain (vertical) flow characteristics by using Section 4.3.6 step (c).

(b)  When the crosswind vector is normal to the interaction plane then this plane will be distorted by the wind and will be displaced from a symmetrical position between the nozzles.  The flow characteristics along the inter- action plane under this condition is assumed to be inde- pendent of normal crosswinds and therefore the design procedures given for no crosswind conditions in Sec- tion 4.3.6 can be utilized.

# SECTION 5

## CONCLUSIONS AND RECOMMENDATIONS

1. Practical engineering methods are presented for predicting velocity and temperature distributions in the vicinity of jet-lift V/STOL aircraft operating in ground proximity. Single-, two- and rectangular four-nozzle configurations are treated by methods which account for variations in engine nozzle pressure ratio, temperature, diameter, height above the ground plane, and crosswinds, however, adequate verification of these methods is not possible until additional test data are obtained.

2. A review of available theoretical studies reveals that, in general, theoretical solutions to describe turbulent flow phenomena are not adequate to provide detailed description of the flow field pertinent to hot gas ingestion. Furthermore, satisfactory solutions for limited elements of the flow field usually require the use of large digital computers.

3. A lack of detailed experimental knowledge on the recirculating flow away from the ground precludes the formulation of adequate definitive methods for predicting the time-varying and spatial temperature distributions across the engine inlets. Mean values of ITR can be obtained on the basis of limited test data.

4. Hot gas ingestion behavior for two primary types of engine intake installation i.e. top and side inlet configurations was considered.

The principal ingestion characteristics for each type of inlet configuration is summarised as follows for typical engine exhaust conditions $((P_{t_j}/P_a) \doteq 1.8, \quad (T_{t_j}) \doteq 1200^{\circ}F)$

For top inlets, in the absence of the hot gas fountain, ingestion due to far-field recirculation is comparatively mild (mean ITR $\leqslant 20^{\circ}F$) and is not strongly affected by either wing geometry, nozzle height, or crosswinds within the range of available experimental measurements. When the fountain effect is present, a severe level of ingestion and inlet temperature distortion may be experienced (mean ITR $\leqslant 150^{\circ}F$) and is sensitive to wing geometry, nozzle height and crosswinds.

Side inlet configurations are prone to the most severe level of ingestion and temperature distortion observed (mean ITR $\leqslant 200^{\circ}F$) which is sensitive to nozzle height and crosswind effects. However, changes in wing and nozzle geometry do not appear to have a critical effect on peak ingestion levels.

5.  For a given nozzle and inlet configuration, hot gas ingestion reaches a peak at particular values of nozzle height and headwind velocity.  The ingestion level generally shows a progressive decline for further increases in either height or velocity until the intakes pass outside the envelope of the recirculating gases.

6.  For top-inlet configurations, ingestion due to near-field recirculation can be alleviated by utilising the airframe geometry (fuselage and wings) to effect a blockage of the direct flow path between the fountain effect and the engine intake.  It is important for the intakes to be as well shielded as possible by large surface areas such as wings.

For side-inlet configurations, it is expected that ingestion can be alleviated by placing the intakes further forward and also higher above the gound plane.

7.  The analytical methods developed in the report can be used as a basis for preliminary design optimization of a general V/STOL configuration.  However, it appears essential that additional large-scale test data is required in order to accurately determine the hot gas ingestion characteristics that may be encountered under all practical operating conditions.

8.  It is strongly recommended that further experimental research be conducted to provide more complete information on the degree of correlation of small scale and full scale tests.  In particular it is considered essential that tests be conducted to determine the form of suitable parameters to correlate inlet temperature rise and to augment and modify if required the engineering methods presented in this report.

9.  Also, detailed experimental studies should be conducted to provide more satisfactory methods for predicting the growth and decay of the velocity and temperature distributions in the hot gas fountain between both two- and four-nozzle (rectangular) configurations.  In addition, the threshold limits that denote the onset of the fountain effect should be redefined and extended for more adequate coverage of four-nozzle (rectangular)configurations.

138

# SECTION 6

## REFERENCES

1. Forstall, W., Jr.; and Shapiro, A. H.: Momentum and Mass Transfer in Coaxial Gas Jets. J. Appl. Mech., vol. 17, 1950, pp. 399-408.

2. Halleen, R. M.: A Literature Review of Subsonic Free Turbulent Shear Flow. AFOSR TN 5444, April 1964.

3. Krzywoblocki, M. Z. V.: Jets - Review of Literature. Jet Propulsion, vol. 26, 1956, pp. 760-779.

4. Kuethe, A. M.: Investigations of the Turbulent Mixing Regions Formed by Jets. ASME J. Appl. Mech., vol. 2, no. 3, 1935, pp. A-87 - A-95.

5. Tollmien, Walter: Calculation of Turbulent Expansion Processes. NACA TM 1085.

6. Hinze, J. O.: Turbulence, McGraw-Hill, 1959, pp. 376-447.

7. Warren, W. R.: An Analytical and Experimental Study of Compressible Free Jets. Report No. 381, Aeron. Eng. Lab., Princeton University, 1957.

8. Donaldson, C. duP.; and Gray, K. E.: Theoretical and Experimental Investigation of the Compressible Free Mixing of Two Dissimilar Gases. AIAA J., vol. 4, no. 11, November 1966, pp. 2017-2025.

9. Corrsin, Stanley; and Uberoi, Mahinder S.: Further Experiments on the Flow and Heat Transfer in a Heated Turbulent Air Jet. NACA Report No. 998, 1950.

10. Pai, S. I.: Fluid Dynamics of Jets. D. van Nostrand Company, 1954.

11. Abramowich, G. N.: The Theory of Turbulent Jets. MIT Press, Cambridge, Massachusetts, 1963.

12. Kleinstein, G.: Mixing in Turbulent Axially Symmetric Free Jets. J. Spacecraft, vol. 1, no. 4, July 1964, pp. 403-408.

13. Tomich, John F.; and Weger, Eric: Some New Results on Momentum and Heat Transfer in Compressible Turbulent Free Jets. Am. Inst. Chem. Eng. J., vol. 13, no. 5, September 1967, pp. 948-954.

14. Cook, E. B.; and Singer, J. M.: Predicted Air Entrainment by Subsonic, Free Round Jets. J. Spacecraft, vol. 6, no. 9, September 1969, pp. 1066-1070.

15. Love, Eugene S.; Grigsby, Carl E.; Lee, Louise P.; and Woodling, Mildred J.: Experimental and Theoretical Studies of Axisymmetric Free Jets. NASA TR R-6, 1959.

16. Gibbings, J. C.: Flow in a Supersonic Jet Expanding From a Convergent Nozzle. FM.3968, British A.R.C. no. 30371, September 1968.

17. Snedeker, R. S.; and Donaldson, C. DuP.: Experiments of Free and Impinging Underexpanded Jets from a Convergent Nozzle. ARAP Report No. 63, Aeron. Research Associates of Princeton, September 1964.

18. Higgins, C. C.; Kelly, D. P.; and Wainwright, T. W.: Exhaust Jet Wake and Thrust Characteristics of Several Nozzles Designed for VTOL Downwash Suppression. NASA CR-373, 1966.

19. Laurence, James C.: Intensity, Scale, and Spectra of Turbulence in Mixing Region of Free Subsonic Jet. NACA Report No. 1292, 1956.

20. Higgins, C. C.; and Wainwright, T. W.: Dynamic Pressure and Thrust Characteristics of Cold Jets Discharging From Several Exhaust Nozzles Designed for VTOL Downwash Suppression. NASA TN D-2263, April 1964.

21. Jordinson, R.: Flow in a Jet Directed Normal to the Wind. R & M No. 3074, British A.R.C., 1958

22. Analysis of a Jet in a Subsonic Crosswind. NASA SP-218, Proceedings of a Symposium at NASA, Langley, September 9-10, 1969.

23. Chang-Lu, Hsiu-Chen: Aufrollung Eines Zylindrischen Strahles Durch Querwind (Rollup of a Cylindrical Jet In a Crosswind). Doctorial Dissertation, Univ. of Gottingen, 1942.

24. Monical, R. E.: A Method of Representing Fan-Wing Combinations for Three Dimensional Potential Flow Solutions. AIAA Paper 65-85, January 1965. (Also published in J. Aircraft, vol. 2, no. 6, November - December 1965, pp. 527-530).

25.  Wooler, P. T.; Burghart, G. H.: and Gallagher, J. T.: The Pressure Distribution on a Rectangular Wing with a Jet Exhausting Normally into an Airstream. AIAA Paper 67-1, January 1967. (Also published in J. Aircraft, vol. 4, no. 6, November - December 1967, pp. 537-543).

26.  Wooler, P. T.:  On the Flow Past a Circular Jet Exhausting at Right Angles From a Flat Plate or Wing. J. Roy. Aeron. Soc., vol. 71, March 1967, pp. 216-218.

27.  Wu, J. C.; McMahon, H. M.; Mosher, D. K.; and Wright, M. A.:  Experimental and Analytical Investigations of Jets Exhausting into a Deflecting Stream. J. Aircraft, vol. 7, no. 1, March-April 1969, pp. 44-51.

28.  Lu, H. C.:  On The Surface of Discontinuity Between Two Flows Perpendicular to Each Other. Eng. Report No. 4, National Tsing Hua University, October 1948.

29.  Vizel, Y. M.; and Mostinskii, I. L.:  Deflection of a Jet Injected into a Stream. J. Eng. Phys., vol. 8, no. 2, February 1965, pp. 238-242.

30.  Shandorov, G. S.:  Calculation of a Jet Axis in a Drifting Flow. NASA TT F-10,638, 1966.

31.  Wooler, P. T.:  Flow of a Circular Jet into a Cross Flow. J. Aircraft, vol. 6, no. 3, May-June 1969, pp. 283-284.

32.  Crowe, C. T.; and Riesebieter, H.:  An Analytical and Experimental Study of Jet Deflection in a Cross Flow. Paper presented at AGARD meeting on Fluid Dynamics of Rotor and Fan-Supported Aircraft at Subsonic Speed, Paris, France, 1967.

33.  Keffer, J. F.; and Baines, W. D.:  The Round Turbulent Jet in a Cross-Wind. J. Fluid Mech., vol. 15, 1963, pp. 481-496.

34.  Braun, Gerhard W.; and McAllister, Jack D.:  Cross Wind Effects on Trajectory and Cross Sections of Turbulent Jets. NASA SP-218, September 1969, pp. 141-164.

35.  LeClerc, A.:  Deflection of a Liquid Jet by a Perpendicular Boundary. M. S. Thesis, State University of Iowa, 1948.

36. Schach, W.: Umlenking eines Kreisformigen Flussigkeits-
    strahles an einer ebenen Platte Senkrecht zur Stromungs-
    richtung, (Deflection of a Circular Fluid Jet by a Flat
    Plate Perpendicular to the Flow Direction), Ingenieur-
    Archiv, vol. VI, 1935, pp. 51-59.

37. Shen, Y. C.: Theoretical Analysis of Jet-Ground Plane
    Interaction. IAS Paper 62-144, June 1962.

38. Strand, T.: On the Theory of Normal Ground Impingement
    of Axi-Symmetric Jets in Inviscid Incompressible Flow.
    AIAA Paper 64-424, June-July, 1964.

39. Vidal, Robert J.: Aerodynamic Processes in the Downwash
    Impingement Problem. IAS Paper 62-36, January 1962.

40. Brady, W. Gordon; and Ludwig, Gary R.: Theoretical and
    Experimental Studies of Impinging Uniform Jets. IAS
    Paper 63-29, January 1963.

41. Brady, W. Gordon; and Ludwig, Gary R.; Theoretical and
    Experimental Studies of Impinging Uniform Jets.
    TRECOM TR 63-11, April 1963.

42. Ludwig, Gary R.; and Brady, W. Gordon: Theoretical and
    Experimental Studies of Impinging Uniform and Non-
    Uniform Jets. TRECOM TR 64-42, August 1964.

43. Tani, I.; and Komatsu, Y.: Impingement of a Round Jet
    on a Flat Surface. Proceedings of the Eleventh
    International Congress of Applied Mechanics (Munich,
    Germany), 1964, pp. 672-676.

44. Barnes, D. A.; and Sullivan, R. D.: Rotational Solutions
    of the Euler Equations. ARAP Report No. 79, Aeron.
    Research Associates of Princeton, September 1965.

45. Schlichting, H.: Boundary Layer Theory. McGraw-Hill,
    1968.

46. Donaldson, C. DuP.: A Brief Review of Research on the
    Impingement of Axially Symmetric Free Jets. AFOSR
    66-1943, Department of Aeron. Eng., University of
    Maryland, September 1966, pp. 74-110. (Available from
    DDC as AD 641 434).

47. Smith, A.M.O.: Rapid Laminar Boundary Layer Calculations
    by Piecewise Application of Similar Solutions. J. Aeron.
    Sci., vol. 23, no. 10, October 1956.

142

48. Dunkelberg, Stephen B.; Fagan, Ralph T.; and Giss, Warren A.: Exhaust Gas Flow Field from the Deflection of Twin Jets. J. Aircraft, vol. 4, no. 4, July-August 1967, pp. 278-283.

49. Strand, T.: Inviscid-Incompressible-Flow Theory of Normal and Slightly Oblique Impingement of a Static Round Jet on the Ground. J. Aircraft, vol. 4, no. 5, September - October 1967, pp. 466-472.

50. Unitt, P. J.: A Comprehensive Review of V/STOL Downwash Impingement with Emphasis on Wind Induced Recirculation. GAM/AE/69-9, March 1969.

51. Glauert, M. B.: The Wall Jet. J. Fluid Mech., vol. 1, December 1956, pp. 625-643.

52. Rajaratnam, N.; and Subramanya, K.: An Annotated Bibliography on Wall Jets. Department of Civil Eng., Univ. of Alberta (Edmonton, Canada), July 1967.

53. Dawson, D. A.; and Trass, O.: Mass Transfer in a Turbulent Radial Wall Jet. Can. J. Chem. Eng., June 1966, pp. 121-129.

54. Poreh, M.; Tsuei, Y. G.; and Cermak, J. E.: Investigation of a Turbulent Radial Wall Jet. ASME Paper 67-APM-10, J. Appl. Mech., June 1967, pp. 457-463.

55. Abbott, W. A.: Studies of Flow Fields Created by Vertical and Inclined Jets When Stationary or Moving Over a Horizontal Surface. Paper CP-911, British A.R.C., October 1964.

56. Cox, M.; and Abbott, W. A.: Studies of the Flow Fields Created by Single Vertical Jets Directed Downwards Upon a Horizontal Surface. Paper CP-912, British A.R.C., October 1964.

57. Bakke, P.: An Experimental Investigation of a Wall Jet. J. Fluid Mech., vol. 2, pt. 5, 1957, pp. 467-472.

58. Bradshaw, P.; and Gee, M. T.: Turbulent Wall Jets With and Without an External Stream. R & M No. 3252, British A.R.C.; 1960.

59. Kruka, K.; and Eskinazi, S.:  The Wall Jet in a Moving
    Stream.  J. Fluid Mech., vol. 20, pt. 4, 1964, pp. 555-579.

60. Snedeker, R. S.; and Donaldson, C. DuP.:  Experiments on
    the Oblique Impingement of Underexpanded Jets on a Flat
    Plate.  ARAP Report No. 64, Aeron. Research Associates
    of Princeton, April 1965.

61. Hess, John L.; and Smith, A.M.O.:  A General Method
    for Calculating Low Speed Flow about Inlets.
    Aerodynamics of Power Plant Installation.  AGARDograph
    103, pt. 1, 1965, pp. 345-372.

62. Stockman, Norbert O.; and Lieblain, Seymour:  Theoretical
    Analysis of Flow in VTOL Lift Fan Inlets Without
    Crossflow.  NASA TN D-5065, 1969.

63. Stockman, Norbert O.:  Potential Flow Solutions for Inlets
    of VTOL Lift Fans and Engines.  Analytic Methods
    in Aircraft Aerodynamics.  NASA SP-228, October 1969,
    pp. 659-682.

64. Alexander, L. G.; Baron, T.; and Comings, E. W.:  Transport
    of Momentum, Mass, and Heat in Turbulent Jets.  Bulletin
    Ser. No. 413, Eng. Experiment Station, University of
    Illinois, May 1953.

65. Hall, Gordon R.; and Rogers, Kenneth H.:  Recirculation
    effects Produced by a Pair of Heated Jets Impinging
    on a Ground Plane.  NASA CR-1307, May 1969.

66. Hertel, H.; and Harmsen, S.:  Wandstromungen und Aufstrome
    aus der Umlenkung von Freistrahlgruppen.  Fortsschritt
    Berichte VDI Zeitschrift, vol. 12, no. 11, July 1966.

67. Skifstad, J. G.:  Aerodynamics of Jets Pertinent to VTOL
    Aircraft.  AFAPL-TR-69-28, March 1969.  (Available
    from DDC as AD 853494).

68. George, M.; Kisielowski, E.; and Douglas, D. S.: Investi-
    gation of the Downwash Environment Generated by V/STOL
    Aircraft Operating in Ground Effect.  USAAVLABS TR 68-
    52, July 1968.  (Available from DDC as AD 674 644).

69. Chao, J. L.; and Sandborn, V. A.:  Evaluation of the
    Momentum Equation for a Turbulent Wall Jet.  J. Fluid
    Mech., vol. 26, pt. 4, 1966, pp. 819-828.

144

70. Anderson, A. R.; and Johns, F. R.: Characteristics of Free Supersonic Jets Exhausting into Quiescent Air. Jet Propulsion, vol. 25, 1955, pp. 13-15.

71. Hall, Gordon R.: Recirculation and Ingestion Characteristics of a Large-Scale VTOL Lift Engine Pod. NASA CR-72410, August 1968.

72. Ryan, Patrick E.; and Cosgrove, Wayne J.: Empirically Determined Wind and Scale Effects on Hot Gas Recirculation Characteristics of Jet V/STOL Aircraft. NASA CR-1445, October 1969. (Also available as Report No. 2099-956005, Bell Aerosystems Co., January 1969).

73. Ryan, Patrick E.; and Cosgrove, Wayne J.: The Effect of Exhaust Conditions, Surface Winds, and Geometric Scale on Hot Gas Ingestion for Two Jet VTOL Configurations. NASA CR-66965, 1970.

74. Adarkar, D. B.; and Hall, Gordon R.: The "Fountain Effect" and VTOL Exhaust Ingestion. AIAA Paper 68-79, January 1968. (Also published in J. Aircraft, vol. 6, no. 2., March - April 1969, pp. 109-115).

75. Fearon, J. R. C.; and Norman, D. H.: VTOL and STOL: Simple Solutions to Some of the Operating Problems During Take-Off and Landing, J. Royal Aeronautical Society, vol. 66, February 1962, pp. 67-76.

76. Speth, R. F.; and Ryan P. E.: A Generalized Experimental Study of Inlet Temperature Rise and Near Field Temperature Contours of Jet V/STOL Aircraft in Ground Proximity. AIAA Paper 66-740, September 1966.

77. Hammond, A. D.; and McLemore H. Clyde: Hot Gas Ingestion and Jet Interference Effects for Jet V/STOL Aircraft. NASA TM-X-60449, Presented At AGARD Flight Mechanics Panel Meeting, Gottingen, West Germany, September 1967.

78. Ryan, Patrick, E.; Heim, Richard J.; and Cosgrove, Wayne, J.: A Generalized Experimental Investigation of Hot Gas Recirculation and Ingestion for Jet VTOL Aircraft. NASA CR-1147, September 1968. (Also available as Report No. 2099-956003, Bell Aerosystems Co., 1968).

79. McLemore, H. Clyde; and Smith, Charles, C., Jr.: Hot-Gas Ingestion Investigation of Large-Scale Jet VTOL Fighter-Type Models. NASA TN D-4609, June 1968.

80. McLemore, H. Clyde; Smith, Charles C., Jr.; and Hemeter, Patricia G.: Generalized Hot Gas Ingestion Investigation of Large-Scale Jet VTOL Fighter-Type Models. NASA TN D-5581, January 1970.

81. Lavi, Rahim: Parametric Investigation of VTOL Hot Gas Ingestion and Induced Jet Effects in Ground Proximity. Report NOR 67-32, Northrop Corporation, February 1967. (Available from DDC as AD 809 224).

## APPENDIX

## DERIVATION OF THE FREE-JET REFERENCE FLOW BOUNDARIES

This appendix summarizes the derivation of methods used to predict the pressure and temperature reference boundaries in the free-jet flow field ($R_e$gion A) for a single engine in a static ambient environment.

An expression for the pressure reference boundary in the characteristic decay region may be obtained from the relationships developed for the jet profile and centerline decay behavior (equations (20) and (23)) by applying a momentum-integral analysis, with approximate allowance for compressibility effects, as follows.

For a free jet with the assumption of ambient static pressure throughout the flow, the axial jet momentum M(s) at any downstream reference location is given by

$$M_{(s)} = 2\pi \int_0^\infty r \rho u^2 \cdot dr \tag{160}$$

Substituting $(\bar{r}) = (r/r_j)$, $(q) = \frac{1}{2}\rho u^2$ equation (160) becomes

$$M_{(s)} = 4\pi (r_j)^2 \int_0^\infty \bar{r} \cdot q \; d\bar{r} \tag{161}$$

In the characteristic decay region, velocities are generally sufficiently small to justify use of the incompressible Bernoulli relation given by:

$$q = (P_t - P) = \Delta P_t \tag{162}$$

Substituting equation (23) and (162) into equation (161) there follows:

$$M_{(s)} = \frac{\pi \cdot (r_p)^2 \cdot \Delta P_{tc}}{\ln 2} \tag{163}$$

At the nozzle exit the jet momentum can be defined as

$$M_{(j)} = \frac{\pi}{2} \cdot (D_j)^2 \cdot q_j \cdot C_D \tag{164}$$

By using the principle that axial momentum is conserved throughout the flow, equations (163) and (164) are combined to yield:

$$\bar{r}_p = \left(\frac{r_p}{r_j}\right) = \left[2 \cdot \ln 2 \cdot C_D \cdot \left(\frac{q_j}{\Delta P_{tc}}\right)\right]^{1/2} \tag{165}$$

Rearranging equation (165) yields:

$$\overline{r}_p = \left[ \frac{2 \cdot \ell_n 2 \cdot C_D}{\Delta \overline{P}_{tc}} \left( \frac{q_j}{\Delta P_{tj}} \right) \right]^{1/2} \qquad (166)$$

Substituting for $(\Delta \overline{P}_{tc})$ from equation (20) gives:

$$\overline{r}_p = \left( C_D \right)^{-0.06} \cdot \left[ 2 \cdot \ell_n 2 \cdot \left( \frac{q_j}{\Delta P_{tj}} \right) \right]^{1/2} \cdot \left[ \left( \frac{P_{tj}}{P_a} \right)^{-0.07} \left( \frac{T_{tj}}{T_a} \right)^{0.25} \frac{\overline{s}}{K_n} \right]^{1.12} \qquad (167)$$

The term in $(C_D)$ can be sensibly neglected since its exponent is small.

Equation (166) is further simplified by using the substitution

$$\left( \frac{q_j}{\Delta P_{tj}} \right) \quad \underline{\quad} \quad \left( \frac{P_{tj}}{P_a} \right)^{-0.36} \qquad (168)$$

which is an approximation derived from compressible flow theory to represent compressibility effects at the nozzle exit. Using equation (168) in equation (167) thus

$$\overline{r}_p = 0.109 \left[ \left( \frac{P_{tj}}{P_a} \right)^{-0.23} \cdot \left( \frac{T_{tj}}{T_a} \right)^{0.25} \cdot \frac{\overline{s}}{K_n} \right]^{1.12} \qquad (169)$$

Comparison between equation (169) and experimental data from References 9 and 18 is presented in Figure 54. The good agreement suggests that the axial correlation function $(S_3)$ given by

$$S_3 = \left( \frac{P_{tj}}{P_a} \right)^{-0.23} \cdot \left( \frac{T_{tj}}{T_a} \right)^{0.25} \cdot \frac{\overline{s}}{K_n} \qquad (170)$$

is also suitable for correlating the pressure reference boundary in the transition and annular mixing regions, where simple analytical representations could not be obtained. While it is necessary to fair in a curve for the transition region, the behavior in the annular mixing region can be adequately represented by substituting the axial correlation parameter $(S_3)$ for $(\overline{s})$ in the empirical equation derived by Ludwig and Brady (Reference 41) for an isothermal incompressible jet, thus:

$$\overline{r}_p = 1.057 + 0.0285 \left( S_3 \right) \qquad (171)$$

Figure 55 shows good agreement between equation (171) and test data from References 17, 18, and 20.

148

Relatively simple integral techniques could not be applied to predict the jet temperature reference boundaries. Therefore, a resort to empirical methods was made. With the assumption that the general form of the empirical representation is similar to that for the jet pressure boundary growth (Equation (169)) the test data of References 7, 9, 13, and 18 were used to develop the following relationship

$$\overline{\tau_t} = 0.141 \left[ \left(\frac{P_{tj}}{P_a}\right)^{0.43} \cdot \left(\frac{T_{tj}}{T_a}\right)^{0.25} \cdot \overline{s} \right]^{1.12}$$  (172)

for the characteristic decay region. Data from References 9 and 18 are compared with equation (171) in Figure 56. The good agreement indicates that the correlation function ($S_4$), given by

$$S_4 = \left(\frac{P_{tj}}{P_a}\right)^{0.43} \cdot \left(\frac{T_{tj}}{T_a}\right)^{0.25} \cdot \overline{s}$$  (173)

is suitable for correlating the temperature reference boundary in all regions of the free jet. ·While a faired curve must be used in the transition region, Figure 57 shows that the value of ($\overline{\tau_t}$) in the annular mixing zone can be represented by substituting ($S_4$) for ($S_3$) in equation (171), thus:

$$\overline{\tau_t} = 1.057 + 0.0285 \left(S_4\right)$$  (174)
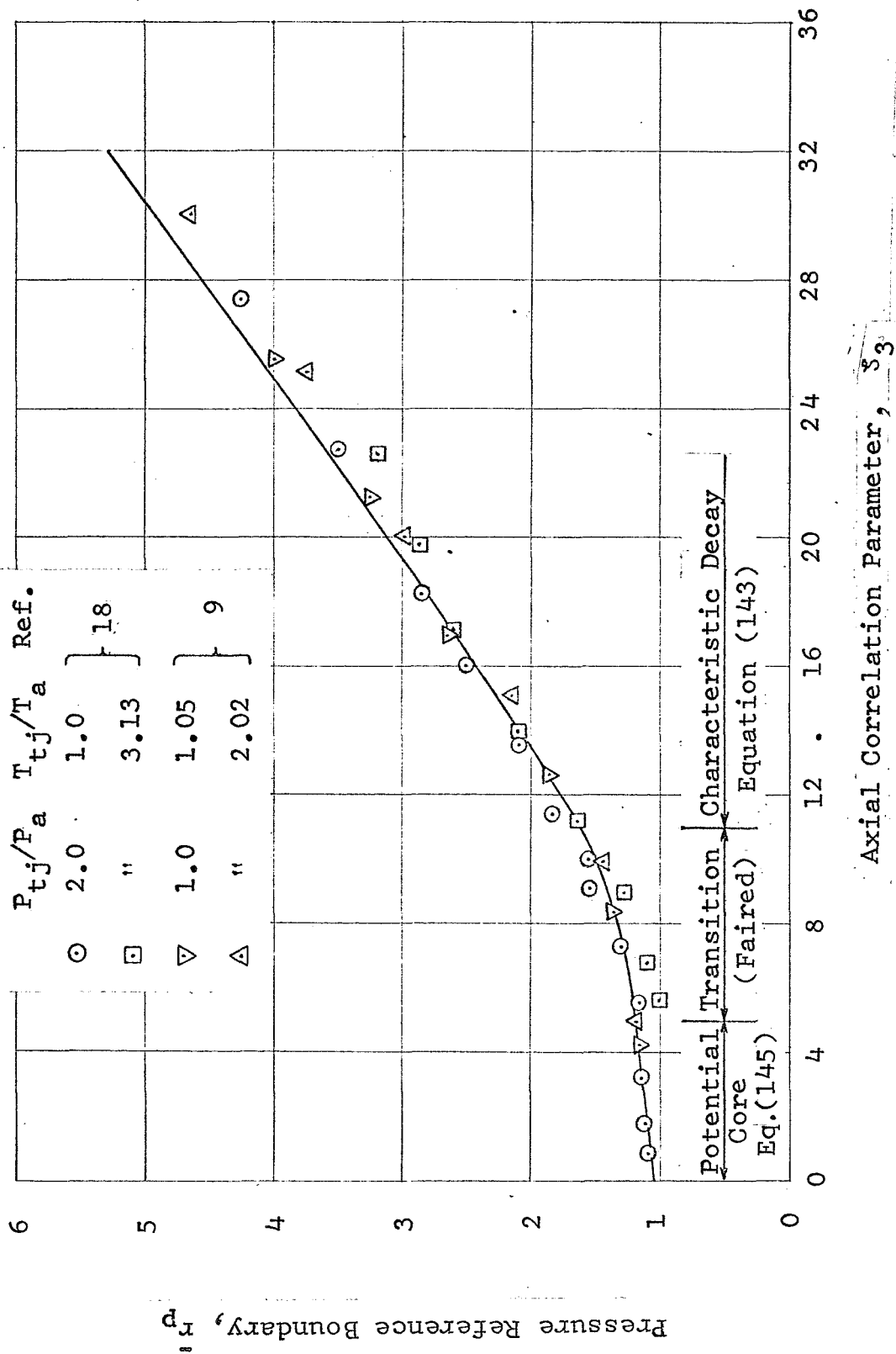
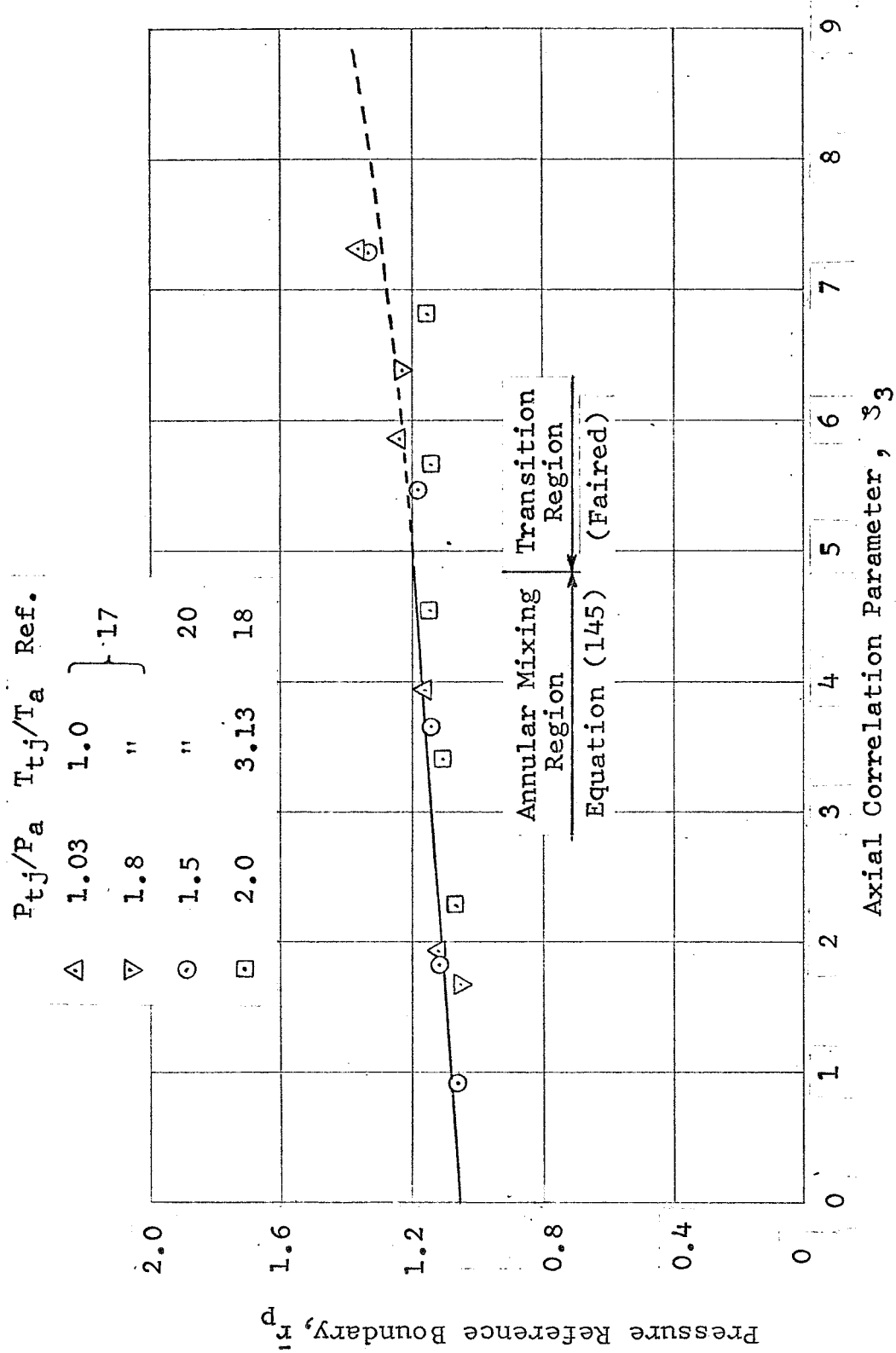Figure 54.– Correlation of Pressure Reference Boundary Growth For Free Jets.

150

Figure 55.— Correlation of Pressure Reference Boundary Growth in the Annular Mixing Region of Free Jets.
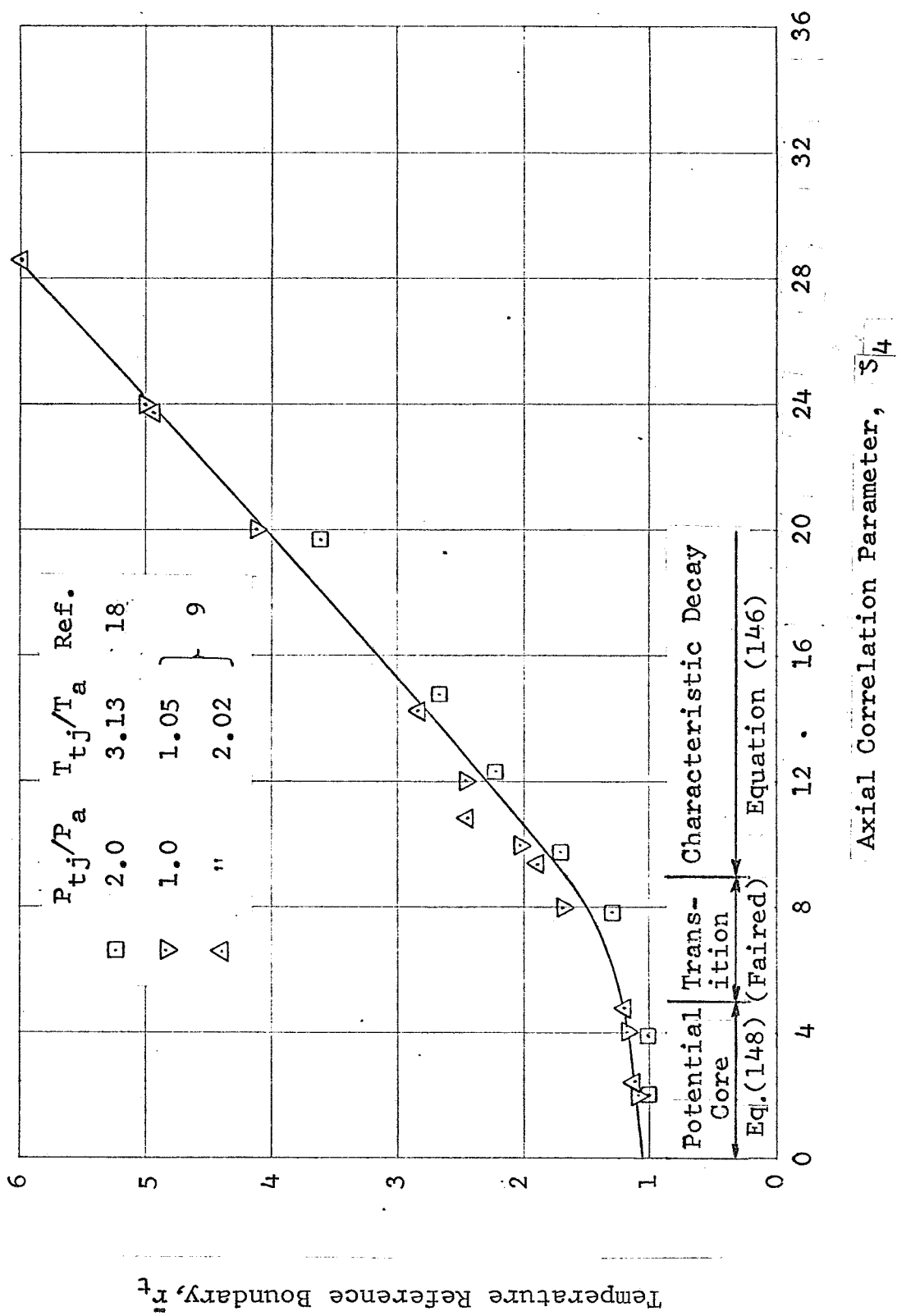
Figure 56.—Correlation of Temperature Reference Boundary Growth for Free Jets.

152
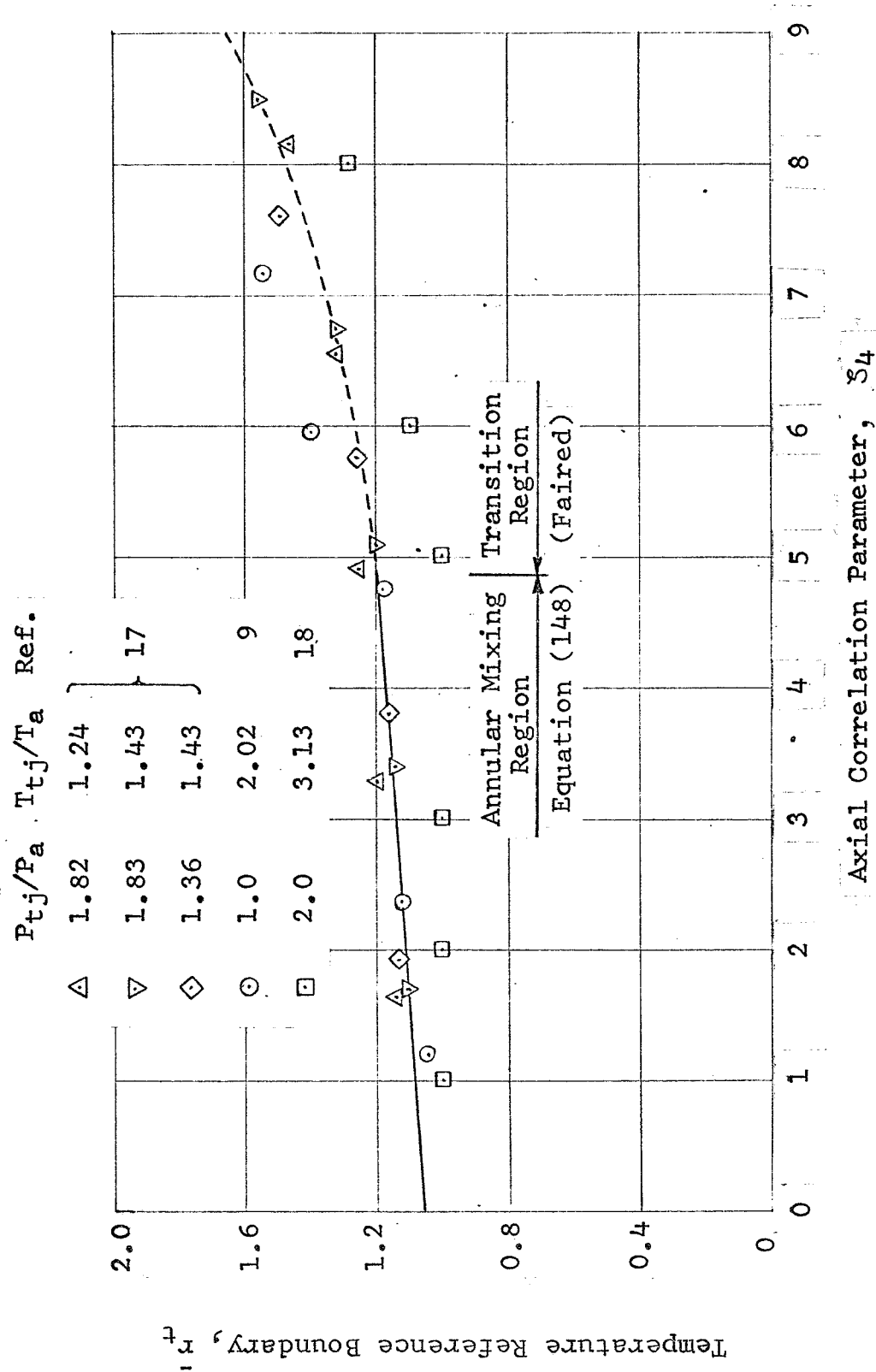
Figure 57.— Correlation of Temperature Reference Boundary Growth in the Annular Mixing Region of Free Jets.

153

# SELECTED BIBLIOGRAPHY

The following references supplement those cited in the main text and provide a more comprehensive background to the study of hot gas ingestion phenomena. This selection includes technical literature reviews and reports on theoretical and experimental investigations into various phenomena related to hot gas ingestion. While a few of these reports are outside the specific scope of the present investigation, these and many others are valuable for their general qualitative conclusions. For convenience, the following references are arranged in alphabetical order by author.

Arbuckle, J. A.:  Investigation of Density Effects on Entrainment by Impinging Jets.  Thesis No. 18/14, Cranfield College of Aeronautics, 1965.

Barrack, Jerry P.; and Kirk, Jerry V.:  Low-Speed Characteristics of High-Performance Lift-Engine V/STOL Aircraft.  (Preprint) 680644, Soc. Automotive Engrs., October 1968.

Bradshaw, P.; and Love, E.M.:  The Normal Impingement of a Circular Air Jet on a Flat Surface.  R & M No. 3205 British A.R.C., September 1959.

Colin, Paul E.:  Ground Proximity and the VTOL Aircraft, AGARD Report No. 409, 1962.

Garner, Jack E.:  A Review of Jet Efflux Studies Applicable to V/STOL Aircraft.  Report No. TR-67-163, Arnold Eng. Development Center, September 1967.

Gedney, Richard T.; and Siegel, Robert:  Inviscid Flow Analysis of Two Parallel Slot Jets Impinging Normally on a Surface.  NASA TN D-4957.  December 1968.

Gelb, G. H.; and Martin, W. A.:  An Experimental Investigation of the Flow Field About a Subsonic Jet Exhausting into a Quiescent and a Low Velocity Airstream. AIAA Paper 65-704, October 1965.

Gittner, U.; Hoffert F.; and Lotz, M.: Interaction Between Airframe-Powerplant Integration and Hot Gas Ingestion for Jet-Lift V/STOL Transport Aircraft. Presented to AGARD 31st Flight Mechanics Panel Meeting on Integration of Propulsion System in Airframe, Friedrichshafen, Germany, September 13-15, 1967.

Goldstein, Marvin E.; and Siegel, Robert: Two Dimensional Inviscid Jet Flow From Two Nozzles at an Angle to a Plane Surface. NASA TN D-5064. February 1969.

Harris, A. E.; Marbert, J. A.; and Tatom, J. W.: VTOL Transport Exhaust Gas Ingestion Model Tests. Paper 67-ENV-17, Seventh Annual National Conference on Environmental Effects on Aircraft and Propulsion Systems, Princeton, New Jersey, September 1967.

Kemp, E. D. G.: Studies of Exhaust Gas Recirculation for VTOL Aircraft. AIAA paper 67-439, July 1967. (Also published in J. Aircraft, vol. 6, no. 2, March-April 1969, pp. 102-108).

Kirk, Jerry V.; and Barrack, Jerry P.: Reingestion Characteristics and Inlet Flow Distortion of V/STOL Lift Engine Fighter Configurations. AIAA Paper 68-78, January 1968. (Also published in J. Aircraft, vol. 6, no. 2, March - April 1969, pp. 116-122).

Kuhn, Richard E.: An Investigation to Determine Conditions Under Which Downwash From VTOL Aircraft Will Start Surface Erosion From Various Types of Terrains. NASA TN D-56, September 1959.

Langfelder: Bodeneffekte bei Senkrechtstart-Flugzeugen. (Ground Effects of VTOL Aircraft). EWR-Nr. 37/62, Entwick lungsring Süd, München, Germany, March 1963.

Lavi, Rahim: Parametric Investigation of VTOL Ground Proximity Effects. AIAA Paper 67-440, July 1967.

Lavi, Rahim; Hall, Gordon R.; and Stark, Wilbur W.: Full-Scale Ground Proximity Investigation of a VTOL Fighter Model Aircraft. NASA CR-1098, July 1968.

Lee, C. C. : A Review of Research on the Interaction of a Jet With an External Stream. Technical Note R-184, Brown Eng. Co. Inc., March 1966. (Available from DDC as AD 630 294).

Margason, Richard J.: The Path of a Jet Directed at Large Angles to a Subsonic Free Stream. NASA TN D-4919, November 1968.

McKinney, M. O., Jr.; Kuhn, R. E.; and Reeder, J. P.: Aerodynamics and Flying Qualities of Jet V/STOL Airplanes. ASME Paper 64-SAE-864A, April 27-30, 1964.

McLemore, H. Clyde: Considerations of Hot-Gas Ingestion for Jet V/STOL Aircraft. Conference on V/STOL and STOL Aircraft, NASA SP-116, April 1966, pp. 191-204.

Mohne, E. A.: V/STOL Exhaust Gas Ingestion Test Hovering Test Facility. Report No. NA 64-1142, North Am. Aviation, Inc., March 1964.

Newman, B. G.: The Prediction of Turbulent Jets and Wall Jets. Can. Aeron. Space J.; vol. 15, no. 8, October 1969, pp. 288-305.

O'Malley, J. A., Jr.: Flow Phenomena Experienced with VTOL Aircraft in Ground Proximity. AGARDograph 46, pt. II, June 1960, pp. 371-408.

Poreh, M.; and Tsuei, Y. G.: Self-Similarity in Turbulent Radial Jets and Radial Wall Jet. Israel Journal of Technology, vol. 3, no. 1, 1965, pp. 454-460.

Rogers, K. H.; Lavi, R.; and Hall, G. R.: Experimental Investigations of Ground-Jet Suppression Fences for VTOL Aircraft Prepared Sites. J. Aircraft, vol. 6, no. 3, May-June 1969, pp. 245-251.

Rolls, L. Stewart: Operational Experiences with the X-14A Deflected-Jet VTOL Aircraft. Conference on Aircraft Operating Problems, NASA SP-83, 1965, pp. 299-307.

Ryan, P. E.; and Speth, R. F.: Model Tests and Analysis of the Temperature Environment Induced by Jet V/STOL Aircraft Operating Near the Ground. Report No. 2099-928004, Bell Aerosystems Co., May 1966.

Ryan, Patrick E.; and Cosgrove, Wayne J.: The Effect of Exhaust Pressure Ratio, Exhaust Gas Temperature and Wind Velocity on the Inlet Temperature Rise of a Small Scale Jet VTOL Model. Report No. 2099-956006, (Contract NAS 1-9584), Bell Aerosystems Co., February 1970.

156

Schwantes, E.:  Survey of the Ground Effect of V/STOL
    Aircrafts With Jet Propulsion - Report of Literature.
    NASA TT F-12573, October 1969.

Searle, N.:  Entrainment by Axisymmetric Jets Imping-
    ing on a Flat Plate.  Thesis No. 17/7, Cranfield
    College of Aeronautics, 1964.

Sherman, E. W., Jr.:  Studies of VTOL Inlet Temperature
    Rise and Lift-Thrust.  ASME Paper 64-SAE-860E, April
    27-30, 1964.

Shumpert, P. K.; and Tibbetts, J. G.:  Model Tests Of
    Jet-Induced Lift Effects on a VTOL Aircraft in Hover.
    NASA CR-1297, March 1969.

Siegel, Robert; and Goldstein, Marvin E.:  Analysis of
    Two Dimensional Inviscid Model of Jet Impingement
    Under Vertical-Takeoff Airplane.  NASA TN D-5288,
    June 1969.

Sinacori, J. B.; and Mehus T. E.:  Report of Experiments
    Conducted to Determine Possible Scaling Laws for Model
    Hot Gas Reingestion Tests of Jet VTOL Aircraft in Close
    Proximity to the Ground.  Report NOR 66-127, Northrop
    Corp., March 1966.

Skifstad, J. G.:  Aerodynamics of Jets Pertinent to VTOL
    Aircraft.  J. Aircraft, vol. 7, no. 3, May - June 1970,
    pp. 193-204.

Smith, Fred:  CL 757 Flight Test Results.  Report No.
    LR 18781, (Contract AF 33(657)-10534), Lockheed-
    California Co., April 1965.

Speth, R. F.; and Ryan, P. E.:  A Generalized Experi-
    mental study of Inlet Temperature Rise of Jet V/STOL
    Aircraft in Ground Effect, Report No. 2099-928003,
    (Contract N600(19)-63320), Bell Aerosystems Co.,
    March 1966.  (Available from DDC as AD 641 610).

Spooner, S. H.:  The V/STOL Aircraft Environment, ASME
    Paper 68-GT-40, March 1968.

Stark, Wilbur W. et al:  Results of a Hot-Gas Ingestion
    and Jet Effects Test Program with a Large-Scale VTOL
    Test Vehicle in Ground Proximity.  Report NOR 66-246,
    Northrop Corp., November 1966.

Taylor, G.: Flow Induced by Jets. J. Aeron. Sciences, vol. 25, no. 7, July 1958, pp. 464-465.

Tolhurst, William H., Jr.; and Kelly, Mark W.: Characteristics of Two Large-Scale Jet-Lift Propulsion Systems. Conference on V/STOL And STOL Aircraft, NASA SP-116, April 1966, pp. 205-228.

Watson, W. W.; Lavi, R.; and Asdurian, H.: A Large Scale Test Vehicle for VTOL Ground Effect Studies. AIAA Paper 67-181, January 1967. (Also published in J. Aircraft, vol. 4, no. 6, November - December 1967).

Zegaroski, B. A.: Data Report for VTOL Inlet Temperature Rise and Lift Thrust Test Program. Report No. 2099-928001, Bell Aerosystems Co.. October 1963.

Zegaroski, B. A.: A Generalized Experimental Study of Inlet Temperature Rise and Lift-Thrust of Jet VTOL Aircraft in GroundEffect, Report No. 2099-928002, (Contract N600(19)-58526, Bell Aerosystems Co.. September 1964.

NASA CR-111845

DISTRIBUTION LIST
NAS1-9465

|  | No. Copies |
|---|---|
| NASA Langley Research Center | |
| Hampton, Va.   23365 | |
| Attention:   Program Reports & Analysis Unit, Mail Stop 122 | 1 |
| Raymond L. Zavasky, Mail Stop 110 | 1 |
| H. Clyde McLemore, Mail Stop 355 | 8 |
| Richard J. Margason, Mail Stop 404 | 3 |
| | |
| NASA Ames Research Center | |
| Moffett Field, CA   94035 | |
| Attention:  Library, Mail Stop 202-3 | 1 |
| Jerry P. Barrack, Mail Stop 221-2 | 3 |
| | |
| NASA Flight Research Center | |
| P. O. Box 273 | |
| Edwards, CA   93523 | |
| Attention:  Library | 1 |
| | |
| Jet Propulsion Laboratory | |
| 4800 Oak Grove Drive | |
| Pasadena, CA   91103 | |
| Attention:  Library, Mail 111-113 | 1 |
| | |
| NASA Manned Spacecraft Center | |
| 2101 Webster Seabrook Road | |
| Houston, TX   77058 | |
| Attention:  Library, Code BM6 | 1 |
| | |
| NASA Marshall Space Flight Center | |
| Huntsville, AL   35812 | |
| Attention:  Library | 1 |
| | |
| Wallops Station | |
| Wallops Island, VA   23337 | |
| Attention:  Library | 1 |
| | |
| NASA Lewis Research Center | |
| 21000 Brookpark Road | |
| Cleveland, OH   44135 | |
| Attention:  Library, Mail Stop 60-3 | 1 |
| Nestor Clough, Mail Stop 100-1 | 3 |
| | |
| NASA Goddard Space Flight Center | |
| Greenbelt, MD   20771 | |
| Attention:  Library | 1 |

DISTRIBUTION LIST
NAS1-9465

No.
Copies

John F. Kennedy Space Center
Kennedy Space Center, FL    32899
Attention:  Library, Code IS-CAS-42B                                           1

National Aeronautics and Space Administration
Washington, DC    20546
Attention:  Library, Code KSS-10                                             .1
            NASA Code RA                                                       1

Lockheed Aircraft Corporation
Lockheed-Georgia Company
86 South Cobb Drive
Marietta, Ga    30060
Attention:  Anthony E. Harris, Dept. 72-74, Zone 455                           2

Nielsen Engineering & Research, Inc.
3967 East Bayshore
Palo Alto, CA    94303
Attention:  Jack N. Nielsen                                                    1

Vanderbilt University
Department of Mechanical Engineering
Nashville, TN    37203
Attention:  Prof. J. W. Tatom, Box 11, Station B                              1

Northrop Corporation
3901 West Broadway
Hawthorne, CA    90250
Attention:  G. R. Hall, Internal Aero & Propulsive Branch
            Organization 3711-31                                               2

Bell Aerospace Corporation
P. O. Box 1
Buffalo, NY    14240
Attention:  Patrick E. Ryan                                                    3

Headquarters
Wright-Patterson Air Force Base, OH    45433
Attention:  D. Hohler                                                          1
            G. Sealy                                                           1
            Lt. V. K. Smith III                                                1
            C. Westbrook                                                       1

DISTRIBUTION LIST
NAS1-9465

No.
Copies

Department of the Navy
Bureau of Weapons
Washington, DC    20525
Attention:  Robert Brown, RAPPI4                                    1

Department of the Navy
Bureau of Ships
Washington, DC    20360
Attention:  G. L. Graves                                            1

North American Aviation, Inc.
International Airport
Los Angeles, CA    90009
Attention:  Rex Carpenter                                           1
            Gordon Campbell                                         1

Pratt and Whitney Aircraft
400 Main Street
East Hartford, CT    06108
Attention:  W. Sens                                                 1

General Electric Company
1000 Western Avenue
Lynn, MA    01906
Attention:  Klem Gunn                                               1

General Motors Corporation
Allison Division
P. O. Box 894
Indianapolis, IN    46206
Attention:  C. E. Hockert                                           1

The Boeing Company
Commercial Airplane Division
P. O. Box 707
Renton, WA    98055
Attention:  Walter Swann                                            1

The Boeing Company
Vertol Division
Morton, PA    19070
Attention:  Bernard Fry                                             1

McDonnell Douglas Corporation
Box 516
St. Louis, MO    63166
Attention:  Ralph Herzmark                                          1

DISTRIBUTION LIST
NAS1-9465

| | No. Copies |
|---|---|
| Lockheed Aircraft Corporation<br>Lockheed-California<br>Burbank, CA    91503<br>Attention:  Richard Shearer<br>Donald Seager | 1<br>1 |
| McDonnell Douglas Corporation<br>Aircraft Division<br>3855 Lakewood Boulevard<br>Long Beach, CA    90808<br>Attention:  W. J. Skillman | 1 |
| Ryan Aeronautical Company<br>2701 Harbor Drive<br>San Diego, CA    92101<br>Attention:  John B. Bain | 1 |
| LTV Aerospace Corporation<br>P. O. Box 6267<br>Dallas, TX    75222<br>Attention:  K. R. Marsh | 1 |
| Republic Aviation Corporation<br>Fairchild-Hiller<br>Farmingdale, L. I., NY    11735<br>Attention:  G. Rosenthal<br>J. Lyttle | 1<br>1 |
| Purdue University<br>Lafayette, IN    47907<br>Attention:  Dr. J. C. Skifstad, Associate Professor<br>Mechanical Engineering | ·1 |
| NASA Scientific and Technical Information Facility<br>P. O. Box 33<br>College Park, MD    20740 | 9<br>plus reproducible |